AD480235

A RESEARCH INVESTIGATION OF THE FACTORS
THAT AFFECT THE SUPERCONDUCTING PROPERTIES OF MATERIALS .

FOREWORD

This report was prepared by the General Electric Research and Development Center, General Electric Company, Schenectady, New York under USAF Contract No. AF-33(657)-11722. The contract was initiated under Project No. 7371, Task No. 737102. The work was administered under the direction of the Air Force Materials Laboratory, Research and Technology Division, Mr. D.J. Evans, project engineer.

This report covers work from June 15, 1963 to October 15, 1965.

Research scientists who contributed to the work presented in this report are: CP Bean, TA Buchhold, RW DeBlois, W DeSorbo, RL Fleischer, CD Graham, HR Hart, Jr., JD Livingston, PJ Molenda, RL Rhodenizer, and PS Swartz.

The manuscript released by the authors November 15, 1965, for publication as an RTD Technical Report.

This technical report has been reviewed and is approved.

JULES I. WITTEBORT
Chief, Thermal and Solid State Branch
Materials Physics Division
AF Materials Laboratory

ii

ABSTRACT

The extension of the critical state model (Bean model) of the inhomogeneous type II superconductor to include alternating field excitation, alternating current excitation, and rotating field excitation is reported. The alternating current and alternating field losses in intermetallic high critical current density superconductors have been measured in several experimental situations and found to be substantially as predicted. The surface flux penetration and alternating field losses in niobium have been measured below H_{c1} as functions of temperature, field, and surface preparation. The concepts of the critical state model have been used to determine the conditions necessary for a magnetic instability or flux jump to develop in a type II superconductor. The theory suggests several ways of forestalling or eliminating flux jumps. These critical state model and instability concepts have been extended to include the prediction of the critical transport current, often found to be much less than the product of critical current density and area. The angular dependence of the critical field of the superconducting surface sheath above H_{c2} has been measured as a function of the Ginzburg-Landau parameter κ. The prediction of a surface barrier to the entry of flux into a type II superconductor in the case of a perfect surface is reported, and the experimental confirmation of this prediction is described. A new method has been developed for determining the critical current density of small amounts of superconducting material. A marked increase has been found in the critical current density of intermetallic type II superconductors following fast neutron irradiation, or irradiation-induced fission of impurity nuclei. (Critical current densities as high as 2×10^6 amp/cm^2 at 30 kOe have been obtained.) Preliminary studies attempting to determine the relationship between metallurgical structure on a local scale and the critical current density are reported. In the Appendices, the following extensions of the above contract-supported studies are reported: the discovery of surface superconductivity in the mixed state, rectification in type II superconductors, and a technical comparison of cryogenic normal metals and inhomogeneous type II superconductors.

TABLE OF CONTENTS

iv

LIST OF ILLUSTRATIONS

ix

xv

SECTION I

INTRODUCTION

This contract has been concerned primarily with fundamental studies of those superconductive properties that are important in the use of electrical equipment. In the technical summary report we present in detail all the work carried on under the contract. However, prior to presenting the technical reports, it seems appropriate to make a number of introductory comments. First, we shall present some general remarks about superconductors that will serve to very briefly introduce the terminology and concepts that will be used in the report. Second, we shall indicate how the field of superconductivity can be conveniently divided up into a number of categories, and show in this context how the program under the contract fits into the general framework. Finally, we shall mention briefly the more important accomplishments that have come out of the present work.

A. GENERAL COMMENTS

It has been learned in recent years that superconductors fall into two classes: type I superconductors and type II or "hard" superconductors, which differ in their behavior in a magnetic field. Further, it has been realized that a distinction must often be made between the bulk superconductive properties and the special surface properties of a superconducting system. The present work has been concerned largely with type II superconductors, and both bulk superconductivity and surface superconductivity have been studied.

The type I superconductors, typically metals such as pure lead, aluminum, tin, and indium (but not pure niobium), show the two unique properties of superconductivity: zero electrical resistivity and zero magnetic flux density, up to a single critical field H_c. For fields above H_c the material is in the normal state; the magnetic field penetrates throughout the bulk of the sample and the bulk electrical resistivity has the normal state value.

The properties of type II superconductors are more complex. Type II superconductors, which are typically alloys and compounds such as Nb-Zr, Pb-Tl, and Nb_3Sn (and, in addition, pure niobium), exhibit two bulk critical fields H_{c1} and H_{c2}. Below H_{c1} there are the two characteristic properties-- zero resistivity and zero flux density--while above H_{c2} the bulk exhibits the normal state behavior. Between H_{c1} and H_{c2} the material is in a "mixed" state, in which there is partial flux penetration and, depending on the metal-lurgical state of the sample and the measuring current density, there is an electrical resistivity less than that of the normal state, sometimes so small as to be negligible. For example, when a current is passed through a wire of type II superconductor, there is no voltage drop below a critical current; while above this critical current the voltage increases, first exponentially, and then linearly, until the wire is forced into the normal state by heating. In

1

many situations, instabilities force a premature catastrophic return to the normal state, and these important instabilities have been studied under this contract. ·

The magnetic flux penetration in the mixed state has been treated theoretically by Abrikosov.[1] In his model, the magnetic flux penetrates in the form of quantized fluxoids or flux threads that can move about freely within the material. The resulting, thermodynamically reversible, magnetization curve is shown in Fig. 1 as curve A. For an imperfect sample, one containing physical imperfections or chemical inhomogeneities, the flux threads cannot move freely enough to achieve the Abrikosov reversible behavior, magnetic irreversibility results, and the hysteretic behavior illustrated by curve B is obtained.[2] Through a model developed by Bean, and explained later in the report, this magnetic hysteresis can be related directly to the critical current densities and a-c losses of imperfect type II superconductors. These properties of fundamental importance to any technological applications of high field superconductors all depend on the inability of the flux threads to move freely in the imperfect specimen, and, therefore, on the fundamental interaction forces between flux threads and defects.
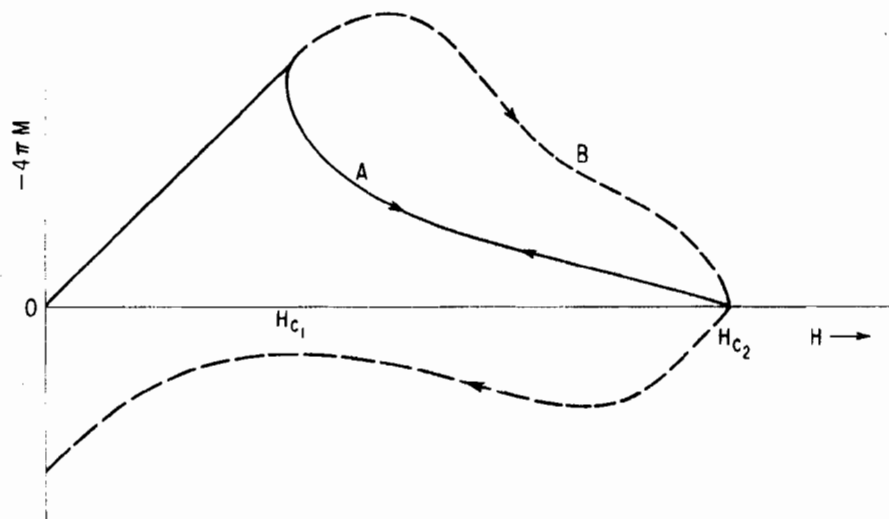
Figure 1 Schematic magnetization curves for type II superconductors. Curve A shows the reversible magnetization behavior characteristic of a homogeneous defect-free type II superconductor. Curve B shows an irreversible magnetization curve typical of an inhomogeneous type II superconductor, also called a hard superconductor. H_{c_1} is the field at which flux first penetrates the superconductor. Above H_{c_2} the interior or bulk properties of the material are those of the normal state.

We have also learned in recent years that superconductivity can sometimes persist on the surface of a sample above H_{c_2} or H_c, after the bulk of

2

the sample has returned to the normal state. This surface superconductivity is very sensitive to the direction that the applied magnetic field makes with the plane of the surface. For the field parallel to the surface, the surface critical field H_{c3} can be as high as nearly twice H_{c2}. Saint-James and deGennes[3] have predicted theoretically that $H_{c3} = 1.69\,H_{c2}$. Even below H_{c2} there is a layer of surface superconductivity that is quite different from the bulk mixed state superconductivity. This surface layer can lead to some surprising consequences, such as the partial rectification of transport super-currents. The interaction of the Abrikosov flux threads with the surface can also lead to a surface barrier to the entry of flux into the mixed state. Several different aspects of surface superconductivity will be discussed in later portions of this report.

B. PROGRAM UNDER THIS CONTRACT

Superconducting properties of materials can be conveniently divided into three categories as depicted in Fig. 2. The primary properties, such as transition temperature and the thermodynamic critical field, are equilibrium properties that are governed by the gross intrinsic parameters of the metal and are relatively insensitive to defect structure and composition. The primary properties are properly treated by the Bardeen-Cooper-Schrieffer theory of superconductivity.

```
┌─────────────────────────────────┐
│  PRIMARY  SUPERCONDUCTING        │
│     PROPERTIES ( e.g.,T_c )      │
└─────────────────────────────────┘
              │                        ┌──────────────────┐
              │                        │ ELECTRON MEAN    │
              │                        │   FREE PATH      │
              │                        └──────────────────┘
              ▼
┌─────────────────────────────────┐
│  SECONDARY  SUPERCONDUCTING      │
│ PROPERTIES ( e.g., H_c1 ,H_c2 ,H_c3 ) │
└─────────────────────────────────┘
              │                        ┌──────────────────┐
              │                        │ INHOMOGENEITIES  │
              │                        │    (DEFECTS)     │
              │                        └──────────────────┘
              ▼
┌─────────────────────────────────────┐
│  TERTIARY  SUPERCONDUCTING           │
│ PROPERTIES (e.g.,J_c ,AC LOSSES, FLUX JUMPING ) │
└─────────────────────────────────────┘
```
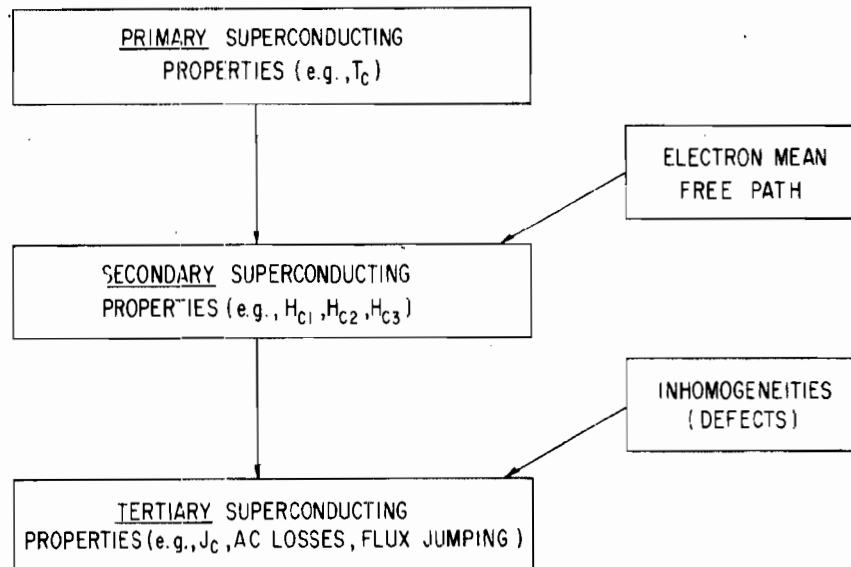
Figure 2 Superconducting properties divided into three categories. The present work is concerned mainly with the tertiary properties.

The secondary properties, such as the various critical fields, H_{c1}, H_{c2}, and H_{c3} of type II superconductors, also are equilibrium properties, and though they are intrinsic properties of defect-free materials, they are very composition-sensitive. The secondary properties are determined by

3

parameters of the material such as electron mean free path and the shape of the Fermi surface, and these properties are treated by the Ginzburg-Landau phenomenological theories of superconductivity.

The _tertiary_ superconducting properties, such as critical currents, hysteresis, flux jumps, a-c losses, are nonequilibrium properties that depend sensitively on specimen inhomogeneities and defects. The work done under this contract deals mostly with tertiary properties.

In the present work we have largely confined our attention to four specific areas:

1. Bulk a-c properties
2. Effect of defects on critical current density
3. Flux jump instabilities
4. Surface properties

1. A major goal of this contract has been to develop understanding of the a-c properties of imperfect type II superconductors. The theoretical approach was based primarily on the Bean model, which had already been shown capable of explaining the d-c magnetic behavior of such materials (Sections II, III, and IV of this report).

2. The fundamental material parameter of the Bean model is J_c, the bulk critical current density, which was known to depend on the interaction between flux threads and internal defects. Part of the present effort was directed at studying the effects on J_c of various intentionally introduced internal defects (Section V).

3. The major limitation to the general application of the original Bean model was known to be the existence of instabilities known as flux jumps that caused premature transitions to the normal state; hence a portion of the contract program was aimed at a fundamental understanding and description of this complex phenomena (Section VI).

4. The remainder of the program dealt with surface properties of type II superconductors, including study of the surface sheath above H_{c2}, the surface barrier to flux penetration above H_{c1}, and the anomalous a-c losses observed below H_{c1} (Sections III, IV-C, and VII).

Prior to the work presented here, Bean developed a phenomenological critical state model of a superconductor, which since has been recognized to be a good model for an inhomogeneous type II superconductor. The critical state model (which is reviewed in Section II-A-1) has proved extremely useful in understanding precisely those tertiary properties of interest under this contract. As indicated schematically in Fig. 3, the model can be used to treat

4

```
MAGNETIC          LOW FREQUENCY        CRITICAL
HYSTERESIS          A C LOSSES         TRANSPORT
                                        CURRENT

                                              FLUX
                                             JUMPING

                   BEAN'S
                CRITICAL STATE
                   MODEL

                    (J_c)

              DEFECT - FLUX THREAD
                 INTERACTION
```
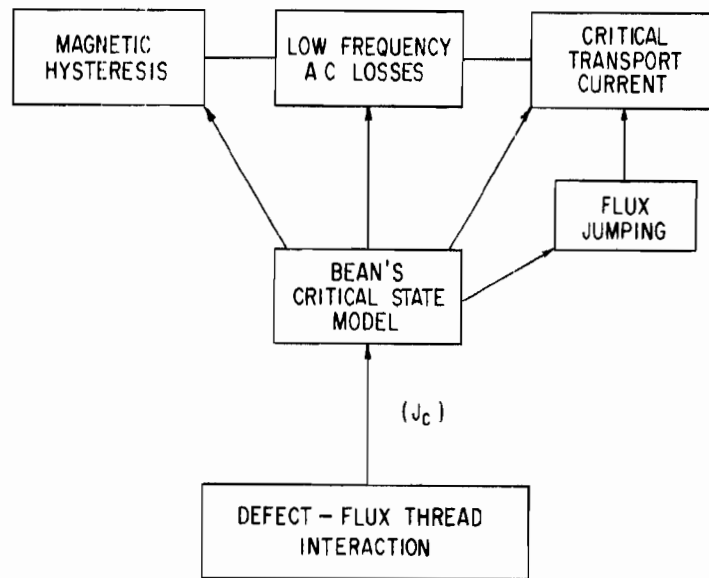
Figure 3 Relationship among tertiary superconducting properties, the Bean critical state model, and the concept of flux thread-defect interactions.

low-frequency a-c losses (Section II) and magnetic hysteresis (Section V-C). The Bean model has proved useful in understanding the phenomena of flux jumps (Section VI-A), and the occurrence of flux jumps in turn can limit the critical transport current (Section VI-B).

Although Bean's model was originally proposed on strictly phenomenological grounds, the model has gained support from the more recently developed concepts of flux thread-defect interactions that determine the critical current density, J_c. The connection between tertiary superconducting properties of interest under this contract and our studies of flux thread-defect interactions is quite apparent.

C. ACCOMPLISHMENTS UNDER THE CONTRACT

Although the complete work under the contract is presented in later portions of this report, it seems appropriate at this point to call attention to what we feel are the major accomplishments of the contract effort:

1. One of the main accomplishments of this contract has been the extension of the critical state model (Bean model) of the inhomogeneous type II superconductor to include (a) alternating field excitation, (b) alternating current excitation, and (c) rotating field excitation. The losses predicted for these various excitations have been tested in various experimental situations and found, within the assumptions of the theory, to be substantially as predicted. The concepts form the foundation for the design of electrical equipment using type II superconductors (Section II).

2. A primary result of this contract has been the measurement of the properties of niobium under excitation with alternating fields. These studies aim at the use of niobium for gyroscopic bearing and motor systems. The considerable advance in the art and science of preparing and understanding the properties of niobium may be grouped under the headings (Section III):

(a) Dependence of a-c losses on temperature

(b) Dependence of a-c losses on surface preparation

(c) Dependence of penetration depth on magnetic field

(d) Measurement of the London penetration depth in niobium.

3. The work supported under this contract led to independent discovery of superconductivity in a surface sheath of type II materials above the upper critical field of the bulk material. This phenomenon has been the object of many investigations by various groups throughout the world and has led to a more detailed understanding of the superconducting state (Section IV-C).

4. A new method has been developed for determining the critical current density of small amounts of superconducting material. This method measures the odd harmonic voltages induced by immersing the sample in an alternating magnetic field (Section V-B).

5. Pioneering experiments of the effects of fast neutron damage as well as internal fission on the current-carrying ability of type II super-conductors have been accomplished under this contract. Internal fission of uranium in V_3Si, in particular, has been shown to give the highest current-carrying capacity ($\sim 2 \times 10^6$ amp/cm^2 at 30 kOe) yet reported for any type II superconductor. These measurements rely on the voltage harmonic technique mentioned in the previous paragraph (Sections V-A and V-B).

6. This contract has supported some of the first studies attempting to determine the relationship between metallurgical structure on a local scale and current-carrying ability in inhomogeneous type II supercon-ductors. Preliminary measurements on martensitic systems, systems that exhibit spinodal decomposition, and simple precipitation systems indicate an important field for research and development. In particular, a concept of "differential diamagnetism" has emerged that can predict and explain minima in current density as a function of temperature (Section V-C).

7. The concepts of the critical state model have been used to determine the conditions necessary for a magnetic instability to develop in a type II superconductor. These magnetic instabilities (flux jumps) have limited

6

the use of these materials in solenoids as well as in their use in shielding and guiding magnetic fields. The theory now suggests several ways in which flux jumping can be forestalled or eliminated (Section VI).

8. For the first time, it has been possible to predict the transport current at which a type II superconductor prematurely returns to the normal state. It had been known for some time that type II superconductors often return to the normal state at a transport current much less than the "true critical current," which is the critical current density, J_c, times the cross-sectional area (Section VI).

9. One study, under this contract, led to the prediction of a surface barrier to the entry of flux into a type II superconductivity in the case of a perfect surface. Experiments carried out under the contract confirmed this prediction and the possibility of significantly lowering the losses in these materials under high alternating field excitation by appropriate surface treatment (Section VII).

Several studies, given in the Appendices of this report, have arisen as extensions of work supported under this contract. They include: (a) the discovery of surface superconductivity in the mixed state (Appendix A); (b) the discovery and explanation of rectification in type II superconductors (Appendix B), and (c) an evaluation of the relative technological advantages of cooled normal metals and inhomogeneous type II superconductors in the production of large alternating magnetic fields (Appendix C).

The contract work has benefited from a great amount of superconductivity research that has been carried on in the General Electric Research and Development Center both prior to and during the contract period. In Section IX is a list of publications relating to superconductivity that originated in the Center in recent years.

7

A-C LOSSES AND HEATING EFFECTS IN THE MIXED STATE

Practical high field superconductors, first announced in 1961, [4] have been very useful in the lossless generation of large steady magnetic fields. [5] Their impact would be greater yet if they could be used in alternating field applications. From the time of their discovery their magnetic hysteresis[6, 7] has indicated that power dissipation and consequent heat generation will exist in alternating magnetic fields. In order to guide one in assessing the losses in a high field superconductor under alternating field or alternating current conditions, we present in this report methods for calculating the power dissipation, tabulated results, and experimental confirmation. In addition, we shall calculate the heating and temperature rise to be expected in turning on or off a high field solenoid, or in testing a wire sample in a pulsed magnetic field. Though we shall not here use our methods to calculate the a-c losses in potential power frequency equipment, our results indicate that such losses are indeed significant and must be estimated in any potential design.

Throughout this section we assume the presence of magnetic fields sufficiently large that bulk flux penetration occurs (i.e., the material is in the "mixed state"). [1] Surface losses such as those found in niobium and lead in fields below H_{c1} and H_c, respectively, are considered in the next section.

A. THE CALCULATION OF A-C LOSSES USING THE CRITICAL STATE MODEL (H. R. Hart, Jr. and P. S. Swartz)

1. The Critical State Model

Soon after the demonstration of the high field capabilities of Nb_3Sn and of alloys such as Nb-Zr, Bean[7] found that a rather simple phenomenological model, here called the critical state model, allows one to predict the magnetic behavior of a high field superconductor in terms of a single empirical parameter. This model is the starting point of our calculation of the a-c losses and will thus be briefly reviewed. The basic assumption of the critical state model is that a changing field induces persistent currents up to a limiting or critical current density, J_c. These persistent currents are induced to flow according to Lenz's law[8] in such a way as to minimize the change in the flux linking the sample. A superconductor carrying this limiting current density is said to be in the "critical state."

A concise way of treating the critical state behavior of a high field superconductor is to use the nonlinear electric field-current relation illustrated in Fig. 4. Here the assumption is made that the electric field vector is zero for current densities less than J_c, but rises vertically at J_c, with the vector E parallel to J. Thus a material cooled through the superconducting transition with no transport current flowing has E and J zero everywhere. However, as

9

E

−J_c

0   +J_c J

$\vec{E} \parallel \vec{J}$
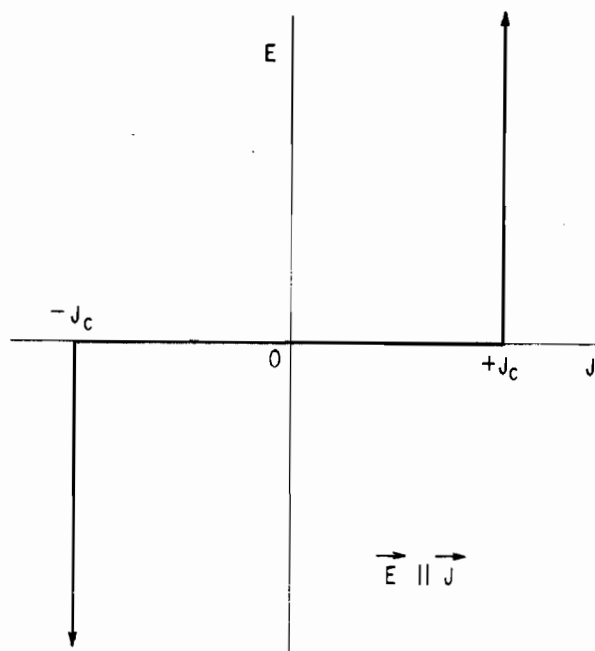
Figure 4 A plot of the nonlinear electric field (E), current density (J) re-
lation assumed in the critical state model.

soon as currents are applied or the magnetic field is changed, transient
electric fields and, thereby, currents of magnitude J_C are induced in portions
of the material. Maxwell's equations plus the characteristic E-J relation-
ship illustrated in Fig. 4 determine the current and field distributions and
thus the heating or power loss.

The critical current density J_c was assumed for simplicity by Bean to be
independent of magnetic field. Over the limited magnetic field range used by
Bean in his experimental tests of the model, the assumption of constant .
critical current density was sufficient to provide excellent agreement between
theory and experiment. Kim, Hempstead, and Strnad, [9] who carried out .
experiments over a much larger range of magnetic fields, introduced a field
dependent critical current density. They found a good approximation to be
$J_C(T, H) = \alpha_C(T)/[B_0(T)+H]$ where H is the applied (transverse) field and
$\alpha_C(T)$ and $B_0(T)$ are empirically determined parameters of the material,
depending strongly on the metallurgical structure of the material. The simple
critical state model allows us to develop analytical expressions for the
magnetic hysteresis of high field superconductors in excellent agreement
with experiment. The knowledge of the magnetic hysteresis allows us to
predict the a-c losses or heat generation in an alternating field.

The application of the critical state model to the calculation of the current
distribution in a wire fed from a current source enables us to calculate the
loss associated with a current flow in a wire. London has published a similar
calculation. [10] Our results agree whenever there is overlap.

10

The phenomenological critical state model received a more physical basis when Anderson introduced his theory of flux creep.[11] In the Abrikosov mixed state of an ideal reversible type II superconductor, the flux filaments are free to move about within the material and are subject only to their mutual repulsive interactions. Nonuniform distributions of flux filaments, equivalent to field gradients or bulk currents, disappear quickly in such a superconductor. Magnetic hysteresis or persistent bulk currents in a mixed state superconductor occur when the motion of the flux filaments is limited by the structure of the material, pinned, for example, by voids, normal inclusions, dislocations, grain boundaries, or compositional variations. According to Anderson, a finite energy barrier is associated with such defects. The flux filament can pass over the barrier if the sum of the thermal energy and an energy equal to the product of the force on it times the distance between barriers is equal to or greater than the barrier energy. This motion is called thermally activated flux creep; the effective barrier energy is equal to the defect energy barrier reduced by the effect of the magnetic pressure gradient or Lorentz force JH acting on one flux filament or a bundle of them.

The flux creep theory predicts that field gradients decay logarithmically with time. This logarithmic decay of field differences has been observed by Kim, Hempstead, and Strnad[12] in several tubes formed of different high field superconductors. The "critical state" is simply the field configuration for which the rate of decay has become so slow as to be unobservable within the time and sensitivity of the experiment. This theory leads to a temperature and field dependence of the critical current density, $J_cH = a-bT$, very close to that observed experimentally.

In the region near the critical state, the effective barrier energies are large compared with kT, and the rate of flux creep is governed by an extremely strong exponential of JH. However, when JH is sufficiently large (as might occur transiently), the effective barrier is no longer large compared with kT, and "flux flow" rather than flux creep occurs. The rate of flux motion becomes linear in JH rather than exponential and ultimately approaches the rate governed by the mixed state flow resistivity. The region of flux flow has recently generated much interest and is now reasonably well understood.[13,14] (See also Appendix A.)

2. Convenient Methods of Calculating Losses

We shall describe several convenient methods of calculating the losses, give three sample calculations, tabulate some results for pertinent geometries, and finally discuss the limitations and approximations involved in these calculations. The system of units will be a hybrid practical-cgs system. The commonly used symbols, definitions, and units are listed in Table I.

11

TABLE I

Definitions, Equations, and Units

Symbol	Definition	Units
---	Distance	Centimeter
---	Mass	Gram
t or τ	Time	Second
f	Frequency ($\omega = 2\pi f$)	Cycles/sec
T	Absolute temperature	°K
I	Current	Ampere
J	Current density	Amp/cm^2
V	Voltage	Volt
E	Electric field	Volts/cm
H	Magnetic field	Oersted
B	Magnetic flux density	Gauss
M	Magnetization	Gauss or Oe
φ	Magnetic flux	Gauss-cm^2
ρ	Electrical resistivity	Ohms
P	Power	Watts
K	Thermal conductivity	Watts/cm°K

Electromagnetic equations in the forms needed for our problems are:

$$\nabla \times \vec{H} = 4\pi \vec{J}/10 \qquad \nabla \cdot \vec{B} = 0 \qquad \vec{B} = \vec{H} + 4\pi\vec{M}$$

$$\nabla \times \vec{E} = -\frac{\partial \vec{B}}{\partial t} \times 10^{-8} \qquad \oint_{\text{loop}} \vec{E} \cdot d\vec{\ell} = -10^{-8} \int_{\text{area}} \frac{\partial \vec{B}}{\partial t} \cdot d\vec{A}$$

(a) If a sample is placed in an alternating magnetic field, the heat generated or power dissipated can be calculated from the area enclosed within the magnetic hysteresis loop. (See Table I for definitions.)

$$P = \frac{f}{4\pi} \cdot 10^{-7} \int_{\text{Volume}} dV \oint_{\text{Complete cycle}} \vec{H} \cdot d\vec{B}$$

We thus need to know B(H, r) for the cyclic steady-state condition.

(b) If the sample is subjected to an alternating current or field, the loss can be calculated by integrating the Poynting vector over the sample surface and over a complete steady-state cycle. The Poynting vector, $(10/4\pi)$ E x H, is the instantaneous energy flow per cm^2 (watts/cm^2). Thus:

$$P = \oint_{\text{Cycle}} dt \int_{\text{Surface}} \frac{10f}{4\pi} (\vec{E} \times \vec{H}) \cdot d\vec{\sigma}$$

where $d\vec{\sigma}$ is the differential element of area normal to the surface. We thus need to know $\vec{E}(\omega t)$ and $\vec{H}(\omega t)$ at the surface only.

(c) In the third method, again applicable to both currents and fields, the electric field E is calculated as a function of position and time, and the local power dissipation is calculated by integrating $\vec{E} \cdot \vec{J}$ over a cycle. (This method is particularly useful in the Bean model in which J is always zero or $\pm J_c$.) For a wire, one can similarly calculate the instantaneous voltage drop, multiply by the instantaneous current, and integrate over a cycle. In all of these methods one has to wait until the starting transient is over and steady cyclic behavior is obtained.

These three methods are fundamentally the same; the particular application dictates which method is most convenient and direct.

To use these methods to calculate the losses in a high field material, however, one must know the field or current distribution throughout the cycle. Here a theoretical model or an empirical E(J) relation is needed. We shall use the critical state model, usually stated in its simplest form, i.e., J_c a constant. The assumptions and limitations implicit in our approach will be discussed in a later section.

3. Calculations of A-C Losses in Slabs and Wires Using the Critical State Model

This section contains some illustrations of methods for calculating a-c losses from the critical state model. The first example is that of a plane slab placed in an alternating magnetic field parallel to its surface. Since the form of the expression for the losses depends on whether or not the alternating component of the applied magnetic field is of sufficient magnitude to penetrate to the midplane of the slab, the cases of small and large alternating magnetic fields will be treated separately. Another example concerns the losses in a wire to which a-c currents are applied. In all of the following calculations we use the Bean critical state model; the critical current density J_c is assumed to be constant.

Example I: Losses in Plane Slabs Subjected to Small A-C Magnetic Fields

Consider a plane slab of thickness 2a cooled through the transition in a magnetic field $H_{c1} < H_a < H_{c2}$. By arguments given earlier, no bulk transport currents will be induced by this cooling procedure. If we now apply an additional magnetic field H directed parallel to the surface plane, currents are induced to flow in such a direction as to oppose the change in magnetic field (Lenz's law). The current density at any point within the bulk is limited to its critical value J_c. Thus the field is not totally excluded from the interior, but instead penetrates to a distance δ, which is calculable from the Maxwell equation

$$\vec{\nabla} \times \vec{H} = 4\pi J/10.$$

In one dimension this expression reduces to

$$\left|\frac{\partial H}{\partial X}\right| = 4\pi J_C/10$$

and reveals that the field gradient is of constant slope, $4\pi J_C/10$, and that

$$\delta = \frac{10H}{4\pi J_C} \ .$$

The "small" a-c magnetic fields discussed in this example are those whose peak values are H_0 is less than $4\pi J_C a/10$ and consequently those which do not penetrate to the center of the specimen. The field and current distributions in small increasing magnetic fields are shown in the uppermost diagrams of Fig. 5.

As the applied field is decreased, the limiting current density J_C is again induced to flow in the direction that opposes the change in magnetic field. This situation is depicted by the second diagram in Fig. 5. When the alternating field is finally reduced through zero to its maximum value in the opposite sense, the direction of the critical current is completely reversed. Following this line of reasoning throughout a cycle of magnetic field will enable us to write the expressions for flux penetration as a function of applied field. Let the alternating field vary according to the expression

$$H = H_0 \sin \omega t \ .$$

The losses are now calculated by integrating the Poynting vector $10\vec{E} \times \vec{H}/4\pi$ over one cycle. H is simply the applied magnetic field and E is calculated from the relationship

$$\oint_{\text{Loop}} E \cdot d\vec{\ell} = -10^{-8} \int_{\text{Area}} \frac{\partial \vec{B}}{\partial t} \cdot d\vec{A} = -10^{-8} \frac{d\varphi}{dt} \ .$$

We begin this integration per unit length of surface at $\omega t = \pi/2$ to avoid the "starting transient." The flux penetrating the sample is the area under the H vs x diagrams in Fig. 5 and is given by the expression

$$\varphi(t) = 2\left[\frac{10H_0^2}{8\pi J_C} - \frac{10H_0^2(1-\sin \omega t)^2}{16\pi J_C}\right] \qquad \frac{\pi}{2} \leqslant \omega t \leqslant \frac{3\pi}{2} \ .$$

For the second half-cycle, $\varphi(t)$ is given as

$$\varphi(t) = 2\left[-\frac{10H_0^2}{8\pi J_C} + \frac{10H_0^2(1+\sin \omega t)^2}{16\pi J_C}\right] \qquad -\frac{\pi}{2} \leqslant \omega t \leqslant \frac{\pi}{2} \ .$$

14

I. MAGNETIC FIELD APPLIED TO A PLATE
a. INITIAL FIELD INCREASE
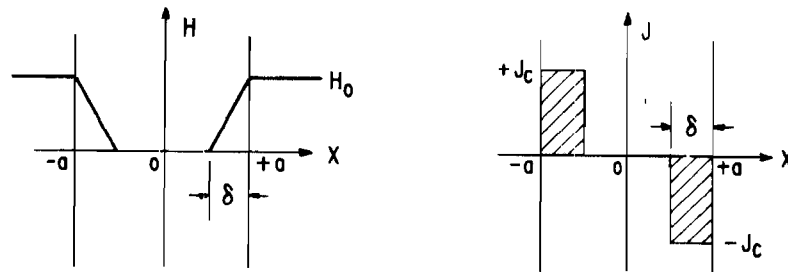
b. DECREASING FIELD AFTER FIELD MAXIMUM
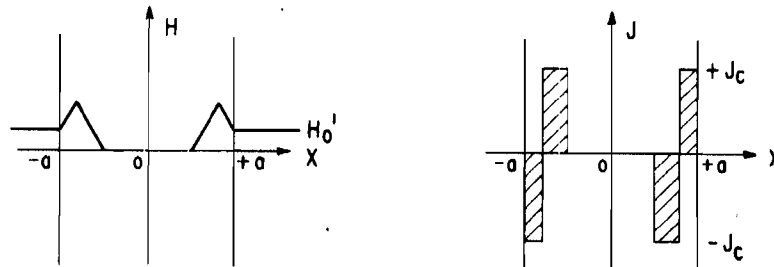
II. CURRENT APPLIED TO A CYLINDRICAL WIRE
a. INITIAL CURRENT INCREASE
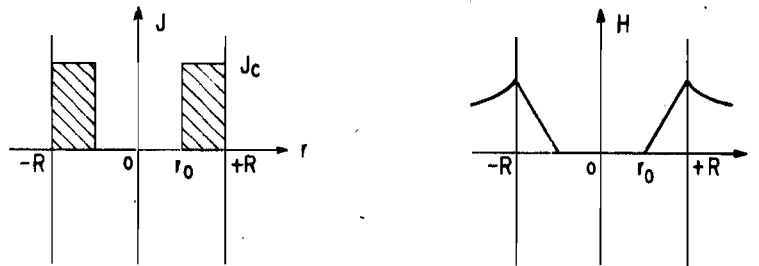
b. DECREASING CURRENT AFTER CURRENT MAXIMUM
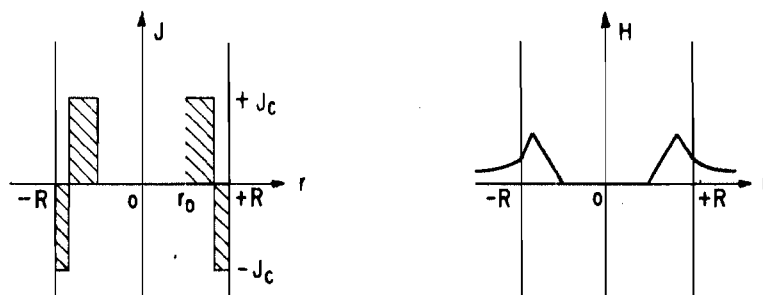
Figure 5 Schematic diagram of the magnetic field and critical current distribution in plates subjected to a-c magnetic fields and in wires through which a-c currents are passed.

We obtain then for $\dfrac{d\varphi}{dt}$

$$\frac{\partial\varphi}{dt} = \frac{5\omega H_0^2(1-\sin\omega t)(\cos\omega t)}{2\pi J_c} \qquad \frac{\pi}{2} \leqslant \omega t \leqslant \frac{3\pi}{2}$$

and

$$\frac{d\varphi}{dt} = \frac{5\omega H_0^2(1+\sin\omega t)(\cos\omega t)}{2\pi J_c} \qquad -\frac{\pi}{2} \leqslant \omega t \leqslant \frac{\pi}{2} \quad .$$

Substituting these values for E and H into the expression for the Poynting vector and integrating over one cycle, one obtains for the loss in joules/cycle/ cm² of surface area the expression

$$\frac{5 \times 10^{-7}\, H_0^3}{12\pi^2 J_c} \quad .$$

If, in this example, we had assumed $J_c H$ a constant instead of J_c a constant, we would have found that the losses varied as H_0^4. (We have called this the Kim limit.)

Example II: Losses in Plane Slabs Subjected to Large A-C Magnetic Fields

Large a-c magnetic fields are defined here as fields whose maximum amplitudes are much greater than $4\pi J_c a/10$. The loss/cycle is calculated from the expression

$$\text{Loss/cycle} = \frac{10^{-7}}{4\pi} \int_{\text{Volume}} dV \int \vec{H} \cdot d\vec{B} = \frac{10^{-7}}{4\pi} \cdot \left\{\begin{array}{l}\text{Area enclosed}\\\text{within the B-H Loop}\end{array}\right\}$$

Under the condition that $H \gg 4\pi J_c a/10$, the induced current density for $x>0$ is $-J_c$ over essentially the entire period that the magnetic field is increasing. Similarly, the induced current density for $x>0$ is everywhere equal to J_c when the applied field is decreasing. We can write for the average flux density B within the specimen:

$$\bar{B} \cong H_0 \sin\omega t - \pi J_c a/5 \qquad -\frac{\pi}{2} < \omega t < \frac{\pi}{2}$$

and

$$\bar{B} \cong H_0 \sin\omega t + \pi J_c a/5 \qquad \frac{\pi}{2} \leqslant \omega t \leqslant \frac{3\pi}{2} \quad .$$

The enclosed loop in the BH plane is simply a parallelogram of area

$$4\pi J_c a H_0/5$$

16

and the loss in joules/cycle/cm^3 is given as

$$10^{-7}a\,H_0 J_C/5 \; .$$

One of the important features of this result is that the loss per unit volume increases with the thickness of the plate.

Example III: Losses in Wires Carrying Small Impressed A-C Currents

Let us assume a current varying according to the expression $I = I_0 \sin \omega t$ and let us restrict the maximum amplitude to be much less than the critical current $\pi R^2 J_c$. The field and current distribution that pertains is shown in the bottom half of Fig. 5. As the currents are increased from zero, they will flow near the surface of the specimen in accordance with Lenz's law.* The depth $(R - r_0)$ to which currents flow can be calculated from the expression

$$I = \pi(R^2 - r_0^2)J_c \; .$$

The losses in this case are given by the dot product of the current and voltage, integrated over one cycle. The voltage is given by the expression

$$\oint_{\substack{\text{Loop} \\ (r=0 \text{ and } r=R)}} \vec{E} \cdot d\vec{l} = E(R) = -10^{-8} \int_0^R \frac{\partial B(r)}{\partial t} \, 2\pi r \, dr$$

where $B(r)$ is the magnitude of the internal magnetic field created by the applied current. After the initial transient has died down ($\omega t = \pi/2$ and $I = I_0$), the internal magnetic field is given as

$$B(r) = 0 \text{ for } r \leqslant r_a,$$

where

$$J_c \pi(R^2 - r_a^2) = I_0,$$

and

$$B(r) = (r-r_a)\, 4\pi J_c/10 \text{ for } r_a \leqslant r \leqslant R \; .$$

---

*This fact is not immediately obvious, but can be shown to be correct from the following argument: If the applied current were to move to the interior of the wire, say, to its axis, the field generated in the interior of the wire by this current would induce a countercurrent to flow at the axis, just balancing the applied current. This countercurrent would return at the surface, in effect transferring the applied current to the surface.

In the present limit that I_0 is much less than the critical current for the wire, the total flux linking the wire at $\omega t = \pi/2$ is given as $(R - r_a)^2 \pi J_c/5$. Over one current cycle, the flux linking a unit length of wire is given as

$$\varphi(t) = \frac{(R-r_a)^2 \pi J_c}{5} - \frac{(R-r_a)^2 \pi J_c (1-\sin \omega t)^2}{10} \qquad \frac{\pi}{2} \leq \omega t \leq \frac{3\pi}{2}$$

$$\varphi(t) = -\frac{(R-r_a)^2 \pi J_c}{5} + \frac{(R-r_a)^2 \pi J_c (1+\sin \omega t)^2}{10} \qquad -\frac{\pi}{2} \leq \omega t \leq \frac{\pi}{2}$$

and

$$10^8 \cdot E = -\frac{\partial \varphi(t)}{\partial t} = -\frac{2\pi\omega J_c (R-r_a)^2 (1-\sin \omega t) \cos \omega t}{10} \qquad \frac{\pi}{2} \leq \omega t \leq \frac{3\pi}{2}$$

$$10^8 \cdot E = -\frac{\partial \varphi(t)}{\partial t} = -\frac{2\pi\omega J_c (R-r_a)^2 (1+\sin \omega t) \cos \omega t}{10} \qquad -\frac{\pi}{2} \leq \omega t \leq \frac{\pi}{2}.$$

By substituting these expressions for E into the dot product of E and I and integrating over a cycle, one obtains for the loss in joules/cycle/cm length of wire the expression

$$\frac{2I_0^3 \times 10^{-9}}{3\pi R^2 J_c} .$$

If, in this example, we had assumed $J_c H$ a constant instead of J_c a constant, we would have found that the losses varied as I_0^4.

Tabulation of Results

In Table II we have summarized some of the more important results calculated from the critical state model. We have included the equation giving the losses for a wire carrying a-c current up to and including the critical current. Note that the loss per cycle is independent of frequency; the power dissipated is thus linear in frequency. Some of these results have been calculated independently by London.[10]

TABLE II

Critical State Model Loss Predictions (Using J_c Independent of H)

A. Magnetic Field, $H = H_0 \sin \omega t$

1. Plane slab (thickness 2a), field parallel to surface:

   (a) $H_0 \leq 4\pi J_c a/10$

   Loss/cycle/unit area for one side $= \dfrac{5H_0^3 \times 10^{-7}}{12\pi^2 J_c}$ joules/cycles/cm^2

18

TABLE II (continued)

(b) $H_0 \gg 4\pi J_c a/10$

Loss/cycle/unit volume $= 10^{-7} a J_c H_0/5$ joules/cycle/cm^3

2. Cylinder (radius R), field parallel to axis:

(a) $H_0 \ll 4\pi J_c R/10$

Loss/cycle/unit area $= \dfrac{5 \times 10^{-7} H_0^3}{12\pi^2 J_c}$ joules/cycle/cm^2

(b) $H_0 \gg 4\pi J_c R/10$

Loss/cycle/unit volume $= 2 \times 10^{-7} R J_c H_0/15$ joules/cycle/cm^3

B. **Current in a Wire of Radius R; $I = I_0 \sin \omega t$**

(a) $I_0 \ll \pi R^2 J_c$

Loss/cycle/unit length $= \dfrac{2 \times 10^{-9} I_0^3}{3\pi R^2 J_c}$ joules/cycle/cm

(b) $I_0 = \pi R^2 J_c$

Loss/cycle/unit length $= 2 \times 10^{-9} I_0^2$ joules/cycle/cm

(c) $0 \leq I_0 \leq \pi R^2 J_c$

Loss/cycle/unit length $=$

$$2 \times 10^{-9} I_C^2 \left\{ 2 \left[1 - \frac{I_0}{I_C}\right] \ln \left[1 - \frac{I_0}{I_C}\right] + \frac{I_0}{I_C} \left[2 - \frac{I_0}{I_C}\right] \right\}$$

joules/cycle/cm where $I_C = \pi R^2 J_c$.

C. **Magnetic Field $H = H_0 \sin \omega t$; Current $I = I_0 \sin \omega t$ (T. A. Buchhold)**

1. Plane slab (thickness 2a) field parallel to surface and perpendicular to current:

(a) $H_0 \gg \dfrac{4\pi}{10} J_c a$

Loss/cycle/unit volume $= \dfrac{1}{5} \times 10^{-7} a J_c H_0 \left(1 + \dfrac{\alpha^2}{3}\right)$ joules/cycle/cm^3

where $I_0 = 2\alpha a J_c = \alpha I_{max}$.

(Note that little error would be made in this case by neglecting the contribution of I_0.)

D. **A-C Solenoid Wound from Thin Foils**

For: Number of turns $\gg 1$,

Thickness of winding $\ll$ Coil diameter, D_0,

19

TABLE II (continued)

Foil thickness = d

Alternating field on the coil axis = $H_c \sin \omega t$,

Alternating foil current per unit length:

$$I_F = \alpha d J_c \sin \omega t = \alpha I_{max} \sin \omega t$$

Coil length $\gg D_0$

Loss/cycle/unit length $\dfrac{1}{8} \times 10^{-7} \, D_0 H_c^2 \, d \, \dfrac{(1+\alpha^2/3)}{\alpha}$ joules/cycle/cm.

4. Assumptions and Limitations in the Use of the Critical State Model for A-C Applications

(a) Assumptions and Limitations in the Critical State Model Common to A-C and Static Applications

(i) We have assumed that the magnetic behavior of a high field superconductor can be characterized by a bulk critical current density J_c. In one form of the model this current density is assumed independent of field; in another, a simple relation between J_c and H is assumed. Numerous static (i. e., very slowly cycled, usually by hand) magnetization experiments involving bulk samples and appreciable fields have indicated rather good agreement with these models. In two experiments on $V_3 Ga$, we have found that the model breaks down for sufficiently small a-c fields (~100 Oe). There are thus limitations on the applicability of the model in very small alternating fields.

(ii) In using the critical state model for real materials we assume that we are in the mixed state throughout the cycle. Only when a small alternating field is applied to a sample in the appropriate steady bias field does this condition hold. For high field superconductors in zero steady field, the error in this assumption is small only if the lower critical field, H_{c1}, is much smaller than the alternating field applied during the cycle. The lower critical fields of the ordinary high field superconductors are less than 500 Oe.

(iii) In using the model we have assumed that no flux jumping occurs during the cycle. Empirically, flux jumps often occur more readily under a-c conditions than under static conditions; this may limit the usefulness of some materials under a-c conditions. The important area of flux jumping or instability is covered in a later section.

(iv) We have assumed that the sample is homogeneous, i. e., that the critical current density does not change through the region of field penetration. We are thus implicitly assuming that the surface barriers of Section VII and Appendices A

20

and B are weak in comparison with the bulk critical current densities, an assumption which seems very reasonable for practical high field superconductors in their present forms.

(b) Limitations in the Use of the Critical State Model Unique to A-C Conditions

(i) We assume that the temperature rise in the sample is negligible. Since the critical current density J_c is a function of temperature, the use of J_c determined from static measurements in a-c situations assumes no temperature rise. Since heating does occur under a-c conditions and since the thermal conductivities of high field superconductors are low, the temperature rise may be significant. Bean has calculated the temperature rise for a simplified model--when J_c and K, the thermal conductivity, are constants. He finds for a magnetic field applied parallel to a plane slab:

$$T_{max} - T_{bath} = \frac{10^{-5} \omega H_0^4}{3(4\pi)^4 K J_c^2} \quad .$$

This calculation holds in the low field limit.

In the low field limit an appreciable temperature rise will cause the power dissipation to increase faster than the third power of field or current. This is because the critical current density will be lowered progressively as the power dissipation is increased.

(ii) We have assumed that the dynamic and static critical current densities are the same. By referring to Fig. 6, a typical plot of E vs J for a real high field superconductor, let us discuss the variation of J_c with experimental conditions. The E(J) relation assumed for the critical state model was shown in Fig. 4. In the latter we see that $|J|$ is a constant, J_c, independent of E for $E \neq 0$. For the real material that this is not strictly true.

Let us calculate the change in J as a function of excitation field and frequency for a simple geometry. Consider a semi-infinite plane interface between a high field superconductor and the bath. We shall apply an alternating field $H_0 \sin \omega t$ in the z-direction parallel to the plane of the surface. Referring to Table I, we find

$$10^{-8} \frac{d\varphi'}{dt} = -E_{surface}$$

where φ' is the flux per unit length within the superconductor. From Bean's model (see Fig. 5) we would expect the maximum flux penetration to be:

$$\varphi'_{max} = \frac{\delta \cdot H_0}{2} = \frac{10 H_0^2}{8\pi J_c} \quad .$$

21
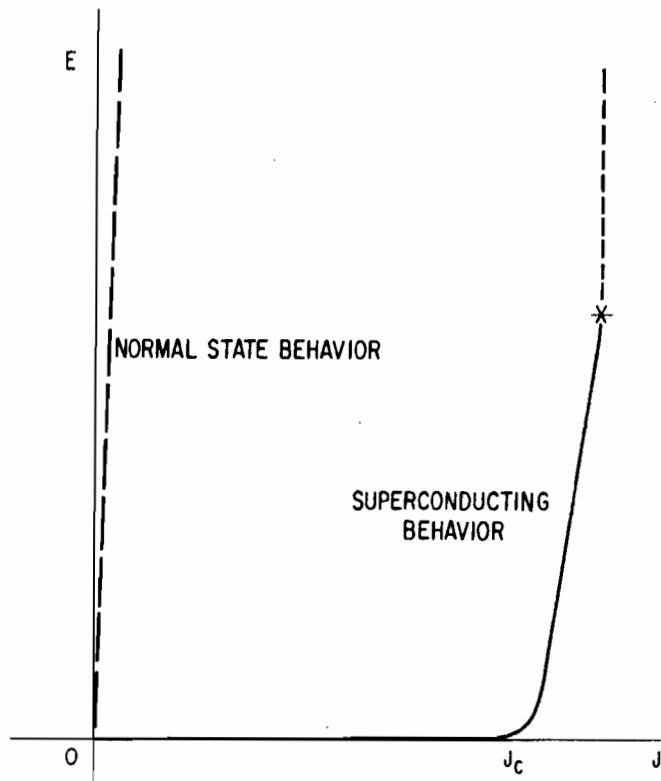
Figure 6 A plot for a typical high field superconductor of the electric field E as a function of the current density J. Near the critical current density J_c, the electric field increases with current density, first exponentially, then linearly until the point (indicated by the cross) where heating forces a catastrophic return to the normal state.

We thus find the electric field for the sample to be:

$$|E^*_{surface}| \lesssim 10^{-8} \cdot 2\pi f \cdot \frac{10 H_0^2}{8\pi J_c}$$

$$\text{or} \quad |E^*_{surface}| \lesssim 10^{-8} \cdot \frac{5 f H_0^2}{2 J_c} \quad .$$

This E^* is an upper limit, but also a typical value for E within the sample. Let us characterize the operating point as E^*, J^*. We can now answer the question: Does the absolute value of J vary appreciably during the cycle? If it does, the critical state model will fail to predict the correct power loss.

The condition required is $\Delta J/J \ll 1$. We may write

$$\Delta J \lesssim \left. \frac{\partial J}{\partial E} \right|_{E^*, J^*} \cdot E^* \quad .$$

22

Therefore, our condition becomes

$$\frac{E^*}{J^*} \cdot \frac{\partial J}{\partial E}\bigg|_{E^*, J^*} \ll 1,$$

or, inverting for convenience:

$$\frac{\partial \ln E}{\partial \ln J}\bigg|_{E^*, J^*} \gg 1$$

where E^* has been calculated from the relation derived earlier. This simple requirement on the steepness of the E-J plot will be considered for real materials at the end of the next section.

(iii) <u>We have assumed that the response of the current field distribution to a change in applied field or current is instantaneous.</u> If there is a time lag in the response approaching $1/2\pi f$, i.e., an appreciable fraction of a cycle, the prediction of the critical state model will again be in error. Certainly for normal metals, where $E = \rho J$, there can be an appreciable time lag. The a-c skin depth is the result of such a lag in response. Are such effects present in high field superconductors?

We shall discuss such effects using again the geometry of the previous Section (ii) and Fig. 6. To discuss the limiting response time, let us say somewhat arbitrarily that the time τ_δ for a change H_0 in applied surface field to penetrate a depth $\delta = 10 H_0/4\pi J_c$ should be much less than $1/2\pi f$.

To calculate τ_δ from $E(J)$ and Maxwell's equations, let us restrict ourselves to the above plane interface in which the magnetic field is parallel to the surface and the z-axis. The x-axis is perpendicular to the plane. We shall assume that $B \simeq H$ for the underlying type II superconductors, a good assumption for an ordinary high field superconductor at fields well above H_{c1}. The first two of Maxwell's equations (Table I) then reduce to:

$$-\frac{\partial H}{\partial x} = \frac{4\pi J}{10}$$

and

$$\frac{\partial E}{\partial x} = -\frac{\partial H}{\partial t} \cdot 10^{-8} .$$

Let us differentiate the upper equation with respect to x, obtaining:

$$\frac{\partial^2 H}{\partial x^2} = -\frac{4\pi}{10} \cdot \frac{\partial J}{\partial x} .$$

Rewriting the second equation we obtain:

$$\frac{\partial E}{\partial x} = \frac{\partial E}{\partial J} \cdot \frac{\partial J}{\partial x} = -\frac{\partial H}{\partial t} \cdot 10^{-8} \ .$$

Combining the last two equations we get:

$$\frac{\partial H}{\partial t} = \frac{10^9}{4\pi} \left(\frac{\partial E}{\partial J}\right) \frac{\partial^2 H}{\partial x^2} \ .$$

In the normal state, where $E = \rho J$ and $\partial E/\partial J = \rho$, the above equation becomes a linear diffusion equation in which the diffusion constant D is $10^9 \rho/4\pi$. In our case the $E(J)$ relation is nonlinear and a linear diffusion equation does not result. However, for rectangular coordinates and for small excursions about the operating point (E^*, J^*) we can estimate the time lag, τ_δ, by a diffusion equation approximation:

$$\frac{\partial H}{\partial t} = \frac{10^9}{4\pi} \left(\frac{\partial E}{\partial J}\right)_{E^*, J^*} \cdot \frac{\partial^2 H}{\partial x^2}$$

$$D = \frac{10^9}{4\pi} \left(\frac{\partial E}{\partial J}\right)_{E^*, J^*} \ .$$

For flux diffusion, [15] the distance a change in flux travels in a time t is $X = \sqrt{2Dt}$; thus the time necessary for the change in flux to travel δ is $\sqrt{2D\tau_\delta}$. (For the normal state the a-c skin depth is, in fact, the distance the flux diffuses in a time $1/2\pi f$. At this depth the time lag or phase shift is appreciable.)

For the high field superconductor we therefore require:

$$\delta^2/2D \ll 1/2\pi f.$$

Substituting in the above inequality to obtain the result in terms of E^* (where $|E^*| \sim 5 \times 10^{-8} f H_0^2/2J_c$ and J^* (where $J^* \sim J_c$), we obtain the required condition:

$$\left.\frac{\partial \ln E}{\partial \ln J}\right|_{E^*, J^*} \gg 1 \ .$$

This is the same condition of the logarithmic slope of $E(J)$ as found in Section (ii) above.

The order of magnitude calculations in the last three subsections indicates that if the logarithmic slope is much greater than unity at the operating point, and if there is negligible heating, the critical state model using J_c determined

24

statically should give reliable estimates of the a-c losses. This is true, of course, only if the critical state model is a good representation of the static magnetic behavior of the material.

From measurements of the voltage drop along a wire as a function of current we can estimate the logarithmic slope of $E(J)$. These estimates will be of limited usefulness because we really do not know the applicable E^*, J^* operating points. As emphasized by Kim et al. [16] the voltage drop may be very nonuniform along the wire; in addition these measurements may not be isothermal. With these reservations we consider Nb-Zr and Nb_3Sn. The data of Kim et al. [16] for Nb-Zr wires in fields of about 3000 Oe show that just below the catastrophic transition current $\partial \ln E / \partial \ln J \gtrsim 5$, whereas for currents two-thirds as large $\partial \ln E / \partial \ln J \sim 20$. For Nb_3Sn we use the unpublished measurements of C.H. Rosner made on GE process Nb_3Sn wires. Here, at 50,000 Oe, at currents about 1% below the transition current, $\partial \ln E / \partial \ln J > 100$; at currents 1.5% to 2.0% below the transition current the logarithmic slope has increased to greater than 400. Thus we would expect that Nb_3Sn satisfies our requirement quite well while Nb-Zr might show small deviations from the critical state model a-c predictions.

The rough argument of this and the previous sections were developed before the details of flux flow were well characterized. A more recent, more exact, treatment of a special case is given by Bean in the next section. The conclusion remains that for power frequencies the critical state model should be applicable.

B. REFINEMENTS IN THE APPLICATION OF THE CRITICAL STATE MODEL TO A-C LOSSES AND HEATING (C. P. Bean)

1. Time Dependence of Flux Penetration in Inhomogeneous Type II Superconductors

The essence of the critical state model for calculating the quasi-static magnetic properties of inhomogeneous type II superconductors is the assumption of a static friction to the motion of flux. This static friction may be expressed as a critical current density or equivalently by Ampere's law as a curl of H or gradient of flux. In the calculation of dynamic properties, however, one must use the concept of a dynamic friction. Figure 7 shows in a schematic fashion the results of measurements of the current density as a function of electric field [13] in type II superconductors. Identifying the electric field with the velocity of flux motion and the current density with the gradient of flux, we see, following Kim, Hempstead, and Strnad, that a close approximation to experimental situation is obtained by assuming a critical current, J_c, and flux-flow resistance, ρ_F. The transition from the static to dynamic state is experimentally not abrupt as implied in this approximation but is continuous and temperature dependent as predicted by the flux-creep theory of Anderson. [11]
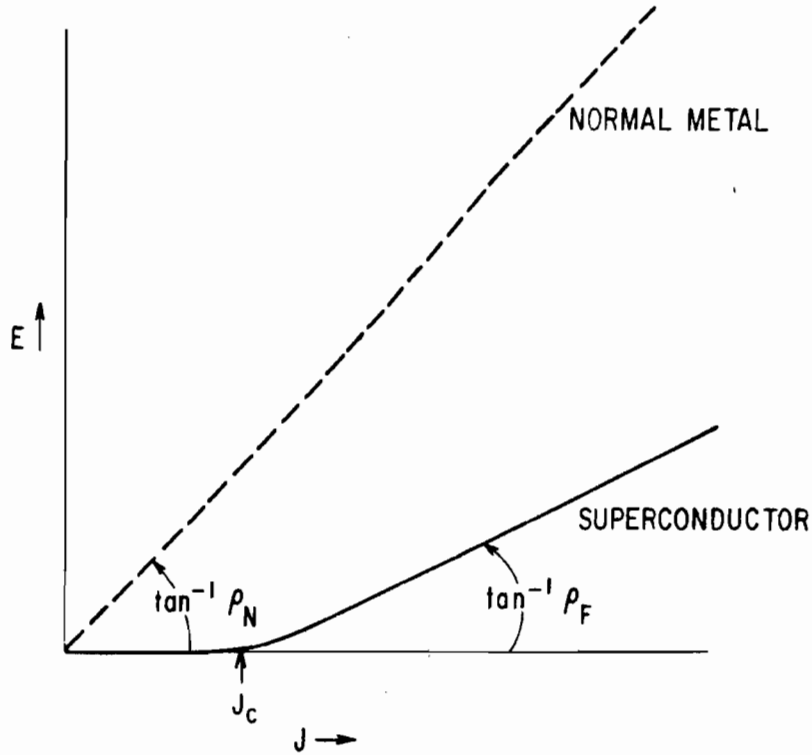
Figure 7 Current density as a function of electric field for a normal metal and an inhomogeneous type II superconductor. The slopes of the curves are the normal state resistivity, ρ_N, and the flow resistivity, ρ_F. The critical current, J_c, of the superconductor is indicated by an arrow. These curves are valid only in the isothermal limit.

Setting down Ampere's and Faraday's laws in practical units

$$\text{Curl } H = 4\pi J/10$$

$$\text{Curl } E = -10^{-8}\,\partial B/\partial t \ .$$

(1)

Using the defining equation for B, i.e., $B = H + 4\pi M$, we may rewrite Ampere's law for an isotropic system as

$$\text{Curl } B = \left(\frac{\partial B}{\partial H}\right)\frac{4\pi J}{10} \ .$$

(2)

We take as an approximation to experiment

$$\rho_F(J-J_c) = E \ .$$

(3)

By elimination of J between Eqs. (2) and (3) we obtain

$$\text{Curl } B = \left(\frac{\partial B}{\partial H}\right) \left[\frac{4\pi J_c}{10} + \frac{4\pi E}{10\rho_F}\right]. \tag{4}$$

The usual critical state theory ignores the second term in the bracket and in most applications replaces $\partial B/\partial H$ by 1 since in a strongly type II superconductor there is a close equivalence between B and H for fields well above that for initial flux penetration. In the remainder of this section we shall make this approximation. Taking the curl of Eq. (4) and using the fact that div B = 0 as well as Faraday's law, we obtain

$$\nabla^2 B = (4\pi/10^9 \rho_F)\, \partial B/\partial t. \tag{5}$$

This is a standard diffusion equation for magnetic flux density.

As a particular problem, let us calculate the flow of flux and transient field that results from increasing the external field suddenly by an amount $\Delta B(0)$ from an initially uniform frozen in field, B_0. All fields are assumed parallel to the surface of a semi-infinite slab. Distance into the slab is measured along a z coordinate whose origin is at the surface. A solution of Eqs. (4) and (5) is given by analogy to the theory of heat diffusion as[17]

$$\Delta B(z) = \Delta B(0) \left[1 - z/\delta' - (2/\pi) \sum_{1}^{\infty} (1/n)\, e^{-n^2 t/\tau} \sin(n\pi z/\delta')\right]$$

where $\delta' \equiv 10\Delta B(0)/4\pi J_c(B_0)$

and $\tau \equiv 4(\delta')^2/\pi 10^9 \rho_F$. (6)

If we define the flux per unit width that has crossed the surface as

$$\Delta\varphi(0) = \int_0^\infty \Delta B(z)\,dz,$$

we have by integration

$$\Delta\varphi(0) = [\Delta B(0)\delta'/2] \left[1 - (8/\pi^2) \sum_{1\,\text{odd }n}^{\infty} (1/n^2)\, e^{-n^2 t/\tau}\right]. \tag{7}$$

Finally, we may express the electric field at the surface as $E(0) = -10^{-8} \partial\Delta\varphi(0)/\partial t$ or from Eq. (7)

$$|E(0)| = [4 \times 10^{-8} \Delta B(0)\delta'/\pi^2 \tau] \sum_{1\,\text{odd }n}^{\infty} e^{-n^2 t/\tau}. \tag{8}$$

27

Replacing the parameters δ' and τ in the pre-exponential factor we obtain

$$|E(0)| = 4\rho_F J_c(B_0) \sum_{\text{odd } n}^{\infty} e^{-n^2 t/\tau} . \tag{9}$$

To estimate some typical values for this electric field and its duration, we assume a ρ_F of 10^{-6} ohm-cm and a critical current density of 10^5 amp/cm^2 to obtain ≈ 0.4 volt/cm for the pre-exponential factor. In the course of time, Eq. (9) becomes a simple exponential of time constant τ. Using the identifications of Eq. (6), the relaxation time τ is found to be $10^2 [\Delta B(0)]^2 / 4\pi^3 J_c^2 \rho_F$. If we assume $\Delta B(0) = 10^2$ gauss and use the earlier estimates of $J_c(B_0)$ and ρ_F, this time is approximately 10^{-9} sec. The shortness of this characteristic relaxation time has several consequences. First, from an experimental point of view direct observation would not be simple and would probably require sampling oscilloscope techniques to obtain the required band width. Secondly, this brief relaxation time indicates that the quasi-static critical state theory should apply to very high frequencies.

One word of caution should be added concerning the reliability of these predictions. The analysis rests upon the relationship between current density and electric field postulated in Eq. (3). The typical electric field that results from this analysis, however, is several orders of magnitude larger than those fields observed in the experiments that led to the empirical relationship of Eq. (3). In particular, although the velocity of flux motion is comparable to velocity of sound in the example given above, we have neglected any inertial effects in the equation of motion of the flux. Recent theoretical considerations by Suhl[18] suggest that this neglect is quite justified. He calculates a natural relaxation time of 10^{-12} sec for isolated flux lines which would be quite unobservable in comparison to the 10^{-9} sec of this calculation. A lower limit to the inertial mass could, however, be obtained from an experiment of this type.

2. Heating of an Inhomogeneous Type II Superconductor Exposed to an Alternating Field

An inhomogeneous type II superconductor experiences a power dissipation when subjected to an alternating magnetic field owing to the hysteretic nature of its magnetization. For the simple case we treat here, a slab with the alternating field in its plane, the rate of energy loss is[19]

$$W_s = 5 \times 10^{-7} f H_0^3 / 12\pi^2 J_c \quad \text{watts/cm}^2 . \tag{10}$$

In this expression, H_0 is the amplitude in Oe of the oscillating field whose frequency is f and J_c is the critical current density (amp/cm^2) of the superconductor. This energy will tend to heat up the specimen and finally a steady state temperature difference will be established between the exterior surface (assumed held at a bath temperature, T_{bath}) and the interior. It is the object of this section to calculate this equilibrium temperature, T_{max}, of the bulk of the specimen.

28

To make this calculation it is necessary to have the rate of energy dissipation per unit volume, Q, as a function of depth within the specimen. One can, in a straightforward though tedious manner, calculate directly the local electric field and current density, multiply them together and average over time. This local heating, however, can be obtained directly from Eq. (10) with a little thought and use of a slight trick. From the usual critical state theory, Eq. (10) represents a loss that takes place throughout a depth δ, defined by

$$\delta = 10H_0/4\pi J_c. \tag{11}$$

Suppose we now take as the origin of coordinates the plane in the material that marks the limit of field penetration and let x represent the distance outward from this plane. We may write the surface energy loss, employing Eq. (11) as

$$W_s = (5 \times 10^{-7} f/12\pi^2 J_c)(4\pi J_c/10)^3 X^3 . \tag{12}$$

This expression is valid for $X = \delta$ and for lesser values of X represents the rate of energy loss between the origin and X. Hence the derivative of $W_X(X)$ with respect to X gives the rate of loss per unit volume at any point, i.e.,

$$Q(X) = 5 \times 10^{-7} f(4\pi J_c)^2 X^2/10^3\pi . \tag{13}$$

Thus the average rate of energy loss rises quadratically from the point of innermost penetration. The temperature distribution in steady state is, by conservation of energy as,

$$K \frac{d^2T}{dX^2} + Q(X) = 0 \tag{14}$$

where K is the thermal conductivity in watts/cm-deg. Again measuring X from the plane of innermost penetration the differential equation for temperature is

$$\frac{d^2T}{dX^2} = -5 \times 10^{-7} (4\pi J_c)^2 X^2/10^3\pi K . \tag{15}$$

The solution of this equation that satisfies the boundary conditions, $T = T_{max}$ and $\partial T/\partial X = 0$ at $X = 0$ is

$$T(X) = -(5 \times 10^{-7} f/12)(4\pi J_c)^2 X^4/10^3\pi K + T_{max} . \tag{16}$$

The temperature at the outside surface is

$$T_{bath} = T(\delta) = (-5 \times 10^{-7} f/12)(4\pi J_c)^2 \delta^4/10^3\pi K + T_{max} . \tag{17}$$

Substituting δ from Eq. (2), we obtain

$$T_{max} - T_{bath} = (25/96\pi^3)(fH_0^4/KJ_c^2) \times 10^{-7} . \qquad (18)$$

We may make a sample evaluation of this quantity by assumption of a thermal conductivity appropriate to Nb_3Sn[20] at 4.2°K, i.e.,

$$K = 5 \times 10^{-4} \text{ watts/cm-deg} . \qquad (19)$$

Picking a frequency of 5 kc and a current density of 10^5 amp/cm^2, a temperature difference of 0.1°K is obtained when H_0 is about 550 Oe.

This result shows that alternating current such as those employed in the harmonic measuring technique[19] have no appreciable effect on the temperature.

C. DIRECT MEASUREMENTS OF A-C LOSSES IN HIGH FIELD SUPERCONDUCTORS (H.R. Hart, Jr. and P.S. Swartz)

1. Experimental Techniques

We have used two principal methods of measuring the a-c losses in high field superconductors, the helium boil-off method and the voltage-current measurement. The first, straightforward in principle, measures the loss or heat developed in a sample by measuring the rate of liquid helium evaporation. In our experiments we used a simple narrow-tailed helium Dewar and measured the total helium evaporation rate using a ball-in-tube flowmeter. Samples of various shapes could be accommodated in the 3/8-inch ID tail of the Dewar.

The alternating magnetic field was developed by a liquid-nitrogen-cooled copper solenoid surrounding the narrow tail of the Dewar. The 60 cps fields were obtained from the power lines and controlled by a 208-volt autotransformer; fields greater than 3000 Oe peak were obtained in this manner. At higher frequencies the coil was driven by a commercial 1.5 kw audio oscillator with the inductive reactance of the coil tuned out by a series capacitor.

There are several difficulties in the use of the helium boil-off method. One is the changing heat leak into the Dewar. Another more subtle difficulty is the following. Starting with the background heat leak and applying additional heat input at the sample, there is a substantial time lag before a change in the flowmeter reading occurs. It is possible under some conditions for the time delay to be so long as to create the illusion that there are no measurable a-c losses. The change in the flowmeter reading results from a change in the vapor pressure over the helium bath, which depends, in turn, on a change in the temperature of the bath. We were able to obtain successful measurements by use of the following technique. By adding a standard resistance heater to the bath, we were able to improve stirring and convection so that the heat

evolved in the superconducting specimen quickly brought the bath to its equilibrium temperature. This standard resistance heater was placed in the narrow tail of the helium Dewar below the sample. A current was applied to the resistor at the beginning of the run, in zero a-c field, to develop a power or heat dissipation larger than any a-c loss expected for the sample during the run. After a sufficient time, this heater established the desired stirring and brought the bath to an equilibrium temperature as indicated by a constant flow-rate meter reading. The data were taken by slowly turning the a-c field up to the desired value while at the same time decreasing the heater current so as to maintain a constant flowmeter reading. The change in heater power at constant flowmeter reading is the a-c loss for the sample. By following this procedure, in which the necessary stirring is present before the data run is started and in which the temperature of the bath is maintained constant, we have been able to minimize (but not eliminate) the effects of the time delay. To minimize the errors due to the changing background, the power input to the heater that maintained a constant flow rate in the absence of superconducting losses was determined between each datum point. With care the reproducibility approached ±1 mw.

The helium boil-off measurement is not well suited for experiments in which large a-c currents are directly applied by a current source, rather than induced by an a-c magnetic field. The current leads add to the background heat leak even when carrying no current and dissipate additional power when carrying current. In the case in which a-c currents were applied, we have measured directly the a-c voltage drop along the wire and, noting the current-voltage phase relationship, calculated the power dissipation. This measurement can be much more valuable than simply a measurement of a-c losses. By measuring the harmonic content of the voltage drop, one can test any proposed model for the current-field distributions, for each model predicts a unique harmonic content. The actual measurements are complicated by pickup and filtering problems.

2. A-C Losses in Sintered Nb$_3$Sn Rings

At the VIIIth International Conference on Low Temperature Physics, Kamper and Chester[21] reported measurements of a-c losses in sintered Nb$_3$Sn rings using the helium boil-off technique and a phase angle technique. Their sensitivity was reported to be about 1% of the expected losses as calculated from expressions similar to those of Section II-A. To their surprise they observed no losses. This finding was the original instigation for the present experiments with Nb$_3$Sn rings and wires.

The first experiments carried out in our laboratories using the helium boil-off technique seemed to confirm the Kamper and Chester results, i.e., no measurable losses. However, when the pitfalls mentioned earlier were discovered and corrected, the more careful measurements indicated losses very nearly those expected for a sintered Nb$_3$Sn ring.

Experiments have been performed on Nb_3Sn rings made by sintering compacted mixtures of Nb and Sn powders in stoichiometric proportion. The rings were 1 cm in diameter and square in cross section, 0.1 cm on a side. The results on two rings are shown in Fig. 8. Here P/f is the dissipated power divided by the frequency, i.e., the energy dissipated per cycle. Bean's model predicts $P/f \propto H^3$; the high field Kim limit ($J_cH = $ constant) predicts $P/f \propto H^4$. The observed field dependence varies from H^3 to $H^{3.5}$. The near linear relationship between dissipated power and frequency is indicated by the data taken at two frequencies for each sample. Recall that sample heating can increase the field dependence of the losses. If heating is significant, the loss/cycle obtained at different frequencies will differ. We see that heating is thus not very significant in this experiment. Sample A was tested at 60 cps in two different setups and the results are indicated as A and A'.
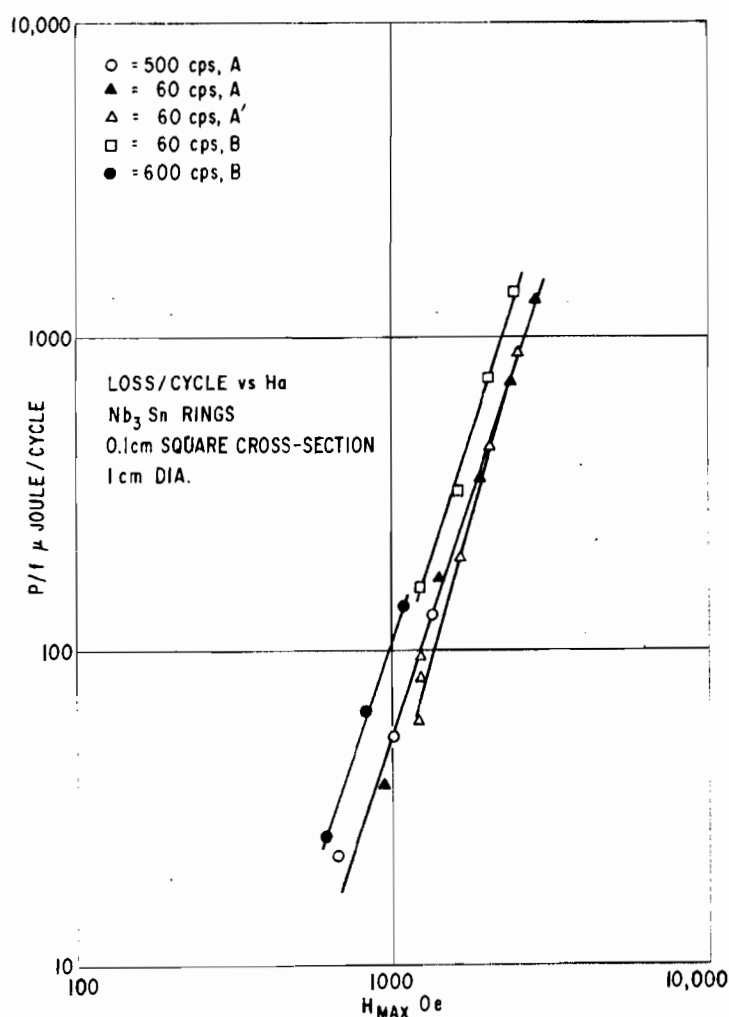
Figure 8 The loss/cycle (P/f) for rings of sintered Nb_3Sn in an alternating magnetic field. The induced ring current is proportional to the field amplitude.

Assuming an equivalent circular cross section and calculating the current from the inductance of a circular ring, we find ring A has a critical current density of 0.75×10^5 amp/cm^2, a value quite reasonable for sintered Nb$_3$Sn.

We were able to avoid field regions where gross flux jumping occurred by checking for flux jumping, using a pickup coil inside the hole of the ring. Flux jumps at low fields prevented us from making reliable measurements in Nb-Zr and Nb$_3$Sn rings of smaller cross section.

The conclusions to be drawn from the ring measurements are:

(a) Measurable losses do occur in rings of sintered Nb$_3$Sn contrary to the results of Kamper and Chester.[21]

(b) These losses are of the order expected from the critical state model (J_c = constant).

(c) The critical state model (in the forms presented by Bean, Kim, or by London) does give a reasonably accurate prediction of the a-c field (or current) dependence of the losses near power frequencies.

3. A-C Losses in a Nb$_3$Sn Wire

The supercurrents in the rings were induced by an applied a-c magnetic field. In this section the results for directly applied a-c currents are presented. These measurements were made on a GE process stranded Nb$_3$Sn wire 10 cm long by 0.009 inch in diameter using the voltage-current method described before. This was a composite wire of very high current density Nb$_3$Sn on a Nb core. The results are illustrated in Fig. 9 where the solid line is drawn through the experimental points. The power is proportional to approximately the 3.8 power of the current, an exponent between the Bean and Kim limits. Since the experiment was done at only one frequency, there was no test for possible sample heating. The current density calculated for the Nb$_3$Sn from the voltage drop and the critical state model, assuming a simple cylindrical wire, is about 7×10^5 amp/cm^2, a reasonable value for GE Nb$_3$Sn and, in addition, roughly the value obtained from the critical current of the wire, taking into account the niobium cross section. For this wire the a-c critical current multiplied by 1.4 is within 10% of the d-c critical current, implying that the maximum instantaneous current is responsible for the transition to the normal state.

The results of this measurement can be considered as justifying the use of the critical state model for estimating losses in wires in which the a-c current is applied directly.

4. A-C Losses in V$_3$Ga Powders

We saw earlier that the critical state model predicts a size dependent loss per unit volume or per unit mass for a high field superconductor in an

33
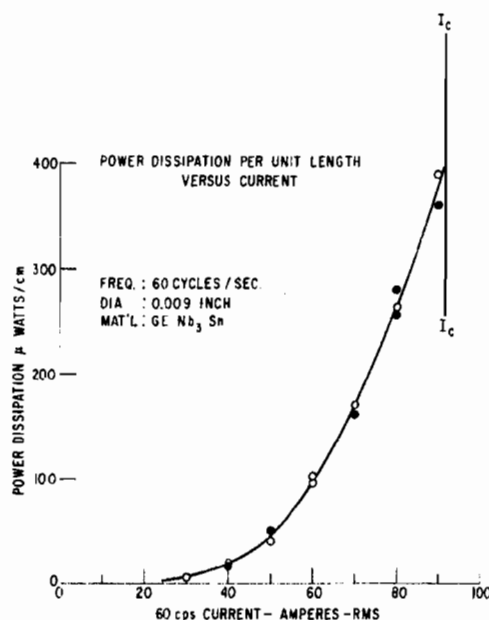
Figure 9 Power dissipation as a function of rms current measured in a GE stranded Nb_3Sn wire.

alternating field. To study losses in samples of widely varying sizes in alternating fields we chose to work with powders of V_3Ga varying from about 1/2 mm (500μ) in diameter down to about 5μ in diameter. An arc-cast V_3Ga ingot was crushed and separated into size ranges varying from 1μ to 500μ. A determination of the distribution of particle sizes within each size range was made from optical and electron micrographs.

Two kinds of experiments were performed. The a-c power dissipation was determined at 60 cps and about 600 cps as a function of the alternating magnetic field in a zero d-c field using the previously described helium boil-off technique. Here it was necessary to be very careful to arrange the powders in an open array allowing liquid helium access. If this precaution was not taken, sample heating sufficient to alter the results was observed. With proper cooling there was no significant discrepancy in the loss/cycle for the 60 and 600 cps results, and both data have been used in drawing the "helium boil-off" curves shown in Fig. 10.

Since the losses are thought to be basically hysteretic, i.e., a constant loss/cycle independent of frequency, another method of predicting the a-c losses is to measure the area enclosed by the "static" magnetization curve for one cycle (experimentally, about 0.001 cps). Portions of three such magnetization cycles are shown in Fig. 11 for the 420μ to 500μ V_3Ga particles. The area enclosed by a B-H loop multiplied by $10^{-7}/4\pi$ is the loss/cycle/cm^3. Thus the area of a $4\pi M$ vs H loop multiplied by $10^{-7}/4\pi$ is also the loss/ cycle/cm^3 as $B = H + 4\pi M$.

34
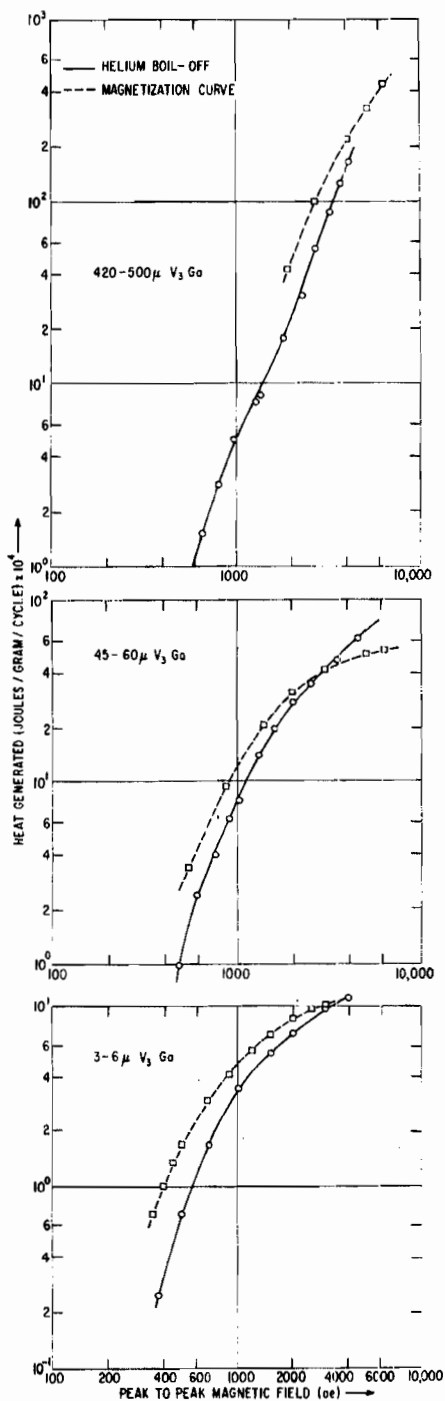
Figure 10 Comparison of losses in V_3Ga powders subjected to a-c magnetic fields as determined both from the helium boil-off method and from integrations around loops of the experimental magnetization curves. The numerical values on the ordinate should be multiplied by 10^{-4} to yield the losses in joules/g/cycle.

Such static magnetization measurements were made for each of the three size ranges for a series of applied field cycles of varying peak fields. These results are also plotted in Fig. 10. The static and dynamic curves are generally within a factor of two of each other and nearly equal at the larger fields. We note the discrepancy is the greatest at the lower fields, fields in the vicinity of H_{c1}. We mention two possible causes for these low field discrepancies.

35
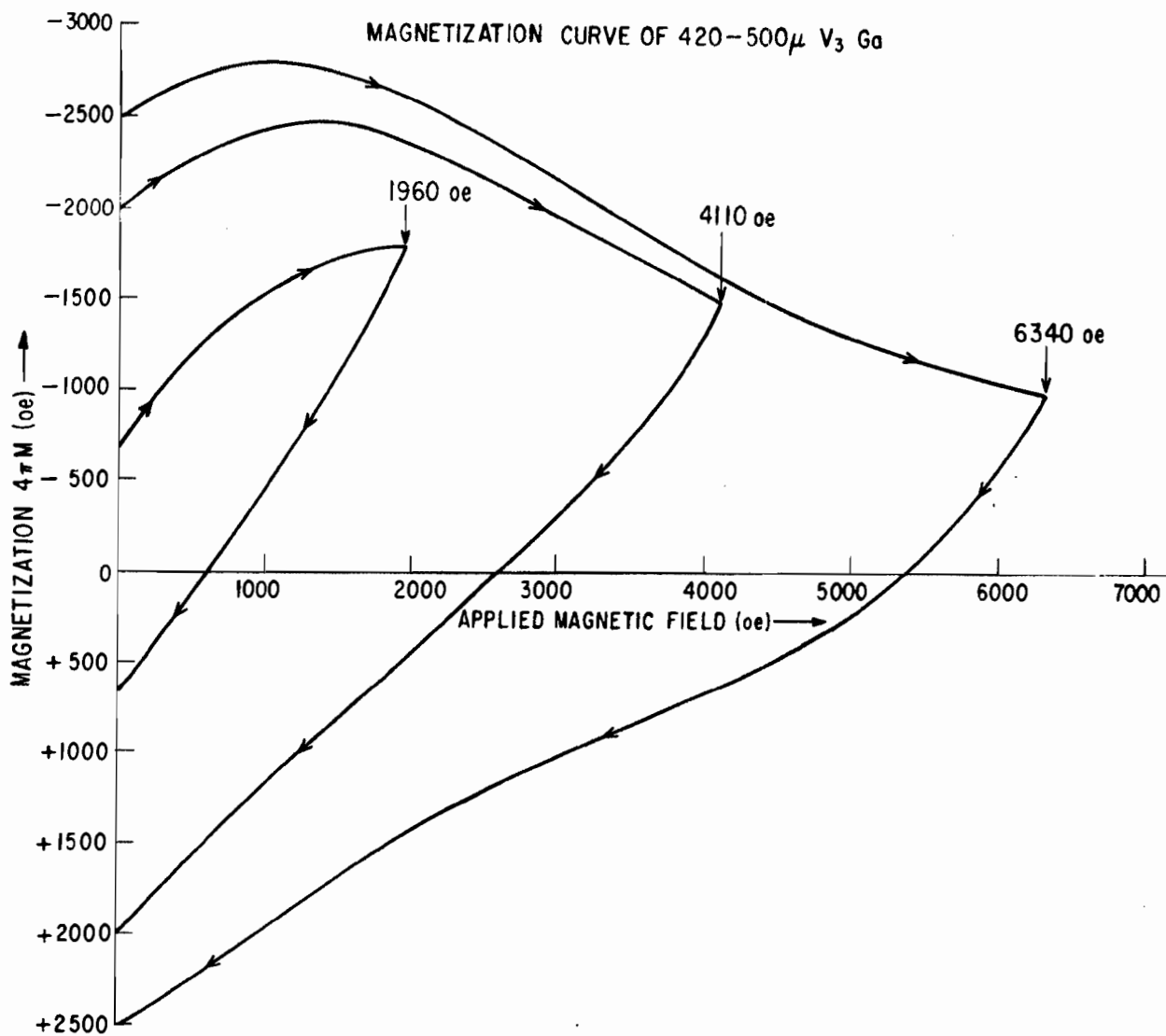
Figure 11 Some of the experimentally determined magnetization loops of the
420μ to 500μ V_3Ga particles from which the losses per magnetic field cycle
are determined. The area enclosed within each half-loop is multiplied by
$10^{-7}/2\pi$ to give the loss in joules/cm^3/cycle.

(a) For both experiments the experimental uncertainties become pro-
portionally greater as the losses become smaller, i.e., at the lower fields.

(b) The samples are mounted quite differently, the a-c boil-off samples
being spread out in a thin open layer for good helium access and the magnet-
ization samples being packed tightly to increase the signal, there being no
heating problem. At the larger fields this makes little difference; however,
at fields near H_{c1} and below, the larger diamagnetism could lead to enhanced
magnetic fields in the packed magnetization samples, increasing the losses
measured from the magnetization curve relative to those in the helium boil-
off experiment. No attempt was made to track down the actual cause of the

36

low field discrepancies. The basic experimental results, of a measured loss that goes with the frequency raised to the 0.95^+ power over six decades of frequency and a loss/cycle that is in fairly good agreement with that expected from the static magnetization curves provide strong confirmation of the critical state model and its prediction that the loss/cycle is frequency independent.

The critical state model also predicts that for a sufficiently large alternating field (much larger than the field required to penetrate to the center of the specimen) the losses should be proportional to the radius of the sample. Though we did not achieve alternating fields of this magnitude, we can see the beginnings of this effect. The losses at 4000 Oe peak-to-peak are in the ratio 1:0.3:0.07 while the radii are in the approximate ratio 1:0.1:0.01.

5. Conclusion

(a) Measurable losses do occur in intermetallic high field superconductors in the forms of rings [contrary to one published account[21]], wires, cylinders, and powders. Losses have been measured and reported by others in Nb-Zr[22, 23] and in several other nonintermetallic systems.[23, 24] Losses are also found in the synthetic high field superconductor produced by forcing lead into the pores of Vycor glass.

(b) The critical state model can be used for preliminary engineering estimates of the losses to be encountered under a-c conditions using the materials we have studied. The parameter $J_c(H)$ can be determined from static experiments and used for power frequency calculations. We caution that our experiments have been performed on samples of very simple geometries in which isothermal conditions can be maintained.

We have found the power to be linear in frequency for mixed state superconductors. In the next section it is shown that the power loss, again for simple geometries, is linear in frequency for flux-excluding superconductors such as niobium (below H_{c1}) and lead. However, this linear dependence has not been found by some other workers[22] using, perhaps significantly, more complex wire-wound coils. It has been suggested[25] that mechanical resonances and mechanical losses are responsible for the discrepancy. As will be seen in the next section, significant temperature rises can occur in solenoids under changing field conditions; higher temperatures lower J_c. Since the temperature rise will be frequency dependent, the loss per cycle will be frequency dependent. We might thus expect departures from the linear frequency dependence in some coil structures. The possibility of small flux jumps in the coil wires further complicate any loss predictions. The situations in which flux jumps are important are considered in Section VI. In short, considerable care is required in the use of our findings based on simple geometries for predicting losses in the more complicated structures needed in practice.

D. HEATING IN HIGH FIELD SUPERCONDUCTING WIRES
AND SOLENOIDS UNDER NONCYCLIC FIELD CHANGES
(H.R. Hart, Jr. and P.S. Swartz)

1. Introduction

In Section II-A the critical state model[7, 12] was applied to the calculation of a-c losses for several geometries and field and current configurations. In all cases these were the losses for cyclic fields and currents. The same model can be used for the calculation of the heat developed in a wire or solenoid when the field is varied in a more general way. If the thermal conductivity and specific heat are known, the temperature rise can be calculated. Since our calculations have indicated that the heat evolved and the temperature increase can be significant, we shall give some simple examples.

2. Methods of Calculation and Example: Wire in Changing Field

Let us note that the local power dissipation per unit volume, $\dot{q}$, is the scalar product of the electric field intensity E and the induced current density J. This relation is particularly simple to use in the original Bean model in which $J = J_c$, a constant, independent of magnetic field. Thus:

$$\dot{q} = \vec{E} \cdot \vec{J} . \tag{20}$$

Maxwell's equations yield:

$$\nabla \times \vec{E} = -\frac{\partial \vec{H}_{loc}}{\partial t} \times 10^{-8} \quad \text{or} \quad \oint_{loop} \vec{E} \cdot d\ell = -10^{-8} \int_{area} \frac{\partial \vec{H}_{loc}}{\partial t} \cdot d\vec{A} \tag{21}$$

and

$$\nabla \times \vec{H}_{loc} = +\frac{4\pi}{10} \vec{J} , \tag{22}$$

where the symbols and units are as defined in Table I.

Using this method to calculate the local power dissipation, we can [see Carslaw and Jaeger[26]] determine the temperature distribution as a function of time. In our examples the effects of the thermal diffusivity are not important, i.e., we are dealing with effectively steady-state solutions. We assume in our quantitative expressions that the temperature rise is sufficiently small that the parameters characterizing the material are unchanged. However, we point out that the temperature rise can under some circumstances be sufficiently large to decrease the critical current density significantly.

Let us, as an example, consider a wire of radius R whose axis is parallel to the applied magnetic field. The wire is placed in a perfect cooling bath. Let the field increase linearly in time, $H = \dot{H}_a t$. Let us consider the solution after $H > (4\pi/10)J_c R$ and after the initial transients have decayed. The Bean critical

state model and Eqs. (21) and (22) yield in this limit:

$$H_{loc}(r) = H - \frac{4\pi}{10} \dot{J}_c \cdot (R-r)$$

and
$$\text{(23)}$$

$$2\pi r E(r) = -10^{-8} \dot{H}_a \cdot \pi r^2$$

or
$$E(r) = \frac{10^{-8} \dot{H}_a r}{2} \ .$$
$$\text{(24)}$$

From Eqs. (20) and (24) we find:

$$\dot{q}(r) = \frac{1}{2} \times 10^{-8} \dot{H}_a J_c r \ .$$
$$\text{(25)}$$

With this dissipation term and the thermal conductivity K we can solve for the temperature profile:

$$K \cdot \frac{1}{r} \cdot \frac{\partial}{\partial r} \left(r \frac{\partial T}{\partial r} \right) + \dot{q}(r) = 0$$

yielding

$$T(r) + 10^{-8} \frac{\dot{H}_a J_c r^3}{18K} + C \ln r + D = 0 \ .$$

Evaluating the constants of integration, C and D, we find:

$$T(r) = T_{bath} + \frac{10^{-8} \dot{H}_a J_c (R^3 - r^3)}{18K} \ .$$
$$\text{(26)}$$

In some cases we need to know only the total heat dissipation, not the local heat dissipation. We can integrate Eq. (20) over the volume of the sample or we can use another method that is in some cases simpler. We note that the rate of storage of magnetic energy within the sample is:

$$\frac{dU}{dt} = \frac{10^{-7}}{4\pi} \int_{Volume} H_{loc} \frac{dH_{loc}}{dt} \ dV$$

or

$$\frac{dU}{dt} = \frac{10^{-7}}{4\pi} \cdot \frac{dH}{dt} \int_{Volume} H_{loc} \cdot \frac{dH_{loc}}{dH} \ dV \ .$$
$$\text{(27)}$$

The rate of doing work on the sample is
$$\frac{dW}{dt} = \frac{10^{-7}}{4\pi} \vec{H} \cdot \int_{Volume} \frac{d\vec{H}_{loc}}{dt} \ dV$$

39

or

$$\dot{\frac{dW}{dt}} = \frac{10^{-7}}{4\pi} \frac{dH}{dt} \cdot \int_{Volume} H \cdot \frac{dH_{loc}}{dH} \, dV \quad . \tag{28}$$

(We are assuming that $\vec{H}_{loc} \| \vec{H}$.) Since the rate of dissipation of power in the sample is $\dot{W} - \dot{U}$ we have:

$$\dot{Q} = \frac{10^{-7}}{4\pi} \frac{dH}{dt} \int_{Volume} (H - H_{loc}) \frac{dH_{loc}}{dH} \cdot dV \quad \text{watts.} \tag{29}$$

If, as in our present example $dH_{loc}/dH = 1$ throughout the sample, Eq. (29) simplifies to:

$$\frac{\dot{Q}}{V} = -10^{-7} M \frac{dH}{dt} \quad \text{watts/cm}^3 \tag{30}$$

where

$$M \equiv \frac{1}{4\pi V} \int_{Volume} (H_{loc} - H) \, dV \quad .$$

In our present example Bean's critical state model yields $M = -(1/30)J_c R$ and thus

$$\frac{\dot{Q}}{V} = \frac{1}{3} \cdot 10^{-8} J_c R \dot{H}_a \quad \text{watts/cm}^3 \quad . \tag{31}$$

The same result is obtained by integrating $\dot{q}(r)$ from Eq. (25).

We have not solved the problem of a round wire with the axis perpendicular to the field. Instead, we note that for a square wire of side $2a$ in a transverse field $H = \dot{H}_a t$:

$$T_{max} \cong \frac{10^{-8} \dot{H}_a J_c a^3}{16K} + T_{bath} \quad . \tag{33}$$

This result is to be compared with Eq. (26).

Let us now consider a wire of a high field superconductor placed in a pulsed field in a critical current measurement. We find from Eq. (31) that the total heat developed varies directly with the intensity of the field, with the radius of the wire, and with the critical current density. Introducing a typical 4.2°K value for the high field specific heat of a high field superconductor such as V_3Ga or $Nb_3Sn(\sim 0.03$ cal/mole-deg), [27] we find that for a thermally isolated wire of radius 0.01 inch and critical current density of 10^5 amp/cm^2 a field of 10^5 Oe

drives the sample well above the critical temperature, $\Delta T \sim 400°K$. Of course, since the specific heat increases with increasing temperature and the critical current density decreases with increasing temperature, the wire temperature would approach, but not exceed, the critical temperature. The measurement of J_c would, however, be meaningless.

Since the thermal conductivities of these materials are so low[28]

$$\left[\begin{array}{c} K \, (4.2°K) \sim \frac{1}{2} \times 10^{-3} \text{ watts/cm°K} \\ Nb_3Sn \end{array} \right]$$

the temperature rise in a fast pulsed field even in a perfect cooling bath [Eq. (26) or (22)] can be detrimental. Note that the temperature rise varies directly with J_c and the rate of rise of field and with the third power of the wire radius. With a 10^5 Oe field pulse having a rise time of 10 msec we find that a solid Nb_3Sn wire for which $J_c = 10^5$ amp/cm^2 must have a radius less than 0.004 inch in order to maintain the temperature rise at the center less than $1°K$.

3. Solenoid

Let us now consider a high field superconducting solenoid. Restricting ourselves to very long solenoids, let us approximate the winding as a multi-layer scroll wound from a sheet of high field superconducting material of thickness d. Let the inside radius of the solenoid be a_1 and the outside radius be a_2. The thermal conductivity of the composite winding (superconductor, insulator, supports, etc.) will be denoted by K. The central field will be given by $H = H_0 t/\tau$.

Note that for such a sheet of thickness d parallel to a field, Bean's critical state model yields, for $H > (4\pi/10)J_c \cdot d/2$, $dH_{loc}/dH = 1$ and $M = -(1/20) \cdot J_c \cdot d/2$. Thus, from Eq. (30) we find $\dot{Q}/V = (1/4) \cdot 10^{-8} \cdot J_c \dot{H}_a d$. Since the field profile in the winding decreases linearly across the winding, we can write:

$$\dot{q}(r) = 10^{-8} \, \frac{\lambda H_0 J_c d}{4\tau} \cdot \frac{a_2 - r}{a_2 - a_1} \tag{33}$$

where λ is the filling factor.

Solving for the maximum temperature in the winding in the two limits of wall thickness we find

$$T_{max} = T_{bath} + 10^{-8} \cdot \frac{\lambda H_0 J_c d (a_2 - a_1)^2}{36\sqrt{3} \, \tau K} \quad \text{for } (a_2 - a_1) \ll a_2 \tag{34}$$

41

and

$$T_{max} = T_{bath} + 10^{-8} \frac{5\lambda H_0 J_C d a_2^2}{144 \tau K} \quad \text{for } a_1 \ll a_2 . \tag{35}$$

If instead of the sheet of thickness d we had a multilayer winding of wires of diameter d', we would replace d with approximately $(\pi/4)d'$ in Eqs. (34) and (35). The wall thickness w is related to the maximum field H_0 by $w = 10 H_0/4\pi\alpha\lambda J_c$, where the operating critical current density $J_0 = \alpha J_c$; α is a factor less than one. Introducing this expression we find for wires of diameter d':

$$T_{max} \cong T_{bath} + 0.80 \times 10^{-10} \frac{H_0^3 d'}{\tau K \alpha^2 \lambda J_c} \quad (a_2 - a_1) \ll a_2 \tag{34'}$$

$$T_{max} \cong T_{bath} + 1.73 \times 10^{-10} \frac{H_0^3 d'}{\tau K \alpha^2 \lambda J_c} \quad a_1 \ll a_2. \tag{35'}$$

Let us consider a rather extreme example of the heating in a coil by using for K the $(1/2) \times 10^{-3}$ w/cm°K characteristic of Nb_3Sn at 4.2°K. Let $H_0 = 10^5$ Oe, d' = 0.030 inch, $\lambda = 1/2$, $\alpha = 1/2$, $J_c = 2 \times 10^5$ amp/cm² (a critical current density characteristic of the lower fields at which the heating is the greatest). Using Eq. (35), we find the shortest time, in which we can increase the field to H_0 without incurring a temperature rise greater than 1°K, to be 800 seconds.

From Eqs. (34') and (35') we see that the solenoid heating problem increases as the cube of the final field, as the first power of the wire diameter and inversely as the critical current density and $\alpha^2\lambda$.

We can also calculate the total heat generated per unit length in energizing the coil and thus the amount of coolant required. We find for the sheets of thickness d:

$$Q/L = 10^{-8} \cdot \frac{\pi}{12} \cdot \lambda H_0 J_c d (a_2 - a_1)(a_2 + 2a_1) \text{ joules/cm} . \tag{36}$$

[For wires rather than sheets d is replaced by $(\pi/4)d'$.]

This result is also of interest in energy storage using superconducting solenoids, for it establishes the fraction of the energy stored in a solenoid available to the user upon discharge. The energy stored in our scroll solenoid per unit length is:

$$U/L = \frac{10^{-7}}{48} \cdot H_0^2 (a_2^2 + 2a_1 a_2 + 3a_1^2) \text{ joules/cm} . \tag{37}$$

42

Thus the fraction of energy lost is:

$$\eta = \frac{2\pi}{5} \cdot \frac{\lambda J_c d}{H_0} \cdot \frac{(a_2 - a_1)(a_2 + 2a_1)}{a_2^2 + 2a_1 a_2 + 3a_1^2} \cdot \qquad (38)$$

In the limit of wall thickness small compared to radius, we find:

$$\eta = \frac{\pi \lambda J_c d w}{5 a_2 H_0} \cdot$$

Since $w = (10/4\pi) \cdot H_0/\lambda \alpha.J_c$, we can write:

$$\eta = \frac{d}{2\alpha a_2} \cdot \qquad (39)$$

Hence the fraction of the energy lost is the ratio of the thickness of the sheet to the diameter of the coil if $\alpha \sim 1$. This fraction can thus be made very small.

SECTION III

A-C LOSSES AND FLUX PENETRATION BELOW H_{c1}
(T. A. Buchhold, P. J. Molenda, and R. L. Rhodenizer)

A. INTRODUCTION

This section is concerned with the study of a-c losses and flux penetration behavior displayed by superconductors below the lower critical field H_{c1}. Although an ideal superconductor is perfectly diamagnetic in this region, except for the London penetration, it has been observed that surface losses normally occur below H_{c1} in real materials when the superconductor is immersed in alternating magnetic fields.

It has been the purpose of this investigation to study the nature of these surface losses from an empirical viewpoint. These investigations have included the dependence of losses on field and temperature for both well-annealed, high-purity samples and less pure specimens. The metal niobium has been used exclusively for these studies. Associated with measurements of the surface losses has been the study of flux penetration behavior in niobium. This has included measurements of the London penetration depth, the influence of field on the penetration depth, and the nonideal flux penetrations normally associated with losses. These experiments have provided the basis for an empirical model expressing surface losses in terms of flux penetration and other experimentally determined parameters.

As a considerable amount of effort has been directed to the development of a sensitive and accurate measurement device, the experimental apparatus will be liberally discussed in the following section. This is done as it is believed that the concept employed would be useful to anyone interested in examining the practical aspects of superconducting materials and also to illustrate the extreme caution that is needed in developing a device to measure properties such as surface losses accurately.

The results presented in the following sections are basically a summary of many experimental measurements made throughout this program. Most of the data presented herein have been discussed in previous progress reports, and results that have been modified or improved by more recent experiments have been omitted. Thus, the results included in this final report represent the most reliable data accumulated from many experiments.

B. THE EXPERIMENTAL METHOD

Throughout the investigation, the experimental device has undergone considerable modification to improve its accuracy and sensitivity. A description of the device in its original form will be given and a discussion of the modifications will follow.

A schematic diagram of the original test data device is shown in Fig. 12. A superconducting cylindrical test specimen approximately 5 mm in diameter by 30 mm long is suspended from a thin-walled stainless steel tube within a 7 mm nylon chamber. The chamber may either be filled with dry helium gas to act as a heat transfer medium, or be evacuated to provide good isolation between the sample and the liquid helium in which the entire device is immersed. A uniform longitudinal magnetic field of the desired frequency and amplitude is supplied by a superconducting niobium coil and a niobium field shaper.

The amplitude of the alternating magnetic field at the surface of the test specimen is measured by a fine-wire copper coil wound on a known diameter of the nylon chamber. If the diameter of the sample is also known, the amplitude of the field is determined from the voltage induced in the coil by the relation:

$$e_{rms} = 4.44 \ nf\left(\frac{\pi}{4}\right) B_0 \ (D_C^2 - D_S^2) \times 10^{-8} \tag{40}$$

HELIUM BATH
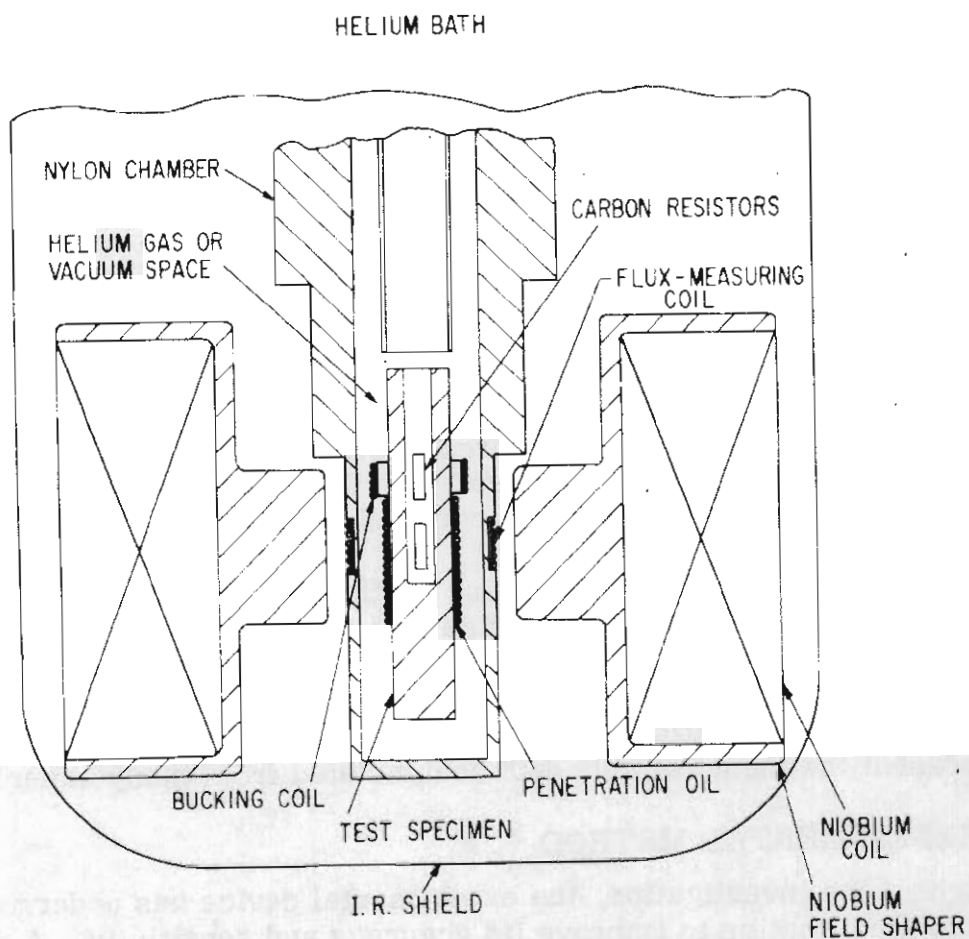
Figure 12 Schematic for cryogenic device to measure a-c losses in super-conductors.

where

D_C is the coil diameter
D_C is the coil diameter
D_S is the sample diameter
n is the number of turns in the measuring coil
f is the frequency of the field
B_0 is the peak value of the applied field.

The test sample contains a calibrated carbon resistor that allows temperature measurement and control. If desired, heat can be supplied to the sample by passing a current through the resistor.

Two fine-wire copper coils are wound on the specimen: a flux penetration coil and a bucking coil. Voltages induced in these coils by the alternating field are due to (a) the physical dimensions of the wires and their separation from the superconducting surface of the test specimen and the conventional London penetration, and (b) additional flux entering and leaving the superconductor itself, which is to be measured. By vertical adjustment of the suspension tube, the bucking coil that is on the fringing field at the corner of the field shaper is positioned so that type (a) voltages are nulled and the type (b) voltages, corresponding to superconductor losses, are obtained for electronic analysis.

For operation below 4.2°K, the specimen temperature is adjusted by using helium gas in the test chamber and adjusting the boiling temperature of the liquid helium bath through vapor pressure control. In the range above 4.2°K, sample temperature is monitored by the internal carbon resistance thermometer and is altered by evacuating the test chamber and supplying heat either from the superconductor surface losses or by passing current through the internal resistor.

The compensated voltage signal given by the penetration coil, bucking coil combination is related to the time rate of change of the flux which enters and leaves the sample exclusive of that due to a constant London penetration. That is:

$$e_c = N \frac{d\varphi}{dt} \times 10^{-8} \tag{41}$$

where N is the effective number of turns in the coil combination.

From this signal, the total flux that enters the sample can be found as

$$\varphi = \frac{1}{2N} \int_0^{T/2} e(t)dt \times 10^8 \ . \tag{42}$$

The value of the integral in this equation can easily be determined from an average voltage measurement of the signal and with appropriate calibration.

It is also convenient in some instances to define an effective penetration depth associated with this flux as

$$\delta = \frac{\varphi}{\pi D_S B} = \frac{\int_0^{T/2} e(t)dt \times 10^8}{2\pi N \, D_S \, B} \tag{43}$$

where

D_S is the sample diameter
B is the amplitude of the field at the surface of the sample.

This quantity is, of course, determined from a measurement of flux by the voltmeter method at any known field.

The density of the a-c losses dissipated in the surface of the sample can be determined by feeding the measured voltage signal to one leg of a light beam wattmeter while a signal proportional to the applied field is fed to the second leg. In using this method, great care is needed in determining the proper phase relationship between the voltage signal and field signals, but methods have been devised for doing this accurately.

In order to measure the London penetration depth for a given sample, the variation of the penetration depth with temperature is observed. To do this, the voltage signal is properly compensated at a given temperature and the change in the penetration depth for various temperatures is measured by the method described previously. Obviously, this must be done at a field level where nonideal flux penetrations are negligible. To determine the penetration depth with this technique, the variation of λ with the temperature must be previously known. This point will be discussed in the section dealing with the experimental results.

In the course of investigations of the superconducting losses exhibited by very low loss samples (i.e., losses less than 10^{-6} watts/cm^2) as a function of absolute temperature, several discrepancies were noted in the measurements which indicated the existence of errors significant enough to influence measurements in the very low loss region. It is emphasized that these error sources were not significant with respect to the losses exhibited by usual superconducting materials, but became more important as more nearly ideal superconducting specimens were produced through improved processing techniques.

It was eventually discovered that a primary source of error was due to penetration of the excitation field in the niobium field shaper that was sensed, in an indirect manner, by the windings on the sample and interpreted as penetration of the field into the sample itself.

It will be recalled (see Fig. 12) that the bucking coil was located near the corner of the niobium field shaper, used to shape the excitation field, where

48

the excitation field gradients are high so that a small change in the vertical position of the sample would alter the voltage induced in the bucking coil. Suppose, for example, as the applied field approaches its peak value, that there is a sudden penetration of the field into the field shaping piece. This would most likely occur at the corners of the field shaper. As the bucking coil is very close to these corners, a negative voltage signal is induced in the bucking coil winding because of a small flux density change due to the unwanted penetration. On the other hand, the penetration coil is far enough away from these corners so that practically no signal is induced in the penetration winding. As the bucking coil is connected in series opposition to the penetration coil during measurement, the negative signal induced in the bucking coil will appear as a positive net signal as one examines the voltage across the two coils in measuring losses. It is easily seen that very logical values can be obtained for the losses as a function of field and frequency which could reasonably be interpreted as sample losses, although they are, in reality, related to losses occurring in the field shaper.

Because of the very logical behavior of the measured losses with respect to field and frequency, this source of error, which was significant in regions below 10^{-6} watts/cm^2, was very difficult to isolate. However, in investigating the properties of low loss niobium samples as a function of temperature, it was found that the results did not follow the expected results as had been found with samples with higher loss characteristics. The discrepancies led to many detailed investigations of the thermal and electrical design of the measuring device which eventually led to the isolation of the source of error.

At this point the bucking coil arrangement was changed by rewinding the bucking coil with the same number of turns and spacing, directly over the penetration coil. The fewer turns of the bucking coil were distributed to cover the same length of the sample as the penetration coil in an attempt to compensate any erroneous signals in the applied field due to external disturbances. In order to obtain the proper magnitude of the bucking signal to correctly compensate the penetration signal, the bucking voltage was divided across a potentiometer, located external to the cryogenic environment, and added in opposition to the penetration signal.

This arrangement led to values of losses measured at 1000 gauss peak field varying at 290 cps of about 1 to 2 x 10^{-7} watts/cm^2 for the good niobium samples. In order to more accurately measure losses at these levels, techniques for aligning the phase and magnitude of the compensation circuits and wattmeter signals were closely examined and improved. However, it was found that certain discrepancies still existed in the measured values.

Among the various factors that were found to have a minor influence on the loss measurements were: erroneous signals due to sample vibrations, magnetic impurities in the copper penetration and bucking windings, and harmonic frequency components originating in the excitation signals and

49

amplifier circuits. Very critical phase adjustments were also necessary due to the need to compensate signals on the order of 500 to 1. Although it was felt that these minor possible sources of error could be controlled in a satisfactory manner, it was found that the small signals due to losses in the field shaper remained as a prevalent source of error.

Because of this it was decided to abandon the superconducting coil and to use a field coil with copper windings and no superconducting materials. This had not been done in the original device as a copper field coil has some obvious disadvantages when compared to a superconducting coil. One of these is the greater power dissipation, accompanied by higher liquid helium consumption and another is the difficulty in achieving a uniform field with a nonsuperconducting coil. Further study showed that a coil could be built that was satisfactory in both respects.

A field coil was then designed and constructed with General Electric funds to be used in making loss measurements on very low loss samples. The coil was designed to meet the field requirements with minimum power dissipation, and to produce a uniform field along the sample being measured.

Experiments which have been conducted using a nonsuperconducting coil have yielded reliable measurements of losses in the vicinity of 1×10^{-7} watts/ cm^2. This has allowed the evaluation of niobium samples with very low loss characteristics which has given more insight into the properties of very nearly ideal superconductors. It is seen from the above discussion that errors encountered in these types of measurements are generally very subtle in nature, and extreme care is required in interpreting measurements. A great deal has been learned regarding the extreme caution that is needed to make accurate measurements on very pure superconducting specimens. However, it is felt that the significant sources of error affecting the measurements have been eliminated to ensure accurate and reliable measurements.

C. THE PENETRATION DEPTH AND SURFACE LOSSES OF ANNEALED SUPERCONDUCTORS FOR FIELDS BELOW H_{c1}

The London theory predicts that the penetration depth in a superconductor is independent of the applied field. However, more advanced theoretical considerations show that the penetration depth is field dependent and also depends on impurities. This has also been shown experimentally.

It is assumed in the following that a cylinder of an annealed superconductor (which may have imperfections) is exposed to an a-c field (H) of moderate frequency: e. g., f = 300 cps. Annealing is assumed in order to avoid unpredictable surface conditions caused by cold-work.

It is further assumed that the penetration depth can be expressed as:

$$\lambda = \lambda\,(0) + aH^2 + bH^4 + \ldots \qquad (44)$$

The equation contains only even exponents of H since λ must be independent of the direction of H [see Fig. 13(b)].

Consider an ideal (i. e., zero leakage) one turn winding surrounding the cylinder [Fig. 13(a)] which measures the flux penetrating the surface of the sample. The flux φ per cm of circumference linked with the coil is:

$$\varphi = \mu\,H\,\lambda \qquad (45)$$

where $\mu = \dfrac{4\pi}{10} \times 10^{-8}$ if H is in $\dfrac{amp}{cm}$ and λ is in cm.
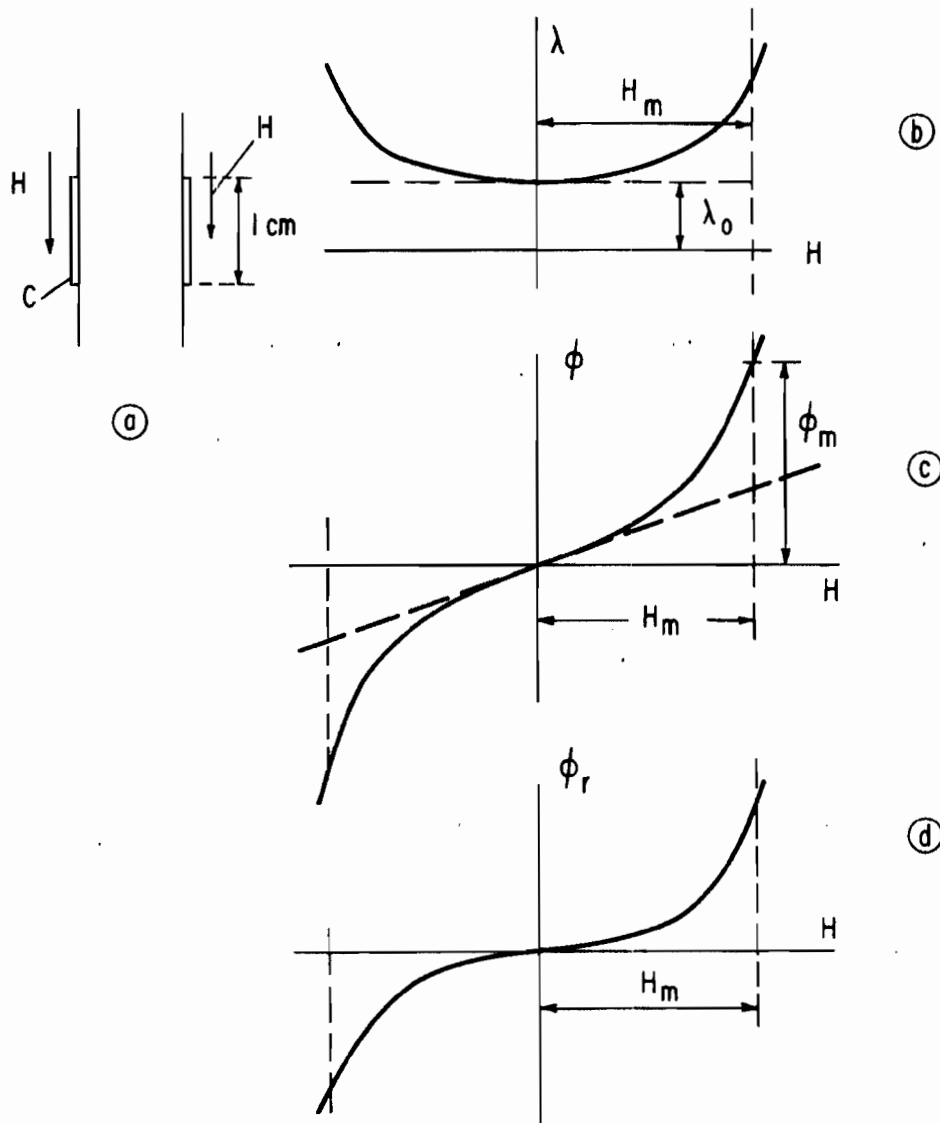
Figure 13   Penetration depth and flux penetration.

51

Equations (44) and (45) yield [see Fig. 13(c)]

$$\varphi = \mu \left[\lambda(0)H + aH^3 + bH^5 + \ldots \right] \qquad (46)$$

with

$$H = H_m \sin \omega t; \qquad (47)$$

the voltage e induced in the measuring coil (C) per cm of circumference is:

$$e = \frac{d\varphi}{dt} = \omega\mu \left[H_m\lambda(0) + 3a\, H_m^3 \sin^2 \omega t \right.$$

$$\left. + 5bH_m^5 \sin^4 \omega t + \ldots \right] \cos \omega t . \qquad (48)$$

With the described measuring technique; the sinusoidal voltage produced by the first term, $\lambda(0) \cos \omega t$, is compensated, leaving the remaining flux

$$\varphi_r = \mu \left(aH^3 + bH^5 + cH^7 + \ldots \right) . \qquad (49)$$

In the following, for matters of simplicity, only the H^3 term will be used. Equation (48) yields:

$$e = 3a\, \omega\mu\, H_m^3 \sin^2 \omega t \cos \omega t . \qquad (50)$$

This equation is plotted in Fig. 14(a). For matters of comparison, Figs. 14(b) and (c) show the calculated voltages e if the H^5 term and the H^7 term are used in Eq. (48).

If the superconductor contains imperfections such as impurities or dislocations where flux lines can be pinned and trapped, the flux curve φ_r of Fig. 15(a) will have a hysteresis loop that is obtained if the curve $\Delta\varphi$ of Fig. 15(b) is superimposed on the original curve (a) of Eq. (49). A simple mathematical expression for $\Delta\varphi$ is:

$$\Delta\varphi = \overline{+}\varphi_0 \left[1 - \left(\frac{H}{H_m} \right) \right]^2 = \overline{+}\varphi_0 (1 - \sin^2 \omega t). \qquad (51)$$

This causes an additional voltage:

$$\Delta e = \frac{d(\Delta\varphi)}{dt} = \pm \omega\varphi_0 \sin 2 \omega t. \qquad (52)$$

The (+) sign is used as H increases from $-H_m \to +H_m$ and the (-) sign as H decreases from $+H_m \to -H_m$.

The net voltage is then:

$$e_r = e \pm \Delta e . \qquad (53)$$

52

$$e = \omega\mu \ 3a \ H_m^3 \ \sin^2 \omega t \ \cos \omega t$$

$$H = H_m \sin \omega t$$

$$H_m$$

(a)

e

t

$$e = \omega\mu \ 5b \ H_m^5 \ \sin^4 \omega t \ \cos \omega t$$

(b)

t

$$e = \omega\mu \ 7c \ H_m^7 \ \sin^6 \omega t \ \cos \omega t$$

(c)

t
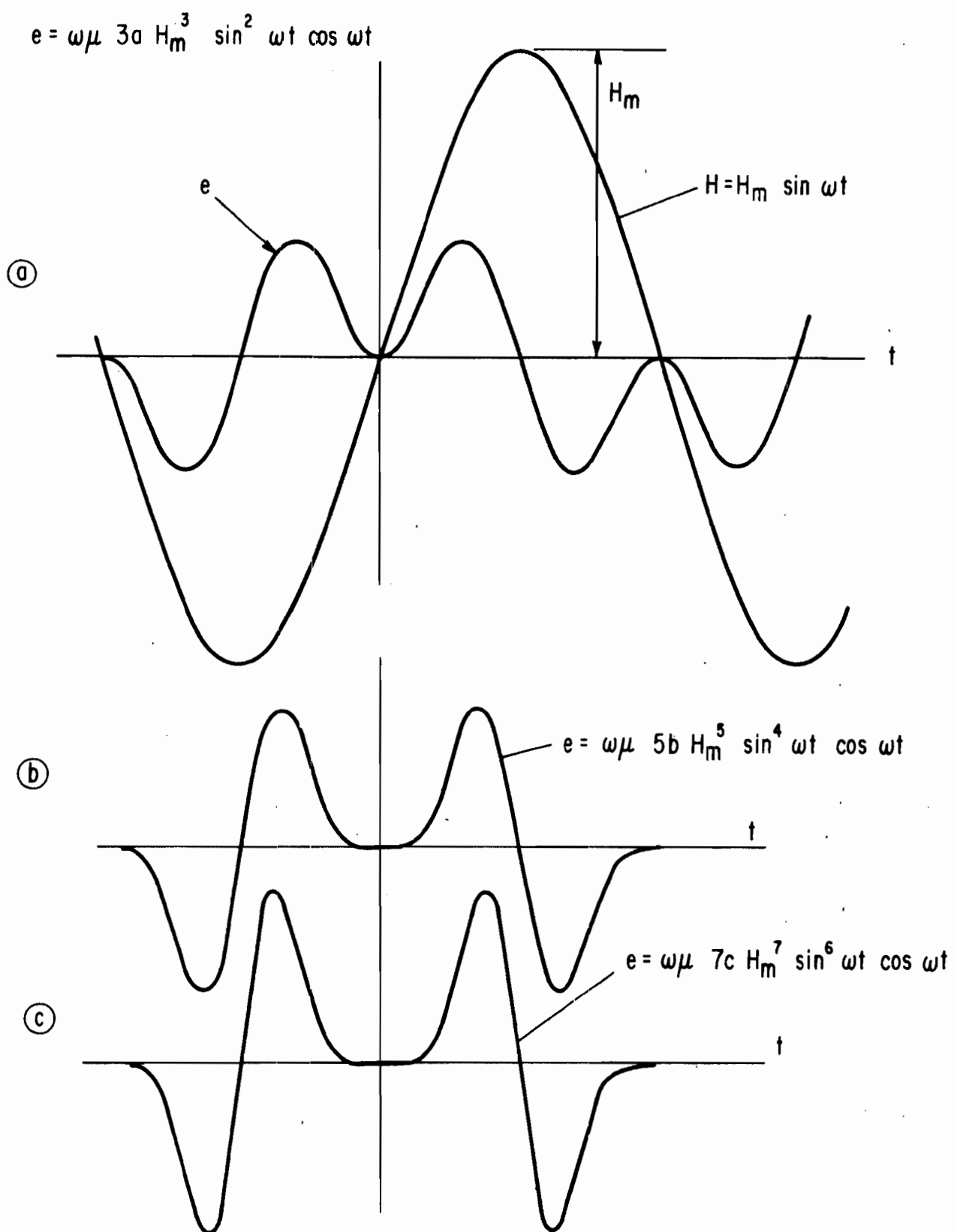
Figure 14 Calculated voltage curves.

53
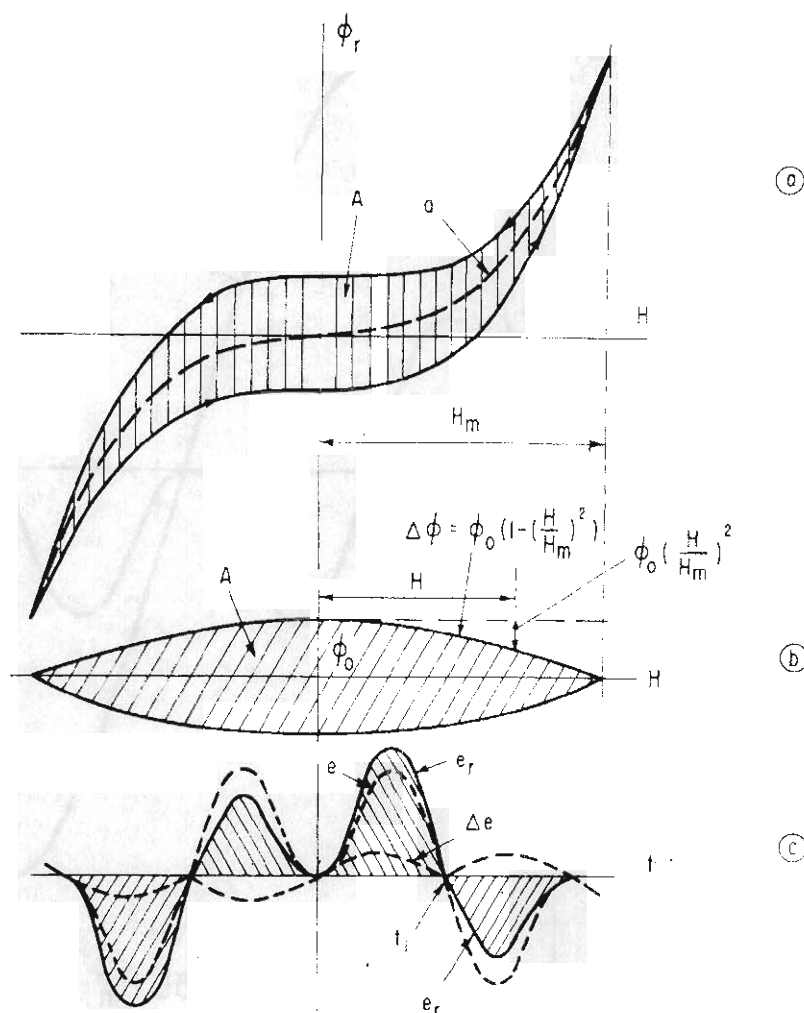
Figure 15 Flux hysteresis and calculated voltage curve e_r.

This is shown by the solid curve of Fig. 15(c). In this curve it is seen that a larger voltage peak alternates with a smaller voltage peak. A break in the slope of the voltage curve is also noticeable as e goes through zero (time t_1).

Figure 16(a) shows an oscillogram of the measured voltage e for H_m = 1000 Oe which shows good agreement with the voltage of Fig. 14(a). The oscillogram of Fig. 16(b) shows the measured voltage e_r for a field H = 1200 Oe [scale factor is different from that of Fig. 16(a)]. The agreement with the theoretical curve of Fig. 15(c) is good.

The losses per cm^2 of the surface are proportional to the enclosed area A of the loop of Fig. 15(a). That is:

$$L = fA \tag{54}$$

54

(a) $H_{max} = 1000$ Oe.

(b) $H_{max} = 1200$ Oe.
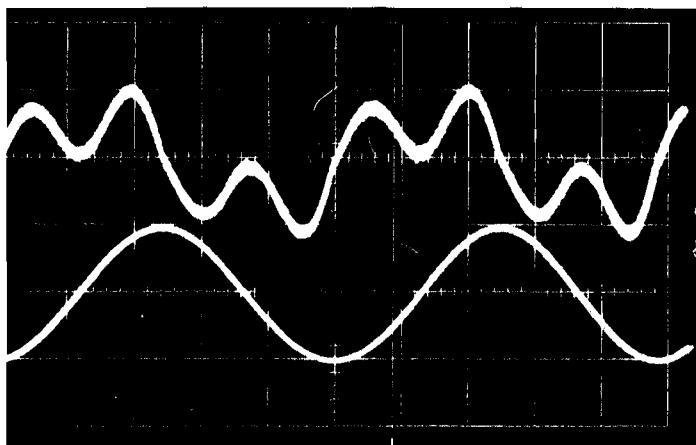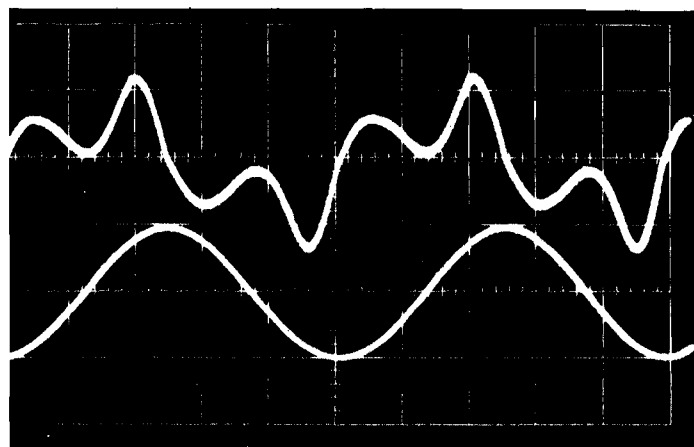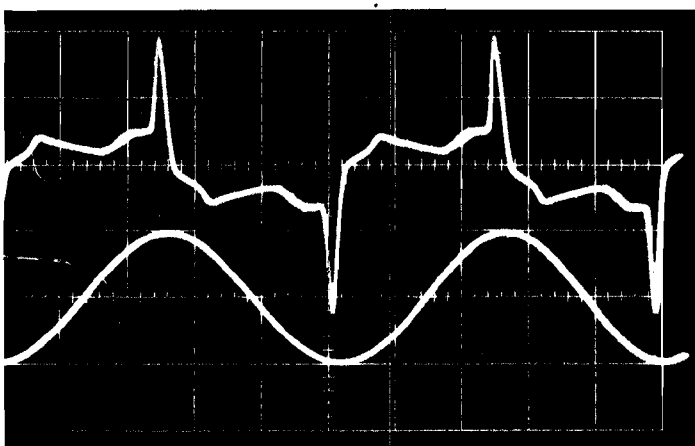
(c) $H_{max} = 1400$ Oe.

Figure 16   Measured voltage curves.

where f is the frequency and φ_r of Fig. 15(a) is referred to 1 cm of circumference.   The area (A) of Fig. 15(a) is equal to the area of Fig. 15(b).   Thus

$$A = \frac{2}{3} (4\varphi_0 H_m) = (8/3).\varphi_0 \, H_m \qquad (55)$$

where φ_0 is the trapped flux at $H = 0$.

With Eq. (54) the losses are

$$L = (8/3) f \varphi_0 H_m = k f \varphi_0 H_m \ . \tag{56}$$

The losses may then be described by two experimentally determined parameters k and φ_0 where k depends on the shape of the hysteresis loop and φ_0 is a measure of flux trapped in the sample at zero field. These factors, of course, depend upon the quality of the sample being tested.

D. EXPERIMENTAL RESULTS

1. The General Nature of Surface Losses

Superconducting surface losses for different samples were investigated as a function of field and temperature. The samples investigated included (a) pure, annealed niobium; (b) machined and lapped niobium; (c) machined, annealed and lapped niobium, and (d) polished, annealed niobium titanium alloys. Loss characteristics for samples (a), (b), and (c) as a function of field are shown in Fig. 17. It is seen that the losses for sample (b) are considerably higher than those for the other samples. This may be attributed to the method used for lapping this sample which undoubtedly introduced a considerable amount of surface impurity and strain. Note that although sample (c) was also lapped, the surface losses displayed by this sample were relatively low even when compared to the annealed sample. This is due to a new method for polishing niobium, developed on other programs, which results in smooth niobium surfaces with excellent superconducting properties. Surface losses for samples (a) and (b) as a function of temperature as well as field are shown in Figs. 18(a) and (b). These curves show that the surface losses at a given field strength increase very rapidly as a "critical temperature" for the particular field strength is approached. Well below this temperature the losses show little dependence upon the temperature. If this "critical temperature" is plotted against field, the familiar parabolic relationship between field and temperature results. That is:

$$H = H_0 \left[1 - \left(\frac{T}{T_c} \right)^2 \right] \tag{57}$$

where

H_0 is the a-c critical field at absolute zero.
T_c is the a-c critical temperature at zero field.
T is the a-c critical temperature at field H.

The a-c critical temperature in this case is defined as the temperature at which runaway breakdown of the sample occurs at a given a-c field. A curve
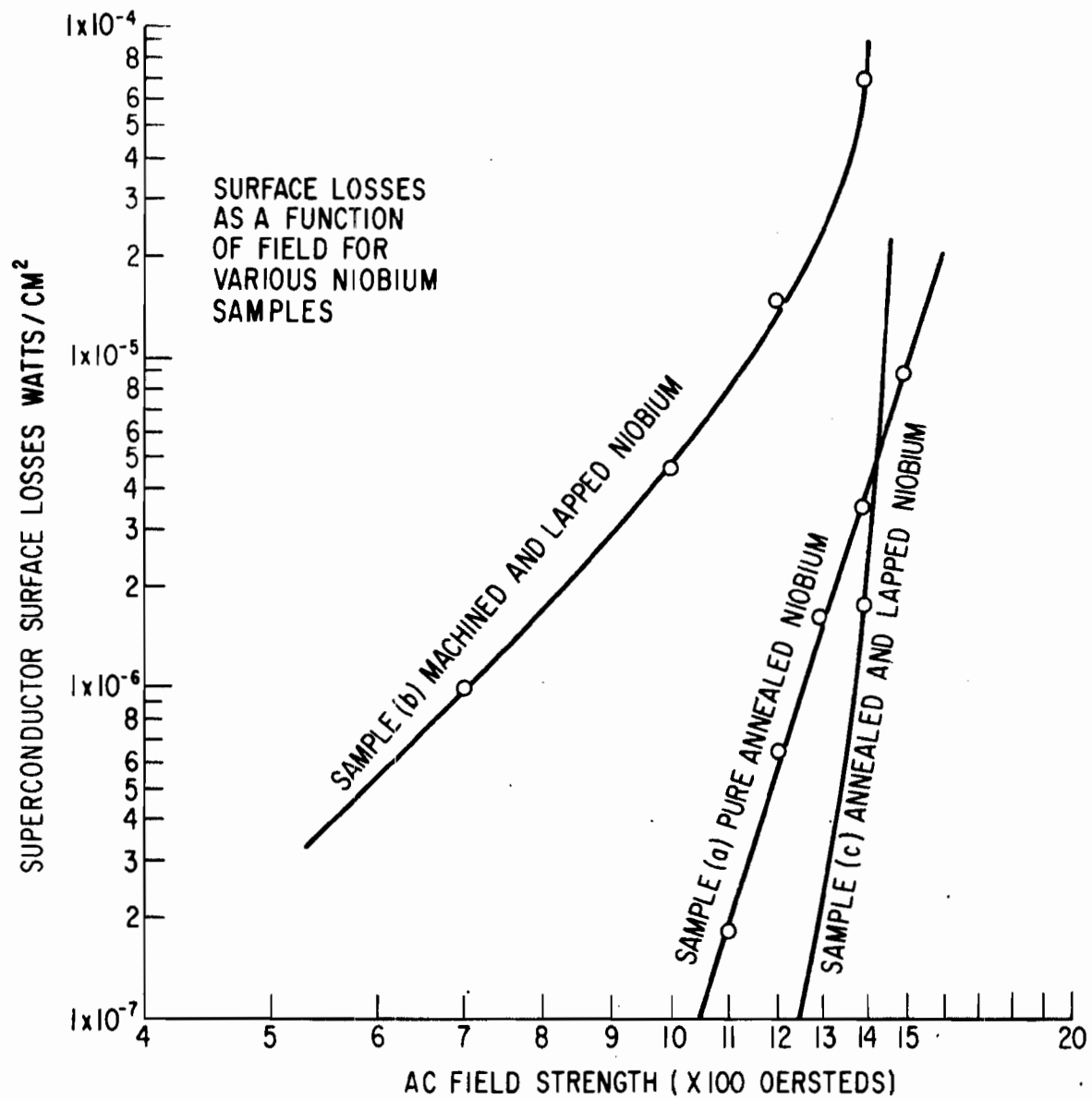
Figure 17 Surface a-c losses as a function of magnetic field for several niobium samples.
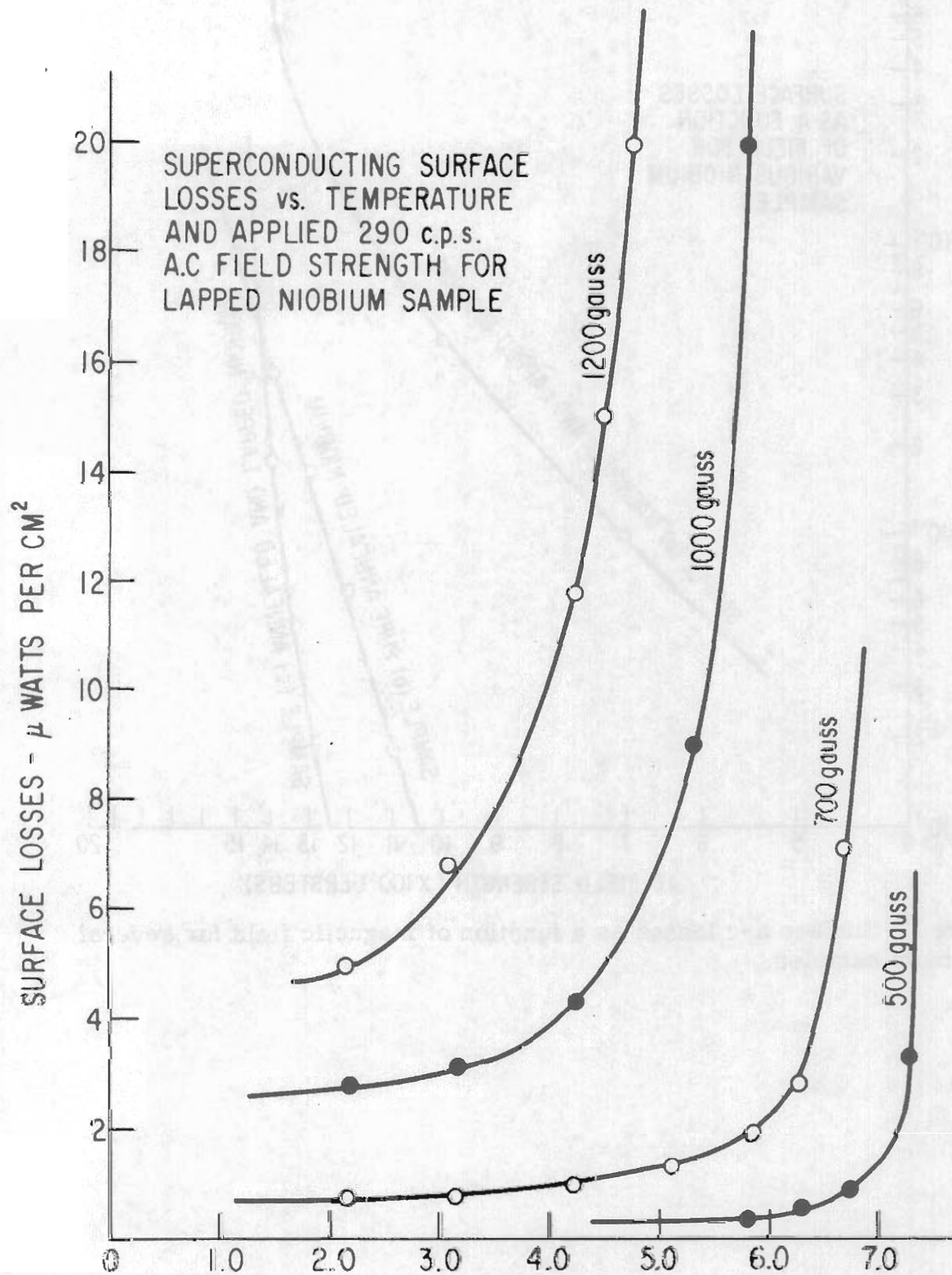
Figure 18(a) Superconducting surface losses vs temperature and applied
290 cps a-c field strength for a lapped niobium sample.
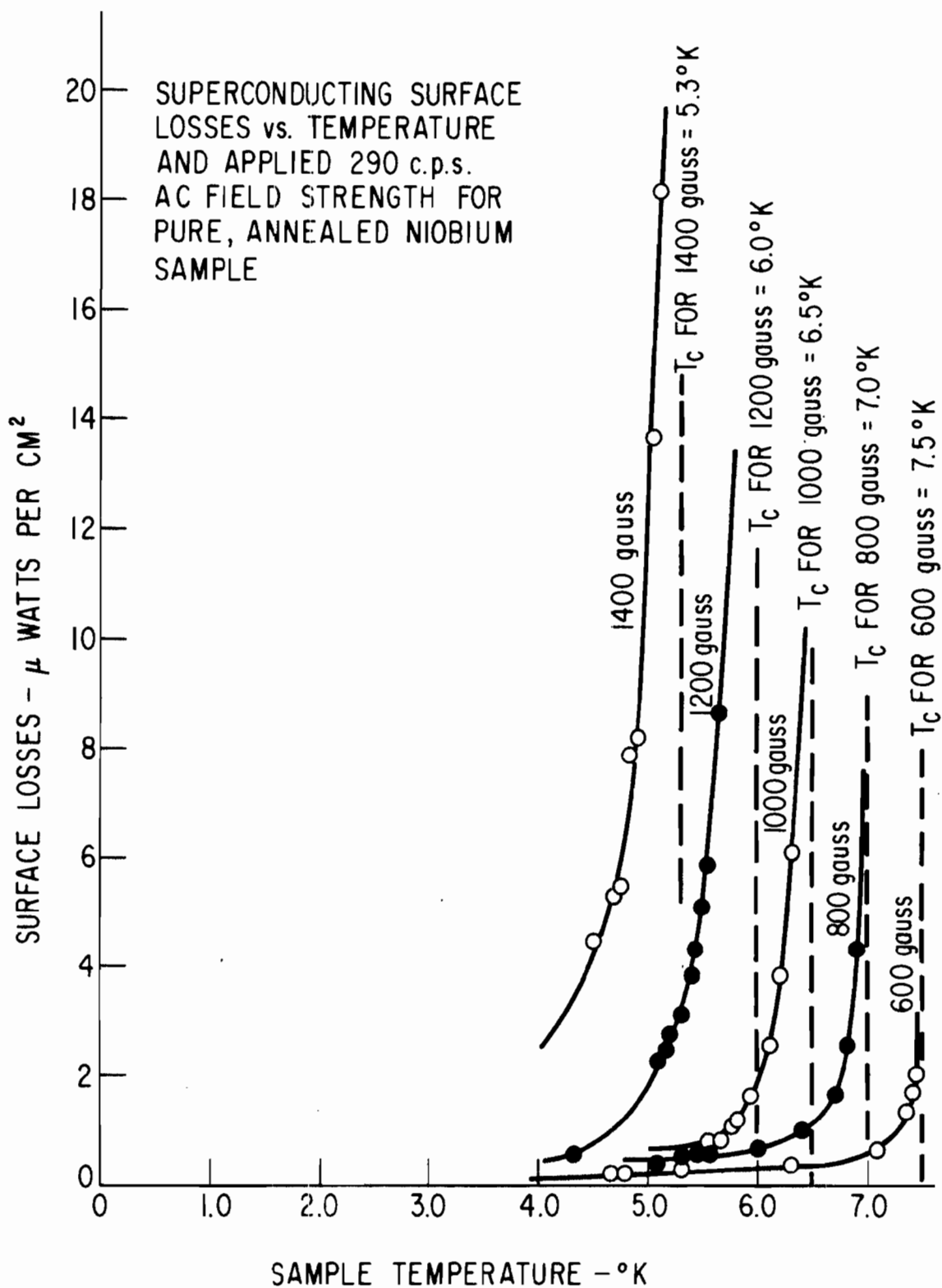
Figure 18(b) Superconducting surface losses vs temperature and applied 290 cps a-c field strength for a pure, annealed niobium sample.

59

showing the values measured for sample (a) is shown in Fig. 19 where it is seen that

$$H_0 = 2200 \text{ gauss}$$
$$T_C = 8.8°\text{K}.$$

It is interesting that the thermodynamic critical field-temperature relationship for niobium follows the same parabolic law with published values for the critical parameter for pure niobium being:

$$H_0 = 1950 \text{ gauss}$$
$$T_C = 9.2°\text{K}.$$

It is emphasized that the measurement reported here was made in alternating fields and it would not necessarily be expected that the critical parameters would be the same in both cases. However, the value $T_C = 8.8°\text{K}$ was considered appropriate for sample (a) under the test conditions and was used in evaluating the penetration depth measurements which will be discussed in a following section.

Typical penetration waveforms for sample (b) at various fields and temperature are shown in the photographs of Fig. 20. Note in these photographs

APPLIED A-C FIELD STRENGTH vs. CRITICAL TEMPERATURE FOR PURE ANNEALED NIOBIUM SAMPLE. CIRCLES ARE MEASURED POINTS AND SOLID LINE REPRESENTS PARABOLIC RELATIONSHIP

$$H = 2200 \left[1 - (T/8.8)^2 \right]$$
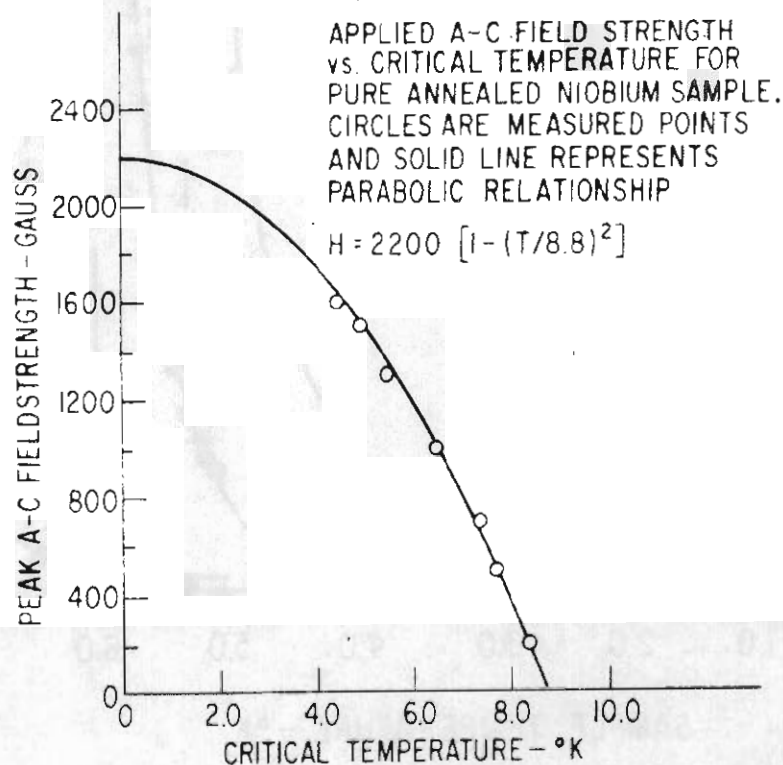
Figure 19 The a-c field strength vs critical temperature of a well-annealed niobium sample. The experimental points are fitted to the parabolic expression given in the figure.
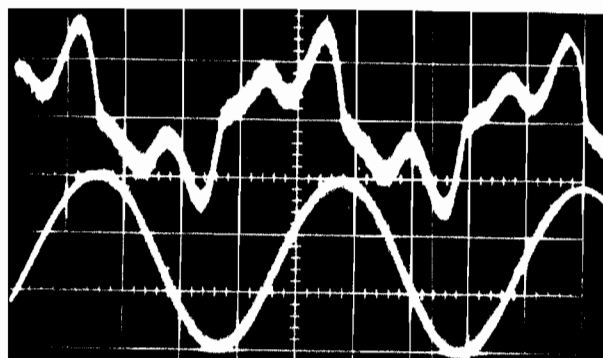
Sample temperature, $T = 4.25°K$
Penetration voltage sensitivity (upper
   trace), $V\varphi = 1 \times 10^{-5}$ volts/cm
Applied field maximum (lower trace)
   $H_M = 1000$ Oe
Operating frequency, $f = 290$ cps
Sensing coil turns, $N = 275$ turns
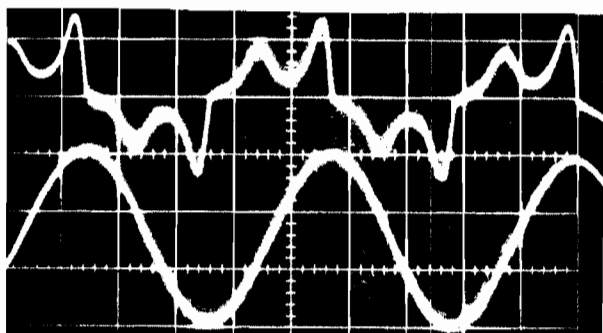
$T = 5.88°K$
$V\varphi = 1 \times 10^{-4}$ v/cm
$H_M = 1000$ Oe
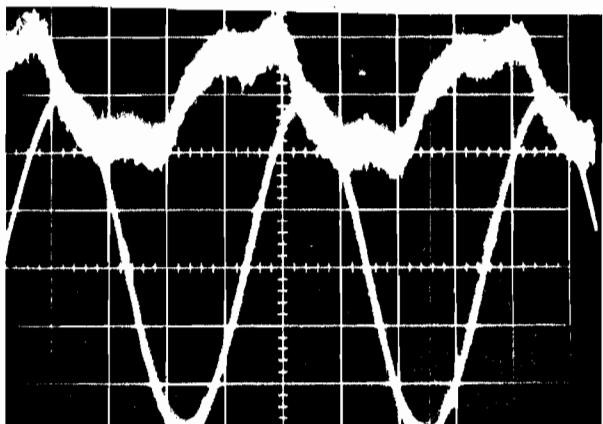
$T = 5.79°K$
$V\varphi = 5 \times 10^{-6}$ v/cm
$H_M = 500$ Oe
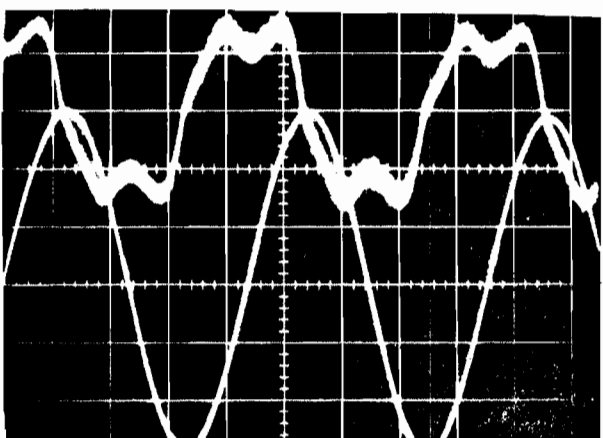
$T = 6.81°K$
$V\varphi = 1 \times 10^{-5}$ v/cm
$H_M = 500$ Oe

Figure 20   Penetration waveforms for a lapped niobium sample showing
relation to applied field and rapid rate of increase with temperature.

61

that peak penetration takes place where the voltage curve passes through zero. Normally this point occurs at the peak of the applied field. From the discussion of Section C, it is seen that these waveforms correspond to the theoretical description of a sample with relatively high losses as given therein. Also noticeable in these photographs is the increase in penetration with temperature as the sample shows correct compensation at $T = 4.25°K$ but becomes uncompensated for higher temperatures.

The photographs of Fig. 21(a) and (b) show some penetration waveforms taken on a high-purity niobium specimen that has not been previously mentioned. This is presented to illustrate a definite change in the mode of penetration as the lower critical field H_{c1} is exceeded. These waveforms show that the mode of flux penetration is similar over a considerable temperature interval but that, for a special field-temperature condition, another flux penetration mode begins, which involves rapid flux penetration and expulsion over the narrow field interval from 970 to 995 Oe [see Fig. 21(b)]. This mode is found to be extremely sensitive to field changes and generally corresponds to rapidly increasing a-c losses. It is believed that this mode is encountered as H_{c1} is exceeded.

The effective depth of penetration of the field in sample (b) is shown in Fig. 22 as a function of temperature. (Note that the effective penetration depth in this case can be significantly different from that for pure niobium due to the relatively high losses displayed by this sample.) This penetration depth was measured by the method discussed in Section B.

(A) Penetration Coil Voltage and Applied Magnetic Field Vs Time for 1000 Oersteds at 3.5°K and 5.5°K.

3.5°K
1.0 x 10^{-5} volts/cm
L ~ 1.6 x 10^{-6} watts/cm^2

5.5°K
1.0 x 10^{-5} volts/cm
L ~ 2.6 x 10^{-6} watts/cm^2

(B) Penetration Coil Voltage and Applied Magnetic Field Vs Time for 970 Oersteds and 995 Oersteds at 6.1°K Showing Onset of Different Mode of Flux Penetration.

970 Oersteds
2 x 10^{-5} volts/cm
L ~ 2.4 x 10^{-6} watts/cm^2

995 Oersteds
2 x 10^{-5} volts/cm
L ~ 2.8 x 10^{-6} watts/cm^2

Figure 21 Flux penetration waveforms for a high-purity niobium specimen exposed to 300 cps magnetic fields.
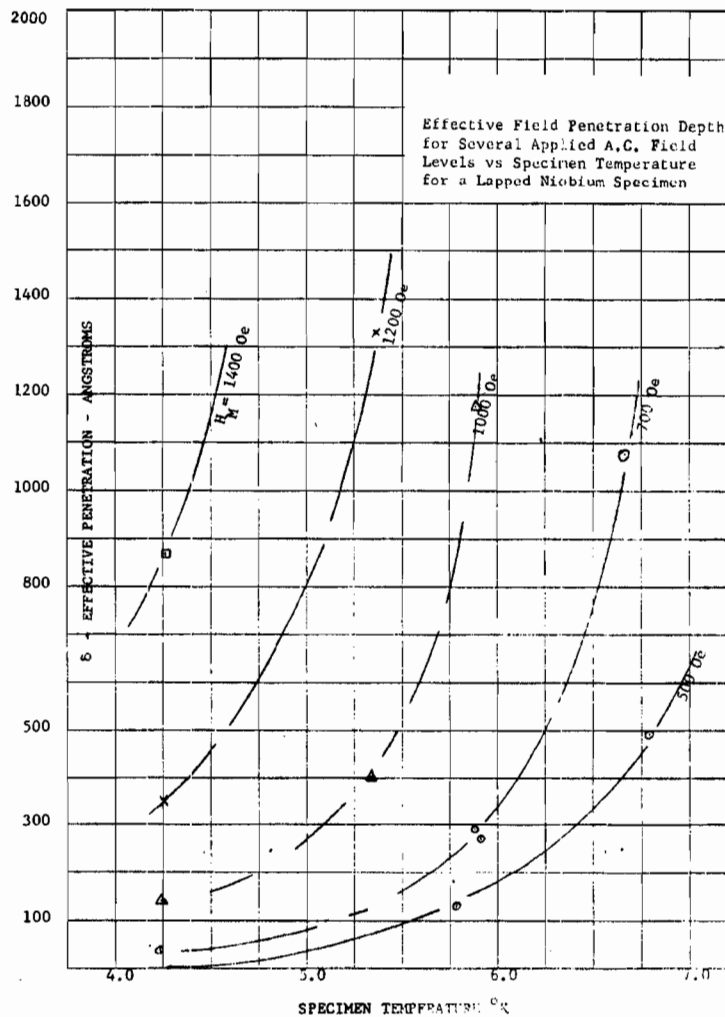
Figure 22 Effective field penetration depth for several applied a-c field
levels vs specimen temperature for a lapped niobium specimen.

The a-c losses and effective penetration depth as noted in a niobium
titanium alloy, sample (d), are shown in Fig. 23. This sample consisted
of 98.43 w/o niobium and 1.57 w/o titanium, and the sample was highly
polished and heat treated at 1600°C for 5 hours at a pressure of 4×10^{-6} mm
Hg. The addition of titanium has the effect of lowering H_{c1} as compared to
that of pure niobium, and it is seen that losses occur at low field strengths
and increase very rapidly with the applied field.

Typical penetration waveforms for this sample are shown in the
photographs of Fig. 24 at different levels of peak field strength. It is seen
that these waveforms are similar to those for pure niobium at high field
strengths where abrupt penetration and expulsion take place. It is interesting
to note the phase relationship between the peak of the penetration waveforms,
which is the upper trace, and the peak of the applied field, the lower trace.
It is seen that the peak of the penetration curve appears very close to the
peak of the applied field.

63
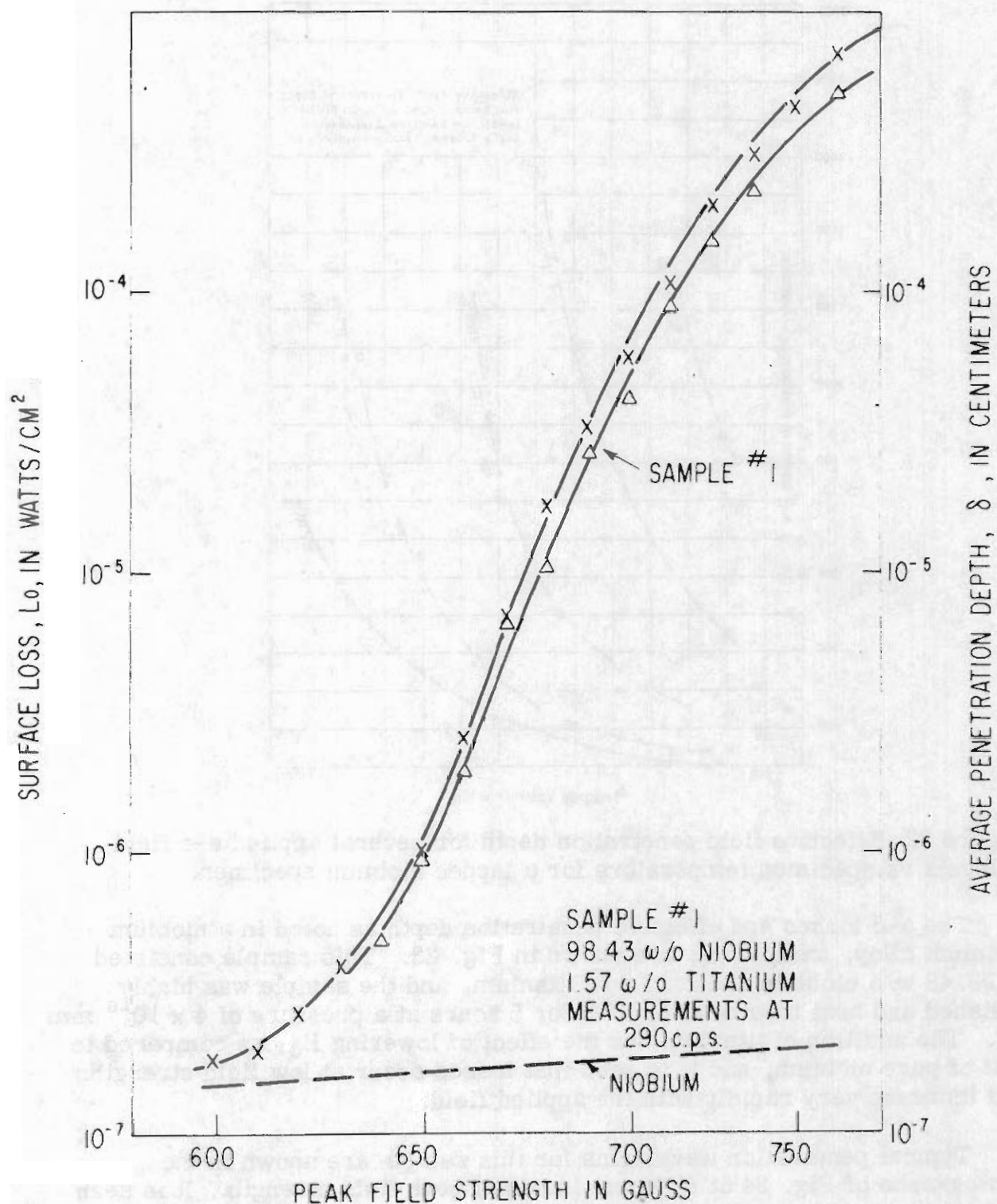
Figure 23 Surface losses and additional penetration depth for 98.43 w/o
Nb + 1.57 w/o Ti.

SAMPLE #1
98.43 w/o NIOBIUM
1.57 w/o TITANIUM
MEASUREMENTS AT
290 c.p.s.

NIOBIUM
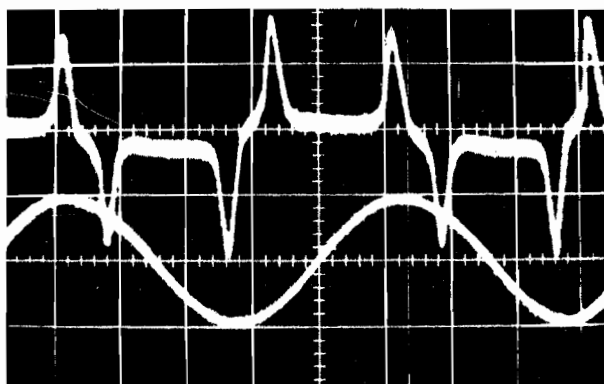
650 gauss:

0.71×10^{-5} v/cm;
$L \sim 1.0 \times 10^{-6}$ w/cm^2.
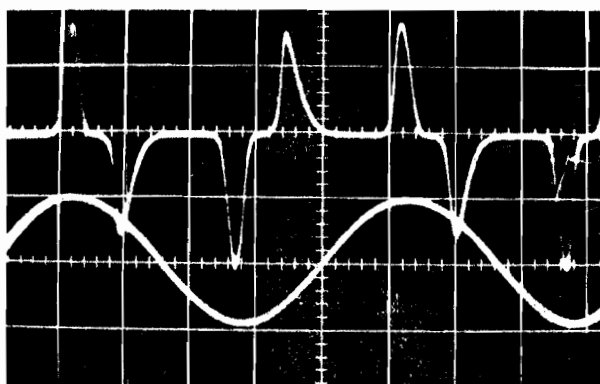
700 gauss:

0.50×10^{-3} v/cm;
$L \sim 6.0 \times 10^{-5}$ w/cm^2.
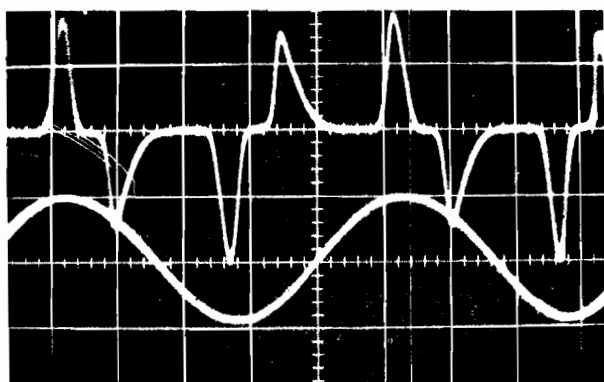
725 gauss:

1.67×10^{-3} v/cm;
$L \sim 2.6 \times 10^{-4}$.
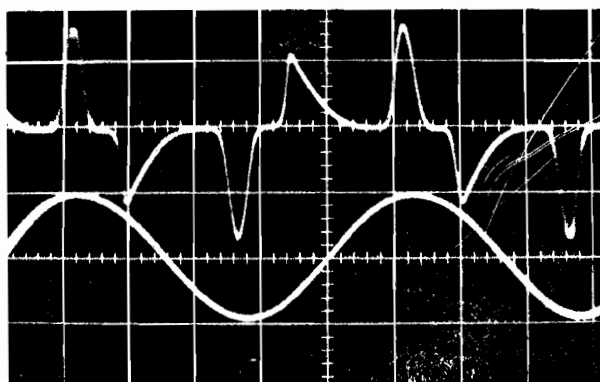
750 gauss:

0.5×10^{-2} v/cm;
$L \sim 7.0 \times 10^{-4}$.

Figure 24 Sample 1. 98.43 w/o Nb + 1.57 w/o Ti. Penetration coil voltage and applied magnetic field vs time for various field strengths.

Figure 25 shows some similar penetration waveforms encountered on a typical high-purity annealed sample of niobium. The sinusoidal trace in these photographs is proportional to the time rate of change of the applied field rather than to the field itself which was the case for the previous photographs. (The zero of the dH/dt curves occur at the peak of the applied field.) The important factor to be noted in these traces is the shift in the peak of the penetration waveform with respect to the zero of the dH/dt curve as the applied field strength is increased. It is noted that at 1400 gauss the zero of the dH/dt curve is aligned very closely with the zero of the penetration waveform. However, as the applied field is increased and as the penetration mode changes, the zero of the dH/dt curve begins to align with the peak in the penetration curve. This means that for lower fields as the applied field reaches a peak, the rate of flux penetration goes to zero. However, for

1400 gauss.

1500 gauss.

1550 gauss.
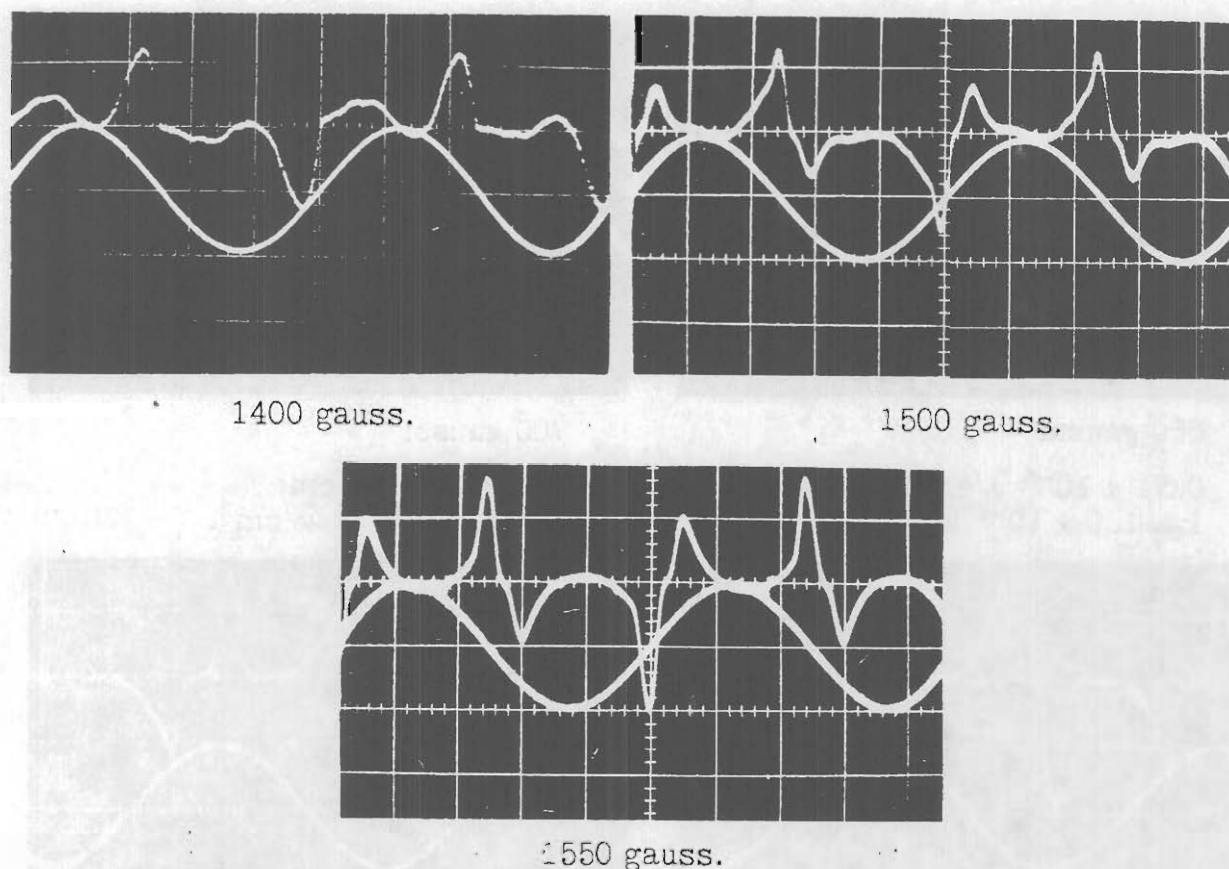
Figure 25 Photographs showing phase relationship between penetration
waveform and time derivative of applied magnetic field at increasing field
strengths. Sample used was a high-purity vacuum annealed niobium
cylinder. (Note shift in peak of penetration waveform with respect to zero
of dH/dt waveform.)

higher field strengths, as the applied field reaches a peak, the rate of
penetration is also reaching a peak. This is often a characteristic of pene-
tration occurring above H_{c1}, the lower critical field in a type II super-
conductor.

2. Flux Penetration Behavior in Niobium

Section C presented preliminary evidence of the dependence of the pene-
tration depth on the applied field strengths. It was seen from the photographs
in Fig. 16 that good agreement between the theoretically derived waveforms
of Fig. 14 and the actual observations was obtained. Direct measurements of
the penetration depth as a function of field were made and the result is shown
in Fig. 26. (Note that in the measurements, the London penetration is
compensated at zero field and the values presented here represent the change
in the penetration depth with field.)

It appears from this curve that, in the field range covered by these measurements, the fourth power term in Eq. (44) is the most significant and that the penetration depth for this particular sample can be quite accurately described as

$$\lambda = \lambda(0) + bH^4 \quad . \tag{58}$$

This appears to be at least valid for the field range from H = 800 gauss to H = 1300 gauss. The coefficient b can easily be determined from the slope of the curve in Fig. 26 and yields a value of b = 8.3 x 10^{-12} Å/(gauss)^4.

The sample used for this measurement was sample (C) mentioned previously. This sample displays considerably lower surface loss characteristics throughout this field range, so that it is felt that this measurement represents a fundamental property of niobium under these conditions.

The theory of Section C was developed on the basis that the second-order term in H was most significant. However, it can be seen from the waveforms of Fig. 14 that the differences in the predicted penetration waveforms would be minor.
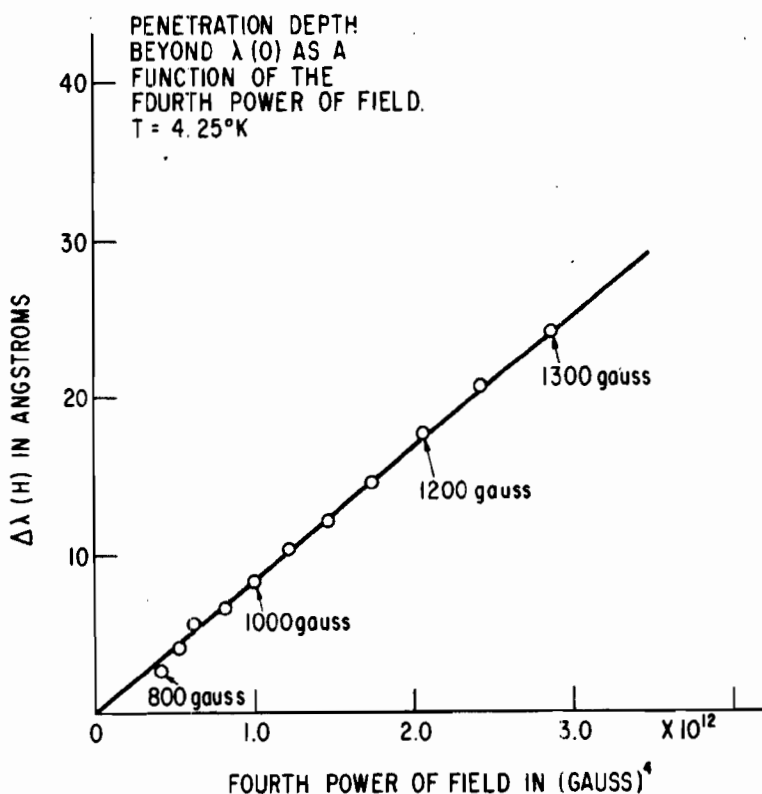
Figure 26 Penetration depth above λ(0) as a function of the fourth power of the field. T = 4.25°K.

67

The London penetration depth in niobium was also investigated using the measurement method described in Section B. This method measures the change in the penetration depth, $\Delta\lambda$, with temperature and it is necessary to know the functional relationship between the penetration depth and temperature in order to deduce the actual value of λ_0, the penetration depth at absolute zero. It is well known that the variation of λ with T fits the following relationship quite well:

$$\lambda(T) = \lambda_0 y = \frac{\lambda_0}{\left[1 - \left(\frac{T}{T_c}\right)^2\right]^{1/2}} \tag{59}$$

This relationship has been shown to be quite accurate for values of T near T_c but as y approaches 1, a plot of λ vs y shows a definite increase in slope. However, as T increases, the curve approaches a constant slope that can be used as a measurement of λ_0.

Figure 27 shows the measured values of $\Delta\lambda$ as a function of y for sample (a). It is seen from these data that, at larger values of y, the curve approaches a straight line whose slope is 580 Å in this region. Also noted is the predicted increase in slope of the curve at lower values of y.

This measurement method is very sensitive to the value used for the critical temperature of the sample being measured. In evaluating these data, the critical temperature of 8.8°K that had been measured by the a-c method described previously was used.

A similar measurement was made on sample (c) which yielded the same result within the experimental accuracy. Again a critical temperature of 8.8°K was observed.
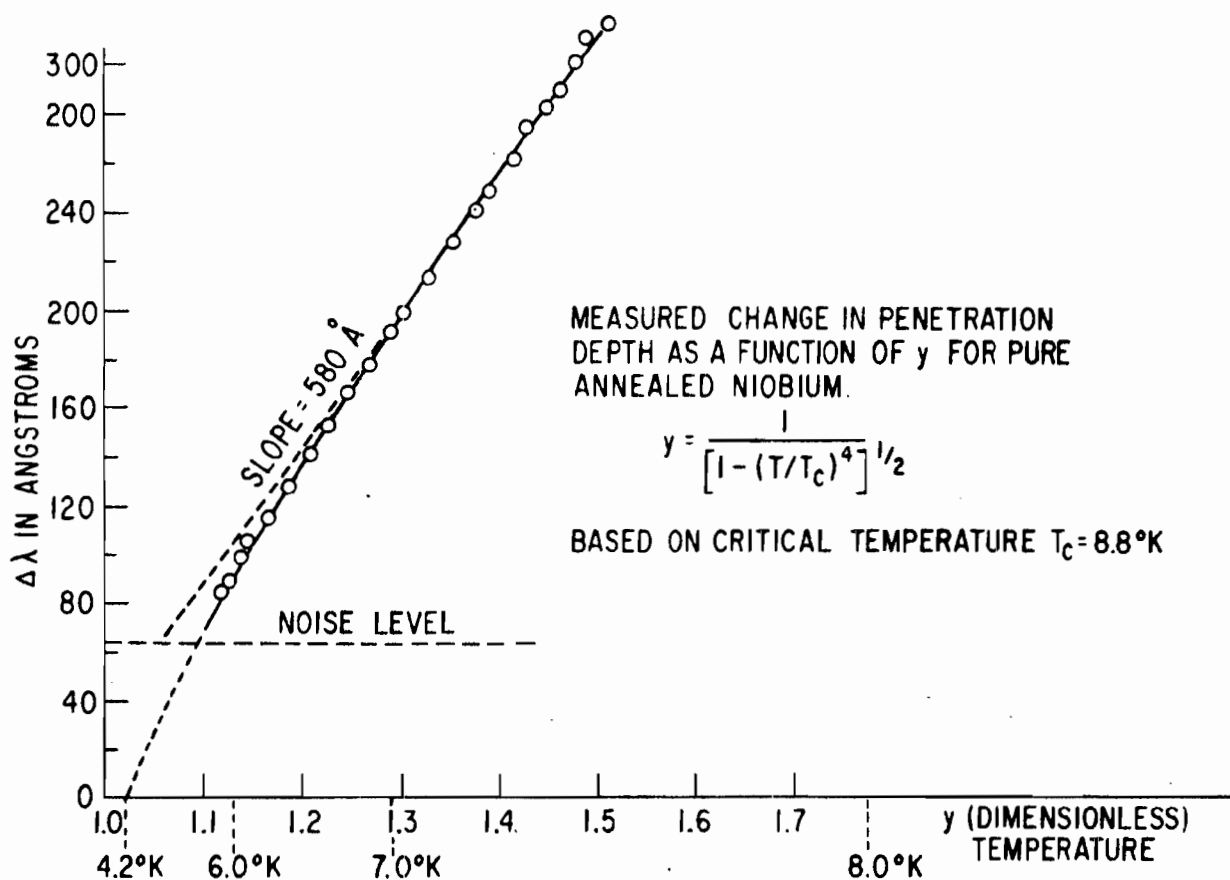
Figure 27 The change in London penetration depth ($\Delta\lambda$) plotted against the dimensionless parameter y.   See text for discussion.

Text within figure:

$\Delta\lambda$ IN ANGSTROMS

SLOPE = 580 Å

NOISE LEVEL

MEASURED CHANGE IN PENETRATION DEPTH AS A FUNCTION OF y FOR PURE ANNEALED NIOBIUM.

$$y = \frac{1}{\left[1-(T/T_c)^4\right]^{1/2}}$$

BASED ON CRITICAL TEMPERATURE $T_c = 8.8\,°K$

y (DIMENSIONLESS) TEMPERATURE

DYNAMIC FLUX MOTION ABOVE H_{c_1}

A. ROTATIONAL HYSTERESIS IN HIGH FIELD SUPERCONDUCTORS
(C. P. Bean and C. D. Graham)

1. Theory (C. P. Bean)

The problem of losses in high field superconductors exposed to an alternating magnetic field has been successfully treated[7, 10, 19] by a phenomenological theory that depends on only one parameter of the material--its superconducting critical current density, J_c. (See also Section II.) The basic assumption is that wherever a local electric field is felt during the process of magnetization, a critical current density J_c is caused to flow in the direction of the electric field and which is sustained even when the electric field falls to zero. The consequence of this assumed state of affairs is illustrated in Fig. 28, which shows the internal field within the specimen after application of a field H_0 parallel to the surface. If the Z direction is measured from the surface, then

$$H = H_0(1-Z/\delta) \tag{60}$$

where δ, the field-dependent penetration depth, is given by

$$\delta = 10H_0/4\pi J_c \quad . \tag{61}$$
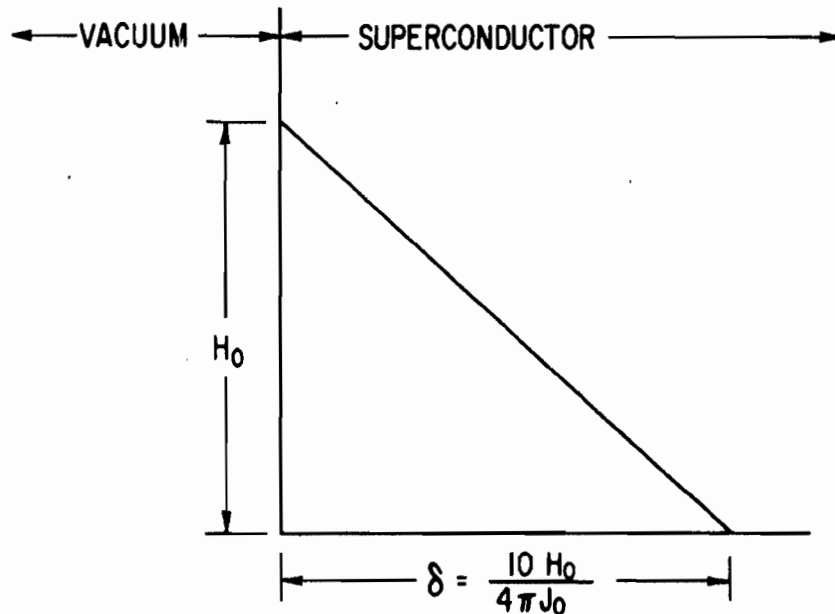
Figure 28 The strength of the magnetic field within the bulk of a hard type II superconductor after the application of a field H_0.

This solution is consonant with Maxwell's equations; in particular, it is governed by Ampere's law--curl $H = 4\pi J/10$. For losses, the theory outlined above gives for losses in alternating fields

$$W(alt)_S = 5H_0^3/12\pi^2 J_c \quad \text{ergs/cm}^2 \text{ - cycle}$$

$$H_0 \leq H^* \tag{62}$$

$$W(alt)_V = H_0 J_c D/10 \quad \text{ergs/cm}^3 \text{ - cycle}$$

$$H_0 \gg H^* \quad . \tag{63}$$

Recently, we have been able to extend the ideas to the case of fields that rotate in the plane of the specimen. The geometry is shown in Fig. 29 where the X-Y plane defines the surface of a semi-infinite slab. We consider the field to have an amplitude H_0 and angular frequency ω and assert a self-consistent expression for the fields in steady state as a function of space and time to be

$$H_X = H_0(1-Z/\sqrt{3}\delta) \cos[\omega t + \sqrt{2}\ln(1-Z/\sqrt{3}\delta)]$$
$$H_y = H_0(1-Z/\sqrt{3}\delta) \sin[\omega t + \sqrt{2}\ln(1-Z/\sqrt{3}\delta] \tag{64}$$
$$H_Z = 0$$

where δ is defined by Eq. (61). This field distribution has an amplitude that decreases linearly with distance but extends $\sqrt{3}$ times as far as that for the
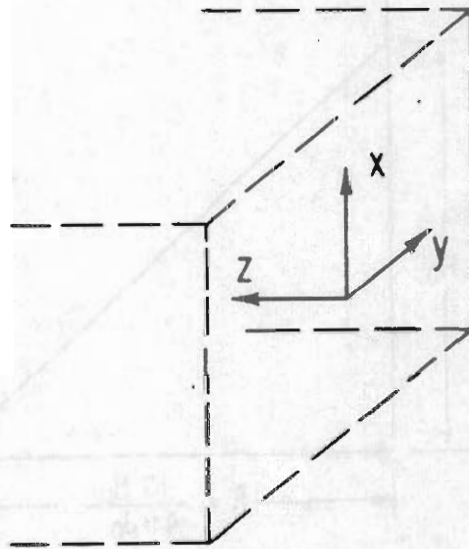
Figure 29 A definition of the reference axes relative to the surface of the superconductor (see text).

alternating field. This is shown in Fig. 30(a). The phase of the field within the specimen lags that of the applied field as shown in Fig. 30(b). At the inner interface of the active region ($Z = \sqrt{2}\delta$) the phase lag approaches infinity. This condition indicates that, strictly speaking, the steady state hypothesized here will be asymptotically approached only after many revolutions of the field. From Fig. 30(b), however, we note that 90% of the thickness of the penetration layer has a phase angle of 180° or less--hence a rotation of 180° will develop a torque close to that of the steady state. Application of Ampere's law gives for the
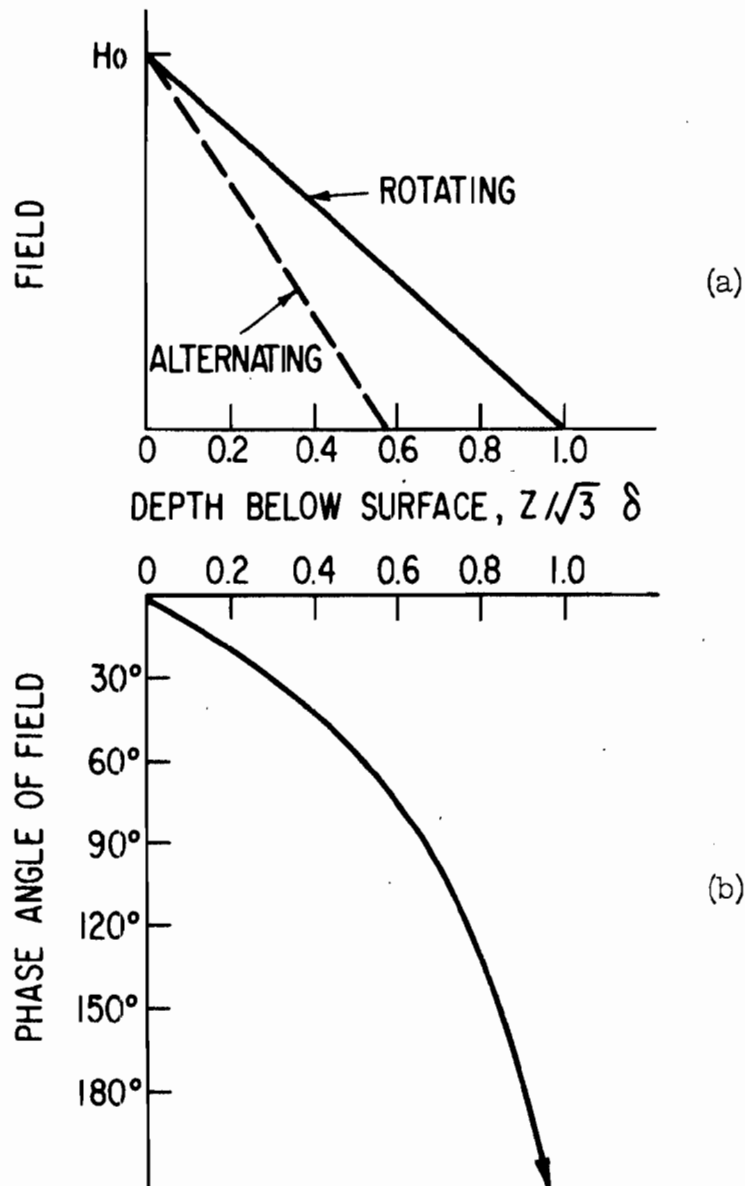
Figure 30 (a) The strength of the magnetic field within the bulk of a type II superconductor after the application of a rotating or alternating field H_0. (b) The phase angle of the magnetic field within the type II superconductor relative to the phase of the applied rotating field at the surface.

current densities within the penetration depth

$$J_x = (J_c/\sqrt{3}) (\sin \varphi + \sqrt{2} \cos \varphi)$$

$$J_y = (J_c/\sqrt{3}) (\sqrt{2} \sin \varphi - \cos \varphi) \tag{65}$$

$$J_z = 0 .$$

In these expressions, and subsequently, the trigonometric argument $[\omega t + \sqrt{2} \ln(1 - Z/\sqrt{3} \delta)]$ is replaced by φ. By expansion

$$J_x^2 + J_y^2 = J_c^2 \tag{66}$$

a condition of the theory. The local electric fields may be found by application of Faraday's law--curl $E = - 10^{-8}(\partial H/\partial t)$ to the fields of Eq. (64). These fields are

$$E_x = [10^{-8} H_0 \omega \delta (1-Z/\sqrt{3} \delta)^2/\sqrt{6}] (\sin \varphi + \sqrt{2} \cos \varphi)$$

$$E_y = [10^{-8} H_0 \omega \delta (1-Z/\sqrt{3}\delta)^2/\sqrt{6}] (\sqrt{2} \sin \varphi - \cos \varphi) \tag{67}$$

$$E_z = 0$$

with the boundary condition

$$E_x = E_y = 0 \text{ at } Z = \sqrt{3} \delta \tag{68}$$

From Eqs. (65) and (67), we may show

$$J \times E = 0 . \tag{69}$$

Hence the current density is parallel to the local electric field. The local rate of energy dissipation in joule heat, W, is given by

$$\dot{W} = E \cdot J = (10^{-8} H_0 \omega J_c \delta/\sqrt{2}) (1 - Z/\sqrt{3} \delta)^2 . \tag{70}$$

The total rotational hysteresis per unit area is

$$W(rot)_S = \int_0^{\sqrt{3}\delta} \dot{W}\, dZ\, (2\pi/\omega)$$

(71)

$$= (10/8\pi\sqrt{6})\,(H_0^3/J_c)\ \text{ergs/cm}^2 - \text{cycle}\ .$$

This gives immediately for the ratio of rotating to alternating loss

$$W(rot)_S/W(alt)_S = \sqrt{6}\,\pi/2 = 3.84\ .$$

(72)

The rotational torque in steady state is given by

$$T(rot)_S = W(rot)_S/2\pi$$

(73)

$$= [10/(4\pi)^2\sqrt{6}]\,(H_0^3/J_c)\ \text{dyne-cm/cm}^2\ .$$

To this point we have assumed that the current density, J_c, is independent of field. This restriction may be lifted by noting that the increase in torque $\Delta T(rot)$ for an increase in field ΔH is from Eqs. (71) and (73)

$$\Delta T(rot)_S = (1/\omega)[\dot{W}(0)]\,[10\sqrt{3}\,\Delta H/4\pi J_c(H_0)]\ .$$

(74)

That gives

$$\Delta T(rot)_S = [10\sqrt{3}/\sqrt{2}(4\pi)^2]\,[H_0^2/J_c(H_0)]\Delta H$$

(75)

or in the differential limit

$$\frac{\partial T}{\partial H}\bigg| = (5\sqrt{3}/8\sqrt{2}\,\pi^2)\,H_0^2/J_c(H_0)\ .$$

(76)

This last expression allows one to calculate $J_c(H_0)$ from an experimental torque curve or alternatively predict the dependence of torque upon field for an arbitrary dependence of J_c upon H_0.

In summary, we have calculated the losses of inhomogeneous type II superconductors in a rotating field, and find the losses to have similar dependence to those in alternating fields but approximately four times as large. In

75

addition, this type of measurement may prove to be a convenient method for determination of critical current densities. Lastly, anisotropies in current densities (not treated here) will give characteristic torque curves that would appear to be simply interpretable.

2. Experiment (C. D. Graham, Jr.)

Torque measurements to check the predictions of the preceding section have so far been unsuccessful because of flux jumping.

Measurements were made on a sample of Nb + 2% Zr, obtained from H. W. Schadler. The sample was a disk, originally 1.283 cm in diameter by 0.13 cm thick. Torque measurements were made at 4.2°K in an apparatus of the kind used to determine magnetic anisotropy in magnetic materials. The sample was suspended from a tungsten torsion fiber with a magnetic field parallel to a diameter of the disk, and the torque acting on the sample was recorded as a function of angular position as the sample was rotated about an axis normal to its surface. Measurements were made in a series of constant fields, and for both clockwise and counterclockwise rotation of the sample.

In the first experiment there was a relatively large torque due to trapped flux in the sample. According to the Bean model, rotational hysteresis is a surface property of the sample, whereas the trapped flux is a volume property. Reducing the sample thickness should, therefore, reduce the torque due to trapped flux, but leave the rotational hysteresis unaffected. When the sample thickness was reduced to 0.025 cm (a factor of five) the torque due to trapped flux was appropriately reduced while the rotational hysteresis torque was approximately unchanged.

There was no significant torque on the sample in fields less than 1 kOe. In constant fields between 1 and 3 kOe, the torque as a function of angle rose smoothly to an approximately constant value in less than half a revolution, as shown in Fig. 31. This behavior is qualitatively in agreement with Bean's
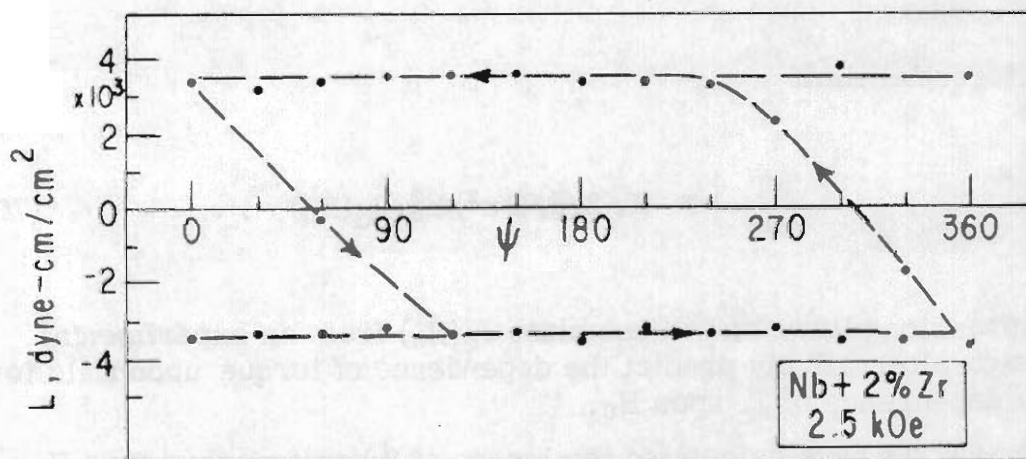
Figure 31 Torque vs angle for Nb + 2% Zr disk, 2.5 kOe, 4.2°K.

prediction. At 3.5 kOe, flux jumping appeared, and prevented the torque from reaching an equilibrium value. An example is shown in Fig. 32. This behavior persisted up to about 9 kOe, and at higher fields the torque vanished.

A magnetization curve and hysteresis loop measured on the same sample are shown in Fig. 33. The magnetization data show that the alloy is highly hysteretic, and confirm the values $H_{c1} = 1$ kOe and $H_{c2} = 9$ kOe which were suggested by the torque data. Flux jumping is evident in the magnetization data, although over a narrower range of fields than was found in the torque measurements.

An attempt to eliminate flux jumping during the torque measurement was made by enclosing the disk sample in a tight-fitting high-purity aluminum holder. No significant change in the flux-jumping behavior resulted.
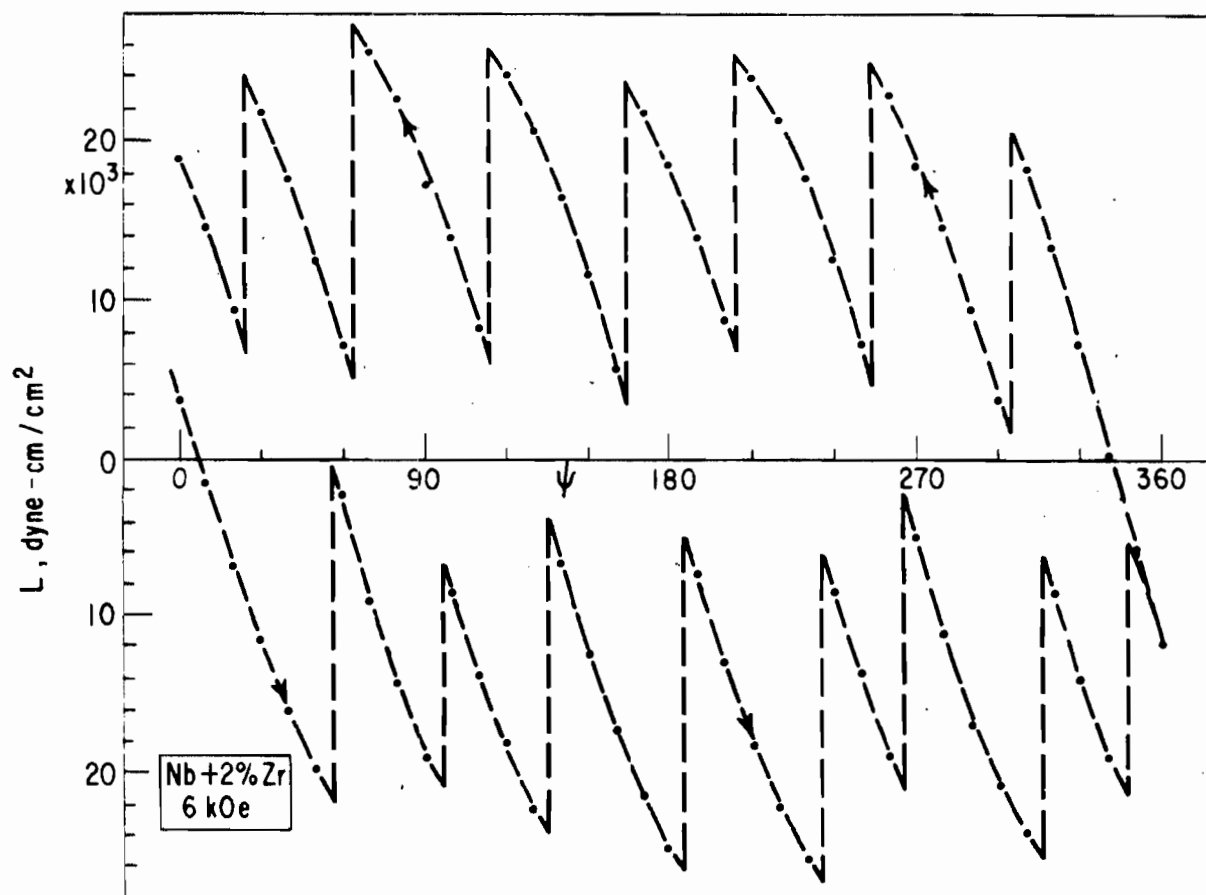
Figure 32   Torque vs angle for Nb + 2% Zr disk, 6 kOe, 4.2°K.
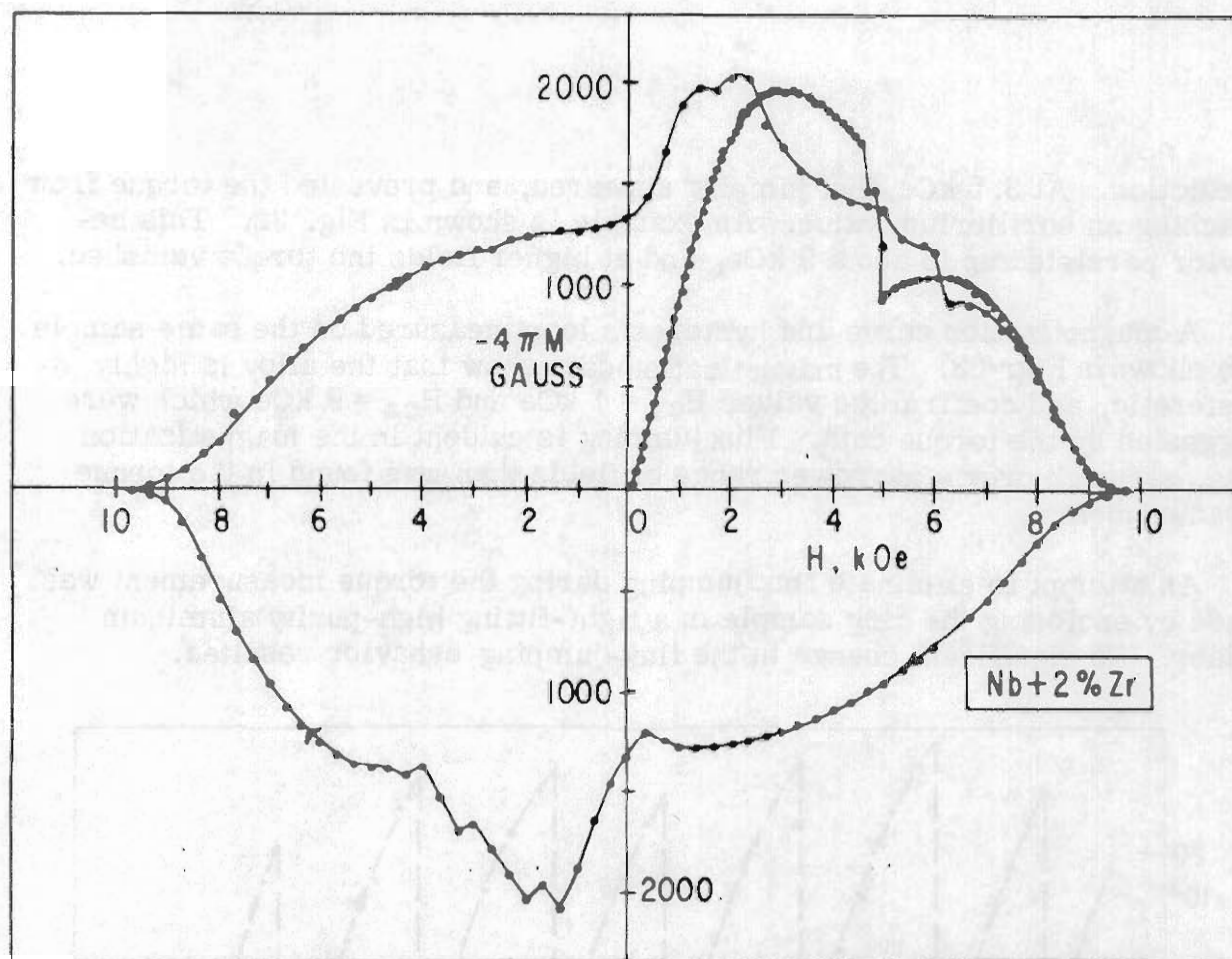
Figure 33 Magnetization curve and hysteresis loop of Nb + 2% Zr disk (same samples as in Figs. 31 and 32).

(a) Future Work

Two lines of approach are open. First, we might try to find another material less susceptible to flux jumping which would permit a straightforward test of the Bean predictions. Some work along this line is under way. Second, we can try to make the best possible use of the data obtainable from the Nb-Zr sample, either by taking extensive measurements in the narrow field region (1 to 3 kOe) which is free of flux jumping, or by extending the theory to conditions other than the equilibrium rotational hysteresis state. The data of Fig. 32 suggest that after a flux jump in rotation, the torque is nearly zero. This in turn implies that the sample has been driven completely normal and that the field in the sample is everywhere equal and parallel to the applied field. Such a state is relatively simple, and may be susceptible to mathematical analysis.

B. DYNAMIC SUSCEPTIBILITY (H. R. Hart, Jr. and P. S. Swartz)

1. Introduction

In order to continue our investigations of a-c losses and dynamic flux motion into frequency ranges higher than power frequencies, we began studies of two widely different classes of materials at audio- and radiofrequencies. The materials chosen were the intermetallic compound V_3Ga, a brittle, magnetically irreversible material with $H_{c2} \gtrsim 200,000$ Oe, and $Nb_{0.70}Ta_{0.30}$, a ductile alloy with H_{c2} less than 10,000 Oe. The Nb-Ta system is very convenient for such studies, for it can be annealed to form a very reversible type II superconductor; in addition, the value of H_{c2} can be varied by varying the alloy composition. Further, the surface can be electropolished to provide a very smooth finish.

2. Experimental Techniques

The experiments described in this section are directed to measurements of dynamic or a-c susceptibilities in powders of V_3Ga or ribbons of $Nb_{0.70}Ta_{0.30}$ that have been placed in steady magnetic fields up to 23,000 Oe. The susceptibility changes are sometimes very small. Our method of measuring the dynamic susceptibility is the frequency shift method of Schawlow and Devlin. [29] The sample is placed in the coil of a tuned circuit that is part of an oscillator. The frequency of the oscillator is determined by the inductance of the sample coil, which in turn depends on the susceptibility of the sample. By measuring the frequency of the oscillator we determine the dynamic susceptibility of the sample, primarily the real part of the susceptibility.

To achieve frequencies of 5,000,000 cps, a modified Clapp oscillator with a series tuned circuit is used.[30] For 10,000 to 100,000 cps, a parallel tuned circuit is used with an audio amplifier and a large feedback resistor. The amplitude of the field at the audiofrequencies can be monitored by measuring the voltage across the tuned circuit. At 30,000 cps with a typical coil and field amplitude can be varied from 0.05 to 25 Oe. The frequency is measured with a commercial cycle counter.

The copper sample coil and a silvered mica capacitor are placed in the liquid helium bath. Superconducting sample coils, ordinarily used in these measurements, cannot be used here because the steady fields applied are as high as 23,000 Oe. In fact, for ordinary copper wire in these fields and at these temperatures the effect of normal state magnetoresistance must be measured and corrections applied to the data.

3. Dynamic Flux Penetration in $Nb_{0.70}Ta_{0.30}$

The field at which flux first enters an ideal type II superconductor is called H_{c1}. The field at which the static magnetization returns to zero in the Abrikosov model, nominally the field destroying all superconductivity, is called H_{c2}. At the time when these experiments were started, experimental studies

79

of type II superconductors had shown a resistivity less than that of the normal state persisting in fields above H_{C2}. This reduced resistivity was thought to be important under a-c conditions because it implies an a-c skin depth smaller than that in the normal state. In some discussions the field at which the resistivity has returned completely to the normal state value was tentatively called H_{C3}. This field was rather nebulous and difficult to define experimentally. These experiments are described in their original context; much has been learned in subsequent work.

In our a-c studies of ribbons of $Nb_{0.70}Ta_{0.30}$ we find clear evidence for superconductivity extending to a well-defined value beyond H_{C2}. When the large steady field is in the plane of the surface, the a-c flux is almost completely excluded up to a field about 1.65 times H_{C2}; at this field (H_{C3}), the a-c flux suddenly penetrates, indicating a rather abrupt return to the normal state (Fig. 34). When the steady field is perpendicular to the plane of the
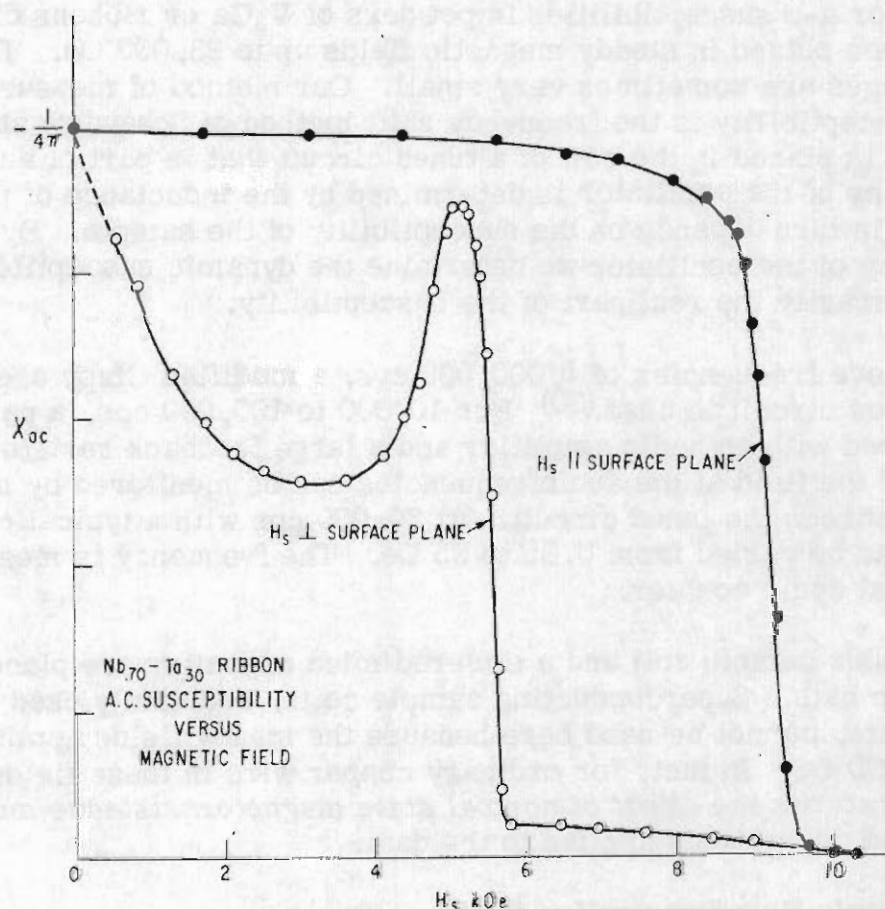
Figure 34 Dynamic or a-c susceptibility as a function of steady magnetic field for a $Nb_{0.70}Ta_{0.30}$ ribbon. The measurements were made at 30,000 cps, with the alternating field in the plane of the surface.

surface the major changes in a-c susceptibility are completed at H_{c2}. Though the behavior of the flux penetration below H_{c2} in the perpendicular field direction is strongly dependent on the mechanical and thermal history of the sample, the behavior in the parallel field direction is quite independent of the history of the sample.

These experiments were carried out with H_{ac} in the plane of the surface. Our experimental value of H_{c3} is independent of the relative directions of H_{ac} and H_S as long as both lie in the plane of the surface. The value of H_{c3} obtained is the same whether the alternating field amplitude is 0.05, 0.5, or 2.5 Oe. This suggests that H_{c3} is a well-defined property of the material. At an amplitude of 20 Oe, however, normal state susceptibilities are observed above H_{c2}. In Fig. 34 the amplitude is 0.05 Oe.

These early experiments were performed in an axial superconducting solenoid making accurate angular alignment and rotation difficult. It was found that rotating the d-c field out of the plane of the surface rapidly decreased the measured H_{c3} and broadened the H_{c3} transition. Though we measured ratios of H_{c3} varying from 1.5 to 1.65, we felt that more accurate alignment would slightly increase this ratio. We then studied the angular dependence of both $Nb_{0.70}Ta_{0.30}$ and other type II superconductors with improved precision in a more convenient iron magnet. (Y. B. Kim had also found a ratio of ~ 1.6 Nb-Ta alloys using ordinary d-c current and voltage drop measurements. Kim informed us of the striking angular effects.)

J. D. Livingston of the General Electric Research and Development Center noted that for a series of lead-indium alloy wires for which H_{c2} (determined from magnetic measurements) varies by a factor of four, the ratios of H_{c3}/H_{c2}, which H_{c3} is determined from resistivity measurements, are always between 1.6 and 1.7.

These results were extremely confusing; none of the tentative explanations were sufficient. Then a preprint of an article by D. Saint-James and P. G. de Gennes apparently explained these results.[3] They calculate, using the Ginzburg-Landau equations, that between H_{c2} and 1.69 H_{c2} a thin superconducting film (~ 350 Å thick at 6500 Oe for $Nb_{0.70}Ta_{0.30}$) persists at the surface of the specimen when the steady field is in the plane of the surface. When the steady field is perpendicular to the surface, this film does not exist. These results are consistent with our observations. This promising theory, substantiated by further study, removed one of the more puzzling problems in type II super-conductivity. In Section IV-C we discuss our measurements of the angular dependence of surface superconductivity for lead-thallium alloys.

4. Behavior of V_3Ga Powder in High-Frequency
Magnetic Fields of Small Amplitude.

We have measured the a-c susceptibility of V_3Ga powder as a function of magnetic field by using the oscillator resonance technique described in the

previous section. The measurements described in earlier sections show that the Bean model applies reasonably well to the behavior of type II superconductors subjected to large-amplitude, low-frequency magnetic fields or currents. In this section we discuss how a type II superconductor like V_3Ga behaves in high-frequency (>10,000 cps), small-amplitude (<10Oe) magnetic fields. Fine powders rather than a bulk specimen were chosen because the resonance technique used provides more sensitivity as a large specimen is subdivided and its surface area increased.

An arc-cast V_3Ga ingot was crushed and separated into size ranges varying from 1μ to 500μ. A determination of the distribution of particle sizes within each size range was made from optical and electron micrographs of the particles. Powder from each size range was carefully weighed and mixed with a measured weight of Lubriseal vacuum grease to form a paste. The pastes were separately packed into paper straws and mounted in the oscillator coils.[31]

The first measurement made was the determination of the a-c susceptibilities at 4.2°K in zero magnetic field for each range of particle size. The results show that the initial susceptibility decreases from -1.58/4π for the 420μ to 500μ particles to -0.166/4π for the 1μ particles. The experimental value of -1.58/4π for the large particles is reasonable when compared with the -1.50/4π expected for spheres much larger than the London penetration depth. The smaller susceptibilities of the smaller particles is also expected since the London penetration occupies a larger volume fraction of the smaller particles. The same susceptibilities were obtained for these particles by measuring the initial slopes of static magnetization curves.

From the knowledge of the size distribution of the particles within each size range and the zero field susceptibility of each size range, a calculation of the London penetration depth was made using a sphere approximation for the particles. These numbers vary from about 7000 Å for the 45μ to 60μ particles down to about 4000 Å for the 1μ particles. They are probably an overestimate of the actual London penetration depth because extra penetration occurs at the sharp corners, an effect virtually impossible to calculate. The smaller calculated London penetration depths for the smaller particles is reasonable since the magnetic field almost completely penetrates the smaller particles and the sharp corners make less difference.

The second subject we investigated was the a-c susceptibility in nonzero magnetic fields. The experimental results are summarized as follows:

(a) The a-c susceptibility decreases smoothly with increasing d-c magnetic field up to the largest magnetic fields in which measurements were taken (23 kOe). The results for the 45μ to 60μ particles and the 1μ particles are given in Figs. 35 and 36.

(b) The plot of a-c susceptibility vs d-c magnetic field is independent of the a-c magnetic field up to about 5 Oe peak to peak in the 45μ to 60μ
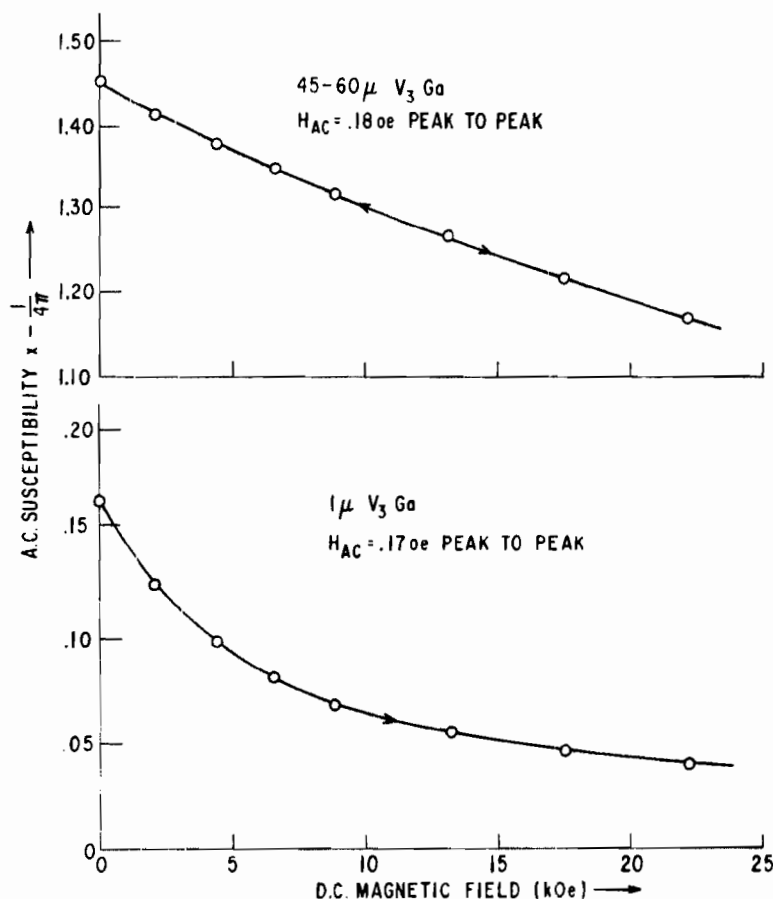
Figure 35 Experimentally determined a-c susceptibilities of 1μ and 45μ to 60μ
V₃Ga particles in steady magnetic fields up to 23,000 Oe. The a-c suscepti-
bility of 45μ to 60μ V₃Ga is reversible to within the thickness of the line
drawn. The a-c susceptibility of the 1μ V₃Ga is hysteretic and is shown only
in increasing magnetic fields. The numerical values along the ordinate are
to be multiplied by - 1/4π to yield the magnitude of the a-c susceptibility.

particles and to the largest a-c fields applied (∼25 Oe) in the 1μ particles. In
a-c fields greater than 5 Oe, the a-c susceptibility of the 45μ to 60μ particles
begins to show an amplitude dependence in the direction of larger decreases
in a-c susceptibility with increasing d-c magnetic field.

(c) The a-c susceptibility as a function of d-c magnetic field is inde-
pendent of the frequency of the a-c field over the range of 10^4 cps to 5×10^6 cps.

(d) The a-c susceptibility is a function of the magnetic history of the
specimen (Fig. 36). At any d-c magnetic field other than zero, hysteresis
exists; the a-c susceptibility is greater when the d-c magnetic field is in-
creased to some value from smaller values than when the d-c field is reduced
to that value from a higher value. For the 45μ to 60μ particles the hysteresis

83
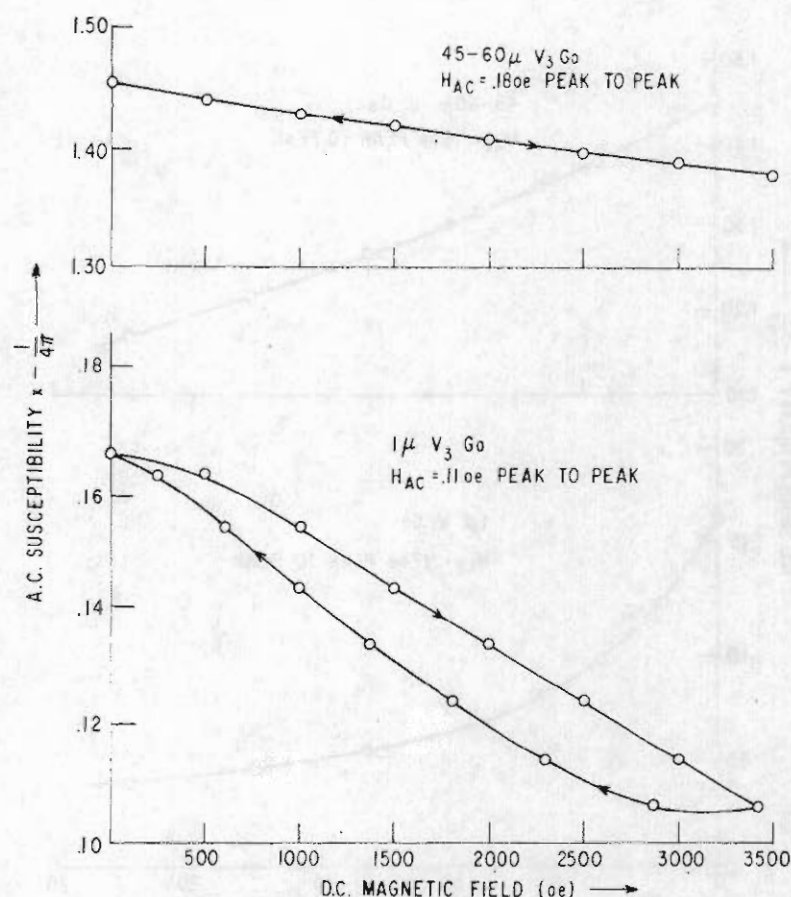
Figure 36 Experimentally determined a-c susceptibilities of 1μ and 45μ to 60μ
particles in steady magnetic fields up to 3500 Oe. The a-c susceptibility of
the 45μ to 60μ particles is reversible to within the thickness of the line
drawn. The hysteretic behavior of the 1μ particles is shown. The numerical
values along the ordinate are to be multiplied by -1/4π to yield the magnitude
of the a-c susceptibility.

is only about the breadth of the line shown in Fig. 36. For the 1μ particles
the hysteresis is as high as 10% of the susceptibility itself.

(e) The a-c susceptibility as a function of d-c magnetic field is indepen-
dent of whether the a-c and d-c magnetic field vectors are parallel or perpen-
dicular.

The lack of dependence of the susceptibility on amplitude, frequency,
and relative direction of the a-c and d-c fields implies that, even though we
are between H_{c1} and H_{c2}, we are measuring a property that does not depend
on the alternating entrance and exit of quantized fluxoids. The dependence of
the zero field a-c susceptibility on the size of the particles is close to that
expected from the London theory; we shall in fact use the London theory and
the associated penetration depth λ in our discussion. For the 45μ to 60μ

84

diameter particles the a-c susceptibility begins to increase slowly (more flux moves in and out) as the a-c field is increased above about 5 Oe. This suggests that about 5 Oe is required to unpin the quantized fluxoids or flux threads. The observation for the 1μ particles that the a-c susceptibility is independent of a-c field up to the largest a-c field applied (~25 Oe) will be discussed below.

Consider first a single sphere of a homogeneous type II superconductor, one in which there is no internal flux pinning and, therefore, no associated magnetic hysteresis. If we also assume, for the moment, that there is no surface barrier to crossing of magnetic flux, then, if the radius $R \gg \lambda$, the equilibrium magnetization of the sphere will be the reversible Abrikosov[1] magnetization. If, however, $R \lesssim \lambda$, we expect to find two kinds of deviations from the Abrikosov large sample magnetization curve. The first is the simple decrease in flux exclusion caused by London penetration[32] ($\chi_R = -R^2/4\pi\lambda^2$ for $R \ll \lambda$). The second is the result of the small cross-sectional area and the finite fluxoid quantum;[33,34] when the radius is less than about 10λ, there is no longer a simple Abrikosov critical field H_{c1}. There are a series of separate critical fields for the first fluxoid quantum, the second quantum, etc. These several critical fields can be separated by as much as several tens or perhaps even hundreds of Oe for very small particles; the results have not yet been calculated for our specific cases.

The first effect, the London penetration, is the cause of the variation of the susceptibility with particle size. Solutions of the Ginzburg-Landau equations[35] following the method of de Gennes[36] show that, for high κ materials into which fluxoid quanta have not yet penetrated, changes in susceptibility and thus penetration depth roughly similar to those seen in Figs. 35 and 36 are to be expected. The solutions for such materials after fluxoid penetration are not yet available.

As is clear from the figures, the field dependence of the susceptibility is not simple; there are striking hysteresis effects for the smaller particles. In Fig. 36 we see that if we increase the d-c magnetic field on the 1μ particles to 3400 Oe, stop, and then decrease the field, about a 500 Oe decrease is required before the susceptibility again begins to change. (Actually there is a barely visible minimum in the curve in this region.) That the critical state or defect pinning hysteresis is too small to account for this hysteresis can be demonstrated from the results of another experiment. Magnetization measurements made[31] on 45μ to 60μ V_3Ga particles taken from the same parent ingot yield a hysteresis of ~100 Oe. Taking into account the size dependence of the hysteresis associated with the critical state and the decreased susceptibility of the 1μ particles, we can account at most for 10 Oe of the 500 Oe hysteresis measured.

Some progress in understanding this hysteresis is made if we assume that the effective penetration depth is not a function of the average internal field as such, but is a function only of the number of the fluxoid quanta threading the particle. For small samples the effects of the finite size of the fluxoid

85

quantum and the surface effects, such as a surface barrier to the crossing of magnetic flux, will lead to a large intrinsic hysteresis in the magnetization and in the number of fluxoid quanta threading the sample. Consequently, if the stated assumption is valid, the a-c susceptibility will show an increasing dependence on magnetic history with decreasing particle size. In addition, the finite change in applied field necessary to change the number of fluxoid quanta yields our amplitude independent small signal susceptibility. The smaller the particle the larger the expected field change necessary to change the number of quanta. This effect is reflected in the larger limiting a-c field amplitude for the smaller particles.

Since the introduction of fluxoid quanta introduces into the material cores of normal electrons replacing superconducting electrons, it is tempting to attribute the increase in penetration depth to this lowering of the average number of superconducting electrons. Unfortunately, this appealing mechanism is quantitatively far too weak to account for our results. Further work is thus necessary to understand these experiments.

C. THE ANGULAR DEPENDENCE OF SURFACE SUPERCONDUCTIVITY
   IN SOME TYPE I AND TYPE II LEAD-BASED SUPERCONDUCTORS
   (H. R. Hart, Jr. and P. S. Swartz)

In the previous section we reported some studies of dynamic flux penetration in $Nb_{0.70}Ta_{0.30}$; our results were consistent with the presence of a superconducting surface sheath in a type II superconductor above H_{c2}. We then made further studies of superconductivity above the bulk critical fields H_c and H_{c2} using a different alloy system and an improved technique. A major portion of the results presented below has been published. [37,38]

We have found additional evidence [39-41] for superconductivity above the thermodynamic critical field H_c and the Abrikosov [1] critical field H_{c2} in type I and type II lead-based superconductors. Because of the agreement of the critical field of this remnant superconductivity with the theory of surface superconductivity proposed by Saint-James and de Gennes, [3] and because of the dependence of this critical field on surface roughness, we attribute its origin to a superconducting surface layer. We find, as have other investigators, [40] that the critical field H_T of this surface film is sensitive to the angle θ between the magnetic field vector and the plane of the surface, being a maximum when $\theta = 0$. We find, in addition, that the normalized angular dependence of H_T on θ is independent of composition for the entire range of the lead-thallium type II superconductors that we tested.

In pure lead and $Pb_{0.99}Tl_{0.01}$, which are type I superconductors, we find evidence for surface superconductivity [41] above the thermodynamic critical field when θ is small. Beyond some value of θ, the critical field of the surface film becomes less than H_c and is not experimentally defined. However, from $\theta = 0$ to this angle where $H_T = H_c$, the normalized angular dependence of H_T is the same as for the type II superconductors.

The specimens were in the form of chemically polished sheets (<0.020 by 1 by 1 inch), which were annealed in vacuo for 40 hours at 10° to 30°C below their melting temperature. The sheets were mounted between thin glass plates. The superconducting-to-normal transition (4.2°K) was obtained by measuring the transmission of a small alternating magnetic field (0.01 Oe at 10^4 cps) through the central portion of the sheet as a function of the externally applied steady magnetic field and angle θ. Care was taken to minimize the amplitude of the alternating field near the edges of the sheet. In Fig. 37 we show a schematic of the experimental configuration. The horizontal axis has been expanded near the sample. The two field coils have been wound in opposition and the copper shields have been employed to minimize the alternating field and induced current near the edges of the sheet. The pickup coils have been wound in opposition to minimize stray pickup voltages.
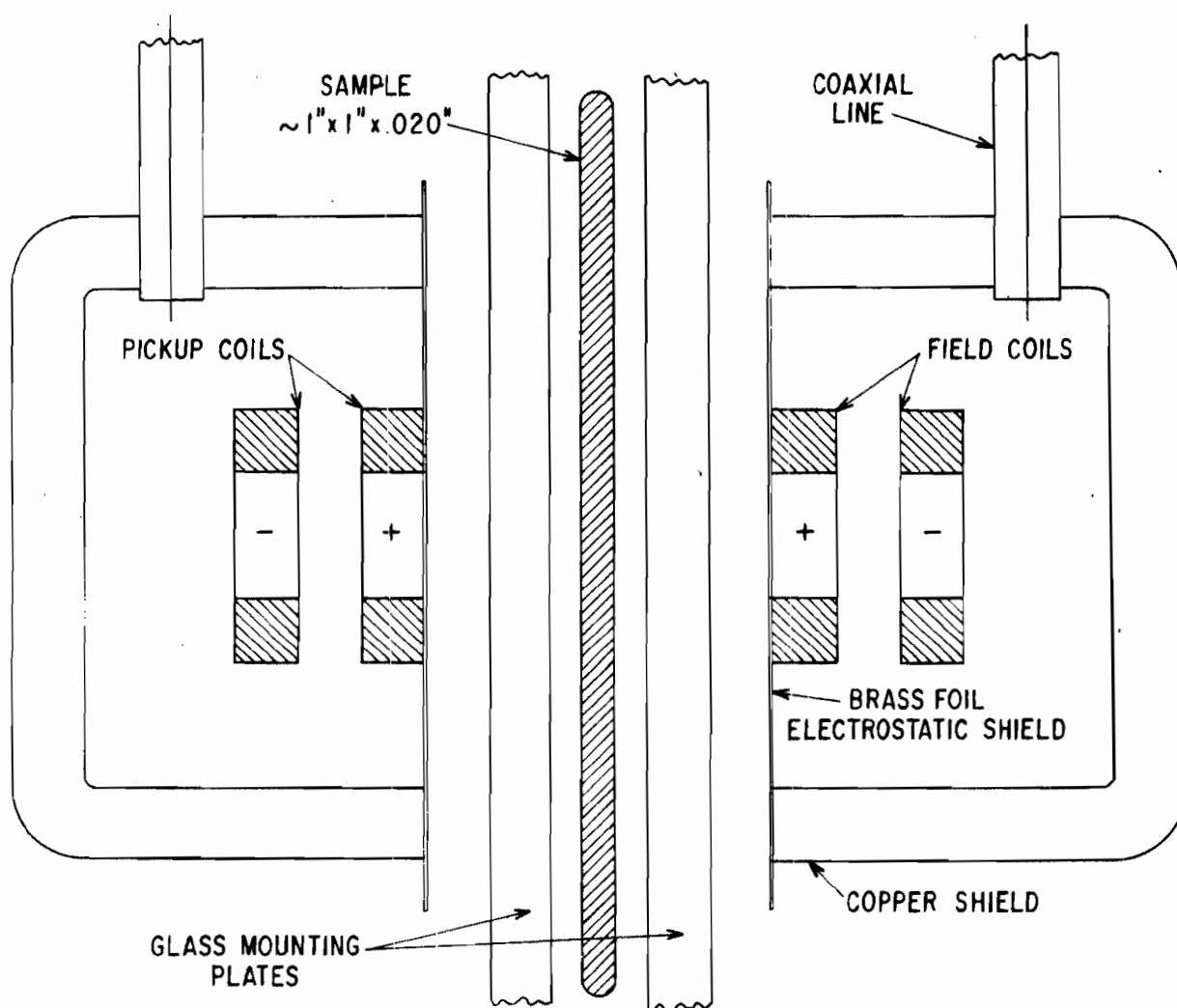
Figure 37 Schematic view of the experimental configuration. The horizontal axis is expanded near the sample.

In the normal state, transmission consistent with the normal state resistivity was observed; when the surfaces were superconducting, no transmission was observed. The breadth of the transition was typically 1% to 3% of the steady field. The critical field $H_T(\theta)$ is defined as the midpoint of the transition. $H_T(\theta)$ was found to change less than 1% upon varying the magnitude of the a-c field over a factor of 100.

Typical transmission curves are shown in Fig. 38. From these curves, $H_T(\theta)$ vs θ can be plotted (Fig. 39). $H_T(0°)$ is identified with H_{C3} and $H_T(90°)$ with H_{C2}. According to Saint-James and de Gennes,[3] $H_{C3}/H_{C2} = 1.695$. Our ratios (see Table III) are in fairly good agreement with this number and those observed by others.[40] We were able to measure H_{C2} accurately for each of the type II superconductors with the exception of $Pb_{0.97}Tl_{0.03}$ and $Pb_{0.70}Tl_{0.30}$. In these two cases, the transition broadened as θ approached $90°$ ($H_T \rightarrow H_{C2}$) in a manner that suggests that the supercurrents carried by these two samples in the mixed state near H_{C2} are less than those carried by the surface films above H_{C2}.
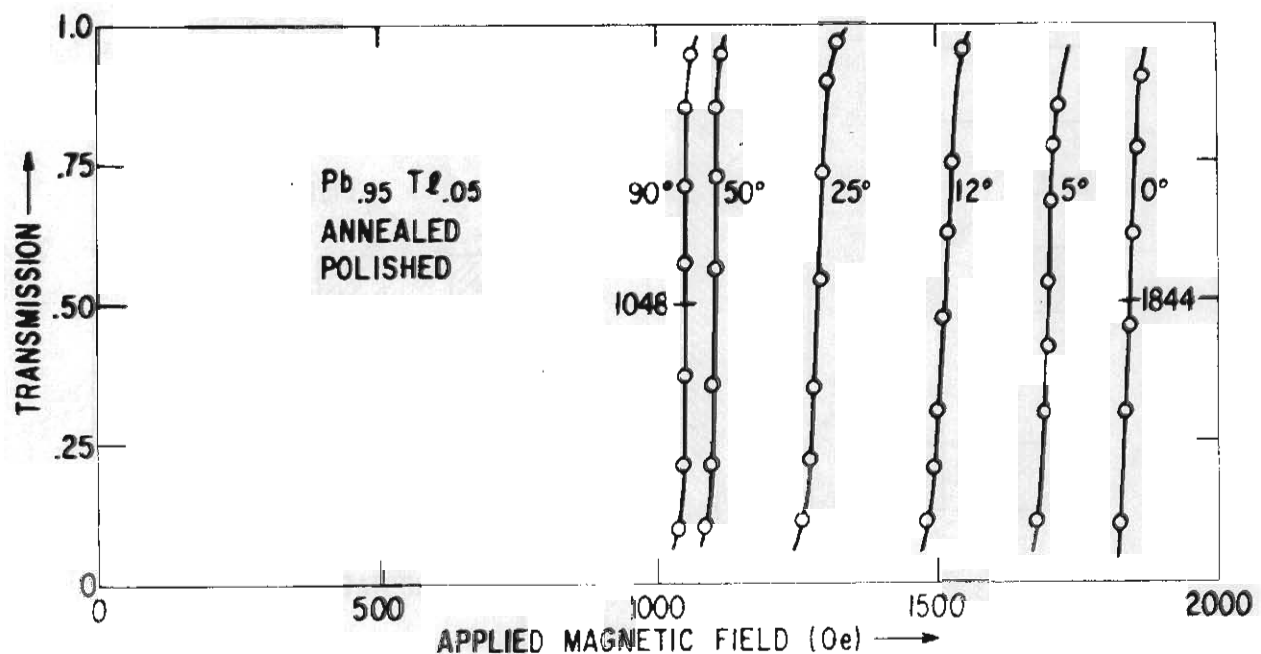
Figure 38 Transmission of a small a-c magnetic field through a $Pb_{0.95}Tl_{0.05}$ sheet as a function of steady magnetic field and its angle θ with the surface of the sheet.
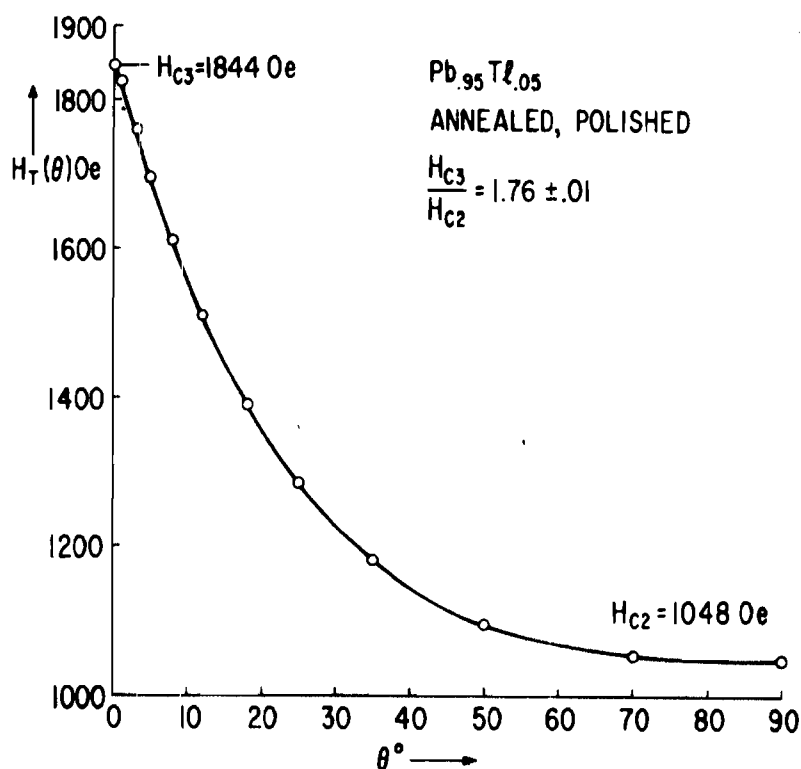
Figure 39 Angular dependence $H_T(\theta)$ of surface superconductivity in a $Pb_{0.95}Tl_{0.05}$ sheet. The normalized angular dependence $H_T(\theta)/H_T(0°)$ is found to be the same for all type I (when $H_T > H_c$) and type II materials tested.

TABLE III

Tabulation of the lead-based materials investigated and their significant superconducting parameters: κ for the type II alloys is determined from the paper of G. Bon Mardion, B. B. Goodman, and A. Lacaze.[42] For the two type I materials (pure lead and $Pb_{0.99}Tl_{0.01}$), κ is determined from the expression $\kappa = H_{c3}/1.695\sqrt{2}H_c$

wt% Tl	K	H_{c3}	H_{c2}	H_{c3}/H_{c2}
0.00[†]	.43	591	TYPE I	
1.06	.7	906	TYPE I	
2.90	1.1	1415		
4.87	1.5	1844	1048	1.76±.01
4.87[†]	1.5	1878	1061	1.77±.01
10.1	2.5	2974	1691	1.76±.01
19.9	4.5	4404	2580	1.71±.01
29.9	6.5	4751	≤2927	≥1.62

† UNANNEALED

89

A sensitive demonstration that the normalized angular dependence of H_T on θ is independent of composition is provided in Fig. 40. Here the normalized derivative $-H_T^{-1}(0°)dH_T(\theta)/d\theta$ is plotted vs θ for all of the specimens investigated, including the type I superconductors. Within our experimental uncertainty the data fit the empirical expression (θ expressed in degrees),

$$\frac{1}{H_T(0°)} \frac{dH_T(\theta)}{d\theta} = -0.023e^{-0.050\,\theta} \tag{77}$$

for $\theta < \sim 60°$

yielding

$$\frac{H_T(\theta)}{H_T(0°)} = 1 - 0.46\left[1 - e^{-0.050\,\theta}\right] \tag{78}$$

The scattering of the points at $\theta < \sim 2°$ is probably related to a small degree of surface roughness that could not be completely eliminated. At $\theta > \sim 60°$

$$\frac{H_T(\theta)}{H_T(0°)} = 1 - .46\left(1 - e^{-.050\theta}\right)$$
$$\text{FOR } \theta < \sim 60°$$
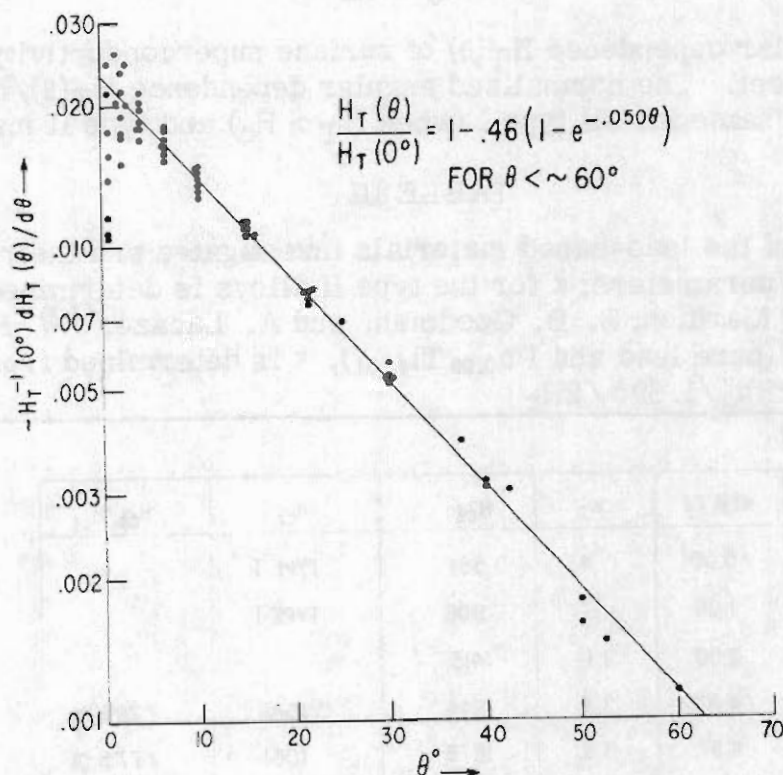
Figure 40 The normalized derivative of the critical field of the surface film $-H_T^{-1}(0°)\, dH_T(\theta)/d\theta$ is plotted vs θ for all of the materials investigated. The results indicate that the normalized angular dependence is independent of κ.

the functional dependence of $-H_T^{-1}(0°)dH_T(\theta)/d(\theta)$ decreases below that given in Eq. (77) and becomes too small to define experimentally.

Saint-James and de Gennes did not determine the surface critical field for angles other than $\theta = 0°$ or $\theta = 90°$. There was at the time of the experiments no explicit theory for the angular dependence of $H_T(\theta)$, or for the κ-dependence of $H_T(\theta)$ for intermediate angles. [The Ginzburg-Landau parameter[1] κ is determined by the alloy composition. In our experiments the materials tested encompass a factor of ~ 15 in κ. Note that $H_{c2} = \sqrt{2}\,\kappa\,H_c$ and $H_{c3} = 1.695\sqrt{2}\kappa H_c$.] Tinkham[43] first, by analogy, applied to this problem his results for the angular dependence of the critical field of an isolated thin film of a type I superconductor. In this first model he finds the angular dependence to be independent of κ and to be qualitatively similar to that observed in his work. At $\theta = 0°$ the normalized derivative predicted from Tinkham's first model is approximately two-thirds of that observed. Subsequently, in a more refined calculation, Tinkham[44] predicted a zero degree normalized derivative very close to that observed in this experiment.

More recently, Saint-James[45] has calculated the zero degree normalized derivative for a range of values of the ratio of the thickness of the sample to the coherence distance. Our experiment yields one limit of this curve, in excellent agreement. Recent measurements by Burger, Deutscher, Guyon and Martinet[46] have shown the curve calculated by Saint-James to be correct for a wide range of thickness to coherence length ratios.

An interesting side result was obtained in this work. In searching for a convenient alloy system having a sharp transition (Fig. 38), we found that the minimum transition breadth is a characteristic of the alloy system itself. In particular, the minimum breadths for lead-bismuth alloys are always greater than those for lead-indium alloys, which in turn are always greater than those for lead-thallium alloys. We believe that this effect can be understood from Fig. 41. Solidification theory tells us that the compositional homogeneity is governed by the separation of the liquidus-solidus lines. The larger the separation, the larger the small-scale inhomogeneity. Since the liquidus-solidus separations for these alloys increase in the same order as our transition breadths, we conclude that our transition breadths are caused by small-scale compositional inhomogeneities in the samples. (Note: Our samples were annealed but probably not homogenized.)
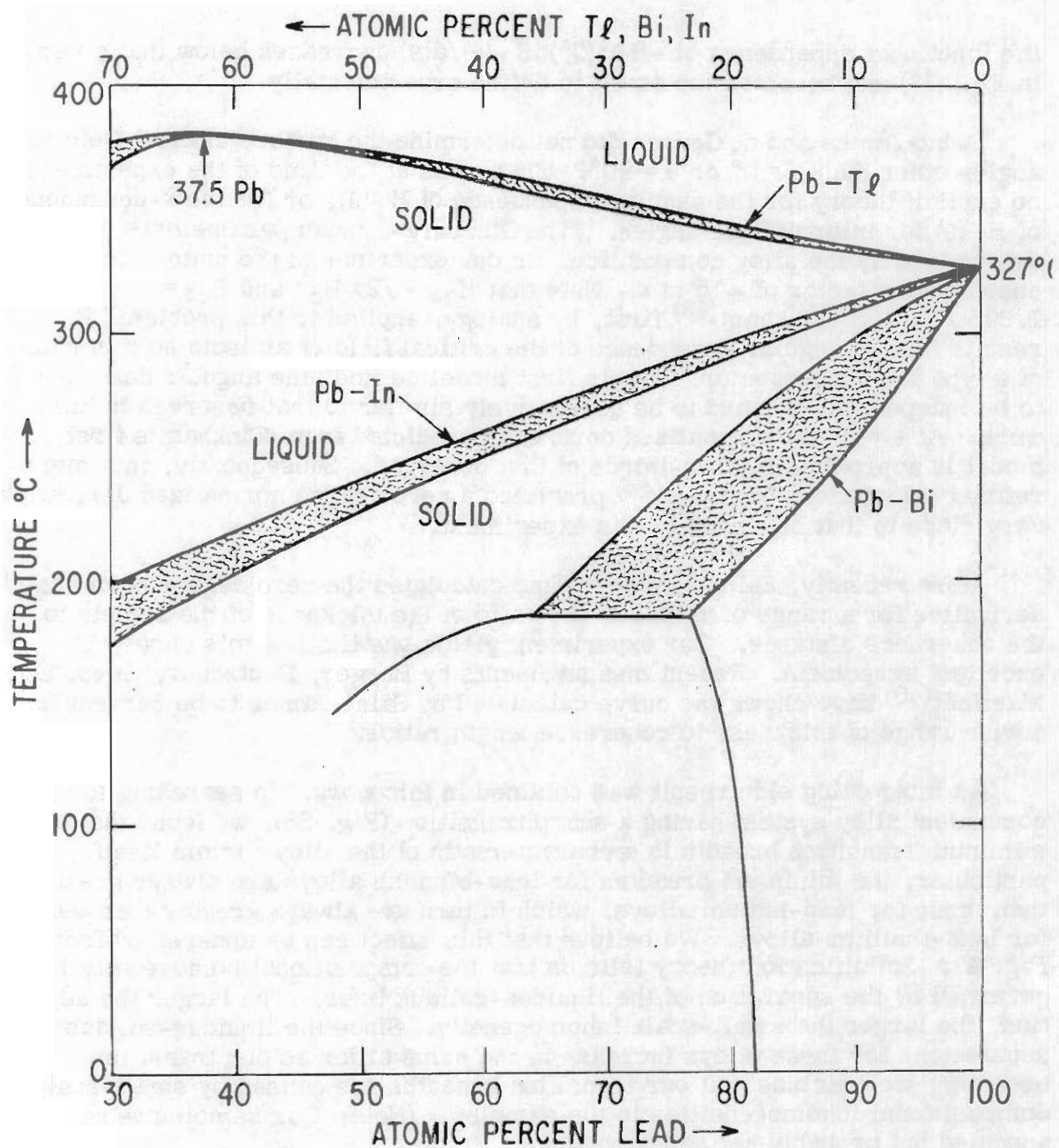
Figure 41 Phase diagrams for three lead-rich alloy systems.

SECTION V

INTERACTION BETWEEN FLUX THREADS AND INTERNAL DEFECTS: CRITICAL CURRENT DENSITY

The critical current density, J_c, has been seen to be the primary material parameter controlling the a-c and d-c properties of high field superconductors. It is generally believed that J_c is determined by the interaction between internal defects and the flux threads of the mixed state. We have sought to improve our understanding of this basic defect-flux thread interaction by studies of the changes in J_c produced by intentionally introduced defects. This has included defects produced by (A) fast neutron irradiation, (B) thermal neutron irradiation of superconductors doped with fissionable impurities, and (C) solid-state phase transformations.

A. FAST NEUTRON IRRADIATION (P. S. Swartz, H. R. Hart, Jr., and R. L. Fleischer)

Niobium wires, $Nb_{0.70}Ta_{0.30}$ ribbons, and ~70µ diameter particles of Nb_3Sn, Nb_3Al, V_3Ga, and V_3Si have been subjected to doses of 5×10^{16}, 3.5×10^{17}, and 1.5×10^{18} fast neutrons/cm^2 (nvt). The superconducting properties of only the ordered intermetallic compounds were found to be sensitive to the radiation. [47]

The RCA group has published results of experiments somewhat similar to ours. [48] The apparent quantitative discrepancy in the increase of critical current density with dose between their results and ours is probably unreal; they count neutrons whose energy is in excess of 5 Mev, while we include in our count neutrons with energy as low as a few tenths of 1 Mev. Thus, for the same reactor irradiation we would count an incident flux about 10 times that of the RCA group.

The specimens were packaged in aluminum foil, wrapped in 0.010-inch cadmium, and irradiated in the Brookhaven reactor. The cadmium absorbs the thermal neutrons so that the primary flux irradiating the samples is composed of energetic neutrons (10^5 to 4×10^6 ev).

In the niobium wires the magnetization curve and the upper critical field (2720 ± 20 Oe at $4.2°$K) are unchanged by the various neutron doses. Similarly, the low neutron dose of 5×10^{16} nvt induced no change in either the upper critical field or the magnetization of the $Nb_{0.70}Ta_{0.30}$ ribbons. The $Nb_{0.70}Ta_{0.30}$ ribbons that received the higher doses are too radioactive to be handled safely in the near future.

The irradiation of the intermetallic powders produced extensive changes in magnetic properties. The techniques employed in preparing the powders and measuring their magnetic properties are described in Refs. 31 and 49.

93

Figure 42 shows the 4.2°K experimental magnetization curves of the V_3Ga powder before the irradiation and after the medium and heavy doses. As these curves demonstrate, the magnetic hystersis (labeled β) is significantly increased by fast neutron irradiation. The <u>change</u> in β with neutron dose at an applied magnetic field of 4000 Oe is given in Fig. 43.

The values of magnetic hysteresis obtained from the heavy dose (1.5 x 10^{18} nvt) V_3Ga, V_3Si, and the "diffusion processed" Nb_3Sn may be misleadingly small. This conclusion is suggested from the following arguments. We found considerably more scatter in the points of the experimental magnetization curves of the heavily irradiated diffusion processed Nb_3Sn, the
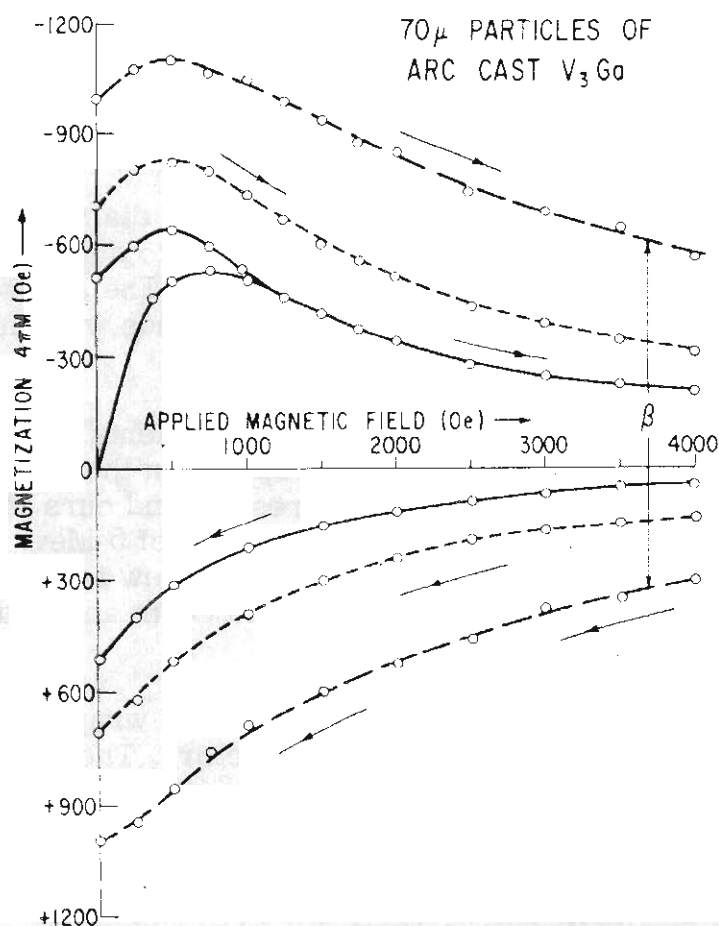
Figure 42 Experimental magnetization curves of ∼70μ V_3Ga powder. The curve obtained from the V_3Ga submitted to the light dose is omitted for clarity. These results indicate that the magnetic hysteresis increases with irradiation.
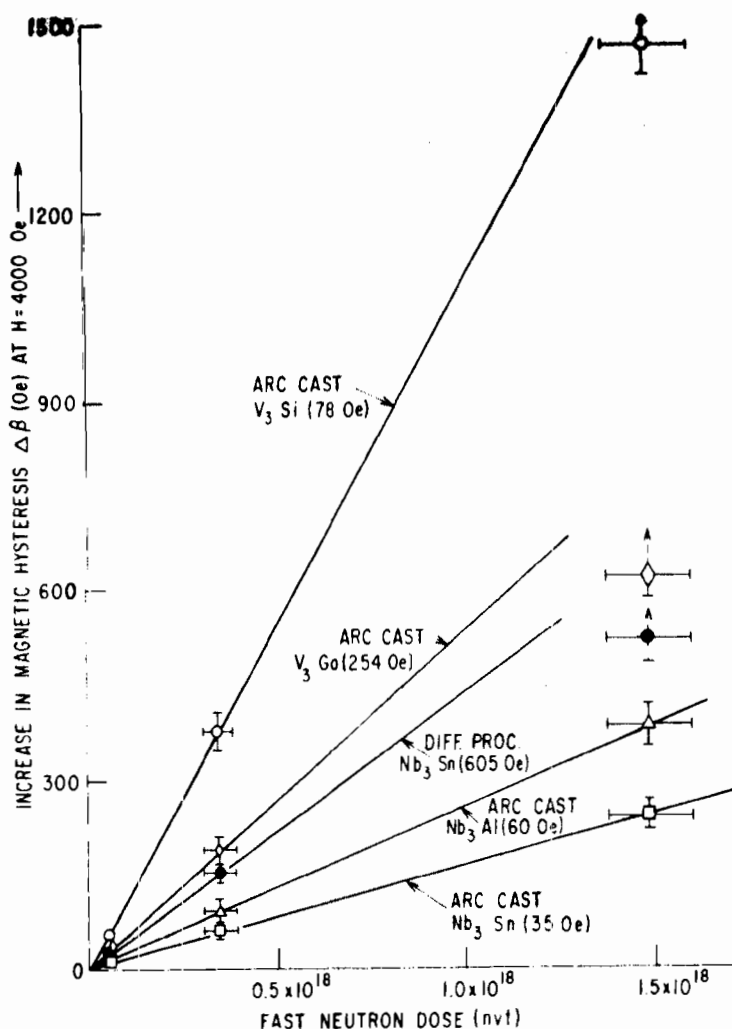
Figure 43   The change in magnetic hysteresis $\Delta\beta$ at H = 4000 Oe is plotted vs
fast neutron dose for each of the intermetallic compounds investigated.
The hysteresis β of the unirradiated specimens is given in the parentheses.
The results suggest that the hysteresis increases linearly with dose.

arc-cast V_3Ga, and particularly the arc-cast V_3Si than we could attribute to
experimental uncertainty.   Since theory[50] and experiment[9] both indicate
that flux jumping (sudden reduction or disappearance of the magnetization) is
more likely in type II superconductors that have large magnetic hysteresis,
our high dose powders may be flux jumping.   This would account for the extra
scatter in these three magnetization curves.   Further, if flux jumping is
prevalent, some of the particles have a magnetization that is less than the
critical state magnetization, and hence the measured hysteresis is too small.
For this reason we do not know where to put the top of the error flag on these
three points in Fig. 43.

95

According to the Bean model,[7] the magnetic hysteresis β in the mixed state is directly related to the magnetic field gradients in the bulk of the specimen or, equivalently, the critical current density J_C of the specimen. For spheres the relationship[†] is

$$J_C(H) \cong \frac{15\beta(H)}{2\pi R} \quad .$$

Thus the change in critical current density ΔJ_C is immediately calculable from the change in magnetic hysteresis $\Delta\beta$. We approximate the irregularly shaped particles as spheres ($R = 35\mu$). In Table IV we have listed ΔJ per 10^{18} nvt measured in an applied magnetic field of 4000 Oe for each of the intermetallic compounds.

TABLE IV

Increase in Critical Current Density Per Unit Flux Measured at
4000 Oe, Initial Critical Temperature, and the Change in
Critical Temperature after 1.5×10^{18} nvt

Material	ΔJ_C/nvt $(10^5$ amp/cm$^2)/10^{18}$ nvt	T_C(°K)	ΔT_C(°K)
Arc-cast Nb$_3$Sn	1.1	17.84	-0.10
Arc-cast Nb$_3$Al	1.75	17.70	- .22
Diffusion processed Nb$_3$Sn	2.7	17.86	- .08
Arc-cast V$_3$Ga	3.3	14.48	- .16
Arc-cast V$_3$Si	7.0	16.87	- .19

The increase in critical current density of the arc-cast samples has a trend that is to be expected from considering energy and momentum transfer. The fraction of the energy of a neutron that can be transferred to an atomic nucleus in an elastic collision is inversely proportional to the mass of the nucleus. The cross section for elastic collision between a neutron and an atomic nucleus increases only as about the two-thirds power of the mass of the nucleus. The net effect is that more energy is transferred per neutron to light atoms than to heavy atoms. If the increased current-carrying capacity is a measure of the extent of the radiation induced damage, then it is reasonable that the two niobium-base intermetallics show a smaller increase in magnetic hysteresis than the two vanadium-base intermetallics, as Nb is heavier than V. It is also reasonable that V$_3$Si has a larger increase than V$_3$Ga and that arc-cast Nb$_3$Al has a larger increase than arc-cast Nb$_3$Sn, as silicon is lighter than gallium and aluminum is lighter than tin. The fact that the Nb$_3$Sn, made by the diffusion process (pressed compacts of Nb and Sn powders in stoichiometric proportion sintered at 950°C for 2 hours), has a larger increase than both the arc-cast Nb$_3$Al and the arc-cast Nb$_3$Sn is not understood.

[†]This expression is valid only if the specimen is in the mixed state and $\beta \ll H$; otherwise, the relationship is more complicated.

The critical temperature of the intermetallic compounds was also measured in both the unirradiated and heavily irradiated condition. Each of the powders was mixed with Lubriseal vacuum grease to form a paste that was packed into the coil of an oscillator (4×10^4 cps). Following the technique of Schawlow and Devlin, [29] the frequency was monitored as the temperature was decreased (see Figs. 44 and 45). From these measurements, the critical temperature (defined here as the onset of the frequency shift) and the breadth of the transition were determined. We find that the critical temperature is lowered and the transition is slightly broadened by the irradiation. Table IV lists T_c, the critical temperature and ΔT_c, the change in critical temperature of the intermetallics irradiated to 1.5×10^{18} nvt.

There are at least four effects of neutron irradiation: (1) the exchange of atoms between sites, (2) the creation of interstitial-vacancy pairs, (3) the clustering of vacancies, and (4) the creation of new elements. Since the superconducting properties of the ordered intermetallic compounds are affected by fast neutron irradiation while those of pure niobium and the unordered $Nb_{0.70}Ta_{0.30}$ alloy are not, it is likely that it is the disordering caused by the exchange of atoms between sites that is important. It should be possible to determine the extent of disordering in the heavily irradiated intermetallics by measuring the change in the relative intensities of certain lines in the x-ray pattern. This technique is not sensitive to less than ~10% disordering and no measurable disordering was detected. Disordering will be studied by investigating the x-ray patterns of intermetallics subjected to much larger doses than those described in this report.
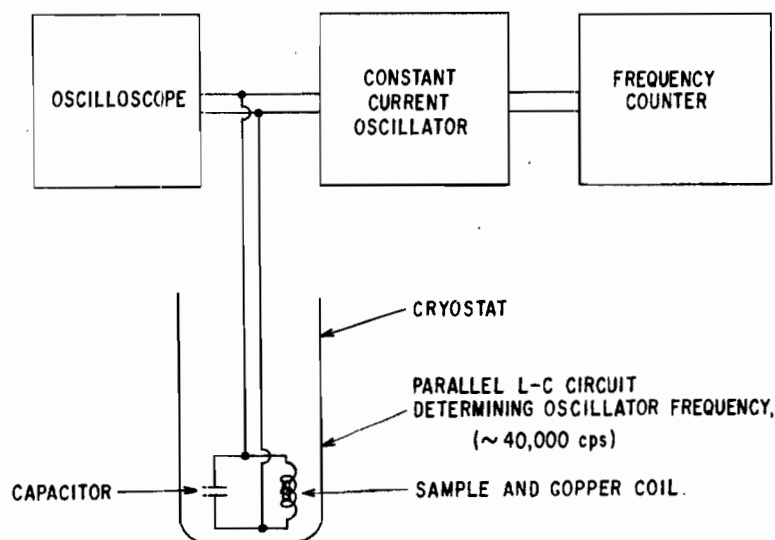
Figure 44 Schematic view of the frequency shift method used for the measurement of critical temperature. The susceptibility of the sample determines the inductance of the coil and thus the frequency of oscillation.
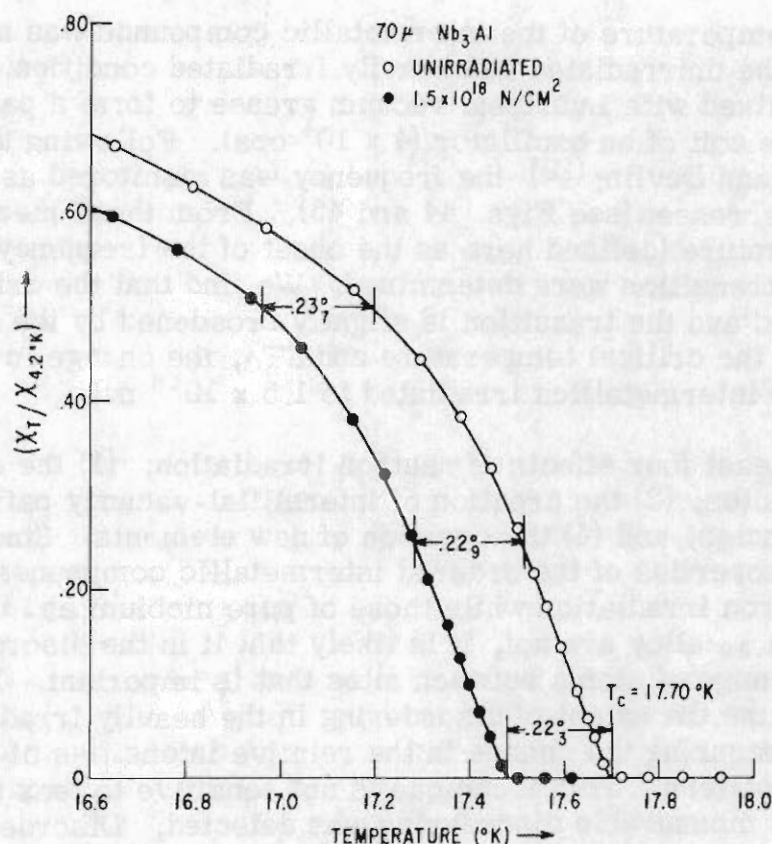
Figure 45 A plot of the normalized a-c susceptibility vs temperature for unirradiated and irradiated (1.5×10^{18} n/cm^2)~70µ particles of Nb$_3$Al. The susceptibility was determined from the frequency shift technique (Fig. 44). The critical temperature is arbitrarily taken as the temperature at which the susceptibility first deviates from the normal state value.

B. THERMAL NEUTRON IRRADIATION OF SUPERCONDUCTORS DOPED WITH FISSIONABLE IMPURITIES (C. P. Bean, R. L. Fleischer, P. S. Swartz, and H. R. Hart, Jr.)

1. Introduction

We have added small quantities of natural uranium or boron to the superconducting compounds Nb$_3$Al and V$_3$Si and exposed them to thermal neutron irradiation to induce fissions or (n, α) reactions. Novel techniques were employed both for observing the distribution of the doped elements and for measuring the critical current densities before and after irradiation. We find that the uranium-doped samples display critical current densities after irradiation that are substantially higher (~ 2 x 10^6 amp/cm^2 at 30 kOe) than any now known, while the critical temperature is decreased only 1% to 2%.

2. Sample Preparation

Six small ingots were produced by arc-casting. The three Nb_3Al ingots contained (A) nominally no impurity, (B) 0.301 A/o boron, and (C) 0.321 A/o natural uranium. The three V_3Si ingots contained (A) nominally no impurity, (B) 0.178 A/o boron, and (C) 0.190 A/o natural uranium. The ingots were then crushed to powder and sized. Powder from each 70μ diameter population was irradiated in the Brookhaven reactor to 1.1×10^{17} and 1.7×10^{18} thermal neutrons/cm^2.

The uranium and boron contents were measured using Price and Walker's technique[51] that also allows the distribution of these elements to be observed. In this procedure, the positions of the fissionable atoms are detected by charged particles emitted as a result of neutron bombardment. The sample to be examined is polished flat and an appropriate nuclear track detector[52] is placed against this surface. The sample plus detector is then irradiated with thermal neutrons; the resulting fission particles enter the detector and leave damage tracks that are subsequently revealed by chemical etching. To detect boron fissions [(n, α) reactions], a detector such as cellulose acetate butyrate or cellulose nitrate, which is sensitive to alpha particles, is used; for uranium-doped samples, any of the known solid-state nuclear track detectors is suitable. [52]

Figure 46 shows the distribution of particle tracks emanating from fragments of boron nuclei in V_3Si and Nb_3Al. In the V_3Si, the tracks are random; in the Nb_3Al, they occur in isolated clusters, indicating that the boron is not in solid solution but is localized in what are probably second-phase regions. The particle track distribution of the uranium-doped ingots (not shown) was random, indicating that the uranium went into solid solution.

Since the concentration of etch channels is a known function[51] of the atomic concentration of fissionable impurity, the neutron flux, and the cross section for fission, we have been able to establish by counting the tracks in the detector that (with the possible exception of boron-doped Nb_3Al) the number of fission tracks observed is consistent with the doping additions initially made to the arc-cast ingots. The neutron flux was measured by counting neutron-induced fission tracks in a calibrated glass dosimeter.[53]

3. Experimental Method and Measurements

In the past, the measurement of critical currents has been accomplished by direct measurement of transport currents in wire samples or measurements of the magnetization loops of bulk samples. In the latter method, the supercurrents are induced by a change in the magnetic field. In an extension of the magnetic technique, Swartz, Hart, and Fleischer[47] have measured the magnetic hysteresis of fine particles of high field superconductors. This type of measurement obviates the necessity for the formation of bulk samples of these brittle materials. There are, however, some

99

(a)   (b)
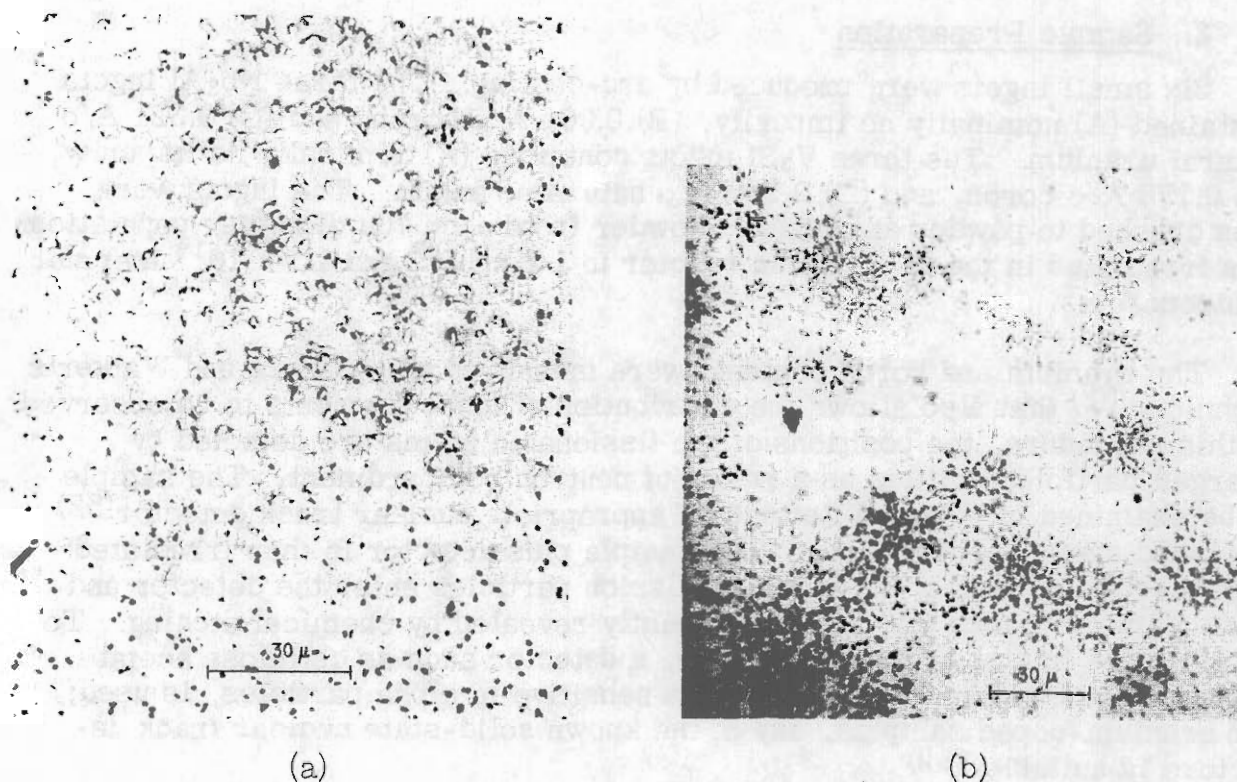
Figure 46 (a) Fission tracks from irradiated, boron-doped V_3Si. The
random distribution of tracks suggests that the boron went into solid
solution; (b) fission tracks from irradiated, boron-doped Nb_3Al. The
clusters of tracks indicate that the boron did not go into solid solution.

limitations to this technique. First, the measurements are quite time con-
suming. Secondly, with samples of a high critical current density, one can-
not always calculate the critical current density in a direct fashion, and
lastly, the flux jumps may becloud the interpretation of the data, leading to
a calculated critical current density that may be too small. The existence
of these difficulties led us to develop an alternative magnetic technique for
measuring the current density in a superconductor with a high bulk current-
carrying capacity. The technique measures the response of the sample to a
small alternating field applied collinearly with a steady magnetic field. From
theoretical considerations, [19] one of us has shown that the voltage output of
the third harmonic of the driving frequency, f, obtained from a coil of N turns
and of length L wound around a cylinder of surface area S whose axis is col-
linear with the field, is:

$$|V_3rd| = [2h_0^2fNS/\pi LJ_C(H)]10^{-8}volts . \qquad (79)$$

In this expression, h_0 is the amplitude of the alternating field in oersteds,
while J_C (H) is the critical current density of the superconductor in amp/cm^2

100

in a field H. The derivation assumes that h_0 is small enough that the currents flow only in a surface layer, small compared to the radius of the specimen. Measurements on large samples have confirmed the a-c field and frequency dependences of this expression. [19]

Equation (79) could be applied directly to the powders if the powder particles were in the form of rods or plates aligned in the field direction. If the powder particles are spheres, as we shall assume, the local field is tangential to the surface as assumed above, but varies from zero at the polar point where the field line intersects the sphere to $(3/2)h_0$ at the equator. Owing to this shielding effect, we would guess that Eq. (79) would be valid for spheres when multiplied by a factor that would be expected to be larger than unity.

We here present the modification of Eq. (79) for samples of spherical particles as opposed to the assumption of the zero demagnetizing factor that underlies Eq. (79). As indicated above, this modification is expressed in terms of an amplification factor γ, that may be guessed to be larger than unity owing to the field enhancement associated with a sphere. The approach we use may appear to be somewhat indirect but is, we believe, easier to follow than a direct attack upon the problem.

Consider a specimen surrounded by a coil that is energized by an alternating current, $I_0 \sin(\omega t)$. If a voltage $V(t) = V_1^1 \sin(\omega t) + V_1^0 \cos(\omega t) + V_{3}\text{rd}$ $\sin(3\omega t) + V_5\text{th} \sin(5\omega t) + \dots$, is induced in the coil by the changing field, then the average rate of energy loss per cycle is $W = \oint I \cdot V dt$ where $\oint$ represents integration over a cycle of the fundamental frequency. This integration yields $W = I_0 V_1^1/2$ joules/cycle, a familar result.

We may express this energy dissipation in terms of material properties by noting that it is equal to the integral over the surface of the sphere of the local surface losses. By Eq. (8) of Ref. 29, this local surface loss is $W_S = 5h^3/12\pi^2 J_C$ ergs/cm^2/cycle. In this expression, h is the amplitude of the local alternating field. For a sphere in an alternating field of amplitude h_0, this local field is $h = (3h_0/2) \sin \theta$ where θ is the polar angle measured from the field direction. The integration above is:

$$W_{total} = \int W_S ds$$
$$= (5h_0^3/12\pi^2 J_C)\,(27/8)\,(2\pi r^2)\int_0^\pi \sin^4\theta\, ds$$
$$= (5h_0^3/12\pi^2 J_C)\,(S)\,(81\pi/128) \quad .$$

Thus, the loss in the sphere is higher than that of a planar surface by a factor $(81\pi/128)$ or approximately two. By the equation for loss in the preceding paragraph, the out-of-phase component of the first harmonic of voltage is also raised by this factor; and since the shape of the hysteresis

101

loop is unaffected by this field amplification, all odd voltage harmonics are raised by this same amplification factor $\gamma = (81\pi/128)$; hence

$$|V_3 rd|_{spheres} = [81h_0^2 fNS/64LJ_c(H)]10^{-8} volts \quad . \quad (80)$$

Figure 47 shows a schematic diagram of the electric circuit employed in the measurement. A 60-watt McIntosh power amplifier drives a primary coil of 1343 turns of No. 32 wire wound on a form of 0.66 cm diameter that is 5.5 cm long. A series LC circuit is tuned to the fundamental frequency to remove higher harmonics from the applied alternating field. The amplitude is monitored by a VTVM that senses the voltage across a 10 ohm resistor. Alternating fields up to about 400 Oe can be generated in the audio range. Two secondary coils of 280 turns, 0.36 cm in diameter, and 1.11 cm in length, fit closely into the primary coil. The sample, consisting of 40 to 50 mg of 70μ particles mixed with Lubriseal grease, is packed in a straw in one coil. The output of the two coils is bucked externally across a voltage divider. In addition, a compensating signal can be injected from a 25 mH mutual inductor. The voltage divider and mutual inductor are adjusted to null the fundamental voltage for a low drive field when the specimen is super-conducting. Not shown in this diagram is the superconducting coil that
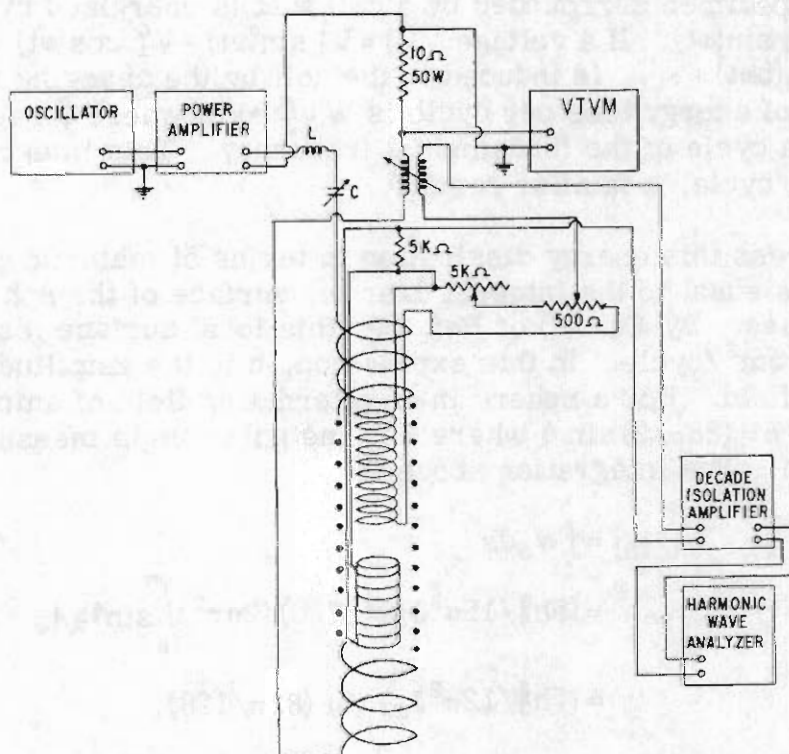
Figure 47 A schematic diagram of the circuit employed in the harmonic analysis technique.

encloses the primary and secondary to provide a steady field up to 30 kOe at 4.2°K and about 26 kOe at 2°K. The output voltage is amplified by a Keithley 102B decade isolation amplifier and detected by a Hewlett Packard 310A wave analyzer. The noise is usually a fraction of a microvolt.

Equation (80) is used to determine the critical current densities of the samples. The experimental factors that are not precisely known are NS/L. These factors can be determined in two separate ways. In the first method, N and L are coil factors that are known quite accurately, while the surface area, S, of the particles is calculated from the weight of the powder packed into the coil and the assumption of a particle radius, r, of 3.5×10^{-3} cm. This method yields a typical value of about 2.0×10^3 cm for NS/L.

In the second method, NS/L is inferred from the measurement of the normal-to-superconducting transition of the sample and the assumption of a particle radius. The fundamental voltage difference between the normal and the superconducting states is given as:

$$|\Delta V|_{rms} = [2\pi NSrh_0 f/3\sqrt{2}L]10^{-8} \qquad (81)$$

or

$$NS/L = [3|\Delta V|_{rms}/\sqrt{2}\pi rh_0 f]10^{+8} \qquad .$$

From this expression, NS/L can be determined for particles with a critical current density sufficiently low that the magnitude h_0 of the alternating field can be made much greater than the magnetic hysteresis, and the consequent penetration of the alternating field complete. By this method, we measure typical values for NS/L of $\sim 1.65 \times 10^3$ cm for an $\sim 8\%$ volume fraction of powder in the coil. The difference between these two estimates is that the first may be high owing to the assumption of perfect coupling and packing, while the second may be low because of incomplete penetration of the particles by the alternating field.

The value for NS/L of 1.65×10^3 is chosen for all calculations of critical current density in this report. From Eq. (80), J_c (H) then becomes:

$$J_c(H) = (1.48 \times 10^{-5})h_0^2 f/|V_{3rd}|_{rms} \qquad . \qquad (83)$$

A test of the method itself rests on the field and harmonic dependence of the output voltage. According to theory,[19] the output voltage should increase with the square of the alternating field and the ratio of the nth harmonic to the third harmonic is given as $5/(n^2-4)$. An experimental test of the method is shown in Fig. 48 for the heavily irradiated, uranium-doped Nb_3Al measured at 15 kOe at 4.2°K. The solid lines are theoretical with the assumption that $J_c(15 \text{ kOe}) = 8.3 \times 10^5$ amp/cm^2. These data indicate a substantial agreement between theory and experiment over a wide range of

103
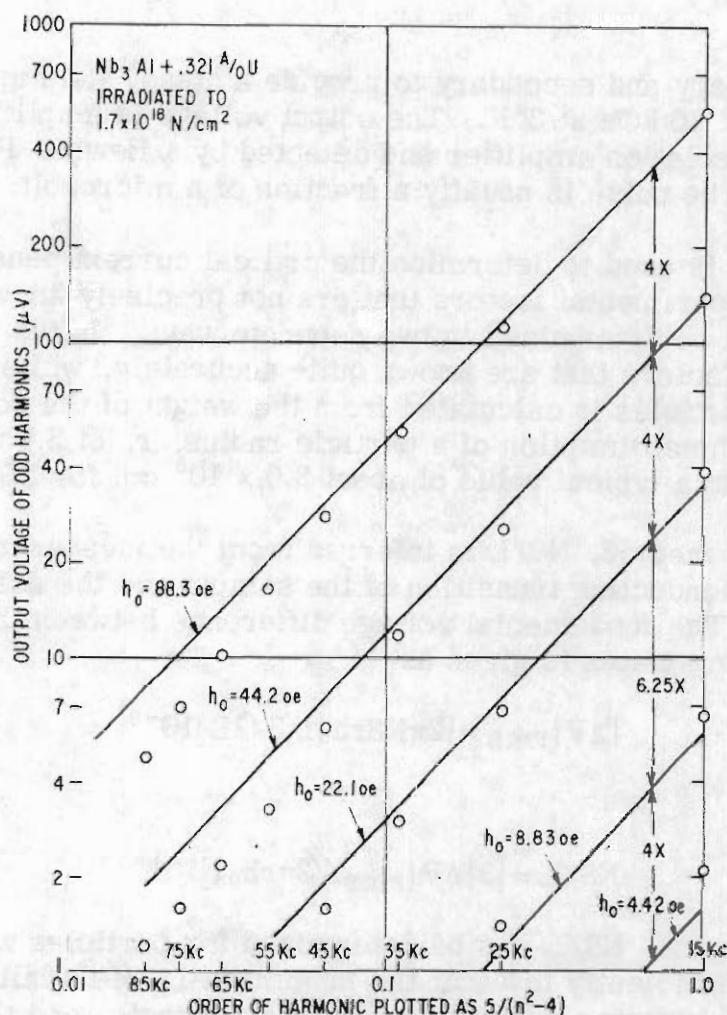
Figure 48 A plot or output voltage of odd harmonics of 5 kc for a sample of
Nb$_3$Al + 0.321 A/o U irradiated with 1.7 × 10^{18} thermal neutrons/cm^2.
The measurement was made at 4.2°K in a steady field of 15 kOe with al-
ternating field amplitudes from 4.4 to 88.3 Oe. The third through the seven-
teenth harmonics are plotted on the horizontal axis as 5/(n^2 - 4) where n
is the order of the harmonic. The solid lines are theoretical, based on
the assumption of a critical current density of 8.3 × 10^5 amp/cm^2.

driving field and measured harmonic. One can estimate from the data of
Fig. 48 and the two independent measurements of NS/L that the precision
of measurement is within ≈± 20% and that the absolute values of the current
density may be low by about 20%.

Some of the determined values of J$_c$(H) as shown in Figs. 49 through
52 encompass a variety of audio-frequencies and alternating fields, selected
so that the output voltage of the third harmonic was generally maintained be-
tween a few microvolts and a few hundred microvolts, and the consequent
penetration of the alternating magnetic field was small.

104
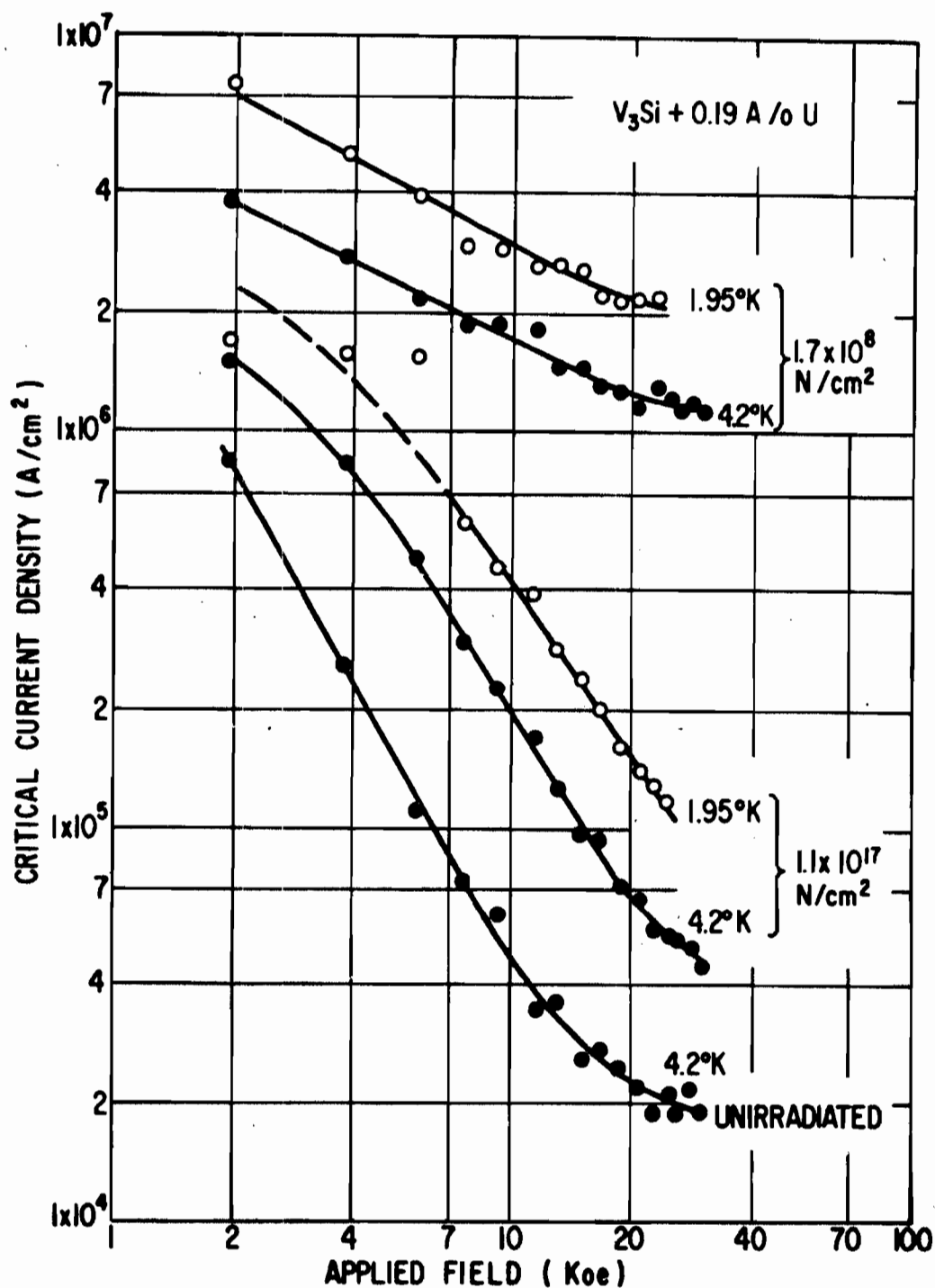
Figure 49 Current density as a function of applied field at 4.2° and 1.95°K
for three samples of 70μ particles of $V_3Si + 0.19$ A/o U with irradiations
of zero, 1.1×10^{17}, and 1.7×10^{18} thermal neutrons/cm².
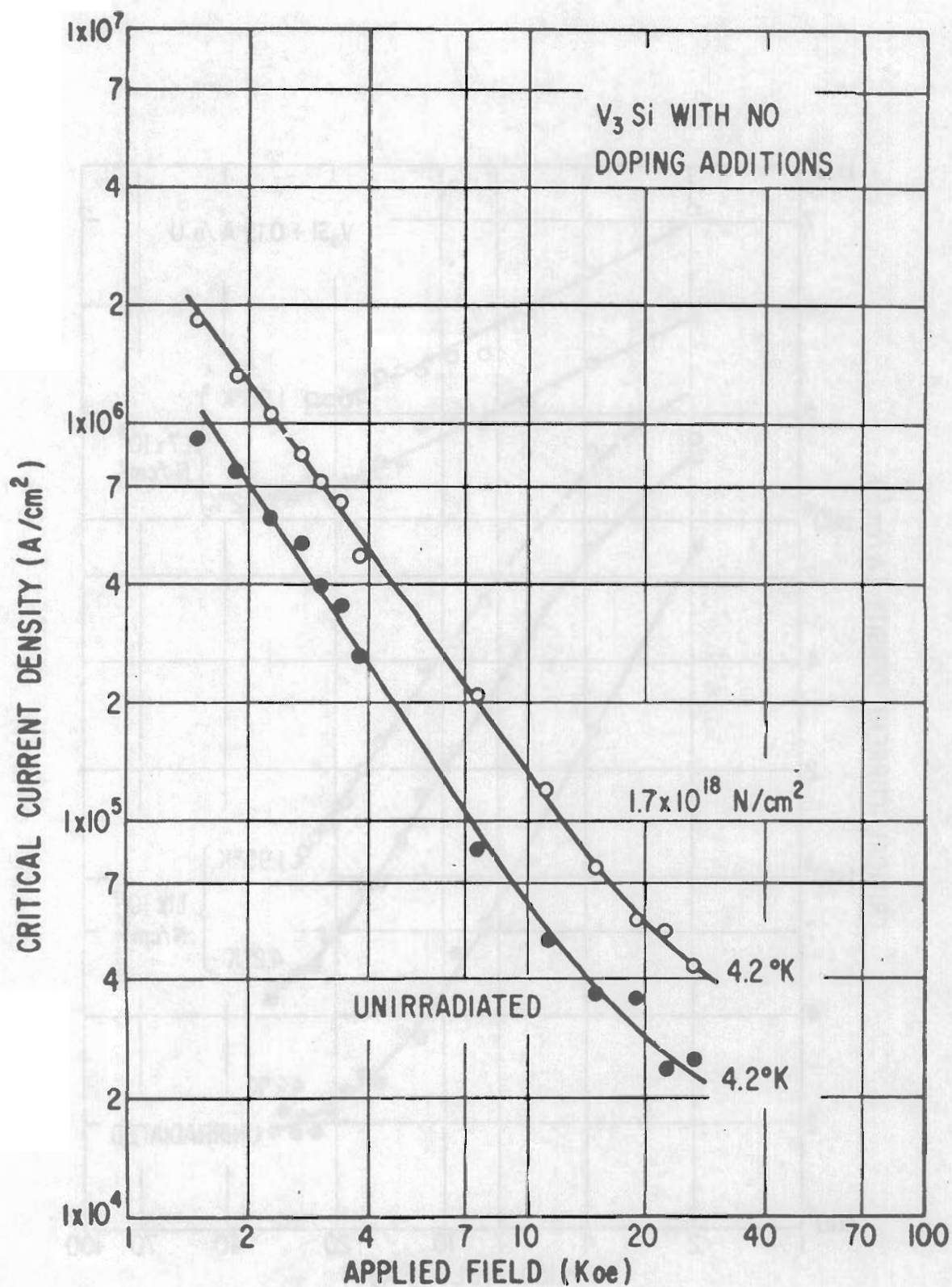
Figure 50   Current density as a function of applied field at 4.2°K for two samples of 70μ particles of V₃Si with no doping additions irradiated to zero and 1.7×10^{18} thermal neutrons/cm².
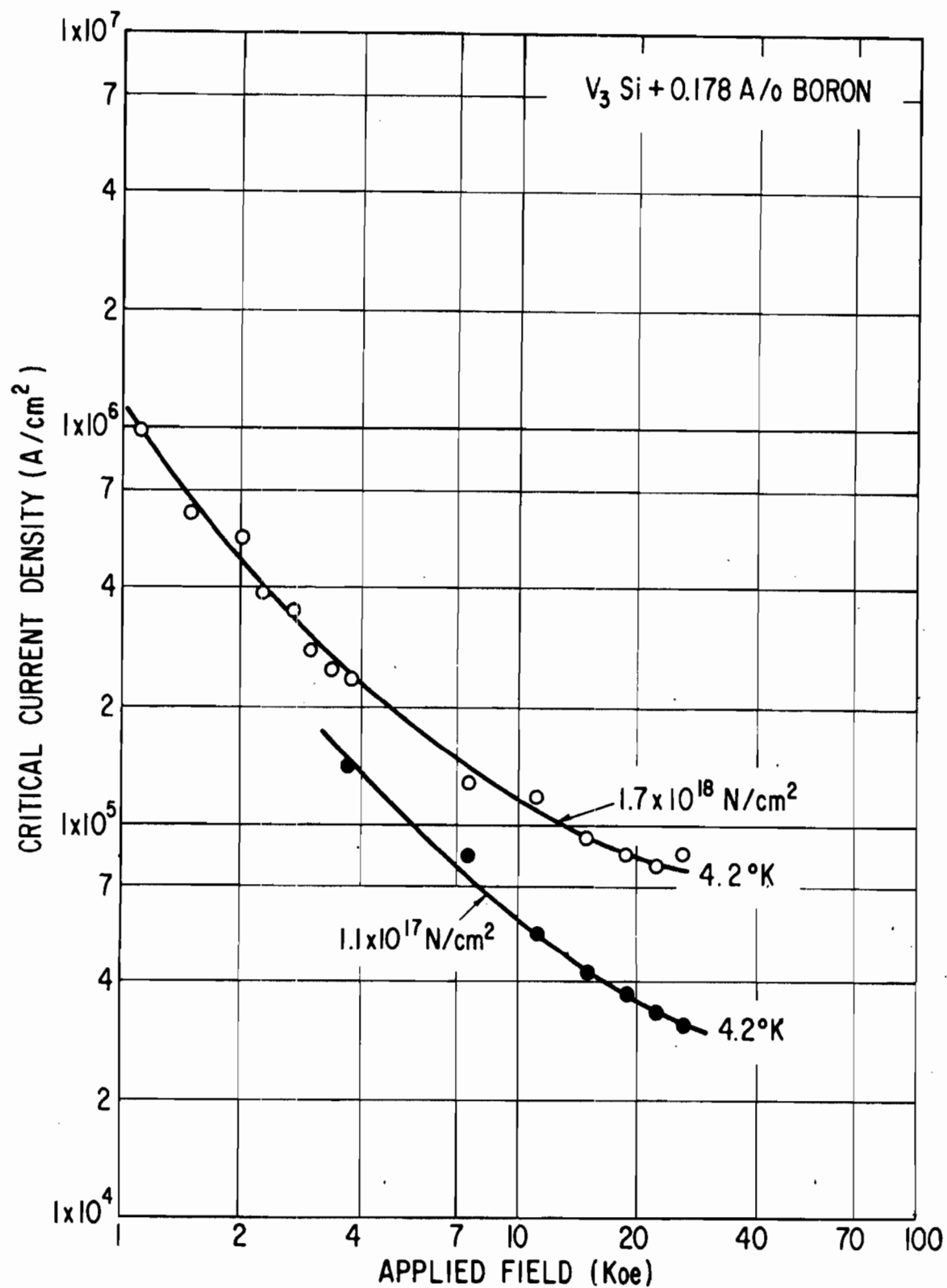
Figure 51 Current density as a function of applied field at 4.2°K for two samples of 70µ particles of V_3Si + 0.178 A/o B irradiated to zero and 1.7×10^{18} thermal neutrons/cm².
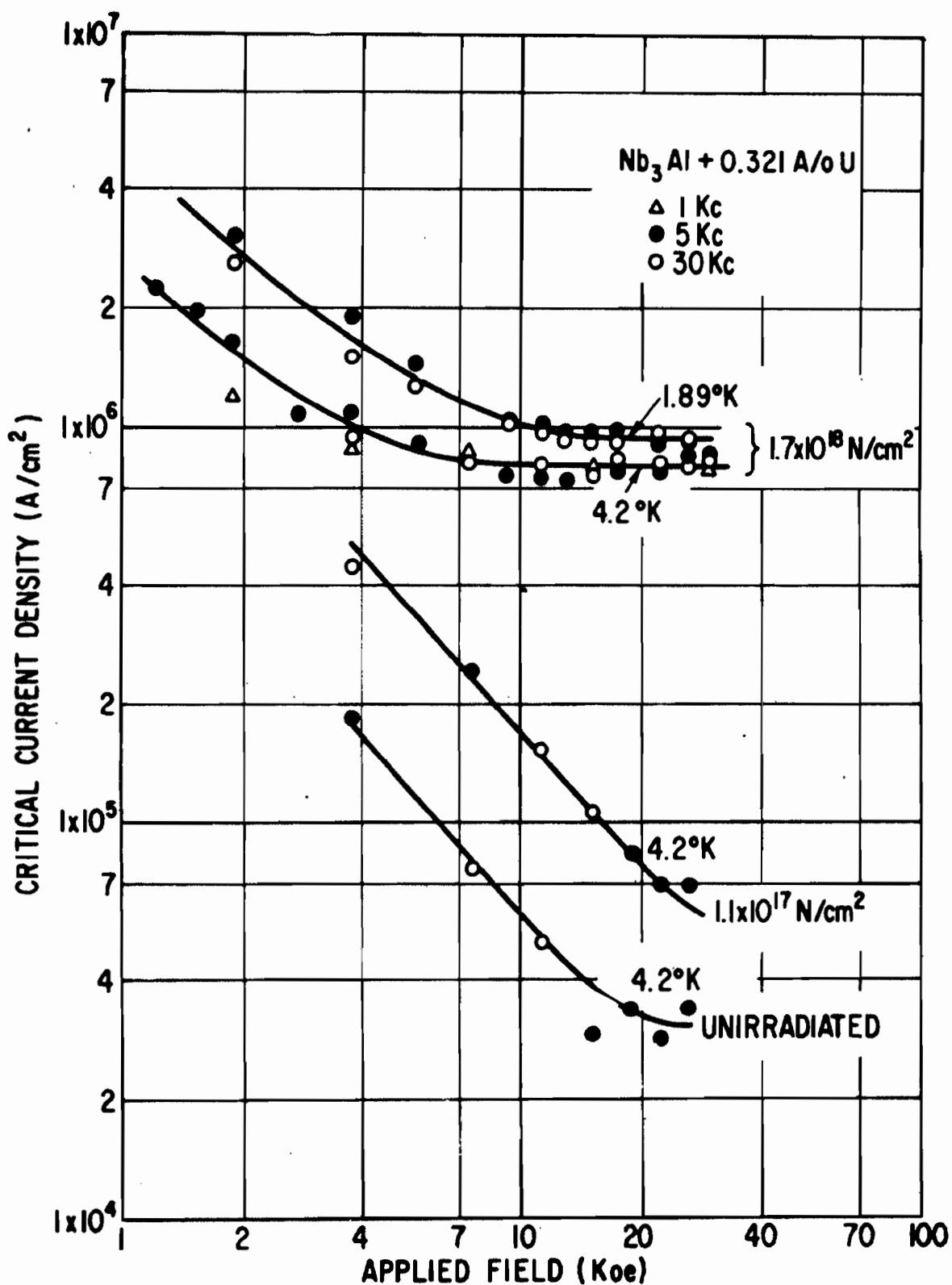
Figure 52 Current density as a function of applied field at 1.89° and 4.2°K
for three samples of 70μ particles of Nb_3Al + 0.321 A/o U with irradiations
of zero, 1.1 x 10^{17}, and 1.7 x 10^{18} thermal neutrons/cm^2.

3. Discussion

The measured values of critical current density are interesting in a number of respects. Perhaps the most significant result is the absolute magnitude of the critical current density of the uranium-doped Nb_3Al and V_3Si after 1.7×10^{18} thermal neutrons/cm^2. The critical current densities of 1 to 2×10^6 amp/cm^2 at 30 kOe (see Figs. 49 and 52) represent an increase of nearly two orders of magnitude over the pre-irradiated values and are nearly an order of magnitude greater than the highest values yet reported for any superconductor in these high magnetic fields. This large increase in critical current density must be attributed to the uranium fissions rather than the thermal neutrons alone, since the undoped V_3Si (Fig. 50) and the undoped Nb_3Al (not displayed) undergo an increase in critical current density of only about 5×10^4 amp/cm^2 at 30 kOe after the bombardment of 1.7×10^{18} N/cm^2.

It is interesting to note the very small fraction, f, of fissions that has produced this large increase in J_c. We have

$$f = CI\sigma\phi \tag{84}$$

where C is the atomic concentration of the uranium, equal to 3.21×10^{-3} for the Nb_3Al, and 1.90×10^{-3} for the V_3Si; I is the atomic abundance of the U_{235} in natural uranium, equal to 7.19×10^{-3}; ϕ is the thermal neutron dose (1.7×10^{18} N/cm^2); and σ is the fission cross section of U_{235} which is $5.82 \times 10^{-22} cm^2$. Equation (84) tells us that the fraction of the total number of atoms that have fissioned is one in each 44 million in the Nb_3Al and one in each 75 million in the V_3Si. The total number, M, of atoms displaced per uranium fission has been calculated on different occasions to be 6×10^4 or 6×10^5 for uranium.[54 55] If these numbers are assumed to apply here also, the fraction, Mf, of atoms displaced by the heavy irradiation in the two uranium-doped intermetallic compounds would be 1/1000 to 1/100.

Earlier work[47] on the increase in critical current in undoped V_3Si and Nb_3Al after fast neutron irradiation has shown that the increase in current density per incident neutron is about 3 to 4 times greater in the V_3Si. The present results indicate that damage produced by the uranium fissions is also more effective in the V_3Si, since the increase in critical current per uranium fission at high magnetic fields is 2 to 3 times greater in the V_3Si.

The increase in critical current with thermal neutron dose in the uranium-doped samples is unusual. In low magnetic fields, the critical current is increasing much slower than linearly with neutron dose. In high magnetic fields, the critical current is increasing somewhat faster than linearly with neutron dose. In magnetic fields greater than about 10 kOe, the critical current of the heavily irradiated, uranium-doped V_3Si and Nb_3Al becomes nearly independent of magnetic field. Apparently, the type of pinning center produced by the fission is as effective in impeding flux motion in high magnetic fields as in low

magnetic fields. This observation runs counter to the typical case in which the more customary relationship of $J_C(H + B_0) = \alpha_C$ is found.

It would be interesting to determine if there is some upper limit to J_C in the beta-tungsten-type superconductor. Perhaps the easiest way to explore this question is to dope with enriched, rather than natural, uranium. Then 140 times as many fissions would be produced per incident thermal neutron.

The critical temperatures of some of the samples were also measured. Following the technique of Schawlow and Devlin,[29] the frequency (near 4 x 10^4 cps) was monitored as the temperature was decreased. The critical temperature of the unirradiated, uranium-doped V_3Si was ~16.90°K, essentially the same as the undoped sample. After the heavy irradiation, the uranium-doped V_3Si showed a decrease of only ~0.22°K (Fig. 53). The critical temperature of the unirradiated, uranium-doped Nb_3Al was only 16.94°K, a decrease of ~0.75°K from the undoped sample. After the heavy irradiation, the critical temperature was further decreased by ~0.45°K.

The critical temperature of the boron-doped V_3Si was also measured before and after the heavy irradiation. The critical temperature was found to decrease only 0.04°K from the pre-irradiated value of 16.85°K. In the boron-doped V_3Si (Fig. 51) and Nb_3Al (not shown) the increase in critical current after heavy irradiation was essentially the same as the increase observed in the undoped samples. This indicates that the boron fissions are either ineffective in providing pinning sites with which the magnetic flux lines will interact, or that relatively few damage sites are produced.

We may use Eq. (84) to calculate the fraction, f, of fissions produced by heavy irradiation in the boron-doped intermetallics. Taking the isotopic abundance, I, of B^{10} as 0.19 and $\sigma = 4$ x 10^{-21} cm^2, then f = 1/2.5 x 10^5 for the Nb_3Al and f = 1/4.2 x 10^5 for the V_3Si. The lithium nuclei and alpha particles produced by the boron fission carry a total kinetic cenergy of ~2.5 Mev, most of which is given to the lighter alpha particle. This number is much less than the 100 to 200 Mev total kinetic energy of the heavy fragments produced by a uranium fission. The subsequent atomic displacements that result from the fission fragments originate in both cases from the repulsive coulomb interactions. Because of its low charge and mass, the alpha particle is less effective in producing atomic displacements than the ratio of 2.5 Mev/ 180 Mev would imply. The number, M, of atomic displacements produced by a 2 Mev alpha particle is only ~40 in germanium.[55]

We can provide a qualitative explanation of the relative ineffectiveness of the boron fissions when compared to the uranium fissions if we assume that the increase in critical current density is proportional to the number of displaced atoms in each case. From the values of C, I, M, and Φ given above for boron and uranium, we calculate that 10 to 100 times as many atomic

110
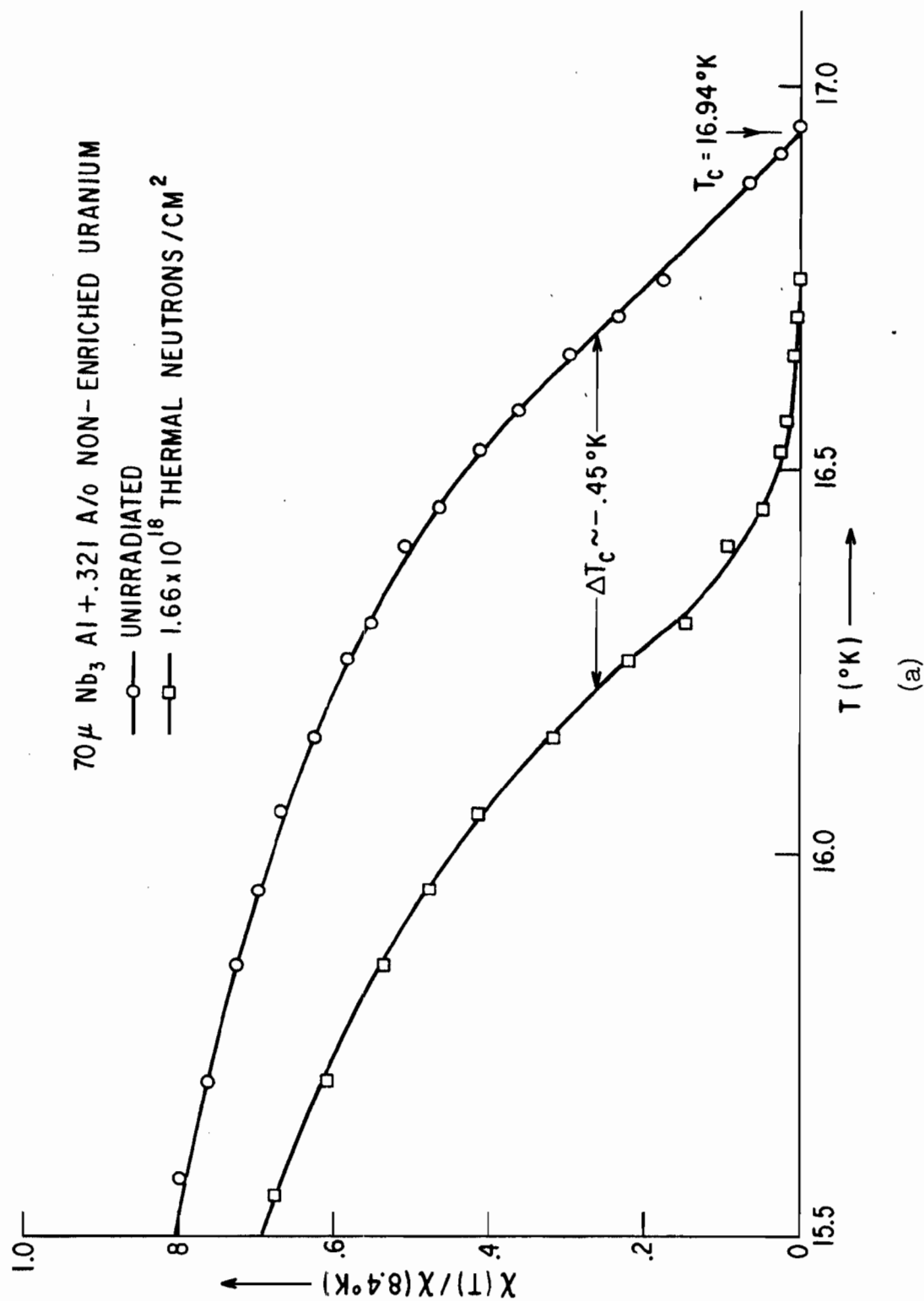
Figure 53 The critical temperature transition before and after the heavy dose irradiation of 70μ particles of (a) $Nb_3Al + 0.321$ A/o U and (b) $V_3Si + 0.190$ A/o U. The measuring technique developed by Schawlow and Devlin(29) was employed.
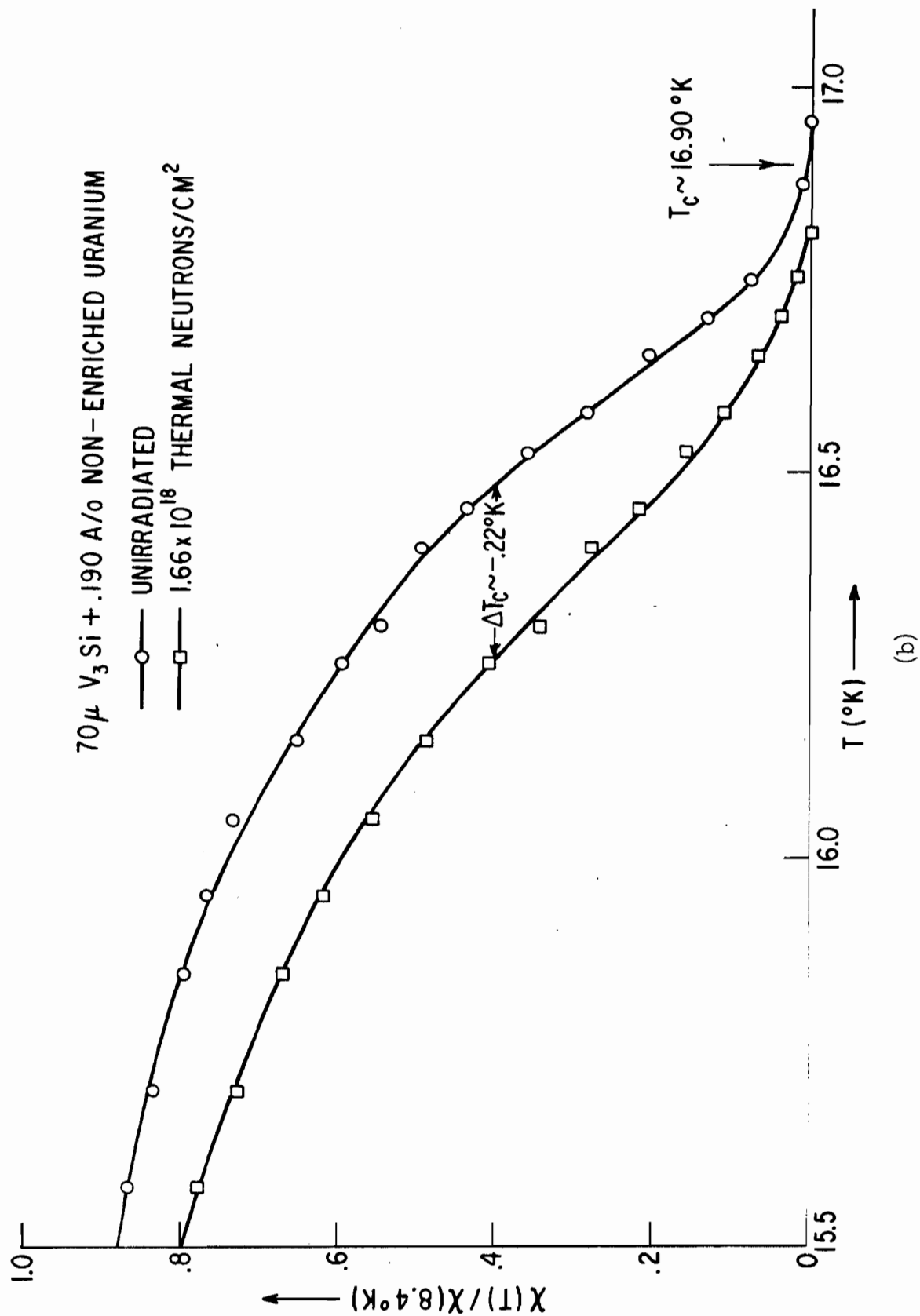
Figure 53   (continued)

displacements occur in the uranium-doped V_3Si and Nb_3Al than in boron-doped samples after comparable thermal neutron irradiations. Further, the damage resulting from the uranium fissions may be somewhat more effective than the multiple of 10^1-10^2 suggests, as each of these damage clusters should be larger and more comparable to the diameter of the flux thread, and hence effective as a pinning site. [56]

4. Summary

The technique used for confirming the amount of uranium and boron additions and its distribution in the samples is novel. This method of detecting small concentrations of a fissionable impurity should lend itself to other applications. The technique employed for measuring the critical current density of small samples is also new and offers certain advantages over the ballistic method.

The major experimental finding is that damage resulting from uranium fission is extremely effective in increasing the bulk supercurrent of the beta-tungsten-type superconductor. The accompanying decrease in critical temperature is small. Thus, the technique of uranium doping followed by thermal neutron irradiation may prove to be a useful processing technique for increasing the supercurrents in systems made from superconductors of the beta-tungsten structure. Further studies of the effects of various types of irradiation-produced damage may provide insight both to the nature of the damage produced and to the nature of the interaction between a structural defect and the quantized magnetic flux thread.

ACKNOWLEDGMENTS

We wish to thank G. E. Nichols for carrying out the current density measurements reported in this section and in addition acknowledge with appreciation helpful conversations with J. W. Corbett, H. R. Killias, and R. M. Walker.

C. SOLID-STATE PHASE TRANSFORMATIONS (J. D. Livingston)

1. Martensitic Transformation in In-Tl

In-Tl alloys undergo, on cooling, a martensitic (diffusionless) transformation from f.c.c. to face-centered tetragonal[57] resulting in an interesting microstructure (see Fig. 54). Within the primary transformation lamellae seen in the figure are much finer secondary lamellae. [57] Since these alloys are type II superconductors, [58] it was decided to study the effect of these unusual microstructures on superconducting properties. The recent indications from Bell Laboratories of similar transformations in V_3Si[59] and other β-W compounds, and the resulting possibility that critical currents in Nb_3Sn are controlled by such a transformation, give added interest to a study of In-Tl.

113

Figure 54   "Nomarski" interference contrast micrograph of In 20.9 A/o Tl
   polycrystal, showing primary transformation lamellae.   200X

The martensitic transformation temperature decreases with increasing
Tl content.   A recent paper[60] shows the transformation temperature de-
creasing from room temperature at 22% Tl, to 77°K at 30% Tl, and to liquid
helium temperatures by 31% Tl.

A series of alloys was annealed at 135°C, and the magnetization curves
tested at about 2°K.   The results in Fig. 55 show a tenfold increase in mag-
netic hysteresis (hence, in J_c) in the vicinity of 31% Tl.

The most likely explanation of these interesting results is a two-phase
structure in the alloys near 31% Tl.   Probably samples (a), (b), and (c) were
fully tetragonal at 2.15°K; samples (g) and (h) fully cubic; and samples (d),
(e), and possibly (f) part cubic and part tetragonal.

Hence, martensitic microstructures of the kind seen in Fig. 54 apparently
do not produce much hysteresis.   Samples (a), (b), and (c), which contain such
structures, are nearly as reversible as (g) and (n), which remained cubic.
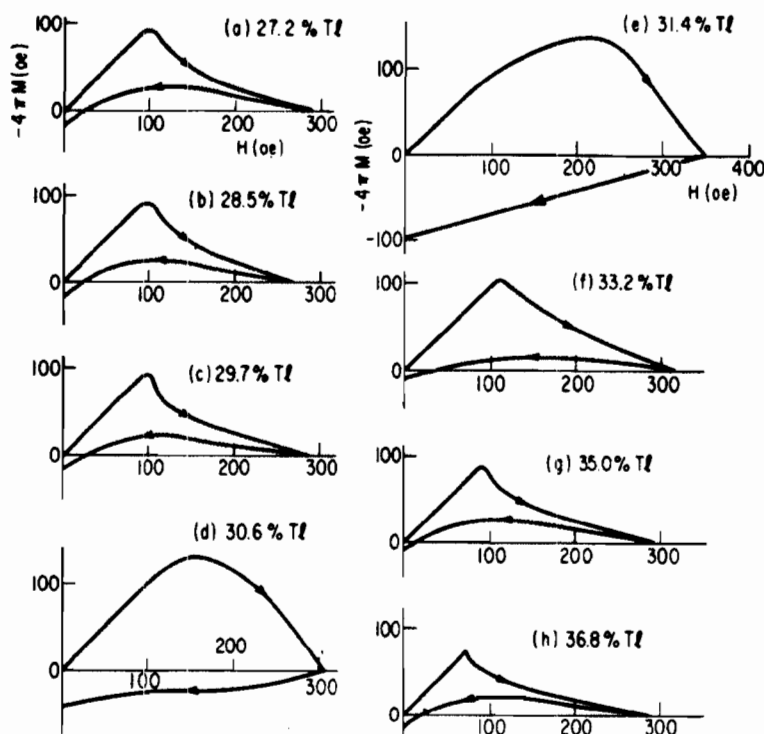
Figure 55   Magnetization curves for In-Tl alloys at about 2.2° K.

The results, therefore, suggest that to obtain high current-carrying capacity from a martensitic transformation, one wants an <u>incomplete</u> transformation, as in specimens (d) and (e).   This conclusion may also be true for V_3Si and Nb_3Sn, which may undergo similar transformations, and where, as here,   local composition is probably the main variable controlling the transformation.

2.   Spinodal Decomposition in Nb Alloys

Spinodal decomposition has recently been recognized as a mode of phase separation that, in solids, can produce an extremely fine and uniform microstructure. [61]   Such a microstructure should be more amenable to quantitative description than the irregular microstructure produced by ordinary deformation and precipitation treatments, and thus more useful for experiments attempting to determine a quantitative relationship between J_C and microstructural parameters.   A uniform microstructure as produced by spinodal decomposition might also be less prone to flux jumping than more irregular structures.   Unfortunately, all alloys known to undergo spinodal decomposition were nonsuperconductors, so metallurgical development work was first necessary to see if "spinodal superconductors" could be produced.

This work, started in the last year of the contract, was delayed by a variety of difficulties, and has not yet achieved success.   Only in the last
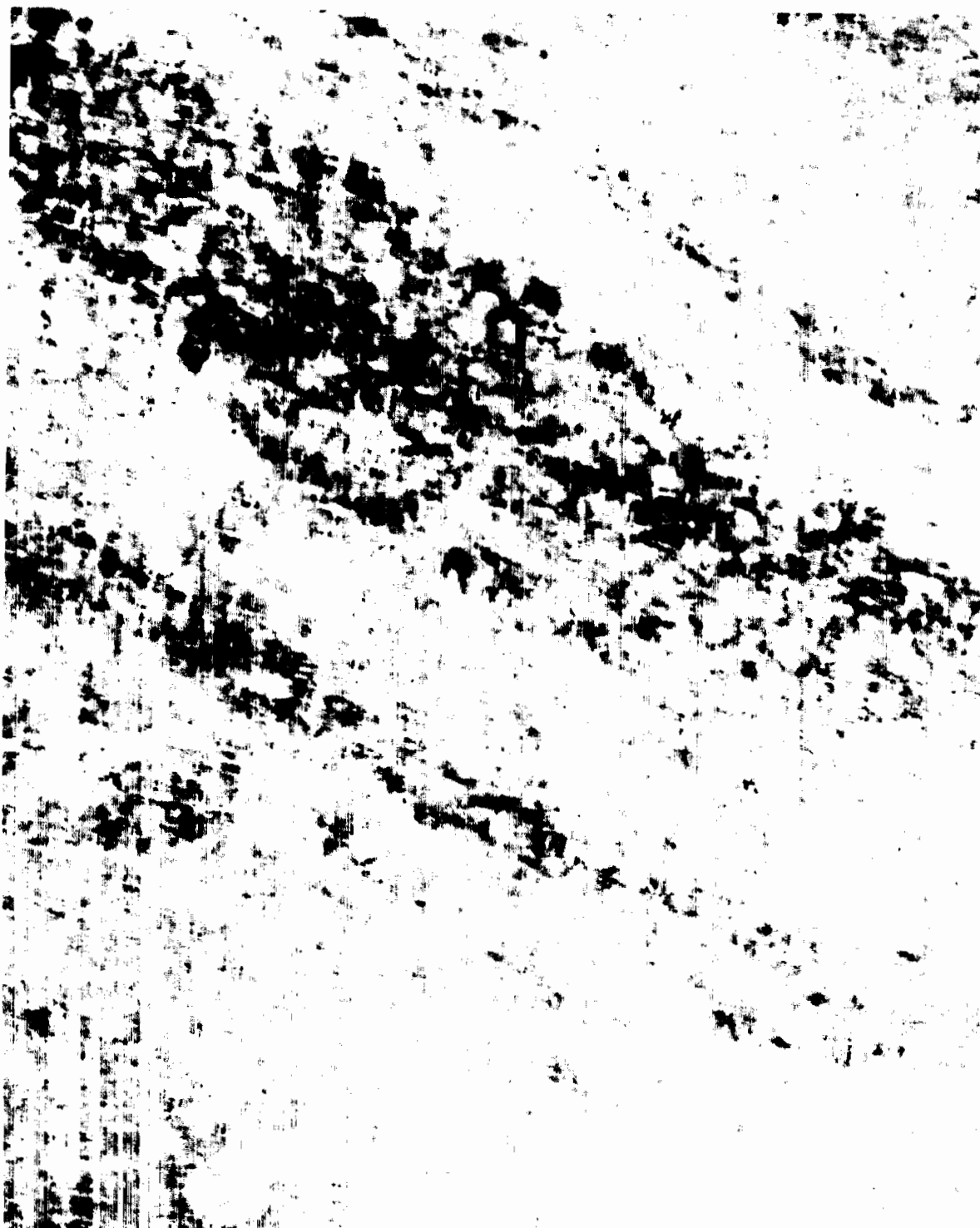
Figure 56 Transmission electron micrograph of Nb - 60% Zr alloy solution
treated at 1500°C and subsequently aged 1 week at 370°C. Faint checker-
board pattern seen on fine scale may be evidence of spinodal decomposi-
tion.   80,000X

116

month have some promising preliminary results been obtained. Transmission electron microscopy of Nb-Zr and Nb-Zr-Ta alloys aged for one week at 370°, 450°, and 510°C has revealed a fine microstructure that has some of the expected features of spinodal decomposition (for example, see Fig. 56). An at least locally periodic structure on a scale of 100 Å or less is visible. More work is necessary to confirm and interpret these results, and to see the effects of these fine microstructures on superconducting properties.

3. Precipitate Particles; "Differential Diamagnetism"

In considering the relative effectiveness of various precipitated particles in interacting with flux threads, it was conceived that a controlling property was the difference in diamagnetic tendencies between particle and matrix, as determined by the difference between the equilibrium magnetization of the two phases. Flux threads will be repelled from particles more diamagnetic than the matrix, and attracted to particles less diamagnetic. The force of the interaction, which governs the critical current density J_c, will vary with this "differential diamagnetism" between particle and matrix.

Considered in detail, this suggests that superconducting particles of lower T_c and H_{c2} than the matrix can produce critical currents that will <u>increase</u> with increasing temperature. (The particle, less diamagnetic than the matrix, also loses diamagnetism faster with increasing temperature, so that the "differential diamagnetism" increases.) This has been observed in an alloy of Pb-In containing Sn-rich precipitates, as seen in Fig. 57. It can be seen that for fields below about 1500 Oe, this alloy has a higher hysteretic magnetization (hence, a higher J_c) at 4.2°K than at 2.0°K. The situation, of course, reverses at higher fields, since the critical field at 2.0°K is much higher than at 4.2°K.

The "differential diamagnetism" argument also suggests that superconducting particles of lower T_c and H_{c2} than the matrix can produce critical currents that will increase with increasing <u>field</u> ("peak effect"). The Pb-In-Sn alloy at 2°K shows a slight peak, as predicted. Applied to particles or regions of different κ than the matrix, a "peak effect" is again predicted, in this case with a minimum in critical current near $H = (1/2)H_{c2}$ (where equilibrium magnetization is independent of κ, hence "differential diamagnetism" is zero). Samples of several cold-worked Pb alloys show such a minimum (Ref. 62), where the dislocation boundaries probably serve as high-κ regions.

Although still in a preliminary state, this concept of "differential diamagnetism" has received some experimental support, and shows promise of improving our understanding of the dependence of J_c on temperature, field, and the nature of second-phase particles. The specific case of materials with J_c increasing with increasing temperature is of particular interest. Since flux jumping is dependent on the normal decrease in J_c with increasing temperature (see Section VI of this report), materials like that shown in Fig. 57 might be unusually resistant to flux jumping.

117
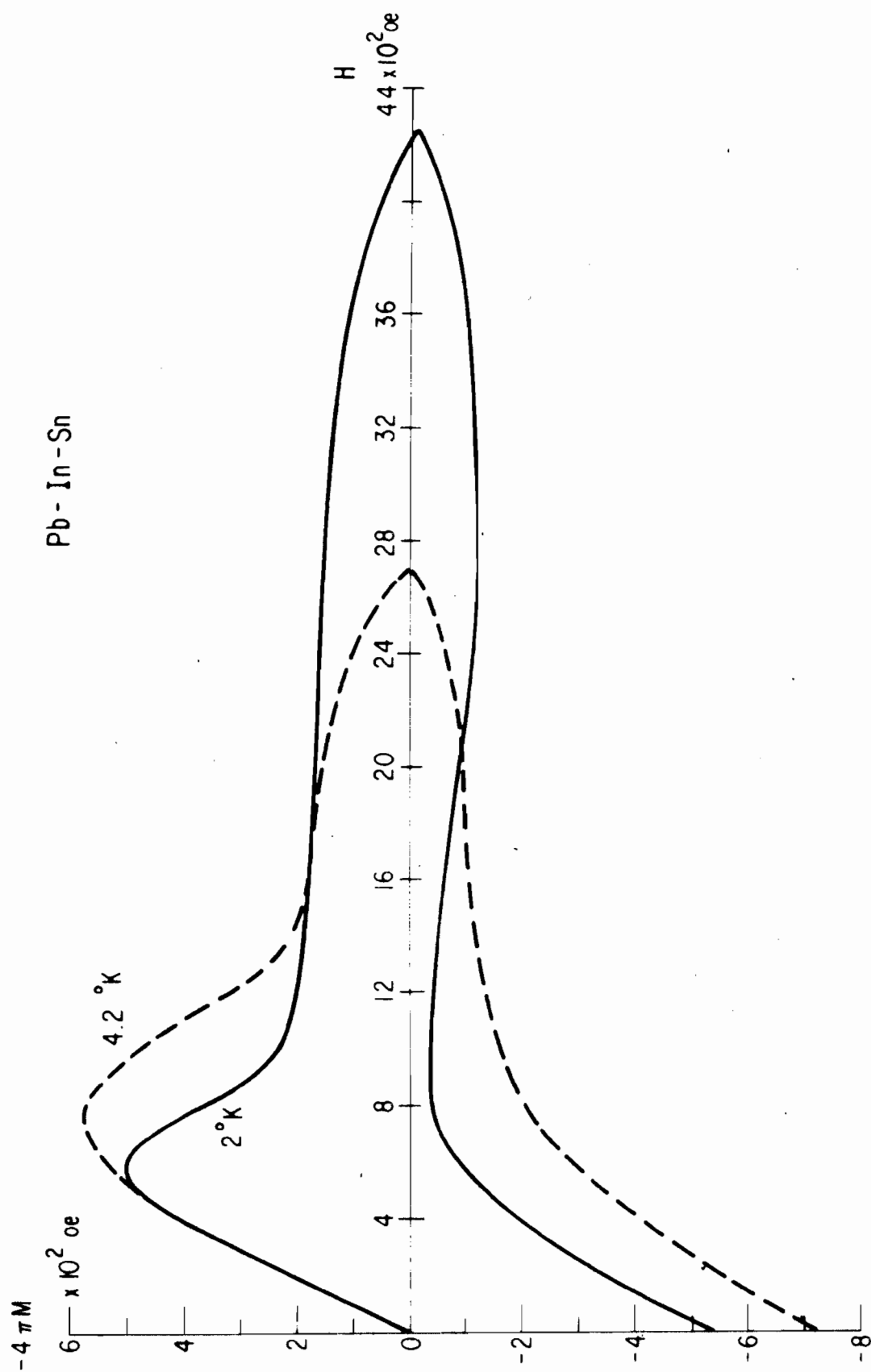
Figure 57 Magnetization curve at 2°K for Pb - 10 w/o In - 10 w/o Sn alloy solution treated at 240°C and subsequently aged 80 minutes at room temperature.   Behavior at low fields indicates that J_C <u>increases</u> with increasing temperature.

MAGNETIC INSTABILITY AND ITS IMPLICATIONS
FOR THE BEHAVIOR OF HARD SUPERCONDUCTORS

A. CONDITIONS FOR MAGNETIC INSTABILITY IN INHOMOGENEOUS TYPE II SUPERCONDUCTORS (P.S. Swartz and C.P. Bean)

1. Introduction

It is a common experience that an inhomogeneous type II superconductor, a hard superconductor, exposed to an increasing magnetic field will shield this magnetic field from the interior of the specimen by the induction of persistent currents. At excess fields on the order of kilo-oersteds or tens of kilo-oersteds, it is commonly found that a magnetic instability develops and the formerly persistent currents are partially or wholly destroyed, and correspondingly the magnetic flux partially or wholly enters the specimen in a discontinuous fashion. The occurrence of these flux jumps is usually not reproducible in detail and, further, depends on sample size and structure as well as the time course of the applied field. The occurrence of these flux jumps has an importance over and above the immediate limitation to the shielding properties of high field superconductors; the analogous effect in coils gives a momentary voltage that may cause enough energy dissipation to trigger a discontinuous transition to the normal state.

It is the purpose of this report to give necessary conditions for these flux jumps in terms of sample and material properties. The question of the sufficient conditions is more complicated and can be dealt with only in a more or less incomplete manner.

2. Incremental Adiabatic Susceptibility

This section treats the following problem:[63] consider a semi-infinite slab of superconductor cooled in a magnetic field directed in its surface plane. Assume further that the field is raised isothermally by an amount H (Oe). (It is important to note that H represents the amount by which the field is raised, rather than the absolute magnitude of the field.) We next consider the field to have received a small increment, ΔH, in a time short compared to an appropriate thermal diffusion time and long compared to an appropriate electromagnetic diffusion time (these limits will be made clear later). This increase of field is termed adiabatic. If the total change in flux per unit width of the specimen is given by $\Delta \omega (H, \Delta)$, then $\Delta \omega / \Delta H$ defines an adiabatic incremental susceptibility. A necessary condition for a flux jump is that this quantity be unbounded--this condition is calculated in this section. The physics of the situation arises from the fact that the impediments to flux motion are, in general, decreased by increasing temperature. Each element of volume exposed to the increment of field receives a thermal pulse. This impulse, in turn, lowers the barriers to flux motion, giving rise to a further impulse. Under appropriate conditions this process may be catastrophic.

119

The calculation rests on the following assumptions: first, the material is assumed to be strongly type II such as $Nb_{0.75}Zr_{0.25}$ or Nb_3Sn, and to be operated in the mixed state region where the equilibrium flux density within the body is closely equal to the applied field; secondly, the material is characterized by a critical current density, $J_c(amp/cm^2)$, a gradient of current density with temperature, $\partial J_c/\partial T \ (amp/cm^2 \, ^\circ K)$ and a specific heat, C $(ergs/cm^3 \, ^\circ K)$. If the slab is cooled in an arbitrary field in the mixed state region and the field is subsequently raised in an isothermal fashion by an amount, H(0), then by simple application of Ampere's law, [7]

$$\partial H/\partial X = -4\pi J_c/10 \tag{85}$$

the excess field decreases with distance, measured in the X direction, to a depth $\delta = 10 \, H/4\pi J_c$. This state of affairs is shown in the lower curve of Fig. 58. The flux per unit width, $\varphi(X)$, that has crossed a position X in the body is defined by

$$\varphi(X) = \int_X^\infty H(X)dX \quad . \tag{86}$$

If the field were increased isothermally by an amount ΔH, as in the dashed curve of Fig. 58, then the increase in flux $\Delta\varphi_{iso}$ is given from Eq. (86) and inspection of figure as

$$\Delta\varphi_{iso} = \delta \cdot \Delta H \quad . \tag{87}$$

Hence the isothermal incremental susceptibility is simply $\Delta\varphi_{iso}/\Delta H = \delta$. If, however, the step of field is applied adiabatically, then each region has an energy $J_c\Delta\varphi(X) \times 10^{-1}$ ergs/cm^3 suddenly dissipated in it. If this occurs in a time short compared to that for heat diffusion, then by the first law of thermodynamics there is a temperature rise $\Delta T(X)$ given by

$$C\Delta T(X) = J_c\Delta\varphi(X) \times 10^{-1} \quad . \tag{88}$$

If we expand the current density $J_c(X)$ in a Taylor expansion in T, i.e.,

$$J_c(T+\Delta T) = J_c(T) + (\partial J_c/\partial T)\Delta T \tag{89}$$

we can by combination of Eqs. (88) and (89) eliminate ΔT to arrive at a specified form of Ampere's law

$$\partial H/\partial X = -4\pi J_c/10 + (1/\lambda^2)\Delta\varphi(X) \tag{90}$$

where λ is a parameter with the dimension of distance, defined by

$$1/\lambda^2 = -4\pi J_c(\partial J_c/\partial T) \cdot 10^{-2}/C \quad . \tag{91}$$
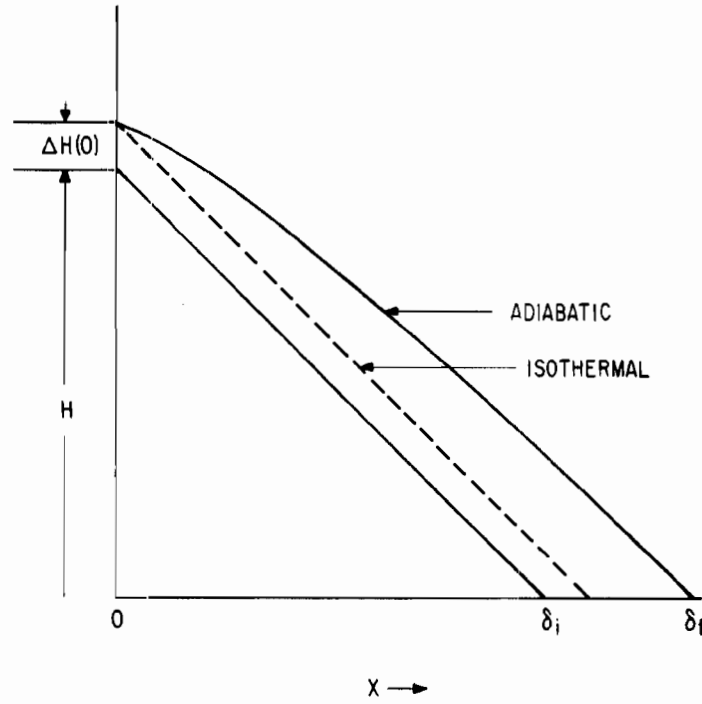
Figure 58 The distribution of field in an inhomogeneous, strongly type II
   superconductor of field-independent, critical current-carrying capacity under
   three conditions. The lower solid curve shows the field distribution into the
   planar specimen with an excess field, H, applied isothermally. The depth
   of penetration is δ_i. The dashed curve marked "isothermal" indicates the
   result of an increment field, $\Delta H(0)$, applied isothermally while the upper
   solid curve marked "adiabatic" indicates the further penetration owing to
   local heating that occurs if $\Delta H(0)$ is applied in a time short compared to that
   for heat diffusion. The final depth of penetration is δ_f.

The final field configuration is that shown in the upper curve of Fig. 58.
A general expression for the increase in local field, $\Delta H(X)$, caused by the
increment $\Delta H(0)$ is

$$\Delta H(X) = \Delta H(0) + \int_0^X \left(\frac{\partial H}{\partial X} \Big|_f - \frac{\partial H}{\partial X} \Big|_i \right) dX \qquad (92)$$

where the subscripts f and i refer to final and initial states or after and before
the increment of applied field, respectively. In deriving equations for the
final field distribution, we must distinguish between two domains of X. The
region of initial field penetration, $0 \leq X \leq \delta_i$; and the extra region exposed
to flux, $\delta_i \leq X \leq \delta_f$. By the conditions hypothesized,

$$\frac{\partial H}{\partial X} \Big|_i = - 4\pi J_c/10 \qquad 0 \leq X \leq \delta_i$$

$$\frac{\partial H}{\partial X} \Big|_i = 0 \qquad \delta_i \leq X \leq \delta_f \quad .$$

(93)

121

Using the final value of the field gradient given by (90) and the initial value given by (85), Eq. (92) becomes

$$\Delta H(X) = \Delta H(0) + (1/\lambda^2) \int_0^X \Delta\varphi(X)dX \qquad 0 \le X \le \delta_i$$

$$\Delta H(X) = \Delta H(0) - 4\pi J_c(X-\delta_i)/10 + (1/\lambda^2) \int_0^X \Delta\varphi(X)dX \qquad (94)$$

for $\qquad \delta_i \le X \le \delta_f$.

The distance of total penetration, δ_f, is defined by setting the increase in field equal to zero, i.e.,

$$0 = \Delta H(0) - 4\pi J_c(\delta_f - \delta_i)/10 + (1/\lambda^2) \int_0^{\delta_f} \Delta\varphi(X)dX \quad . \qquad (95)$$

Differentiating Eqs. (94) with respect to distance with substitution of first and second derivatives of $\Delta\varphi(X)$ for $-\Delta H(X)$ and $-\partial\Delta H(X)/\partial X$, respectively, from Eq. (86) gives differential equations for $\Delta\varphi(X)$

$$\frac{\partial^2\Delta\varphi}{\partial X^2} = (1/\lambda^2)\Delta\varphi \qquad 0 \le X \le \delta_i$$

$$(96)$$

$$\frac{\partial^2\Delta\varphi}{\partial X^2} = -(1/\lambda^2)\Delta\varphi + 4\pi J_c/10 \qquad \delta_i \le X \le \delta_f \quad .$$

The appropriate boundary conditions are

$$\Delta\varphi \quad \text{and} \quad \partial\Delta\varphi/\partial X \qquad\qquad \text{continuous at } \delta_i$$
$$\qquad\qquad\qquad\qquad\qquad\qquad\qquad\qquad\qquad (97)$$
$$\Delta\varphi = \partial\Delta\varphi/\partial X = 0 \qquad\qquad\qquad \text{at } \delta_f \quad .$$

Solutions of Eqs. (96) that satisfy the boundary conditions given in (97) are

$$\Delta\varphi(X) = (4\pi J_c\lambda^2/10)[\cos\{(X-\delta_i)/\lambda\} - \cos\{(X-\delta_f/\lambda)\}], \ 0 \le X \le \delta_i$$

$$(98)$$

$$\Delta\varphi(X) = (4\pi J_c\lambda^2/10)[1-\cos\{(X-\delta_f)/\lambda\}] \qquad \delta_i \le X \le \delta_f \quad .$$

122

From the first equation of the set above, we can immediately write down the total pulse of flux that enters the samples as

$$\Delta\varphi(0) = (4\pi J_c \lambda^2/10) \left[\cos(\delta_i/\lambda) - \cos(\delta_f/\lambda)\right] \quad . \tag{99}$$

To determine the value of $\Delta H(0)$ we take the negative derivative of the first equation of (98) and evaluate it for $X = 0$:

$$\Delta H(0) = (4\pi J_c \lambda/10) \left[\sin(\delta_f/\lambda) - \sin(\delta_i/\lambda)\right]. \tag{100}$$

Equations (99) and (100) given by elimination of δ_f, the desired relationship between $\Delta\varphi(0)$ and $\Delta H(0)$,

$$2[\Delta H(0)] \sin(\delta_i/\lambda) + [\Delta H(0)]^2 (10/4\pi J_c \lambda) = \tag{101}$$

$$2[\Delta\varphi(0)] (1/\lambda) \cos(\delta_i/\lambda) - [\Delta\varphi(0)]^2 (10/4\pi J_c \lambda^3) \quad .$$

In the approximation of small $\Delta H(0)$ and $\Delta\varphi(0)$, this gives for the adiabatic incremental permeability

$$\Delta\varphi(0)/\Delta H(0) = \lambda \tan(\delta_i/\lambda) \cdot . \tag{102}$$

In the limit of small penetrating fields, $\delta_i \ll \lambda$ and $\Delta\varphi/\Delta H \to \delta_i$ in agreement with the isothermal case of Eq. (87). The first possibility for an instability occurs when this adiabatic incremental permeability becomes unbounded, i.e., when $\tan(\delta_i/\lambda) \to \infty$ or $\delta_i/\lambda = \pi/2$. Using the earlier definitions of δ and λ, this gives an instability limit field of

$$H_{instability} = [-\pi^3 C J_c/(\partial J_c/\partial T)]^{1/2} \quad . \tag{103}$$

Using approximations appropriate to Nb_3Sn, [64, 65] $C = 2.3 \times 10^2 T^3$ ergs/cm^3, and $J(T) = J(0)(1 - T/T_c)$, this instability field has the values shown in the dashed curve of Fig. 59. The peak value is about 9 kOe at 14°K, and it falls to zero both at absolute zero and the critical temperature.

We emphasize that this is merely a necessary condition for a flux jump and is not necessarily a sufficient condition for partial flux jump, let alone a complete one. The next section calculates the necessary condition for a full flux jump.

The argument of this section rests on the assumption of an adiabatic pulse. This condition requires in turn that the time of application of the field step $\Delta H(0)$ is less than an appropriate thermal diffusion time, τ_{therm}. The thermal diffusivity, D_{therm}, is K/C where K is the thermal conductivity in erg-sec/cm-°K and C is the specific heat in ergs/cm^3-°K. For Nb_3Sn below 10°K, [20] $K \approx 75T^3$ erg-sec/cm-°K. Hence, with the value of C
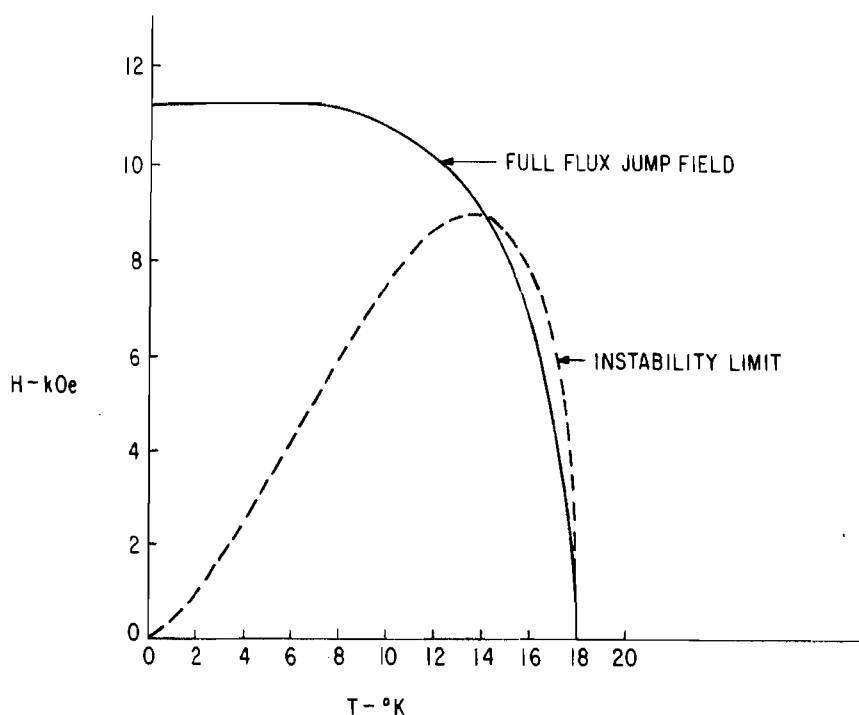
Figure 59 The temperature dependence of two necessary conditions for flux
jump in solid Nb$_3$Sn. The dashed curve plots H$_{instability}$, the excess field
at which the adiabatic, incremental permeability first becomes unbounded.
The solid curve plots the excess field necessary to destroy superconductivity
in a specimen.

previously employed, i.e., $2.3 \times 10^2 T^3$, D$_{therm}$ becomes approximately
0.3 cm^2/sec. For a thickness of δ, the thermal diffusion time is τ_{therm}
$\approx \delta^2/4$D$_{therm}$. If δ were 10^{-2}cm, then τ_{therm} would be about 10^{-4} sec. In
general, then, rise times in the microsecond range ensure adiabatic conditions.
The arguments of this section have neglected the magnetic diffusivity
owing to the viscous motion of flux lines. This diffusivity, D$_{mag}$, can be
expressed[66] in terms of a flow resistivity of flux lines as D$_{mag}$ =
$10^9 \rho_f/4\pi$. While we know of no direct measurements in Nb$_3$Sn, Strnad,
Hempstead, and Kim[67] have found a simple empirical relationship for
Nb-Ta alloys at low temperatures, $\rho_f = \rho_n |H|/H_{c2}$ where ρ_n is the resistance
of the normal state; $|H|$ is the magnitude of applied field; and H$_{c2}$ is the upper
critical field of the material. Assuming the generality of this result and using
a value of 10^{-5} ohm-cm for the normal state resistance of Nb$_3$Sn, D$_{mag}$~10^3
H/H$_{c2}$. Using a value of 2.5×10^5 Oe for H$_{c2}$, it is seen that D$_{mag}$ is greater
than D$_{therm}$ if the applied field, H, is greater than 75 Oe. Hence, for most
cases of interest, the magnetic diffusivity is greater than the thermal diffusivity;
and thus the retardation of flux motion owing to flow resistivity will not prevent
a sample of Nb$_3$Sn from receiving an adiabatic pulse of flux.

124

3. Necessary Condition for a Complete Flux Jump

Following the concepts of Wipf and Lubell, [68] the necessary condition for a complete flux jump at a temperature T_0 is determined through equating the decrease in field energy of complete penetration to the energy necessary to heat the sample to a higher temperature, T_u, at which it is not superconducting in the presence of the field in question. This latter temperature, as Wipf and Lubell point out, is usually very close to the critical temperature, T_c, of the sample. The equations that determine this full flux jump field, H_{crit}, are

$$H_{crit}^2 (T_0)/8\pi = \int_{T_0}^{T_u} C(T)dT \tag{104}$$

and

$$H_{crit}(T_0) = H_{c2}(T_u) \quad . \tag{105}$$

We may evaluate this critical field for a material such as Nb_3Sn by the use of the following analytic approximations

$$C(T) = \gamma T^3, \quad H_{c2}(T) = \beta(1 - T/T_c) \tag{106}$$

where the latter approximation is valid near the critical temperature. Using Eqs. (102) and (105) together with the approximations given in Eq. (106), we find an equation for T_0 in terms of T_u

$$(T_0/T_c)^4 = (T_u/T_c)^4 - (\beta^2/2\pi\gamma T_c^4)(1-T_u/T_c)^2 \quad . \tag{107}$$

To evaluate this for the specific case of Nb_3Sn, we choose [65, 69] $\gamma = 2.3 \times 10^2$ ergs/cm^3-°K^4, $\beta = 3.2 \times 10^5$ Oe, and $T_c = 18°K$. The results of this calculation of T_u and hence by (106) and (105) of $H_{crit}(T_c)$ are shown in the full line of Fig. 59.

4. Discussion

Treatments whose physics is similar to ours for instability conditions have been recently announced by Wipf and Lubell [68, 70] as well as by Hancox. [71] Their results apparently differ by numerical constants of the order of one from our result given in Eq. (103). Both authors note that for usual dependences of $J_c(T)$ and $\partial J_c/\partial T$, the field is independent of the magnitude of J_c. It appears, however, that Hancox confuses this instability limit with the field required for full penetration. A detailed treatment by Wipf and Lubell is promised to appear. [68]

This report has presented two conditions necessary for flux jumps; an important question remaining is that of sufficient conditions. At low temperatures (< 14°K for Nb_3Sn) the considerations of the present report do not permit an identification of the sufficient conditions. Inspection of Fig. 59 shows that for Nb_3Sn above 14°K, the instability field both decreases with increasing temperature and, in addition, is larger than the field required for a full adiabatic flux jump. These conditions are sufficient for a catastrophic jump. We conclude that from 14° to 18°K the dashed line of Fig. 59 represents the flux-jump limit for Nb_3Sn.

The instability condition of Eq. (103) suggests two methods for the elimination of flux jumps. The first is to distribute a second phase within the superconductor that imparts a high specific heat or latent heat such that the instability field of Eq. (103) is raised. Goldsmid and Corsan[72] have found that porous Nb_3Sn in a helium bath will withstand fields up to 50 kOe, and have attributed this strength against flux jumping to efficient cooling by the liquid helium. Hancox[71] has further shown that impregnating such a cylinder with wax reduces the flux-jump field to about 17 kOe, in agreement with this concept. A second method, implicit in the letter by Wipf and Lubell, is to reduce the thickness of the specimen sufficiently so that the critical distance of penetration, $\pi\lambda/2$, is greater than the half thickness of the specimen. Given the thickness as W, this condition becomes

$$W \leq \{-10^2 \pi C/[4 J_c (\partial J_c/\partial T)]\}^{1/2} \quad . \tag{108}$$

For a given specific heat and functional dependence of J_c upon T, this thickness depends inversely on the critical current density. Inasmuch as this criterion is based upon a necessary condition for a flux jump, it undoubtedly is unduly restrictive at low temperatures.

B. AN UPPER LIMIT TO THE CURRENT-CARRYING CAPACITY OF HARD SUPERCONDUCTORS (P.S. Swartz)

1. Introduction

It is well known that the transport current that can flow in a type II superconductor in the mixed state is primarily a bulk, rather than a surface supercurrent. It is customary to describe the current-carrying capacity of such a superconductor in terms of a bulk current density $J_c(H, T)$ that is related to the degree of flux pinning at imperfections and that often adopts the Kim-Anderson form of

$$J_c (H + B_0) = \alpha_c(0) \left(1 - \frac{T}{t_e T_c}\right) \tag{109}$$

where H, B_0, $\alpha_c(0)$, and T_c have their usual meaning[11, 12] and t_e is an experimentally defined parameter that can adopt values between zero and unity. The expected critical current $I_c(H, T)$ for a superconductor characterized by a bulk current density is simply the product of $J_c(H, T)$ and the cross-sectional

area, A, of the superconductor. In practice, however, one finds that a quench or an abrupt return to the normal state (i.e., the sudden appearance of a large voltage) often occurs at a transport current $I_t \ll J_c \times A$. In this report we extend the model for magnetic instability as developed by Swartz and Bean (see first section of this report) to the case where the transport current is applied to the superconductor directly from a battery, rather than induced by a changing external magnetic field. We find that under certain well-defined conditions, the state of the superconductor becomes magnetically unstable and a flux jump occurs that quenches the sample well before the "true critical current" $I_c (\approx J_c \times A)$ is reached.

It will be useful in the analysis that constitutes the body of this report to look upon $I_c(H, T) = J_c(H, T) \times A$ as a phase boundary separating the superconducting and normal states. At a given magnetic field H, the "true" critical current I_c vs reduced temperature $t(\equiv T/T_c)$ takes the form $I_c(t) = I_c(0)(1-t/t_e)$ shown in Fig. 60. At any temperature t_0, if there is no intervening instability, no steady voltage will be detected until the transport current I_t intercepts the phase boundary, $I_c(t)$. We define also a second transport current I_Q. I_Q is defined as that transport current level where, <u>if an instability occurs,</u> sufficient heat will de dissipated to raise the superconductor from t_0 to a higher temperature t_u where $I_Q(t_0) = I_c(t_u) \equiv J_c(t_u) \times A$ and a consequent quench would result. This quench current $I_Q(t)$ may be regarded as a phase boundary that is conditional to the superconductor being unstable when $I_t = I_Q$. A third-phase boundary $I_{fj}(t)$ is defined as that transport current at which a flux jump or instability occurs. This phase boundary is operative in limiting the maximum transport current only when $I_Q \leq I_{fj} \leq I_c$. Typical curves for I_Q and I_{fj} for an unshielded superconducting film are also displayed in Fig. 60.

These three phase boundaries may be used to determine an instability induced upper limit to the transport current in a hard superconductor. In the case of a hard superconducting film, at reduced temperatures between t_2 and t_e (see Fig. 61), the transport current will first intercept the $I_c(t)$ phase boundary and the true critical current, $J_c \times A$ is measured. At reduced temperatures between t_1 and t_2, the transport current will first intercept the conditional phase boundary $I_Q(t)$. No transition will take place here, however, as the superconductor is still stable against flux jumps (i.e., $I_Q < I_{fj}$). When the transport current is raised to I_{fj}, a quenching flux jump will occur, as $I_{fj} > I_Q$ and an abrupt, rather than smooth increase in voltage will be measured at I_{fj}. In the region $t_1 \leq t \leq t_2$, the maximum transport current will follow the phase boundary of $I_{fj}(t)$ and <u>decrease</u> with decreasing temperature. At reduced temperatures below t_1, the transport current will first intercept the conditional $I_{fj}(t)$ phase boundary. The flux jump that will occur at this boundary is nonquenching as $I_{fj} < I_Q$. The sample will quench abruptly at the first flux jump beyond $I_Q(t)$. The upper limit to the transport current I_t at temperatures t_1 cannot be precisely defined to a single value at each temperature, but only to a <u>range,</u> $I_Q(t) \leq I_t \leq [I_Q(t) + I_{fj}(t)]$. The upper limit to transport current as a function of temperature is shown schematically by the band below t_1 and the heavy line between
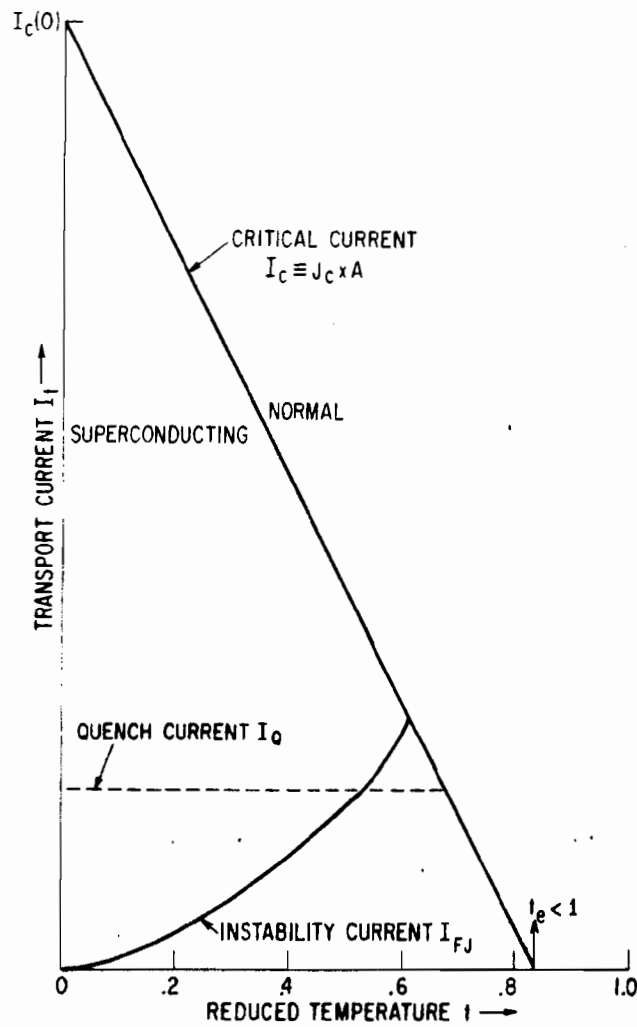
Figure 60 Typical phase boundaries for a hard superconducting film as a
function of reduced temperature of (1) the critical transport current, I_c,
(2) the quench transport current, I_Q, and (3) the instability or flux jump
transport current, I_{fj}.
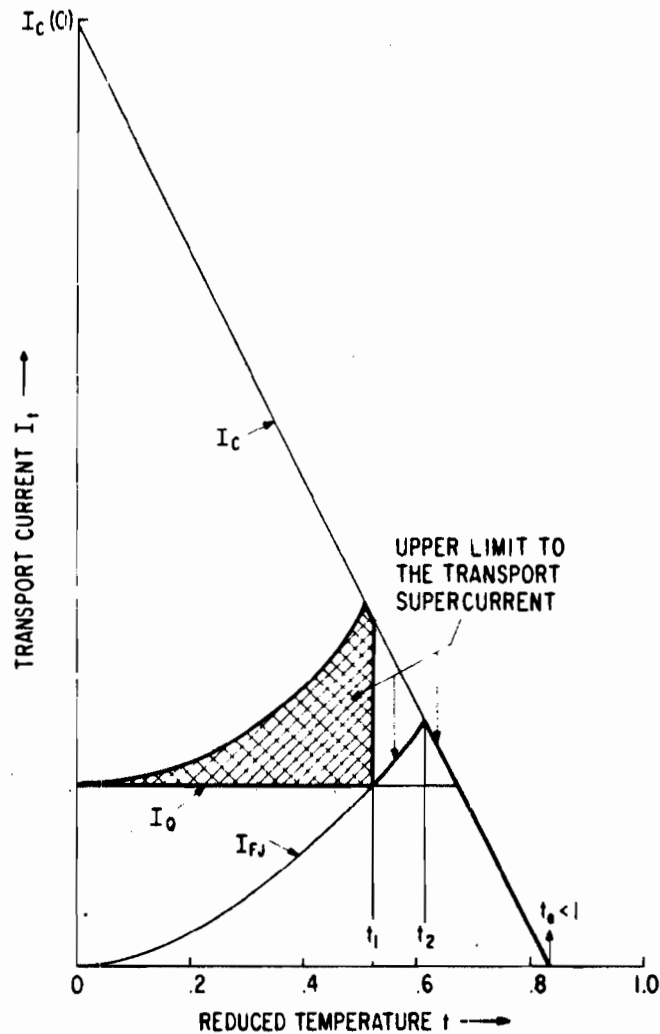
Figure 61 The dark boundary and the shaded area give the upper limit to the transport current in a hard superconducting film.

t_1 and t_e. The essential interesting feature of this boundary is that the limiting transport equals the true critical current only at high temperature; at intermediate reduced temperatures the limiting transport current decreases with decreasing temperature and becomes essentially independent of temperature at low reduced temperatures. For the case of the superconducting wire, I_{fj} does not intercept I_c. Typical phase boundaries are shown in Fig. 62. Here the heavy lines give the upper limit to the transport current.

In the sections to follow derivations of I_{fj} (t) and I_Q (t) are given for a ribbon and a wire. Experimental results for a niobium-oxygen film are also given and provide substantial agreement with the model.

129
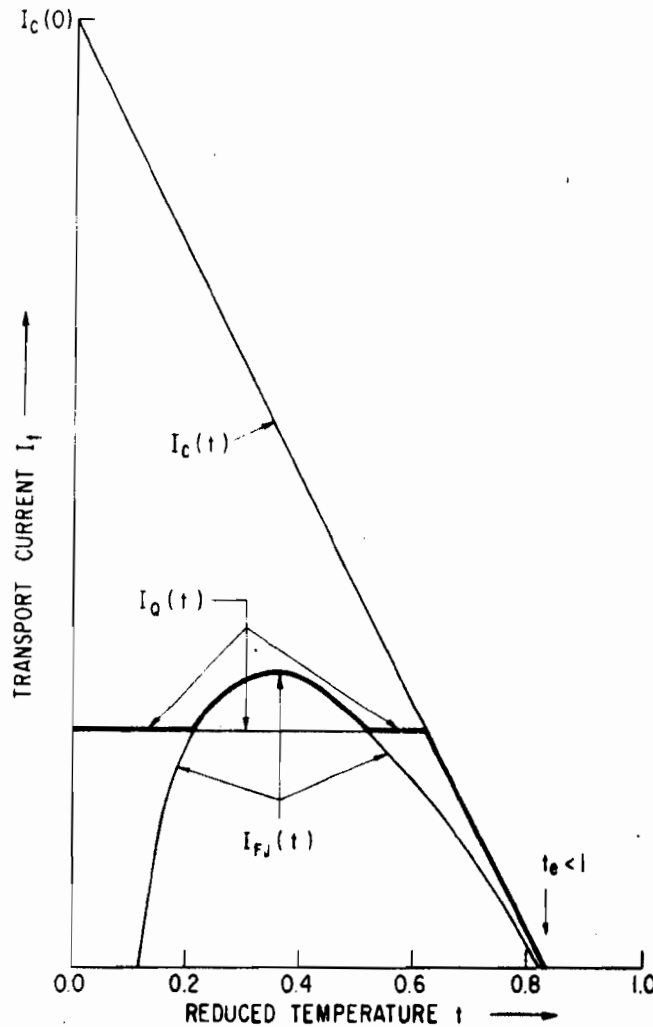
Figure 62 Typical phase boundaries for a hard superconducting wire as a function of reduced temperature of (1) the critical transport current, I_c, (2) the quench transport current, I_Q, and (3) the instability or flux jump transport current I_{fj}. The dark boundary is the predicted upper limit to the transport current.

2. Derivation of I_{fj}

(a) Wire

In the first section of this report, Swartz and Bean have derived a condition for when a hard superconductor exposed only to an increasing magnetic field will become unstable. They predict that when the difference H_0 between the applied field and the frozen-in field becomes equal to a critical value given by

$$H_{fj} = [-\pi^3 C J_c / (\partial J_c / \partial T)]^{1/2} \tag{110}$$

130

$\Delta\varphi/\Delta H$ becomes unbounded and a flux jump ensues. The problem of a hard superconductor supporting a transport current bears important analogies to the magnetic case treated in the previous report. Consider a hard super-conducting wire cooled in a magnetic field H. The wire is characterized by a critical current density $J_c(H, T)$ and a specific heat C. An applied transport current will flow first near the perimeter of the wire to its local critical value J_c. If no instability occurs, then as the transport current is increased, its depth of penetration δ increases until the entire cross section supports a critical current. The transport current I_t produces some self-field difference H_0 between the outer surface of the wire and the distance δ to which the transport current penetrates. Consider first the simple case where $I_t \ll I_C = J_c\pi R^2$. Under this condition, the expression

$$\frac{1}{r}\frac{\partial}{\partial r}(H \cdot r) = -\frac{4\pi J_c}{10} \tag{111}$$

that relates the field gradient and transport current in cylindrical coordinates reduces to the simple expression

$$\frac{\partial H}{\partial r} \approx -\frac{4\pi J_c}{10} \quad . \tag{112}$$

In general, the self-field H_0 at the surface of the superconducting wire is related to the transport current by $H_0 = I_t/5R_1$ where R_1 is the radius of the wire. For the condition that $I_t \ll I_C$, the derivation of the condition for which a transport current induced flux jump occurs (i.e., $\Delta\varphi/\Delta I$ becomes unbounded) is the same as the derivation for H_{fj} with the substitution only that $H_0 = I_t/5R_1$. This transport current I_{fj} is thus given as

$$I_{fj} = 5H_{fj}R_1 = 5R_1\left[\frac{-\pi^3 CJ_c}{(\partial J_c/\partial T)}\right]^{1/2} \quad . \tag{113}$$

It is necessary to calculate I_{fj} also for the general case, i.e., where the restriction that $I_t \ll I_C$ is relaxed. One can follow the approach of Swartz and Bean and set up the differential equations for the general case, but they are complicated and difficult to solve analytically. However, a simple, approximate derivation of I_{fj} is possible, as outlined below. We note first that the superconductor is characterized at each temperature by [see Eq. (109)]

$$\frac{\partial J_c}{\partial T} = -\frac{J_c(0)}{t_e T_c} \quad . \tag{114}$$

Equation (114) is valid everywhere within the superconductor and is independent of the magnetic state (i.e., the depth δ to which supercurrents flow). This expression tells us that any increase in temperature $\Delta T(X)$

131

(where X is measured from the surface) must be accompanied by a decrease in critical current density

$$\Delta J_c(X) = - \frac{\Delta T(X) J_c(0)}{t_e T_c} \quad .$$ (115)

Now if the transport current I_t is raised by ΔI_t, some magnetic flux $\Delta \varphi$ will cross each point in the superconductor to the depth $\delta + \Delta \delta (\Delta I_t)$ to which the supercurrent flows. If the increase in transport current takes place in a time short compared to that for thermal diffusion, then each point in the superconductor within a depth $\delta + \Delta \delta (\Delta I_t)$ of the surface will experience an increase in temperature given by

$$\Delta T(X) = \frac{10^{-1} J_c(T) \Delta \varphi (X)}{C(T)} \quad .$$ (116)

Combining Eqs. (109), (115), and (116) gives

$$\Delta \varphi (X) = - \frac{10 \, C \, (t_e T_c - T)}{J_c^2(T)} \, \Delta J_c(X) \quad .$$ (117)

Equation (117) provides a relationship between the decrease in local current density that the superconductor will allow as a function of the magnetic flux crossing that point. A second relationship between $\Delta J_c(X)$ and $\Delta \varphi (X)$ that depends on the transport current that flows must also be satisfied.

Consider a wire of radius R_1 carrying a transport current $I_t < J_c \pi R_1^2$ that has been cooled in some external magnetic field. An inner radius R_2 that is defined as the radius to which supercurrents flow is given as

$$R_2 = R_1 \left(1 - \frac{I_t}{I_c}\right)^{1/2} \quad .$$ (118)

If the transport current is increased by some small amount, additional magnetic flux will cross into the superconducting wire, resulting [see Eq. (117)] in some decrease, $-\Delta J_c$, of the local current density between R_1 and R_2. Since total current must be conserved, and the critical state model obeyed, any small decrease in the local current, $\Delta I(R_i) = -\Delta J_c \cdot 2\pi R_i dR_i$ where $R_2 < R_i < R_1$, will relocate at the position R_2. The amount of magnetic flux $[\Delta \varphi (R_0)]_i$ crossing any radius $R_2 < R_0 < R_1$ due to the relocation of any current $\Delta I(R_i)$ to R_2 where $R_i < R_0$ is given as

$$[\Delta \varphi (R_0)]_i = - \int_{R_2}^{R_1} \frac{\Delta I(R_i)}{5R} \, dR = - \frac{\Delta I(R_i)}{5} \ln \frac{R_i}{R_2} \quad .$$ (119)

132

Equations (123) and (124) differ only in that the result from the self-consistent calculation [Eq. (124)] gives an instability current about 10% larger than the approximate approach used to derive (123). The approximate approach can be brought to excellent agreement with (124) by assuming that the decrease, $-\Delta J_c$, in the current density brought about a small increase ΔI_t in the transport current is not constant, but is largest at the surface where the associated $\Delta \varphi$ is the largest, and decreases with distance from the surface according to

$$\Delta J_c(R_i) = \Delta J_c(R_1) \left[1 - \left(\frac{R_1 - R_i}{R_1 - R_2}\right)^2\right] . \qquad (125)$$

When the substitution

$$\Delta I(R_i) = 2\pi R_i dR_i \Delta J_c(R_1) \left[1 - \left(\frac{R_1 - R_i}{R_2 - R_1}\right)^2\right]$$

is made in evaluating the integral in Eq. (120), an expression may be derived for I_{fj} that contains a number of correction terms. In the limit of $I_t \ll I_c$ that expression agrees with Eq. (124) to about 1%. For our present purposes, however, we will keep the mathematics simple and treat Eq. (122) as if it were exact. From Eq. (122), I_{fj} at any field and temperature t_0 is the solution of the equation:

$$\frac{I_{fj}}{I_c(0)\left(1 - \frac{t_0}{t_e}\right)} + \ln\left[1 - \frac{I_{fj}}{I_c(0)\left(1 - \frac{t_0}{t_e}\right)}\right] + \left[\frac{I_m^2}{I_c^2(0)}\right]\frac{t_e t_0^3}{\left(1 - \frac{t_0}{t_e}\right)} = 0 \qquad (126)$$

where $C \equiv \gamma T^3$ and I_m^2 may be regarded as a scaling factor defined equal to $100\, \gamma T_c^4 \pi R_1^2$. From (126) it can easily be seen that $I_{fj} < I_c$ at all temperatures since the logarithmic term $\to \infty$ as $I_{fj}(t_0) \to I_c(t_0)$. In Fig. 63 we plot $I_{fj}(t)$ vs t for various values of $I_c(0)/I_m$ with an assumed value of $t_e = 1$.

(b) Film

The derivation of I_{fj} for a film is very much the same as the calculation for the wire. We calculate the increase in flux $\Delta \varphi$ that crosses the edges of the ribbon per decrease $-\Delta J_c$ in critical current density. When the coefficient of $-\Delta J_c$ equals that of Eq. (117), an instability condition is reached.

The transport current I_t applied to a film characterized by a bulk current density J_c will flow first near the edges up to the local critical value J_c. The boundary that separates the region between zero and critical current flow is shown schematically in Fig. 64(a). In the derivation below we shall simplify the problem somewhat by assuming that the value of the local critical current

133

The total magnetic flux crossing R_0 due to the relocation of the current at all radii $R_i < R_0$ is given by

$$\Delta\varphi(R_0) = -\int_{R_2}^{R_0} \frac{\Delta I(R_i)}{5} \ln\left(\frac{R_i}{R_2}\right) = \frac{2\pi\Delta J_c}{5} \int_{R_2}^{R_0} R_i \ln\left(\frac{R_i}{R_2}\right) d R_i$$

$$= \frac{2\pi\Delta J_c}{10} \left[R_0^2 \ln \frac{R_0}{R_2} - \frac{1}{2} (R_0^2 - R_2^2) \right] \tag{120}$$

and, from Eqs. (118) and (120),

$$\Delta\varphi(R_1) = \frac{\pi R_1^2}{10} \left[\frac{I_t}{I_c} + \ln\left(1 - \frac{I_t}{I_c}\right) \right] \Delta J_c . \tag{121}$$

Equation (121) provides the second relationship between the change in critical current density and the change in flux crossing any point in the system; unlike Eq. (117), Eq. (121) depends on the magnitude of the transport current that flows. When

$$- \left\{ \frac{I_t}{I_c(T)} + \ln\left[1 - \frac{I_t}{I_c(T)} \right] \right\} > \frac{100 \, C \, (t_e T_c - T)}{J_c^2 \, (T)\pi \, R_1^2} \tag{122}$$

condition (117) can no longer be satisfied, and a condition for instability is defined. The critical current will continue to decrease and magnetic flux will continue to flow into the surface, i.e., a flux jump will occur and I_t is then identified as I_{fj}. It is interesting to compare (122) with (113) in the limit where $I_t \ll I_c$. Here (122) reduces to

$$\frac{I_{fj}}{I_c} = \left[\frac{200 \, C \, (t_e T_c - T)}{J_c^2 \, (T)\pi \, R_1^2} \right]^{1/2}$$

or
$$\tag{123}$$

$$I_{fj} = [200 \, C \, (t_e T_c - T) \, \pi \, R_1^2]^{1/2}$$

while from (113) and (109)

$$I_{fj} = [25\pi^2 \, C \, (t_e T_c - T)\pi R_1^2]^{1/2} . \tag{124}$$

134

Figure 63 The calculated instability current I_{fj} (t) and the critical current I_c(t) for a hard superconducting wire as a function of I_c(0) and reduced temperature.
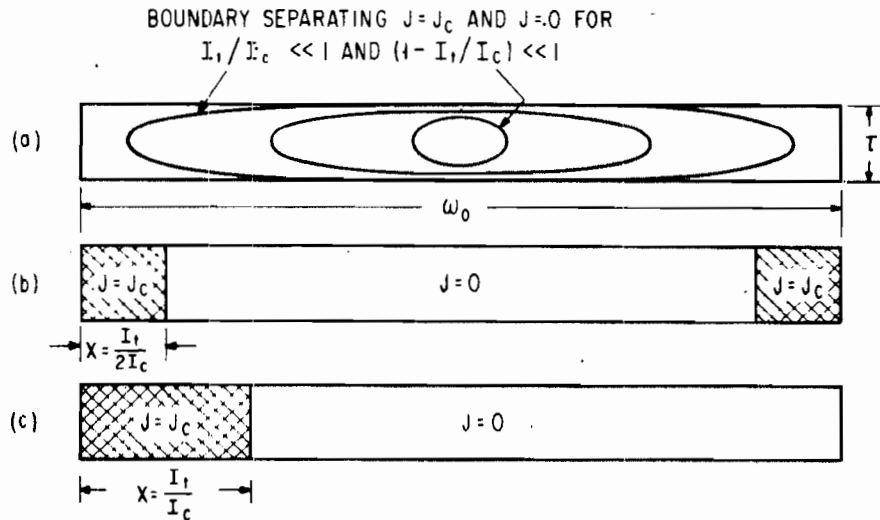
Figure 64 (a) A schematic diagram for a hard superconducting film of the boundary separating the region of $J = J_c$ and $J = 0$ in the presence of various transport currents; (b) distribution of transport currents assumed for calculation purposes; and (c) an assumed distribution of transport currents used for calculating the conditions necessary for a quenching flux jump.

135

density is J_c to within a distance $X_0 = I_t/2J_c\tau$ of each edge (τ is the film thickness) and zero otherwise [see Fig. 64(b)]. This simplification will introduce but a small error in the result when the film width $W_0 \gg \tau$. Following the derivation for the wire, we calculate first the magnetic flux $[\Delta\varphi(\pm W_0/2)]_i$ crossing $\pm W_0/2$ when the current flowing at $x = x_i$ and $x = W_0 - x_i$ is decreased by $(\Delta J_c)(\Delta x_i)$ and moves to the positions $X = I_t/2J_c\tau$ and $X = W_0 - I_t/2J_c\tau$ respectively:

$$\Delta\varphi(\pm W_0/2) = -\frac{\Delta I}{5}\left(\int_{x_i}^{x_0}\frac{dx}{x} + \int_{W_0-x_i}^{W_0-x_0}\frac{dx}{x}\right)$$

$$= -\frac{\Delta I}{5}\left[\ln(x_0/x_i) + \ln\left(\frac{W_0-x_0}{W_0-x_i}\right)\right] \quad . \tag{127}$$

The total change in magnetic flux $\Delta\varphi(\pm W_0/2)$ associated with the decrease in current density $-\Delta J_c$ of all elements $x_i < x_0$ by the addition of a current $\Delta I = x_0\Delta J_C$ at $x = x_0$ and $x = W_0 - x_0$ is given by

$$\Delta\varphi(\pm W_0/2) = -\frac{\tau\Delta J_c}{5}\left\{\int_{\tau/2}^{x_0}\left(\ln\frac{x_0}{x_i}\right)dx_i + \int_{W_0}^{W_0-x_0}\left[\ln\left(\frac{W_0-x_0}{W_0-x_i}\right)\right]dx_i\right\}$$

$$= -\frac{I_t(t)}{10J_c(t)}\left\{2 + \frac{2I_c(t)}{I_t(t)}\ln\left[1 - \frac{I_t(t)}{2I_c(t)}\right]\right\}\Delta J_c \quad . \tag{128}$$

As before I_{fj} is then defined for the film as the solution to the equation

$$I_{fj}(t_0)\left\{2 + \frac{2I_c(t_0)}{I(t_0)}\ln\left[1 - \frac{I_{fj}(t_0)}{2I_c(t_0)}\right]\right\} - \frac{I_m^2}{I_c(0)}\cdot t_e t_0^3 = 0 \tag{129}$$

and, as before, $I_m^2 \equiv 100\,\gamma T_C^4 \times$ cross-sectional area $= 100\,\gamma T_C^4 W_0\tau$. In the limit where $I_{fj}(t) \ll I_c(t)$ [at low t and $I_m \ll I_c(0)$], then (129) leads to the interesting result that I_{fj} increases with the cube of the temperature and is inversely proportional to the critical current, $I_c(0)$. From (21), $I_{fj}(t_0)$ becomes equal to $I_c(t_0)$ when

$$I_c(t_0) = I_m\left[\frac{t_0^3(t_e-t_0)}{0.614}\right]^{1/2} \quad . \tag{130}$$

Equation (130) represents the largest possible value of the "true" critical current at any temperature t_0 without first having encountered a flux jump.

136

It is noteworthy that Eq. (130) scales with the square root rather than the first power of the cross-sectional area. It should be pointed out that Eq. (130) is the locus of the points where $I_{fj}(t) = I_c(t)$. It does not represent the largest possible value of the measured transport current at some temperature t. For instance, when $I_c(0) \gg I_m$, the maximum value of the transport current at low temperature is I_Q which, as we shall see in the following section, is much greater than the values given by Eq. (130). In Fig. 65 we plot $I_{fj}(t)$ vs t for various values of $I_c(0)/I_m$ for the film. In Fig. 66 we plot Eq. (130) for $t_e = 1$.

As pointed out in the introduction, I_{fj} does not necessarily represent the value of the transport current at which a quench occurs, but is the value of the transport current at which the first flux jump or instability occurs. The derivation of the quench current I_Q follows in the next section.
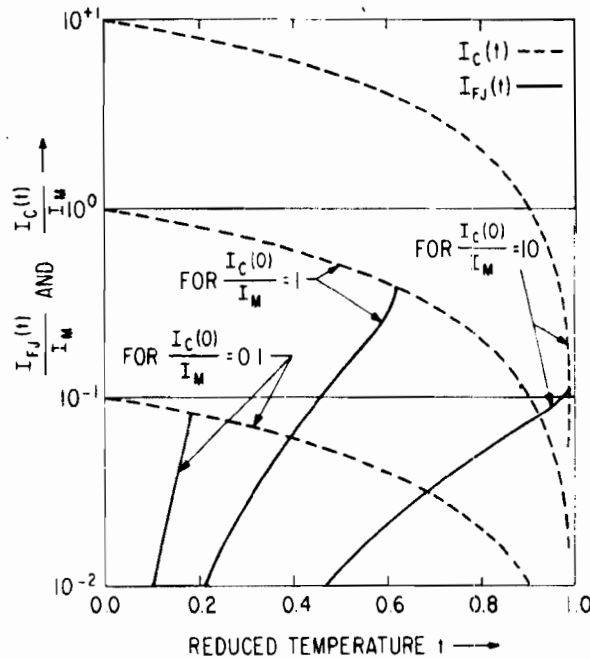
Figure 65 The calculated instability current $I_{fj}(t)$ and the critical current $I_c(t)$ for a hard superconducting film as a function of $I_c(0)$ and reduced temperature.

137
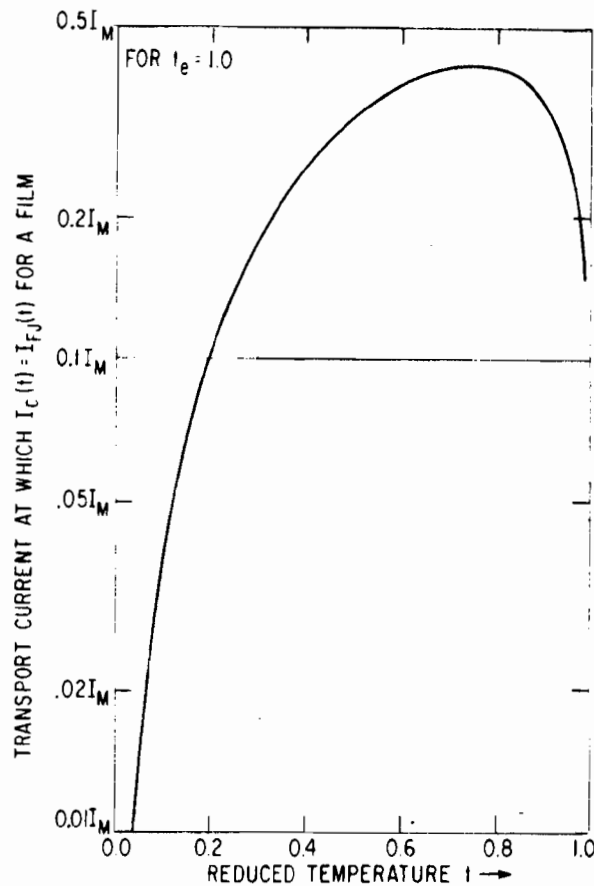
Figure 66   The calculated locus of the transport currents at which $I_c(t) = I_{fj}(t)$ as a function of reduced temperature.

3.   Derivation of the Quench Current I_Q

(a)   General Remarks

In this section we derive a condition where, if an instability occurs, sufficient heat will be developed to quench the wire. We designate the lowest possible transport current for which this condition is met as I_Q. A self-consistent derivation of I_Q involves the question of how far an instability proceeds before a stable flux configuration within the sample is again achieved. Consider a superconducting sample supporting a transport current $I_t < I_c$ that is in the critical state (i.e., the local current density $= J_c$ everywhere that the transport current flows). When a flux jump occurs, flux will continue to flow into the sample until a spatial current distribution is attained such that (1) the local current density $J_c(t)$ at each position is consistent with the local temperature rise proportional to the flux φ that has crossed that point, and (2) total current is conserved. This calculation is not trivial and is being set up on the computer at the present time. Within this framework the quench current I_Q will be defined as that current for which the first stable flux configuration following an instability brings the leading edge of that flux front to the depth to which the transport currents on the opposite side of the superconductor are flowing. Since the results of this

138

calculation are not yet available, we shall instead develop an approximate method for calculating I_Q.

(b) Wire

Consider a wire of type II superconductor in the critical state at temperature t_0 and supporting a transport current I_t that has become unstable. Let us assume that the total current is maintained constant as flux rushes into the sample and a transient voltage is measured. (Constant current can be maintained by having a large reactance in series with the superconductor.) During the flux jump, the transport current moves from the periphery toward the center of the wire. If sufficient driving energy is available to drive the current to a position where the moving flux fronts meet and current flows at the center of the wire, then the wire will enter a resistive state, i.e., a quench will occur. We can determine I_Q approximately by calculating the heat dissipated when the transport current is brought from an initial critical state where the current flows near the periphery at its local critical value $J_C(t_0)$ to a second state in which the current flows uniformly within a cylinder at the center of the wire of radius

$$R_1 \left[\frac{I_c}{I_c(t_0)} \right]^{1/2} .$$

If the total heat dissipated is sufficient to bring the superconductor to a temperature t_u where $I_c(t_u) = I_t(t_0)$, then the flux fronts indeed have enough driving energy to meet at a center of the wire and a quench will result. Stratton[73] has shown that for such a redistribution of currents the work done on the system splits evenly between the increase in stored magnetic energy and the heat dissipated. Since the field is unchanged for $R > R_1$, the increase in stored energy ΔE is calculated according to

$$\Delta E = \frac{1}{8\pi} \int_0^{R_1} \frac{2\pi R[H_2^2(R) - H_1^2(R)]}{\pi R_1^2} \, dR \tag{131}$$

where the subscripts 2 and 1 refer, respectively, to the total magnetic field in the assumed states after and before the flux jump. It can be shown that the cross terms in H^2 cancel and that (131) reduces to

$$\Delta E = \frac{1}{4\pi R_1^2} \int_0^{R_1} [\Delta H^2(R)]_{1 \to 2} \, dR \tag{132}$$

where $\Delta H^2(R)$ is the square of the change in self-field of the transport current. Equation (132) leads to the result that the total heat dissipated $\Delta Q = \Delta E$ is

$$\Delta Q = \frac{I_t^2(t_0)}{100\pi R_1^2} \left[\ln \left[\frac{I_t(t_0)}{I_c(t_0)} \right] + \right.$$

$$\left. + \left[\frac{I_c(t_0)}{I_t(t_0)} - 1 \right] \left(1 + \left[\frac{I_c(t_0)}{I_t(t_0)} - 1 \right] \left\{ \ln \left[1 - \frac{I_t(t_0)}{I_c(t_0)} \right] \right\} \right) \right]. \tag{133}$$

The temperature t_u to which the superconductor will rise with a heat input ΔQ is given as

$$\Delta Q = \int_{T_0}^{T_u} CdT = \frac{\gamma}{4} (T_u^4 - T_0^4) . \tag{134}$$

If we assume that a quench will occur when $I_t(t_0) = I_c(t_u)$ and $I_c(t) = I_c(0)$ $[1 - (t/t_e)]$, then (133) and (134) yield an expression for the quench current I_Q as the solution to the equation

$$I_Q^2(t_0) \left[-\ln \left[\frac{I_Q(t_0)}{I_c(0)(1-t_0/t_e)} \right] + \left[\frac{I_c(0)(1-t_0/t_e)}{I_Q(t_0)} - 1 \right] \left(1 + \left[\frac{I_c(0)(1-t_0/t_e)}{I_Q(t)} - 1 \right] \times \right. \right.$$

$$\left. \left. \left\{ \ln \left[1 - \frac{I_Q(t_0)}{I_c(0)(1-t_0/t_e)} \right] \right\} \right) \right] - \frac{I_m^2}{2} \left\{ t_e^4 \left[1 - \frac{I_Q(t_0)}{I_c(0)} \right]^4 - t_0^4 \right\} = 0 . \tag{135}$$

The computer solutions for I_Q show that I_Q is essentially independent of temperature for a given $I_c(0)$. See Fig. 67. The dependence of $I_Q(0)$ on $I_c(0)$ is shown in Fig. 68.

We can summarize the results of Eqs. (126) and (135) in Fig. 69. This figure applies, to the limits of the various approximations, to all hard superconducting wires. It predicts, as a function of the specific heat, $I_c(0)$, and the wire radius, the temperature below which the maximum transport current will become instability limited. Within the I_Q phase space the maximum transport current is given by the solution of Eq. (135) and is essentially temperature independent. Within the I_{fi} phase space the maximum transport current is given by the solution of Eq. (126).

(c) Film

The approach for calculating the total heat dissipated in a film during a flux jump is the same as that used for the wire. The initial current
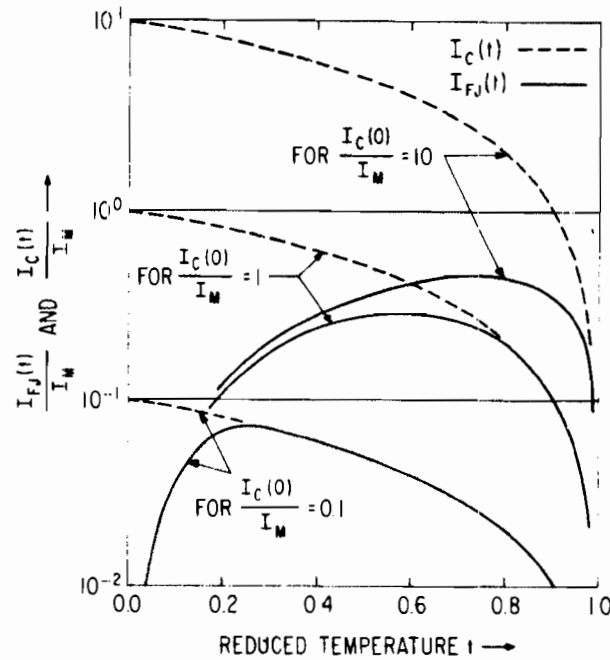
140
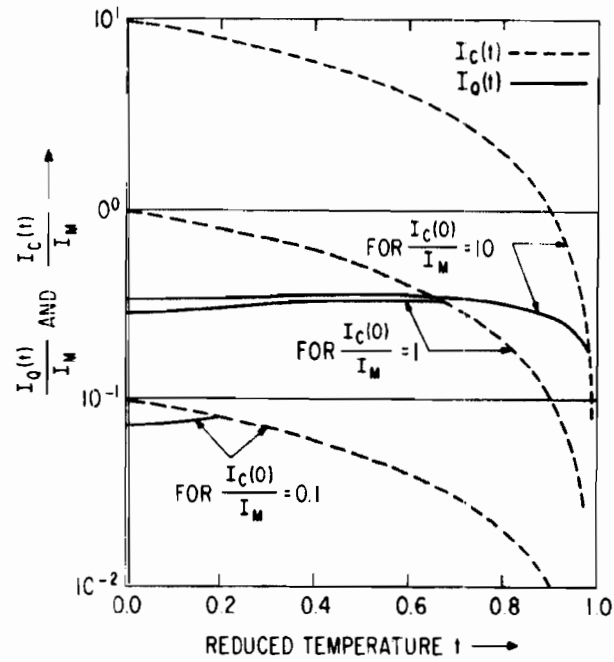
Figure 67   The calculated quench current $I_Q(t)$ and the critical current $I_c(t)$ for either a hard superconducting wire or film as a function of $I_c(0)$ and reduced temperature.
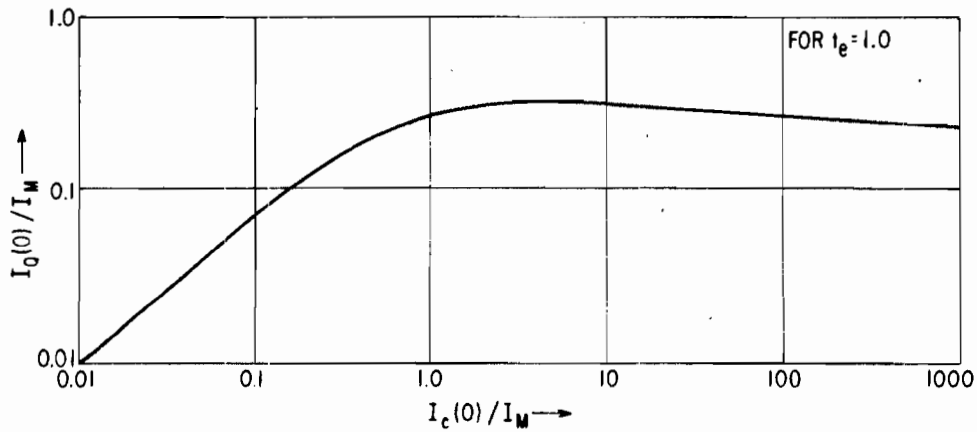

Figure 68   The calculated quench current I_Q at zero temperature as a function of the critical current at zero temperature for either a hard superconducting wire or film.

141
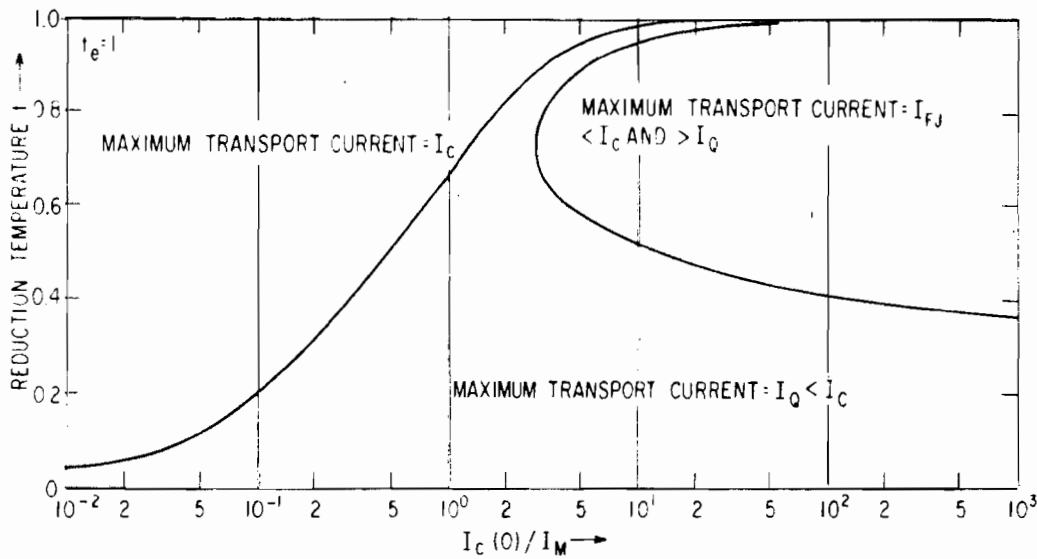
Figure 69 A summary diagram of the regions where (1) the critical current, I_c, (2) the quench current, I_Q, and (3) the instability current I_{fj} determine the maximum transport current that can be carried by a hard superconducting wire.

distribution is that shown in Fig. 64(b) and the final current distribution, for calculation purposes, is shown in Fig. 64(c). Stratton[73] shows that the change in magnetic energy of the total system when the currents are redistributed is given by

$$\Delta E = \frac{1}{2} \sum_{i=1}^{n} I_i \Delta \varphi_i \tag{136}$$

where $\Delta \varphi_i$ is the change in flux threading circuit i due to the other n-1 circuits. Equation (136) is less cumbersome than Eq. (132) where, for a film, the change in the field squared must be integrated over all space. Equations (136) and (134) lead to the following defining equation for the quench current $I_Q(t)$ in a film

$$I_Q^2(t_0) \left\{ \left[-\frac{1}{2} \ln \left(\frac{2I_Q(t_0)}{I_c(0)(1-t_0/t_e)} \right) \right] - 2 \left[\frac{I_c(0)(1-t_0/t_e)}{I_Q(t_0)} - \frac{1}{2} \right]^2 \ln \left| 1 - \frac{I_Q(t_0)}{2I_c(0)(1-t_0/t_e)} \right| + \right.$$

$$\left. + \left[\frac{I_c(0)(1-t_0/t_e)}{I_Q(t)} - 1 \right]^2 \ln \left[1 - \frac{I_Q(t_0)}{I_c(0)(1-t_0/t_e)} \right] \right\} - \frac{I_m^2}{4} t_e^4 \left[1 - \frac{I_Q(t_0)}{I_c(0)} \right]^4 - t_0^4 = 0. \tag{137}$$

The computer solutions of Eq. (137) are equal to within 2% those of Eq. (135). Thus Figs. 67 and 68, which are solutions of Eq. (135), may also be regarded

142

as the solutions of Eq. (137). Temperature ranges at which the maximum transport current follows I_c decreases with decreasing temperature, and becomes temperature independent is given in Fig. 69. The finding that the solutions for I_Q are virtually identical, when scaled to I_m for cross sections as different as those of a wire and a film, suggests that these solutions are valid for any ellipsoidal cross section. The summarizing plot of the predicted phase boundary of all planar, unshielded, hard superconducting films is given in Fig. 70.
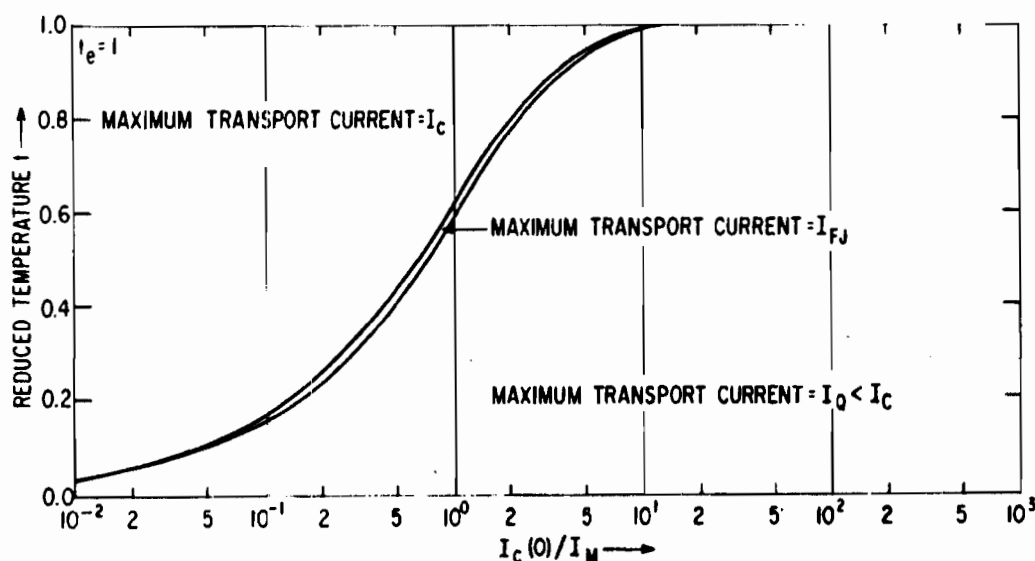
Figure 70 A summary diagram of the regions where (1) the critical current I_c, (2) the quench current, I_Q, and (3) the instability current I_{fj} determine the maximum transport current that can be carried by a hard superconducting film.

4. Experimental Measurements and Discussion

Measurements of the critical current of a number of niobium-oxygen films (0.050 inch by $\sim 1\mu$) evaporated at various azimuthal angles (see Fig. 71) has been carried out as a function of magnetic field, orientation of the magnetic field relative to the surface plane, and temperature. The films were made by J. R. Rairden, M. A. Cocca, and J. Furey by the techniques described in Ref. 74. H_{c2} for the films reported below was determined from critical current measurements to be ~ 15 kOe (results not displayed).

In Fig. 72 is displayed the critical current I_c at 4.2°K vs azimuthal angle φ that a magnetic field of 8000 Oe makes with the surface plane for three niobium films evaporated simultaneously at the azimuthal angles of 78°, 86°, and 90°. The critical current goes through a sharp local maximum when the applied magnetic field is aligned parallel to the surface plane ($\varphi = 0°$).

143
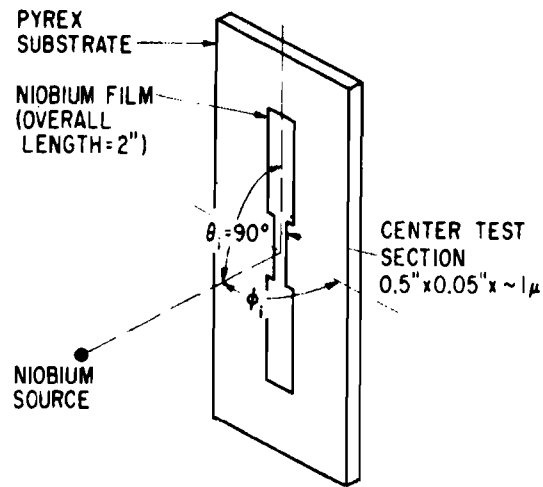
Figure 71 A schematic of the evaporation of the niobium-oxygen films.
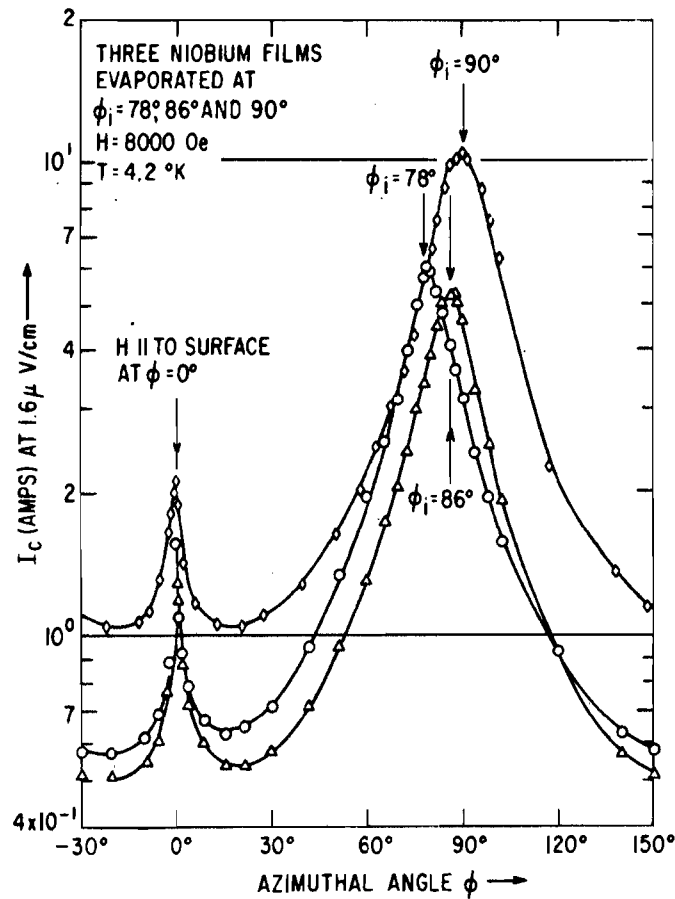
Figure 72 The critical transport current as a function of azimuthal angle of
three different niobium-oxygen films. The critical current peaks when the
magnetic field vector (8000 Oe) is either aligned parallel to the surface
($\varphi = 0°$) or coincident with the evaporation angle, I_i.

144

Following the work of Swartz and Hart[75] (see Appendix A), these maxima are taken as further evidence that the surface of a type II superconductor can support a superconducting transport current in the mixed state if the magnetic field is aligned parallel to the surface plane.

The second interesting feature of these results is the maximum in critical current that occurs when the magnetic field is coincident with the direction of the bombarding niobium atoms during the evaporation. These currents are most likely bulk, rather than surface, currents. The surfaces of the niobium films were carefully examined for any surface structure or protrusions that could be associated with the incident angle of the bombarding niobium atoms. Examination both under the optical microscope and of replicas of the surface under the electron microscope showed none. X-ray diffraction patterns (which average over the bulk of the film) and electron diffraction patterns (which average only to a few angstroms depth below the surface) showed no preferred crystalline orientation within the film. In view of these negative results, we can only speculate about the origin of this "angle of incidence" effect. Although the individual crystallites are randomly oriented, they may tend to grow antiparallel to the incident direction of the bombarding atoms. If this is so, the grain boundaries, or subgrain boundaries, separating the crystallites may take the form of cylindrical surfaces aligned parallel to the incident direction. Such boundaries have a two-dimensional character and disturb the lattice over a few atomic spacings; thus they may be effective as pinning sites that give rise to the large observed supercurrents when the magnetic field direction is coincident with the bombarding niobium atoms.

The "angle of incidence" effect may be rather general to superconducting films made by evaporation. I have observed the same effect, but of smaller magnitude, in evaporated Pb and Pb-Tl films.

The transition to the normal state of the data points in Fig. 72 was always smooth; the first appearance of voltage was exponential with current, but became linear with current at a few microvolts. As the magnetic field was lowered, leading to larger critical currents, the maximum measured values of the transport current never exceeded a value of about 13 to 15 amperes (depending on the film). Further, when the extrapolated critical current exceeded this maximum level (see Fig. 73), the measured transport currents (1) exhibited training, (2) were defined by an abrupt transition from zero voltage to several millivolts, and (3) were fully trained on the second trial. The fully trained values (those plotted in Fig. 73) bore an inverse relationship to the expected or extrapolated critical current; the larger I_c in excess of 13 to 15 amperes, the smaller was the measured fully trained current. Each of these observations is consistent with the model proposed in the earlier sections. From Eq. (130) we can calculate a predicted upper limit to the transport current without adjustable parameters. To calculate I_m we assume $T_c = 9.0°K$, [74] $W_0 = 0.125$ cm, $\tau = 10^{-4}$ cm, $\gamma_{Nb}(4.2°K) = 0.98 \times 10^{-4}$ cal/deg-mole, [76] yielding a value for I_m of 56.5 amperes. t_e is independently
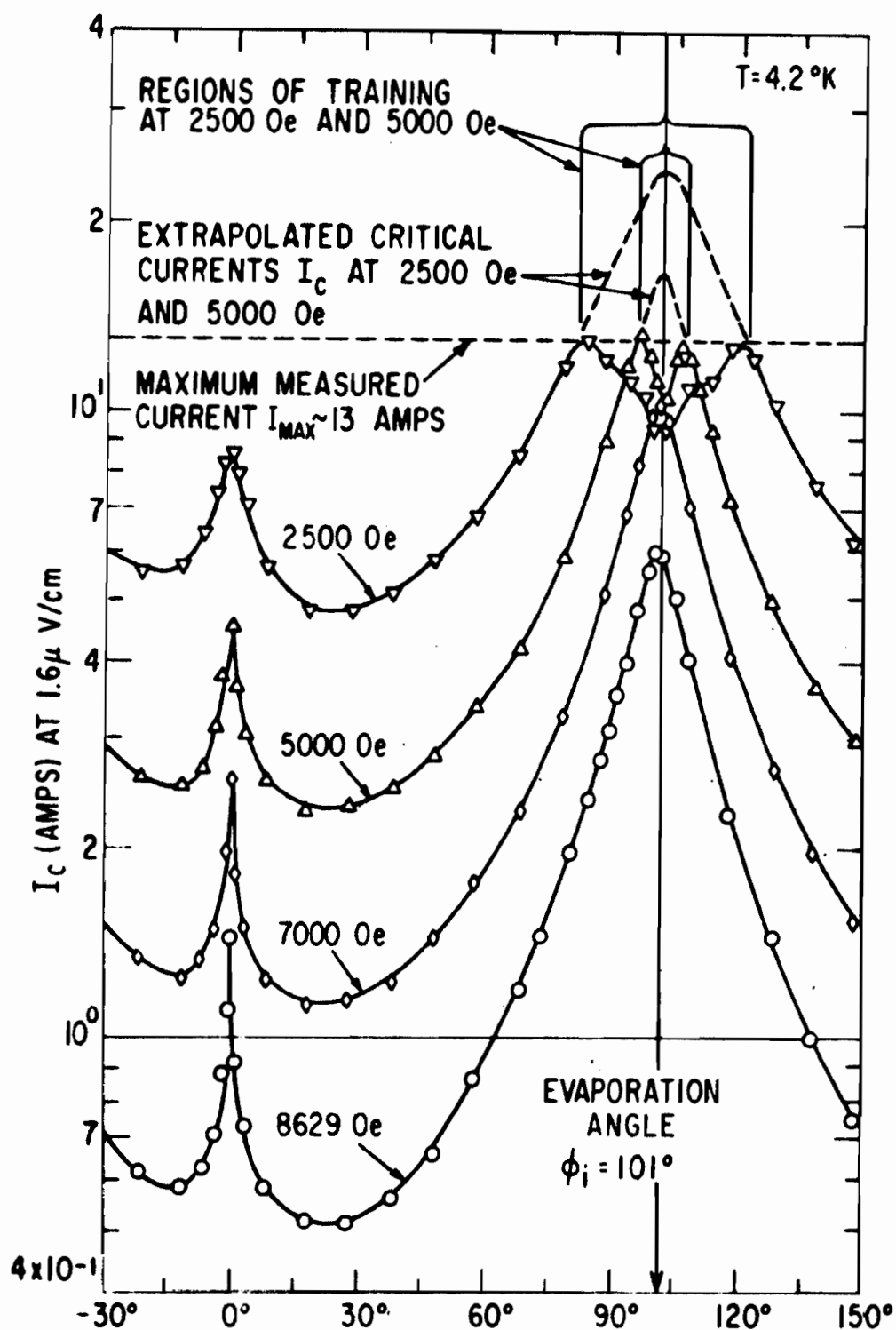
Figure 73 Critical current as a function of azimuthal angle of a niobium-oxygen film evaporated at $\varphi_i = 101°$. In the region where training is observed the fully trained current is less than the extrapolated critical current. The maximum transport current that could be measured at any field never exceeded 13 amperes.

146

determined from measurements of the critical current (defined when the current-voltage transition is smooth) as a function of temperature to be ~ 0.7 and at $4.2°K$, $t_0 = 0.467$. The upper limit to the current-carrying capacity of these films at $4.2°K$ [i.e., where $I_{fj}(4.2°K) = I_c(4.2°K)$] should, according to Eq. (130), be about 11.0 amperes. This predicted value is in good agreement with the experimentally determined values of 13 to 15 amperes. The change from smooth to abrupt voltage transitions is also consistent with the model.

The observation that the experimentally measured maximum transport current bears an inverse relationship to the critical current when the critical current is in excess of 13 amperes is also consistent with Eq. (129). For $I_{fj}(t_0)/I_c(t_0) \approx 1$ in Eq. (129) yields

$$I_{fj}(t_0) = \frac{1}{I_c(t_0)}\left[\frac{I_m^2 t_0^3 (t_e - t_0)}{0.614}\right] \quad . \tag{138}$$

In terms of the model developed here, the training is not difficult to understand. Each time a new field and/or angle is set, supercurrents of opposite signs are induced to flow near the edges of the film up to the local critical value J_c that shields the interior from the changing fields. A subsequently applied transport current will add to the already flowing supercurrents at one edge and will subtract at the opposite edge. At the edge where the currents add, a quenching flux jump will occur when the applied transport currents and the initially present transport current sum to I_{fj} (or to I_Q, depending on the temperature). Thus the first measured value of the current at which the abrupt transition takes place will be less than that measured on the second and subsequent trials, since the prior quench destroys the transport currents induced initially by the changed setting.

Equation (130) predicts that the maximum measured transport currents should decrease with decreasing temperature below $3t_e/4 = \sim 4.7°K$. An experimental test of this point is shown in Fig. 74 for a film that showed a maximum current at $4.2°K$ of ~ 15 amperes. As this figure shows, the maximum current I_{max} decreases as the temperature is lowered. Below about $2.3°K$ ($t < \sim 0.25$), (1) the transition is abrupt at all angles and at all fields up to the highest field tested (8355 Oe), (2) the values of the critical current at each angle and field setting become essentially temperature independent (see curves labeled "$1.7°K$" and "$2.1°K$" in Fig. 74), and (3) the maximum value of the critical current varied more slowly with angle and field than at high temperatures where the true critical current I_c was measured. According to the model developed in the earlier sections, at low temperatures $I_{fj} < I_Q$, and the measured maximum values of the transport current equal I_Q and are essentially temperature independent, as observed. The numerical agreement without adjustable parameters is also good.

147
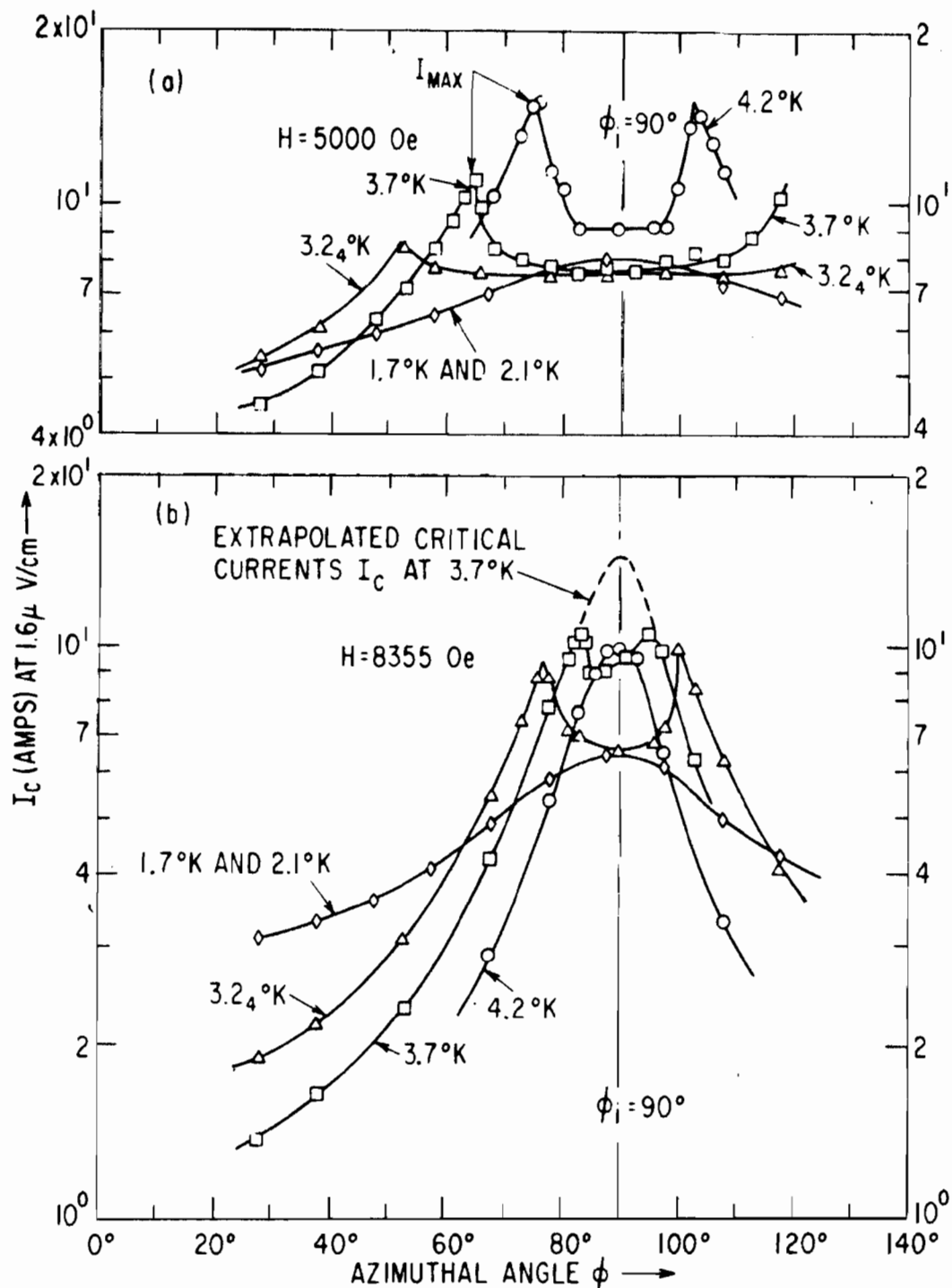
Figure 74 The critical current as a function of angle φ, temperature, and field [H = 5000 Oe in (a) and 8355 Oe in (b)] of a niobium-oxygen film evaporated at φ_i = 90°. The results are in agreement with the proposed model that, if instabilities exist, the maximum measured transport current (I_{max} on diagram) decreases with decreasing temperature to some low temperature at which the measured transport current becomes temperature independent.

When we extrapolate the critical current at high temperatures to zero temperature to obtain $I_c(0)$ as a function of angle and field and solve Eq. (137), values for I_Q as a function of angle and field agree with the experimental measurements to within about +15%.

5. Summary

In this report we have introduced the concepts of real $[I_c(t)]$ and conditional $[I_{fj}(t)$ and $I_Q(t)]$ phase boundaries in the transport current-reduced temperature phase space. We have also presented approximate derivations of these phase boundaries which are found to be a function of the "true" critical current, $I_c(t) = J_c(t) \times A$, and the size and specific heat of the superconductor. The conditional phase boundary $I_Q(t)$ scaled to I_m is probably the same for a hard superconductor of any ellipsoidal cross section, as the calculated results for a circular cross section and a film agree to 2%. The conditional phase boundary $I_{fj}(t)$ seems to be very sensitive to the ratio of the major and minor axes as the results of a circular wire and a film are very different. A universal phase diagram each for a hard superconducting circular wire and film are given in Figs. 69 and 70. An experimental test of the various predictions using a hard niobium-oxygen film demonstrates rather remarkable agreement in spite of the approximations used in the derivations. Independently reported results of Mercereau and Crane[77] also are in excellent agreement with the model developed here.

Journal publication will be sought shortly, when certain refinements of the derivations and further extension to the degradation of solenoids are completed. Further experimental work in this area will continue.

149

SECTION VII

SURFACE BARRIER TO FLUX PENETRATION

Experimental observations of magnetic hysteresis apparently associated with the specimen surface[78] led us to consider the possibility that an ideal surface presents a barrier to the penetration and expulsion of flux threads. The resulting theoretical[79] and confirmatory experimental[80] work are outlined below. This concept has already stimulated other theoretical[34, 36] and experimental[33, 81] papers. An effective surface barrier to flux thread penetration may also eventually have practical consequences in reducing a-c losses, since losses are known to increase substantially once flux threads penetrate and the specimen enters the mixed state.

A. THEORY (C. P. Bean and J. D. Livingston)

We present here an elementary treatment of the interaction between a flux thread and the specimen surface.

Consider a semi-infinite type II superconductor with a flux thread within it lying parallel to the single plane surface. There are two separate forces which the flux thread feels near the surface.

1. Image Force

The necessary boundary condition of zero current normal to the surface is satisfied by adding an image flux thread of opposite sign, outside the surface [Fig. 75(a)] There is thus an _attractive_ force to the surface, and the energy E per unit length of the flux thread increases with x, the distance from the surface, as shown in Fig. 76 for H = 0. From the interaction energy between two flux threads,[1] for $x \gg \xi$ and $\lambda \gg \xi$, $E(x) = \epsilon - (\varphi_0/4\pi\lambda)^2 K_0(2x/\lambda)$. Here ξ is the coherence length; λ is the penetration depth; ϵ is the energy per unit length of a single flux thread far from the surface and is approximately[56] equal to $(\varphi_0/4\pi\lambda)^2 \log(\lambda/\xi)$; φ_0 is the flux quantum; and K_0 is a modified Bessel function of the second kind. For $x \gg \xi$, the image term in E(x) vanishes as $e^{-2x/\lambda}$. For $x \approx \xi$, E(x) must be altered so that E goes smoothly to zero as $x \to 0$ rather than going to $-\infty$ with K_0.

2. External Field

An external field H penetrates into the superconductor [Fig. 75(b)] as $H^{-x/\lambda}$. If this field is of the same sign as the fields of the flux thread, this produces a _repulsive_ force from the surface, and a contribution to E(x) of $(\varphi_0 H e^{-x/\lambda})/4\pi$. This interaction energy is obtained by straightforward integration of the total energy of the superposed fields and currents of the flux thread and the surface layer. Note that for any nonzero H, this term will eventually dominate the image contribution to E(x) for $x \gg \lambda$.
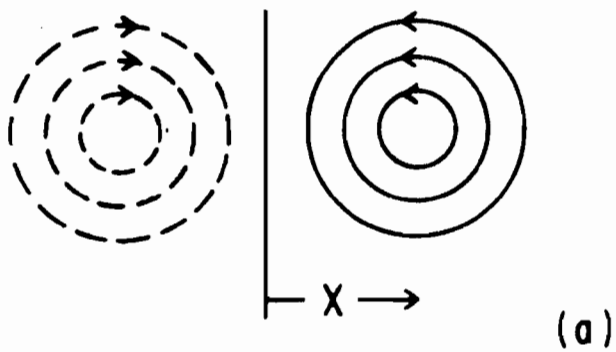
IMAGE FORCE
ATTRACTIVE

(a)
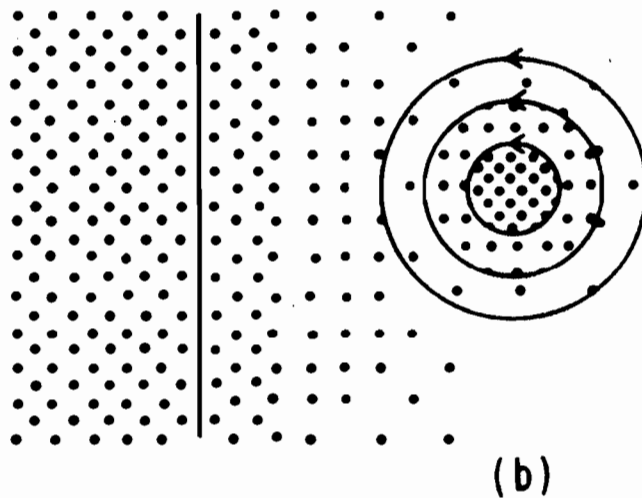
INTERACTION WITH
SURFACE FIELDS
REPULSIVE

(b)

Figure 75 Schematic representation of the forces on a flux thread near a
specimen surface: (a) attractive force produced by an "image" flux thread
of opposite sign; (b) repulsive force from interaction with the surface
fields (density of dots represents density of local field).
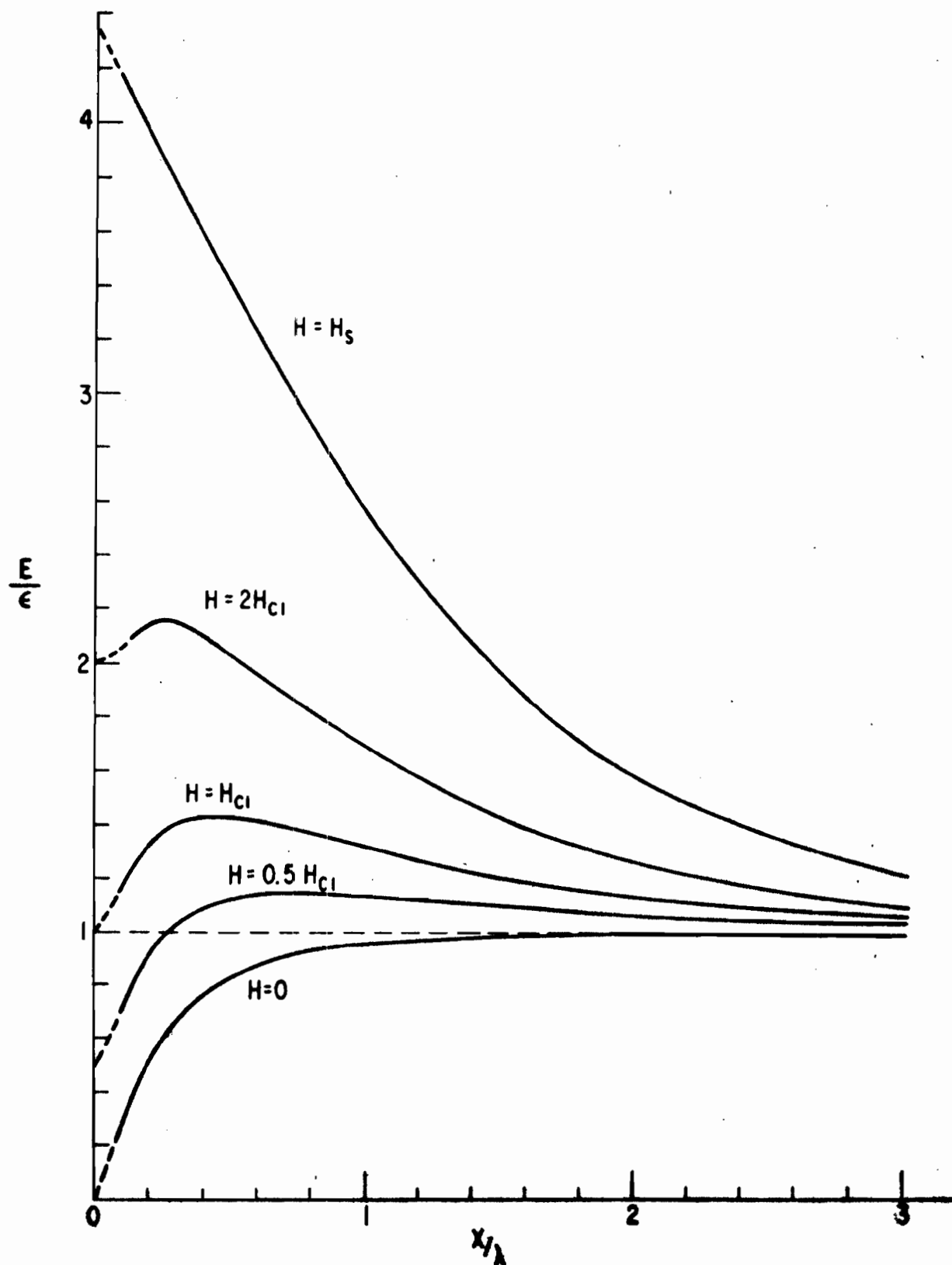
Figure 76 Dependence of the line energy E of the flux thread on x, distance
from the surface, for various applied fields. Results presented are for
$\lambda = 10\xi$.

153

The addition of these two contributions to $E(x)$ will lead to different total $E(x)$ curves for various values of H. Curves calculated for $\lambda = 10\xi$ are seen in Fig. 76. Note that an energy barrier to flux motion into or out of the specimen exists at low fields. Without these surface effects, internal flux threads become energetically favorable[1] at a field H_{c1}, defined by $\varphi_0 H_{c1}/4\pi = \epsilon$ [i. e., in present terms, $E(0) = E(\infty)$]. However, the presence of this surface energy barrier suggests that with a perfect surface, at absolute zero, flux threads may not be able to enter until a higher field, H_s (see Fig. 76), at which the barrier to flux penetration no longer exists.+ The barrier to flux escape, on the other hand, does not disappear completely until H is reduced to zero.

Although the above considerations indicate that a plane surface provides an energy barrier to flux thread motion, it is likely that field concentrations at specimen ends or surface irregularities may create local fields equal to H_s when the average applied field is considerably less. Thus flux may enter at these irregularities, and may then spread into the remainder of the specimen when it becomes energetically favorable, i.e., at H_{c1}. These same field concentrations, however, will block flux escape at these irregularities in decreasing fields. At other spots, surface concavities may produce lowered local surface fields that may encourage flux escape, but since a barrier to flux escape exists down to H=0, flux escape should still be difficult. Thus with surface irregularities and end effects, the magnetization curve in increasing field may be nearly the thermodynamically reversible one (as is commonly assumed), whereas surface hysteresis in the form of delayed flux expulsion will appear in decreasing field. This is consistent with the form of the surface hysteresis observed.[78] Experiments are currently under way to see if improved surface preparation and avoidance of end effects will produce evidence of the large nucleation barrier to flux penetration calculated here.

The present elementary treatment has only considered $E(x)$ for a single flux thread. To calculate the detailed hysteresis curves expected, one must consider an assembly of flux threads and the interactions between them. For a more exact calculation of H_s and removal of the limitation $\lambda \gg \xi$, detailed consideration of the core of the flux thread and use of the Ginzburg-Landau equations will be required.

We gratefully acknowledge discussion with P. G. de Gennes, who had independently considered the image flux thread and the resulting energy barrier.

+Our calculation of H_s in this approximation is inexact because of uncertainties in the image term in $E(x)$ for $x \lesssim \xi$. Choosing to cut off $K_0(2x/\lambda)$ at $x = \xi$, the maximum image force then occurs here, and we get $H_s = \varphi_0/4\pi\lambda\xi \approx H_c/\sqrt{2}$, where H_c is the thermodynamic critical field.

B. EXPERIMENT (R. W. DeBlois and W. DeSorbo)

Through arguments presented above, Bean and Livingston predicted the existence of an image-effect surface barrier to the penetration of magnetic flux into type II superconductor. We report here the experimental observation of a greatly enhanced superconducting to mixed state transition field in some regions of an electropolished specimen of $Nb_{0.993}O_{0.007}$ and in another of $Nb_{0.33}Ta_{0.67}$. Our observations are consistent with the predictions of the Bean-Livingston theory that a plane surface on a type II superconductor will produce nucleation barrier that will increase the initial flux penetration field to near the thermodynamic critical field H_c, and that roughening the surface will permit flux penetration near the superconducting to mixed state transition field H_{c1}. They are also shown to be inconsistent with the most plausible alternative explanation that electropolishing may have produced a chemically or structurally altered surface sheath. Joseph and Tomasch have also recently found experimental evidence for the existence of the surface barrier by a different technique from ours. [81]

The preparation of the $Nb_{0.993}O_{0.007}$ wire[†] specimen has been described earlier. [82] The $Nb_{0.33}Ta_{0.67}$ specimen was sectioned from a 0.76 mm wire annealed 291 hours at $1650°C$ and 10^{-7} mm Hg. Electropolishing was carried out in an acid mixture of two parts H_2SO_4 to one part HF. Several minutes near 10 volts were followed by several minutes near 3 volts. The voltage measurements were between the specimen and a platinized platinum cathode.

Since the existence of localized imperfections--for example, at grain boundaries--is to be expected even along the lengths of electropolished specimens, we have probed the specimens by applying localized pulsed magnetic fields along their lengths. The specimens were tested at $4.2°K$ in one of the matched pairs of field and pickup coil units connected in series. With the specimen either withdrawn or normal the dB/dt voltages from the two pickup coils canceled each other during a field pulse. The specimen unit consisted of 29 pickup turns of 50μ wire wound on a 1.24 mm quartz capillary for an axial length of 1.25 mm, and of 90 field-coil turns wound over the pickup coil to an outside diameter of 2.14 mm. The section of the specimen at the field coil was varied by means of a draw thread leading out of the top of the Dewar.

The field at the surface of the superconducting specimen is the sum of the applied field and that produced by induced surface currents. This total is best determined experimentally by adding a known biasing field and measuring the change in the field-trace voltage needed to rematch that trace with a fiducial break in the dM/dt trace. The field varies from 580 to 660 Oe/amp, with a probable error of about 3%, for specimens from 0.30 to 0.65 mm in diameter.

[†] On the scale of the image-force distances involved in the theory, the wire presents an essentially planar surface.

155

Figure 77 shows two sets of oscilloscope traces of pickup-coil voltage and applied magnetic field vs time for the $Nb_{0.993}O_{0.007}$ specimen. The field trace is of the voltage over a resistance in series with the field coil. Trace A is for the specimen in an optimum position. (The trace bottoms near -18 mv.) For trace B the specimen was moved 1.4 mm upward. The trace of dM/dt is proportional to dH/dt as long as no flux penetrates into the specimen. For trace A this condition holds to a field H_s of 1330 Oe, while for trace B the main penetration starts near 725 Oe. In most traces other than type A, a slight flux penetration is detectable before the main penetration, at a field near H_{c1}.

Conventional tests in an electromagnet on an adjacent section of wire and, earlier, on a similarly prepared specimen[82] give a superconducting to mixed state transition field H_{c1} of 580 Oe, a thermodynamic critical field H_c of 1360 Oe, and upper limit H_{c2} for the mixed state of 7000 Oe, and a critical temperature T_c of 8.8°K. Thus the penetration field H_s experimentally observed here is more than twice H_{c1} and is approximately equal to H_c. In other tests on this specimen penetration fields up to 1500 Oe (10% above H_c) have been observed. It is not yet clear what the theoretical limit for H_s should be. Bean and Livingston made a rough estimate of $H_c/\sqrt{2}$ for a material with the penetration depth much greater than the coherence length. κ, a measure of their ratio, equals 4.0 for $Nb_{0.993}O_{0.007}$.

Figure 78 shows the penetration field contour along the length of the $Nb_{0.993}O_{0.007}$ specimen after a particular electropolish. The open circles show regions where flux penetration occurred abruptly, as in trace A of
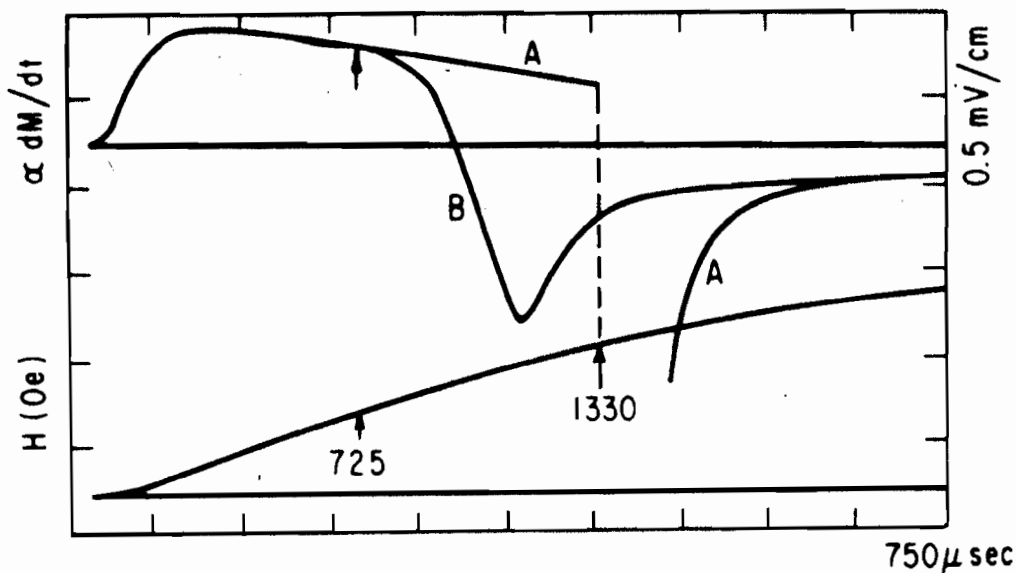
Figure 77 Oscilloscope traces showing initial penetration of flux into an electropolished $Nb_{0.993}O_{0.007}$ wire at a field of 1330 Oe with the field coil at an optimum position, and at 725 Oe with it 1.4 mm away (H_{c1} = 580 Oe).

156
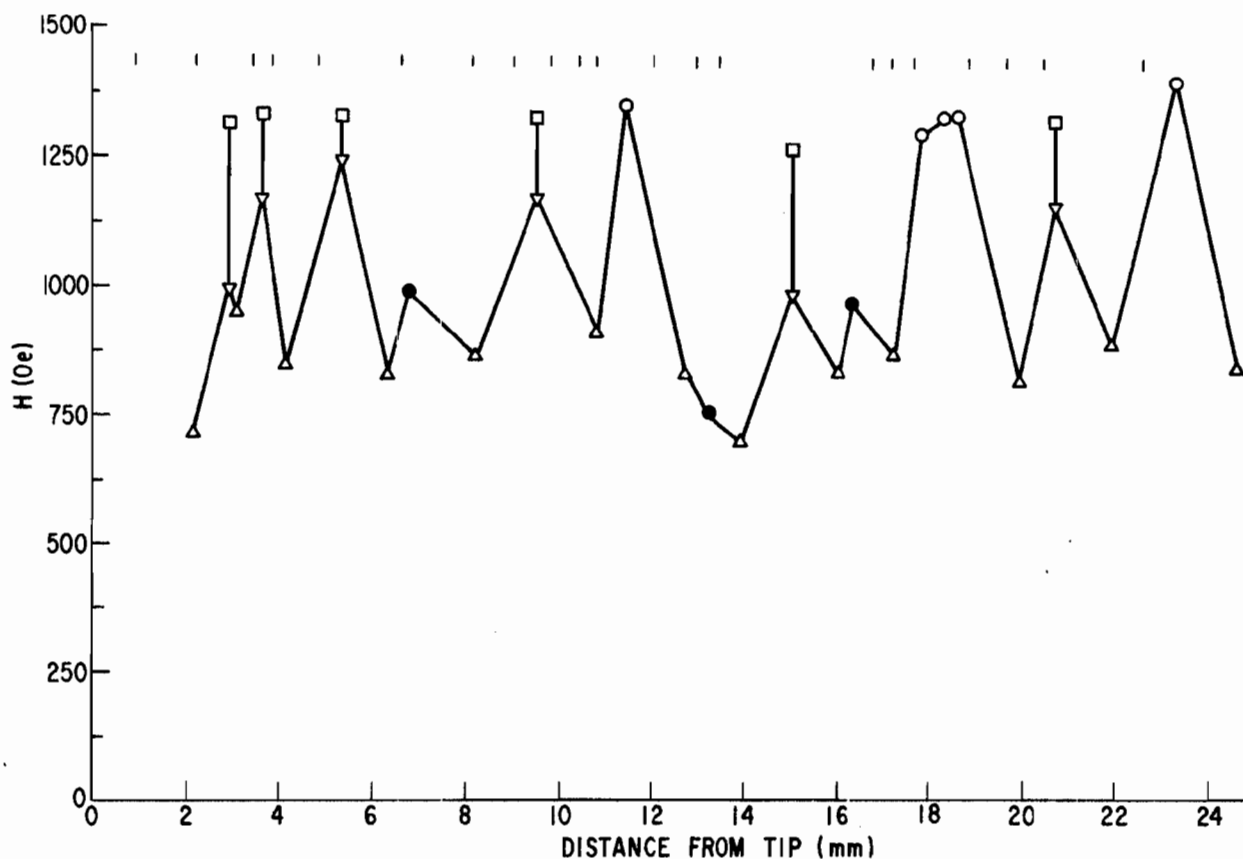
Figure 78   Maximum $(\bigcirc, \square)$ and minimum $(\triangle)$ initial flux penetration fields along the length of an electropolished $Nb_{0.993}O_{0.007}$ wire.   The positions of grain boundaries are indicated by the row of dashes just above the field data.   For explanation of other symbols, see text.

Fig. 77.   Tests of one of these optimum positions show that the penetration field H_s does not vary with field rise rate (ΔH generally less than 20 Oe) in the observed range of 8×10^4 to 22×10^7 Oe/sec.   Thus it is unlikely that dynamic effects account for the high penetration field.   Abrupt penetrations also occurred at regions shown by the squares, but they were preceded by gradual penetrations starting at coil-center fields shown by the inverted triangles $(\triangledown)$.   One may note that the abrupt penetrations (1270 to 1400 Oe) all occur near the thermodynamic critical field H_c of 1360 Oe.   The gradual penetrations $(\triangledown)$ probably arise at weak spots in the fringing field of the coil. The triangles $(\triangle)$ and solid circles $(\bullet)$ show regions with traces like B of Fig. 77 and with penetration fields at the local minima and maxima, respectively.   These less perfect regions still have penetration fields above H_{c1} (580 Oe).   However, gently circumscribing the specimen with a razor blade at two positions reduced the penetration fields there to about 645 and 590 Oe, respectively.

The dashes above the data points show the positions of grain boundaries along the length of the specimen.   The abrupt penetrations all fall between

157

these boundaries. Microscopic examination of the specimen under oblique lighting revealed minute surface steps at the grain boundaries that would, from the theory, be expected to make flux penetration easier than at a smooth planar surface. However, grain boundaries need not be weak spots. Subsequent tests on another specimen of niobium with probably somewhat less than 0.7 A/o oxygen showed a continuous region of 2.3 cm over which only abrupt penetrations occurred, all at 1560 ± 20 Oe. These results followed a thus far uniquely superior electropolish at 9 volts.

Tests on the electropolished specimen of $Nb_{0.33}$ and $Ta_{0.67}$ showed a range of penetration fields from 180 to 320 Oe. The specimen was also tested after the surface was roughened with emery paper. The average penetration field then became 175 Oe, with a maximum of 200 Oe. The average before roughening was about 245 Oe, and after the next electropolish, about 235 Oe. Conventional tests on similar material give values of $H_{c1} = 110$ Oe, $H_c = 310$ Oe, $H_{c2} = 1600$ Oe, and $T_c = 5.6°K$. Thus the upper penetration field of 320 Oe is about equal to H_c.

Whether flux penetrates abruptly at a high field or gradually at a low field makes no difference in the manner of flux expulsion as the field pulse falls. For all positions along the length of the $Nb_{0.993}O_{0.007}$ specimen it becomes abruptly complete near 650 Oe, independent of the amount of flux that originally entered. This is what one would expect from inspection of the bulk magnetization curve of Fig. 9 of Ref. 82. If, on the other hand, electropolishing chemically or physically altered the structure of the surface material, one might expect the sheath producing the high penetration field to trap the interior flux near the high field and to prevent the abrupt completion of flux expulsion near the field H_{c1} of the bulk of the specimen.

ACKNOWLEDGMENTS

SECTION VIII

RECCMMENDATIONS FOR FUTURE WORK

In the past 4 years, there have been impressive advances in our general understanding of superconductivity. As indicated in this report, there have been advances in our understanding of those properties of superconductors that are important in the eventual use of these materials in electrical systems. There remain, however, a number of specific areas where further research is necessary to enlarge our fundamental understanding and to enable us to evaluate the potential technological uses of certain types of superconductors.

We would like to recommend several areas for future work, the principal criterion for the choices being that contributions in these areas will advance the application of superconducting materials in electrical systems.

1. There should be a further development of the theories of magnetic instability in high current-carrying type II superconductors and the undertaking of experiments to confirm or qualify theoretical work. A thorough understanding of these instabilities is an absolute necessity in order that we may _fully_ exploit the intrinsic properties of type II superconductors in actual applications.

Early research in this area (Section IV) already has provided important new upper limits to the performance of type II superconductors. Further theoretical and experimental work should provide additional criteria and restraints to the application of type II superconductors in a-c and d-c electrical equipment.

2. There should be further studies of the superconductive properties of niobium and interpretation of these properties on the basis of recent theories. The reason for this emphasis on niobium is quite straightforward. At present, niobium appears to be the principal contender for use in superconducting gyroscopes, in power cryotrons, and in superconducting transformers. It also appears that niobium may in the future be the principal superconductor used in Josephson tunnel junction devices and in adiabatic magnetization refrigeration cycles. In short, niobium will be one of the workhorses of superconductivity. Specific properties of niobium that should be studied are:

(a) Effects of preparation techniques and cooling rates on the a-c losses below H_{c1}.

(b) Low level flux trapping and its relation to field penetration, losses, and structural and compositional parameters.

(c) Surface supercurrents between H_{c1} and H_{c3}, especially the factors governing these currents and the elimination of them.

3. There is need for research aimed at providing a quantitative description of the interaction between the magnetic flux threads and well-characterized metallurgical defects. The attack might be chosen from among the following three possibilities: (a) a study of the superconducting properties of alloy systems that undergo spinodal decomposition or martensitic transformation; (b) the study of superconducting systems to which ferromagnetic precipitates have been added; or (c) a detailed analysis of the effects of particular types of radiation-induced damage.

4. In view of our rapidly advancing understanding of properties of super-conductors, it seems appropriate to embark on pioneering studies of the relative advantages of (a) inhomogeneous type II superconductors; (b) cryogenic nonsuperconducting metals; and (c) conventional metals at environmental temperatures for application in large scale a-c electrical equipment. The extension and confirmational studies of the critical state model (Bean model) performed under this contract (Parts II and V) has provided the foundation for the important engineering studies which should now be undertaken.

GENERAL ELECTRIC PUBLICATIONS ON SUPERCONDUCTIVITY

(This is a list of publications of recent years from the General Electric Research Laboratory, now a part of the General Electric Research and Development Center.)

1. W. DeSorbo, "The Intermediate State of Tin," Proc. 7th Intern.Conf. on Low Temperature Physics (1960).

2. W. DeSorbo and V. L. Newhouse, "Optical Detection (Observation) of Domain Structure and Current Flow in Superconducting Lead Films," J. Appl. Phys., 33, 1004-1009 (1962).

3. H. H. Edwards and V. L. Newhouse, "Superconducting Film Geometry with Strong Critical Current Asymmetry," J. Appl. Phys.; 33, 868-874 (1962).

4. R. W. Schmitt and W. DeSorbo, "Uses of Superconductivity," Research/ Development, 13, 26-31 (1962).

5. I. Giaever, "Study of Superconductors by Electron Tunneling Through Thin Insulating Films," Proc. Conf. on the Electric and Magnetic Properties of Thin Metallic Layers, Leuven, Belgium (1961).

6. I. Giaever, H. R. Hart, and K. Megerle, "Tunneling into Superconductors at Temperatures below 1°K," Phys. Rev., 126, 941-948 (1962).

7. W. DeSorbo and W. A. Healy, "The Intermediate State of Some Super-conductors," Cryogenics, 257-326 (1964).

8. B. W. Roberts, "Superconducting Materials and Some of Their Properties," Progr. Cryogenics, 4, 161-231 (1964).

9. C. P. Bean, "Magnetization of Hard Superconductors," Phys. Rev. Letters, 8, 250-253 (1962).

10. I. Giaever and K. Megerle, "Study of Superconductors by Electron Tunneling," Phys. Rev., 122, 1101-1111 (1961).

11. C. P. Bean, M. V. Doyle, and A. G. Pincus, "A Synthetic High-Field, High-Current Superconductor," Phys.Rev. Letters, 9, 93 (1962).

12. P. S. Swartz, "Evidence for the Negative Surface Energy Models of Super-conductivity in Nb_3Sn, Nb_3Al, V_3Ga, and V_3Si," Phys. Rev. Letters, 9, 448-451 (1962) and J. Appl. Phys., 34, 1365-1366 (1963).

13. W. DeSorbo, "Magnetization Studies on Some Superconducting Transition Metal Solutions," J. Appl. Phys., 34, 1378-1379 (1963).

14. C. P. Bean and M. V. Doyle, "Superconductors as Permanent Magnets," J. Appl. Phys., 33, 3334-3337 (1962); and 34, 1364 (1963).

15. J. D. Livingston, "Magnetic Properties of Superconducting Lead-Base Alloys," Phys. Rev., 129, 1943-1949 (1963).

16. C. H. Rosner and H. W. Schadler, "Relating Measurements on Short Superconducting Wires to Solenoid Performance," J. Appl. Phys., 34, 2107-2108 (1963).

17. C. H. Rosner, M. G. Benz, and D. L. Martin," 'Coil Simulation' Testing on Niobium-Tin Wire Samples," J. Appl. Phys., 34, 2108-2109 (1963).

18. C. L. Kolbe and C. H. Rosner, "Processing and Superconducting Properties of Nb_3Sn Wires," Met. Advan. Electronic Materials (1962).

19. D. L. Martin, M. G. Benz, C. A. Bruch, and C. H. Rosner, "A 100,000 Gauss Superconducting Solenoid," Cryogenics, 3, (1963).

20. D. L. Martin, M. G. Benz, C. A. Bruch, and C. H. Rosner, "A 101,000 Gauss Niobium-Tin Superconducting Solenoid," Cryogenics, 3, 161-166 (1963).

21. W. DeSorbo, "Size Factor and Superconducting Properties of Some Transition Metal Solutions," Phys. Rev., 130, 2177-2187 (1963).

22. W. DeSorbo, "Resistive Transition Characteristics in Superconducting Niobium Containing Some Dissolved Gases," Phys. Rev., 134, A1119-A1135 (1964).

23. W. DeSorbo, "Effect of Dissolved Gases on Some Superconducting Properties of Niobium," Phys. Rev., 132, 107-121 (1963).

24. W. DeSorbo, "The Influence of Impurities and Solutes (Primarily Zirconium) on the High-Current Carrying, High-Field Nb_3Sn Superconductor," Cryogenics, 218-232 (1964).

25. W. H. Meiklejohn, "Temperature Dependence of the Critical Current of Tantalum and Indium-Tin Alloy Films," Revs. Mod. Phys., 36, 302-305 (1964).

26. W. DeSorbo, "The Peak Effect in Substitutional and Interstitial Solid Solutions of High-Field Superconductors," Revs. Mod. Phys., 36, 90-94 (1964).

27. M. D. Fiske, "Temperature and Magnetic Field Dependences of the Josephson Tunneling Current." Revs. Mod. Phys., 36, 221-222 (1964).

28. B. W. Roberts, "Superconductive Materials and Some of Their Properties," Progr. Cryogenics, 4, 161-231 (1964).

29. J. D. Livingston, "Precipitation and Superconductivity in Lead-Tin and Lead-Cadmium Alloys," J. Appl. Phys., 34, 3028-3036 (1963).

30. C. P. Bean and R. W. Schmitt, "The Physics of High-Field Superconductors," Science, 140, 26-35 (1963).

31. J. D. Livingston, "Defects and Magnetic Hysteresis of Type II Superconductors," Rev. Mod. Phys., 36, 54-57 (1964).

32. C. A. Neugebauer and R. A. Ekvall, "Evaporated Superconductive Films of Nb, Ta, and V," J. Appl. Phys., 35, 547-553 (1964).

33. C. P. Bean and J. D. Livingston, "Surface Barrier in Type II Superconductors," Phys. Rev. Letters, 12, 14-16 (1964).

34. H. R. Hart, Jr., and R. W. Schmitt, "Superconductivity," Science, 143, 57-60 (1964) and Physics Today, 31-44 (1964).

35. W. DeSorbo, "Resistive Transition and Current Density Characteristics in Superconducting Niobium Containing Dissolved Gases," Phys. Rev., 134, A1119-A1135 (1964).

36. W. DeSorbo, "Concerning the Ratio H_{c3}/H_{c2} in Superconducting Nb and Nb-O Solutions," Phys. Rev., 135, A1190-A1193 (1964).

37. C. P. Bean, "The Magnetization of High Field Superconductors," Revs. of Mod. Phys., 36, 31-39 (1964).

38. H. R. Hart, Jr. and P. S. Swartz, "The Angular Dependence of Surface Superconductivity in Some Type I and II Lead-based Super-Conductors," Phys. Letters, 10, 40-41 (1964).

39. M. D. Fiske and I. Giaever, "Superconductive Tunneling," Proc. IEEE, 52, 1155-1163 (1964).

40. M. D. Fiske and D. D. Coon, "Josephson A-C and Step Structure in the Supercurrent Tunneling Characteristic," Phys. Rev., 138, A744-A746 (1965).

41. J. D. Livingston, "Magnetic Hysteresis and Critical Currents in the Mixed State," Proc. Type II Superconductivity Conf., Cleveland (1964).

42. W. DeSorbo, "Flux Penetration and Mobility in Types I and II Superconductors," Proc. 9th Intern. Conf. on Low Temperature Physics, Columbus, Ohio (to be published).

43. T. A. Buchhold, "Superconductive Power Supply and Its Application for Electric Flux Pumping," Cryogenics (August 1964).

44. B. W. Roberts, "Superconductive Intermetallic Compounds," Intermetallic Compounds.

45. P. S. Swartz, H. R. Hart, Jr., and R. L. Fleischer, "Effect of Fast Neutron Irradiation on the Magnetic Properties and the Critical Temperature of Some Type II Superconductors," Appl. Phys. Letters, 4, 71-73 (1964).

REFERENCES

1. A. A. Abrikosov, J. Phys. Chem. Solids, $\underline{2}$, 199 (1957). For a minor improvement in this model, see W. H. Kleiner, L. M. Roth, and S. H. Autler, Phys. Rev., $\underline{133}$, A1226 (1964); J. Matricon, Phys. Letters, $\underline{9}$, 289 (1964).

2. For a review of the effect of metallurgical variables on superconducting properties, and for references, see J. D. Livingston and H. W. Schadler, Progr. Mat. Sci., $\underline{12}$, 183 (1964).

3. D. Saint-James and P. G. de Gennes, Phys. Letters, $\underline{7}$, 306 (1964).

4. J. E. Kunzler, E. Buehler, F. S. L. Hsu, and J. H. Wernick, Phys. Rev. Letters, $\underline{6}$, 89 (1961); T. G. Berlincourt, R. R. Hake, and D. H. Leslie, Phys. Rev. Letters, $\underline{6}$, 671 (1961); J. E. Kunzler, Rev. Mod. Phys., $\underline{33}$, 501 (1961).

5. D. L. Martin, M. G. Benz, C. A. Bruch, and C. H. Rosner, Cryogenics, $\underline{3}$, 114, 161 (1963); C. H. Rosner and M. G. Benz, Proc. Intern. Symp. on Magnet Technol., Stanford (September 1965), to be published; E. R. Schrader and F. Kolondra, RCA Rev., $\underline{25}$, 582 (1964); H. T. Coffey, R. Span, D. Fox, W. Reynolds and J. Hulm, Bull. Am. Phys. Soc., $\underline{9}$, 454 (1964); C. Laverick, Cryogenics, $\underline{5}$, 152 (1965); and Z. J. J. Stekly, E. J. Lucas, T. A. DeWinter, and C. Laverick, Rev. Sci. Instr., $\underline{36}$, 1291 (1965).

6. R. M. Bozorth, H. J. Williams, and D. D. Davis, Phys. Rev. Letters, $\underline{5}$, 148 (1960).

7. C. P. Bean, Phys. Rev. Letters, $\underline{8}$, 250 (1962).

8. G. P. Harnwell, Principles of Electricity and Electromagnetism, McGraw-Hill Book Co., Inc., New York (1949).

9. Y. B. Kim, C. F. Hempstead, and A. R. Strnad, Phys. Rev., $\underline{129}$, 528 (1963).

10. H. London, Phys. Letters, $\underline{6}$, 162 (1963).

11. P. W. Anderson, Phys. Rev. Letters, $\underline{9}$, 309 (1962).

12. Y. B. Kim, C. F. Hempstead, and A. R. Strnad, ibid., p. 306.

13. Y. B. Kim, C. F. Hempstead, and A. R. Strnad, Phys. Rev., $\underline{139}$, A1163 (1965).

14. J. Volger, F. A. Staas, and A. G. Van Vijfeijken, Phys. Letters, 9, 303 (1964); M. J. Stephen and J. Bardeen, Phys. Rev. Letters, 14, 112 (1965); M. Tinkham, Phys. Rev. Letters, 13, 804 (1964); P. H. Borcherds, C. E. Gough, W. F. Vinen, and A. C. Warren, Phil. Mag., 10, 349 (1964).

15. E. H. Kennard, Kinetic Theory of Gases, McGraw-Hill Book Co., Inc., New York and London (1938), pp. 286-287.

16. Y. B. Kim, C. F. Hempstead, and A. R. Strnad, Phys. Rev., 131, 2486 (1963).

17. H. S. Carslaw and J. C. Jaeger, Conduction of Heat in Solids, Oxford Univ. Press, London (1959), p. 100.

18. H. Suhl, Phys. Rev. Letters, 14, 226 (1965).

19. C. P. Bean, Rev. Mod. Phys., 36, 31 (1964).

20. R. W. Cohen, G. D. Cody, and Y. Goldstein, RCA Rev., 25, 433 (1964).

21. R. A. Kamper and P. F. Chester, Proc. of the VIIIth Intern. Congress on Low Temperature Physics, Butterworth and Co., London (1962).

22. Jacob L. Zar, Rev. Sci. Instr., 34, 801 (1963); C. H. Jones and H. L. Schenk, Advances in Cryogenic Engineering, Vol. 8, K. D. Timmerhaus, ed., Plenum Press, New York (1963), p. 579.

23. G. Bogner and W. Heinzel, Solid State Electronics (GB), 7, 93 (1964); R. G. Rhodes, E. C. Rogers, and R. J. A. Seebold, Cryogenics, 4, 206 (1964); T. Pech, J. P. Duflot, and G. Fournet, Phys. Letters, 16, 201 (1965).

24. R. A. Kamper, Phys. Letters, 2, 290 (1962); P. R. Doidge and Kwan Sik-hung, Phys. Letters, 12, 82 (1964); T. A. Buchhold and P. J. Molenda, Cryogenics, 2, 344 (1962); T. A. Buchhold, Cryogenics, 3, 141 (1963); see also, P. F. Chester, Proc. IEE, 111, 411 (1964).

25. N. Chandra and W. D. Jackson, Bull. Am. Phys. Soc., 10, 60 (1965).

26. H. S. Carslaw and J. C. Jaeger, Conduction of Heat in Solids, Oxford Univ. Press, London (1959).

27. F. J. Morin, J. P. Maita, H. J. Williams, R. C. Sherwood, J. H. Wernick, and J. E. Kunzler, Phys. Rev. Letters, 8, 275 (1962); F. J. Morin and J. P. Maita, Phys. Rev., 129, 1115 (1963).

28. G. D. Cody and R. W. Cohen, Revs. Mod. Phys., 36, 121 (1964).

29. A. L. Schawlow and G. E. Devlin, Phys. Rev., 113, 120 (1959).

30. J. K. Clapp, Proc. I. R. E., 36, 356 (1948).

31. P. S. Swartz, Phys. Rev. Letters, 9, 448 (1962).

32. D. Shoenberg, Superconductivity, Cambridge Univ. Press, Cambridge (1952), Appendix II.

33. G. Boato, G. Gallinaro, and C. Rizzuto, Solid State Commun., 3, 173 (1965).

34. G. Bobel and C. F. Ratto, Solid State Commun., 3, 177 (1965).

35. V. L. Ginzburg and L. D. Landau, J. Expt. Theoret. Phys. (USSR), 20, 1064 (1950).

36. P. G. de Gennes, Solid State Commun., 3, 127 (1965).

37. H. R. Hart, Jr. and P. S. Swartz, Phys. Letters, 10, 40 (1964).

38. P. S. Swartz and H. R. Hart, Jr., Bull. Am. Phys. Soc., 9, 252 (1964).

39. S. H. Autler, E. S. Rosenblum, and K. H. Gooen, Phys. Rev. Letters, 9, 489 (1962); W. DeSorbo, Revs. Mod. Phys., 36, 92 (1964); W. C. H. Joiner and R. D. Blaugher, Revs. Mod. Phys., 36, 69 (1964); S. Gygax, J. L. Olsen, and R. H. Kropschot, Phys. Letters, 8, 228 (1964).

40. W. J. Tomasch and A. S. Joseph, Phys. Rev. Letters, 12, 148 (1964); C. F. Hempstead and Y. B. Kim, ibid., p. 145; M. Cardona and B. Rosenblum, Phys. Letters, 8, 308 (1964); J. P. Burger, G. Deutscher, E. Guyon, and A. Martinet, Phys. Rev., 137, A853 (1965).

41. W. F. Druyvesteyn, D. T. van Ooijen, and T. J. Berben, Revs. Mod. Phys., 36, 60 (1964); G. Bon Mardion, B. B. Goodman, and A. Lacaze, Phys. Letters, 8, 15 (1964); B. Rosenblum and M. Cardona, Phys. Letters, 9, 220 (1964).

42. G. Bon Mardion, B. B. Goodman, and A. Lacaze, Phys. Letters, 2, 321 (1962).

43. M. Tinkham, Phys. Letters, 9, 217 (1964).

44. M. Tinkham, Conf. on the Physics of Type II Superconductivity, Cleveland, Ohio (1964), unpublished.

45. D. Saint-James, Phys. Letters, 16, 218 (1965).

46. J.P. Burger, G. Deutscher, E. Guyon, and A. Martinet, Phys. Letters, 16, 220 (1965).

47. P.S. Swartz, H.R. Har, Jr., and R.L. Fleischer, Appl. Phys. Letters, 4, 71 (1964).

48. J.P. McEvoy, Jr., R.F. Decell, and R.L. Novak, Appl. Phys. Letters, 4, 43 (1964); G.W. Cullen and R.L. Novak, ibid., p. 147.

49. C.P. Bean, M.V. Doyle, and A.G. Pincus, Phys. Rev. Letters, 9, 93 (1962).

50. P.W. Anderson and Y.B. Kim, Rev. Mod. Phys., 36, 39 (1964).

51. P.B. Price and R.M. Walker, Appl. Phys. Letters, 2, 23 (1963).

52. R.L. Fleischer, P.B. Price, R.M. Walker, and E.L. Hubbard, Phys. Rev., 133, A1443 (1964).

53. R.L. Fleischer, P.B. Price, and R.M. Walker, J. Nucl. Sci. Eng., 22, 154 (1965).

54. J.A. Brinkman, Proc. Intern. School of Phys. Enrico Fermi, Radiation Damage in Solids, Academic Press, New York (1962).

55. D.S. Billington and J.H. Crawford, Jr., Radiation Damage in Solids, Princeton Univ. Press (1961), pp. 93-97.

56. J. Friedel, P.G. de Gennes, and J. Matricon, Appl. Phys. Letters, 2, 119 (1963).

57. L. Guttman, Trans. AIME, 188, 1472 (1950).

58. J.W. Stout and L. Guttman, Phys. Rev., 88, 703 (1952).

59. B.W. Batterman and C.S. Barrett, Phys. Rev. Letters, 13, 390 (1964).

60. H.L. Luo, J. Hagen, and M.F. Merriam, Acta Met., 13, 1012 (1965).

61. J.W. Cahn, Acta Met., 9, 795 (1961); 10, 179 (1962).

62. J.D. Livingston, Phys. Rev., 129, 1943 (1963).

63. P.S. Swartz and C.P. Bean, Bull. Am. Phys. Soc., 11, 359 (1965).

64. L. Vieland and A.W. Wicklund, in "Phenomenon of Superconductivity," Tech. Rept. No. AFML-TR-65-169, Air Force Materials Lab., Wright-Patterson Air Force Base, Ohio (1965), p. 17.

65. G. D. Cody and G. W. Cullen, _ibid._, p. 48.

66. C. P. Bean, R. W. DeBlois, and L. B. Nesbitt, J. Appl. Phys., 30, 12 (1959).

67. A. R. Strnad, C. F. Hempstead, and Y. B. Kim, Phys. Rev. Letters, 13, 794 (1964).

68. S. L. Wipf and M. S. Lubell, Phys. Letters, 16, 103 (1965).

69. J. J. Hanak and R. Enstrom, in "Phenomenon of Superconductivity," p. 86 of Ref. 64.

70. S. L. Wipf and M. S. Lubell, Bull. Am. Phys. Soc., 10, 60 (1965).

71. R. Hancox, Phys. Letters, 16, 208 (1965).

72. H. J. Goldsmid and J. M. Corsan, Phys. Letters, 10, 39 (1964).

73. J. A. Stratton, _Electromagnetic Theory_, McGraw-Hill Book Co., Inc., New York (1941), pp. 118-123.

74. J. R. Rairden and C. A. Neugebauer, Proc. IEEE, 52, 1234 (1964).

75. P. S. Swartz and H. R. Hart, Jr., Phys. Rev., 137, A818 (1965).

76. C. Chou, D. White, and H. Johnston, Phys. Rev., 109, 788 (1958).

77. J. E. Mercereau and L. L. Crane, Phys. Rev. Letters, 9, 381 (1962).

78. J. D. Livingston, Rev. Mod. Phys., 36, 54 (1964).

79. C. P. Bean and J. D. Livingston, Phys. Rev. Letters, 12, 14 (1964).

80. R. W. DeBlois and W. DeSorbo, _ibid._, p. 499.

81. A. S. Joseph and W. J. Tomasch, _ibid._, p. 219.

82. W. DeSorbo, Phys. Rev., 132, 107 (1963).

ABSTRACT FOR APPENDIX A

Measurements of the critical transport current above H_{c1} in a variety of $Pb_{0.95}Tl_{0.05}$ samples reveal that the surface can support a large transport current in the mixed state when the magnetic field vector is aligned with the surface. When a geometry is chosen such that the magnetic field vector can be aligned with a single surface (e.g., a cylinder of triangular cross section), the critical currents of opposite polarities differ by over a factor of three when the magnetic field vector is parallel to a surface plane; partial rectification is thus observed. The larger critical current is always in a direction that indicates that magnetic flux crosses out the surface of a type II superconductor more easily than into the surface. The "anomalous peak effect" (a maximum in the critical current just below H_{c2}) is observed in annealed samples and is identified with the strength of the Saint-James and de Gennes surface film below H_{c2} because of the manner in which it is affected by a thin surface film of copper. The nature of critical transport current results suggests that two separate mechanisms contribute to the surface transport current in the mixed state. One of these mechanisms is identified with the Saint-James and de Gennes surface film below H_{c2}; the second is tentatively associated with a bulk penetration depth. We measured a mixed state resistivity and separated the contributions from the surface and the bulk. The bulk mixed state resistivity is found to be independent of the density of bulk defects.

APPENDIX A

SURFACE EFFECTS IN THE MIXED SUPERCONDUCTING STATE
(P. S. Swartz and H. R. Hart, Jr.)

A. INTRODUCTION

It has been established that superconductivity in a type II superconductor can persist above the Abrikosov[1] upper critical field H_{c2} in a thin surface layer.[2-6] The critical field of this surface layer is sensitive to the angle the magnetic field vector makes with the surface. When the magnetic field vector is parallel to the surface being explored, superconductivity persists to $H_{c3} = 1.69\ H_{c2}$.[6] As the magnetic field vector is turned out of the plane of the surface, the critical field is reduced rapidly, becoming equal to H_{c2} at 90°.

A second surface phenomenon has been predicted by Bean and Livingston.[7] They calculated that the surface acts as a barrier to the nucleation of the mixed state at H_{c1}, delaying the entrance into the mixed state until magnetic fields somewhat greater than H_{c1}. The work of DeBlois and DeSorbo[8] and Joseph and Tomasch[9] supports the Bean-Livingston prediction.

In the Appendix we explore various surface phenomena in the mixed state ($H_{c1} \leqslant H \leqslant H_{c2}$) and between H_{c2} and H_{c3}. Our more significant findings are as follows. (1) The surface of a type II superconductor is capable of carrying significant transport supercurrents in the mixed state when the magnetic field vector is parallel to the plane of the surface. (2) The magnitude of the critical surface transport current is sensitive to the polarities of the transport current and the magnetic field in a manner revealing that, in a type II superconductor, magnetic flux crosses the surface more easily from within the sample than from without; partial rectification can occur in a superconductor. (See Note Added in Proof.) (3) The "anomalous peak effect"[10, 11] near H_{c2} (sometimes called the "dip effect") exists in an annealed lead-based alloy. Studies using copperplating indicate that in our sample the peak effect is a surface phenomenon, apparently a manifestation below H_{c2} of the Saint-James and de Gennes surface sheath.[6]

B. SAMPLE PREPARATION

All of the experiments described in this report have been performed with the solid solution $Pb_{0.95}Tl_{0.05}$, a type II alloy for which $H_{c1} \approx 350$ Oe[12] and $H_{c2} = 1030$ Oe. We found previously[3] that the lead-thallium alloys undergo very sharp superconducting transitions between H_{c2} and H_{c3}; these alloys have a very narrow liquidus-solidus range, suggesting little microsegregation upon cooling from the melt. The experiments reported here have been performed with two geometries--thin ribbons 2 inches by 0.250 by 0.003 inch and

a 2-inch-long cylinder with a cross section approximating an isosceles right triangle about 0.120 inch wide across the hypotenuse.

The ribbons were prepared by first rolling the cast ingot to 0.004-inch sheet from which samples were cut. The samples were then cotton swabbed with either acetone or ethylene dichloride to remove organic films that would otherwise cause pits to appear on the surface during polishing. The ribbons were polished to a mirrorlike finish by immersing them for 1 to 2 minutes in a vigorously stirred solution of 100 parts glacial acetic acid to 26 to 30 parts of 30% H_2O_2. Following the polish, the samples were immediately washed in ordinary tap water and dried in a fast-flowing gaseous nitrogen stream. (If distilled water is used for the wash, a dull film is left on the surface.) The ribbons were then annealed for 1 to 2 weeks (at $320° \pm 2°C$) in a vacuum ranging between 10^{-6} and 10^{-7} mm. The ribbon specified as "annealed" in this report was held at 326° to 327°C for a few minutes after annealing at 320° for a week. The ribbon was mounted between glass plates and current and voltage leads attached (see Fig. A-1). The ribbon sample that we designate in this report as "unannealed" was mounted and tested after the polishing operation.

The cylinders of triangular cross section were prepared by milling from 0.100-inch rolled sheet. Each surface was then sanded flat by rubbing the faces of the triangle against a piece of crocus cloth (No. 685) glued to a flat surface. The subsequent polish, wash, and anneal were then identical to that for the ribbons. A surface layer about 0.002 to 0.003 inch thick was removed by the polishing operation.
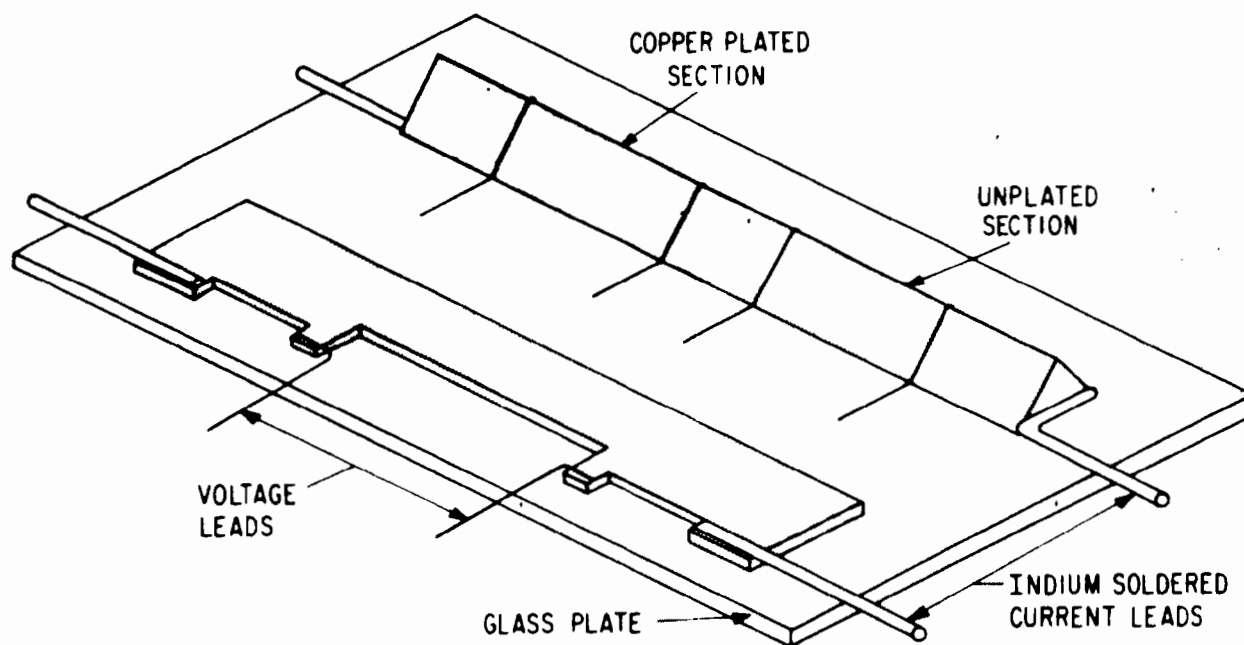
Figure A-1 A schematic of the mounting arrangement of a ribbon and a cylinder of triangular cross section. The glass cover plates are not shown.

C. EXPERIMENTAL DETAILS

The mounted samples were placed in a helium Dewar between the pole faces of a 12-inch Varian magnet. Two sample orientations have been used-- in the first the long axis of the sample is vertical, and in the second, horizontal. In the first case the transport current direction and the magnetic field vector are always orthogonal ($\theta = 90°$) and the magnetic field vector is rotated in the plane perpendicular to the current direction (azimuthal angle φ is varied). In the case of the ribbon, we define $\varphi = 0°$ when the magnetic field vector is parallel to the planar faces of the ribbon. For the cylinder of triangular cross section, we define $\varphi = 0°$ when the magnetic field vector is parallel to the widest of the three planes. In the second orientation, in which the axis of the sample is mounted horizontally, the magnetic field vector is kept in a surface plane (azimuthal angle $\varphi = 0°$) while the angle θ between the transport current and the magnetic field vector H is varied from $0°$ to $90°$.

The transport current is provided by a Kepco voltage-regulated d-c supply and the accompanying voltage drop is measured after amplification by a Liston-Becker d-c breaker amplifier. The critical transport current is defined in all experiments as the current at which a voltage drop of 1.4 $\mu v/cm$ is detected. All experiments were performed at 4.2°K.

D. SURFACE SUPERCURRENTS; $\theta = 90°$ (I $\perp$ H), φ VARIED

1. Data

In this subsection we report the critical transport current measured as a function of angle φ and magnetic field H for ribbons in various conditions and for a well-annealed cylinder of triangular cross section. In the following subsections (2 through 4) we show that these data provide evidence for surface transport currents in the mixed state.

We determine $\varphi = 0°$ (H parallel to the plane of the ribbon and, for the cylinder of triangular cross section, to the widest of the three planes) to less than 0.05° by rotating a constant magnetic field of magnitude between H_{c2} and H_{c3} and searching for the voltage minimum. The results for ribbons in three different conditions are displayed in Figs. A-2 through A-4. The ribbon of Fig. A-2 is in the as-rolled, unannealed condition; that of Fig. A-3 is in the annealed condition (1 week at 320°C plus a few minutes at 326° to 327°C in vacuo); Fig. A-4 shows the ribbon of Fig. A-3 after electroplating ~1000 Å of copper. The following noteworthy features are common to all three families of curves:

(a) The critical currents are strongly angular dependent both below and above H_{c2}.

173
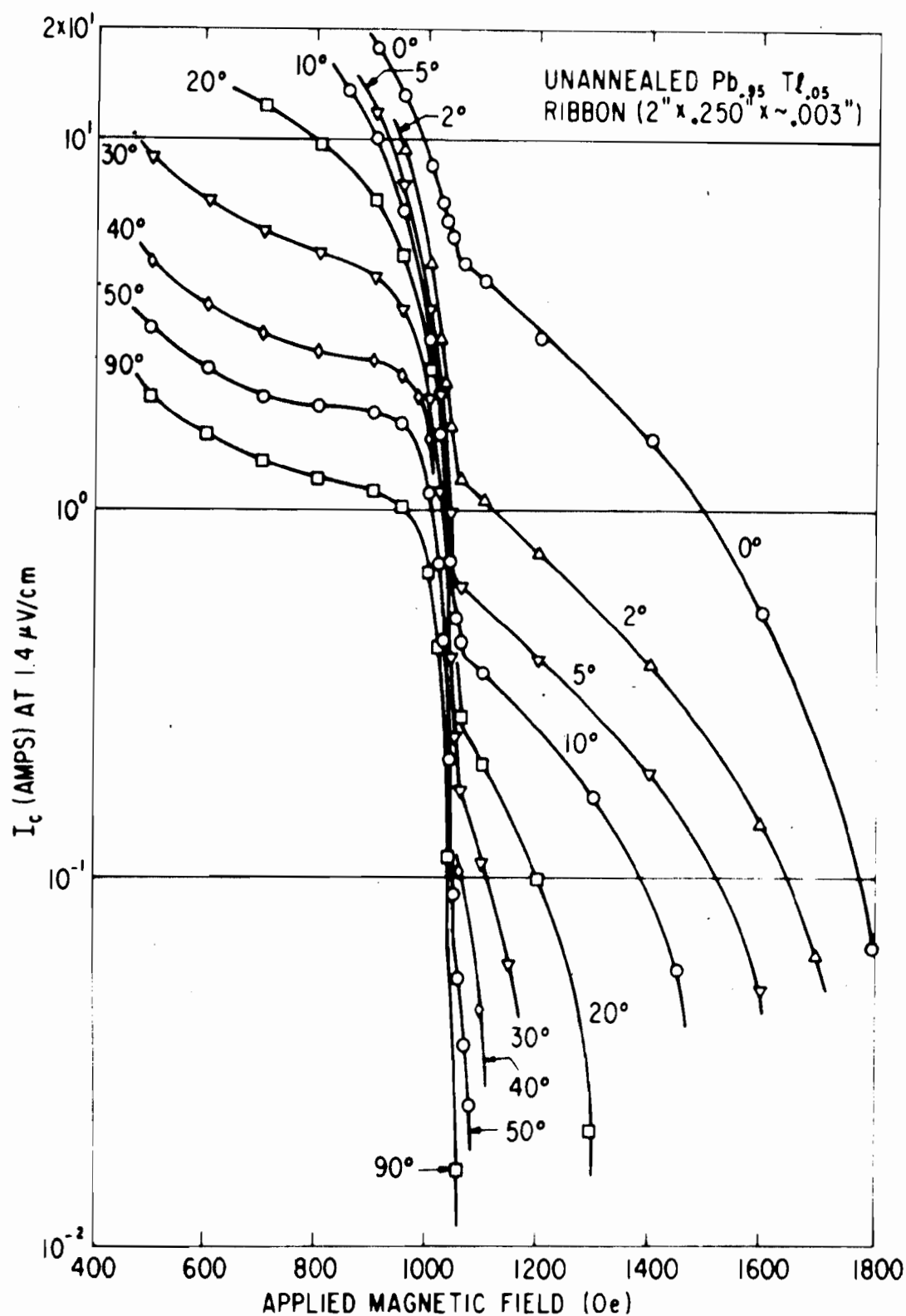
Figure A-2 The experimental family of critical current curves as a function of magnetic field H and azimuthal angle φ(H⊥I) for an as-rolled, unannealed, and polished $Pb_{0.95}Tl_{0.05}$ ribbon.

174
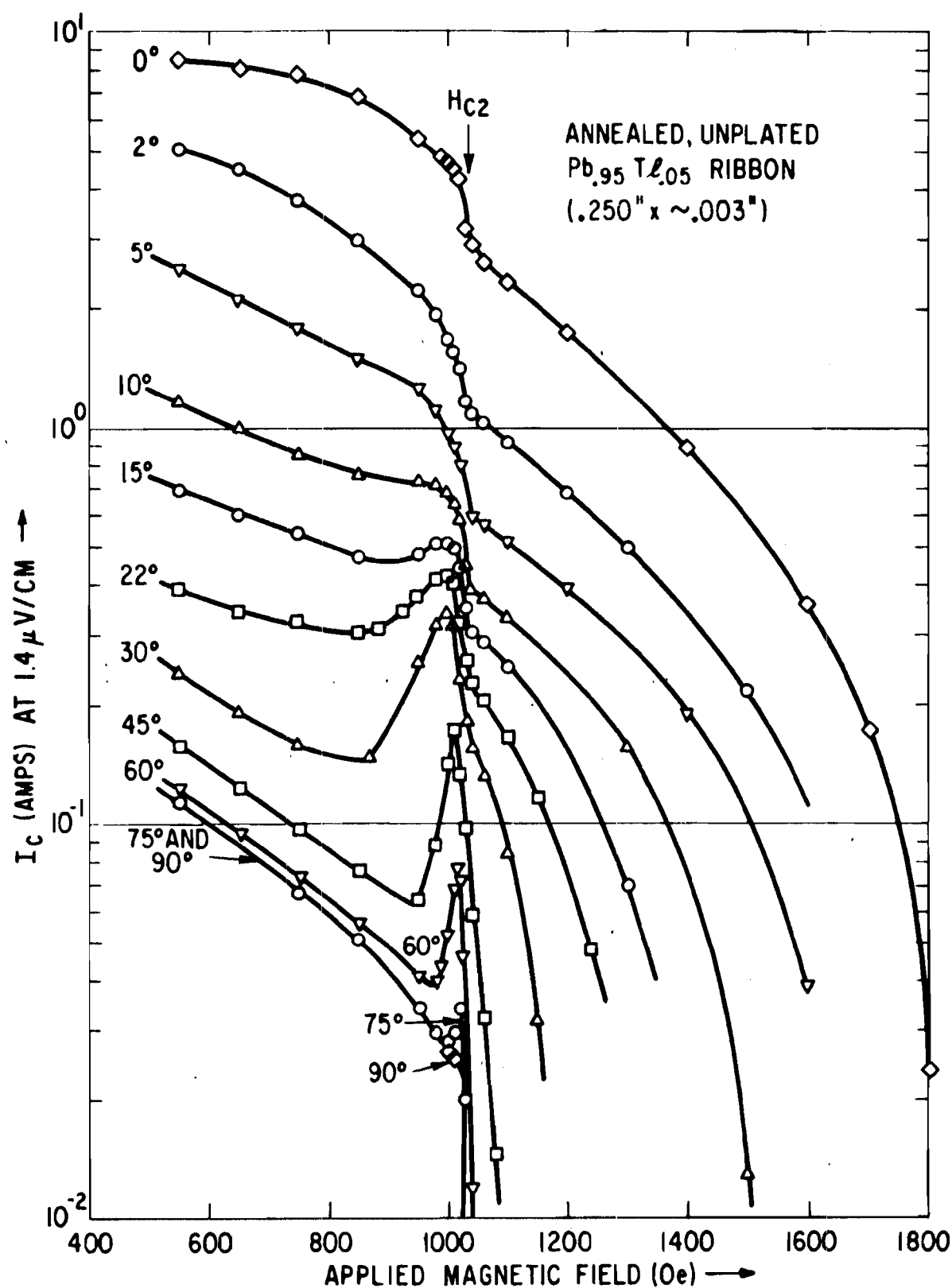
Figure A-3 The experimental family of critical current curves as a function
of magnetic field H and azimuthal angle $\varphi(H \perp I)$ for a polished, well-annealed
ribbon of $Pb_{0.95}Tl_{0.05}$.
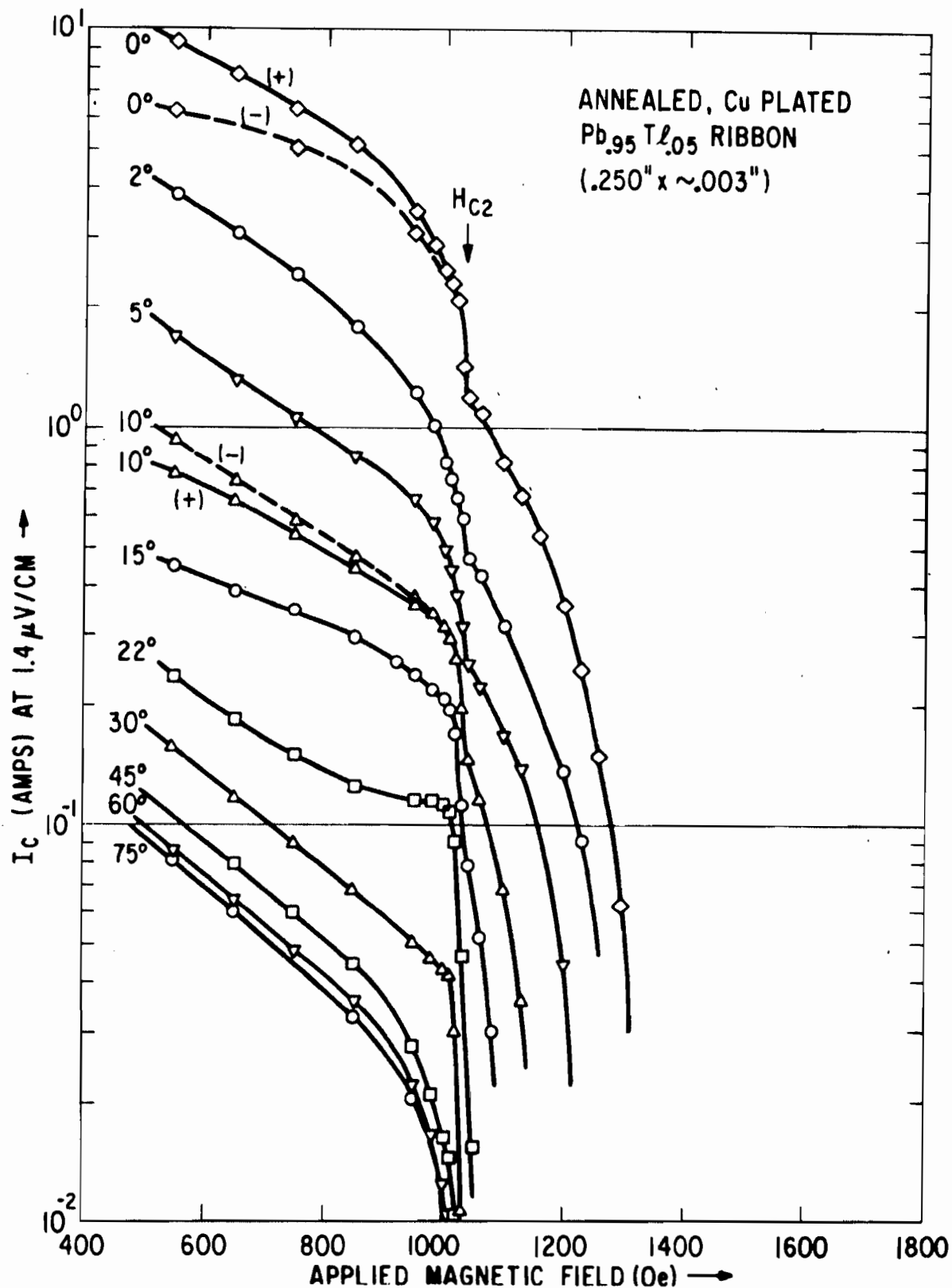
Figure A-4 The experimental family of critical current curves as a function
of magnetic field H and azimuthal angle φ(H⊥I) for the same ribbon as in
Fig. A-3 after electroplating ∼1000 Å of copper on the surface.

176

(b) At H_{c2} there is a sudden change in the magnitude of the critical current.

The following noteworthy features are **not** common to all three families of curves:

(a) At every angle and field the magnitude of the critical current below H_{c2} is greatest for the unannealed ribbon and least for the copperplated ribbon.

(b) Above H_{c2} the magnitude of the critical current is the same for the unannealed and annealed unplated ribbons at all angles except $\varphi = 0°$.

(c) The magnitude of the critical currents above H_{c2} of the annealed, plated ribbon is significantly less at all angles than the critical currents of the other two ribbons.

(d) At intermediate angles the critical current goes through a maximum just below H_{c2} only on the annealed, unplated ribbon. The breadth of these current peaks becomes narrower as the angle φ is increased.

The annealed cylinder of triangular cross section was copperplated over one-half its length[†] (Fig. A-1). A pair of voltage leads was attached separately to each half. The critical transport current of the unplated section was determined as a function of azimuthal angle φ at $H = 700$ Oe (about halfway between H_{c1} and H_{c2}). The results are displayed in Fig. A-5. These results have the following noteworthy features.

(a) The critical current of each polarity goes through a very sharp maximum when the magnetic field vector is aligned parallel to one of the faces.

(b) The magnitude of the critical currents of opposite polarities is significantly different at and near the peaks.

(c) The signs of the larger and smaller critical current peaks interchange at each successive surface.

(d) The larger and smaller critical currents interchange polarity when the sign of the magnetic field vector is reversed (rotation of 180°).

---

†The plating of one-half of a specimen in order to study plated and unplated behavior simultaneously was suggested to us by R. W. Shaw.
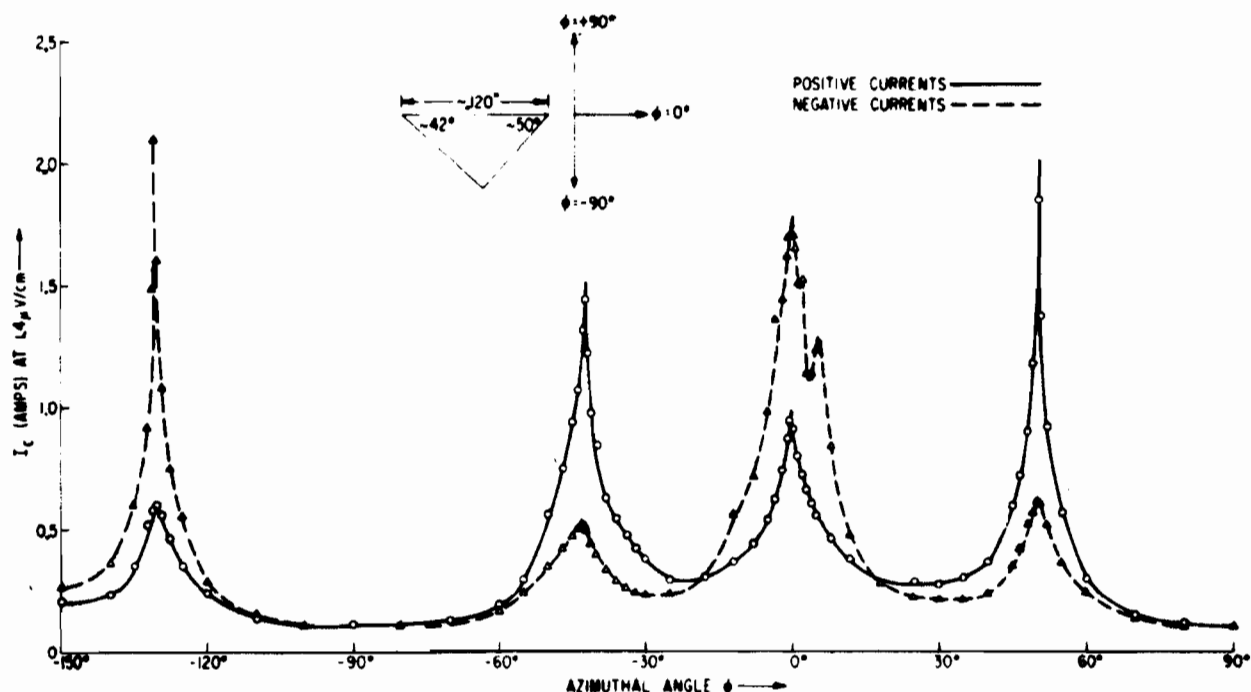
Figure A-5 The critical current of a well-annealed cylinder of triangular
cross section as a function of azimuthal angle $\varphi(H \perp I)$ at a magnetic field
H = 700 Oe. The results demonstrate that critical currents of opposite
polarities go through maxima of significantly different magnitudes when
the magnetic field vector is aligned parallel to a surface.

Below H_{C2} the copperplated portion of the cylinder demonstrated results
essentially the same as those displayed in Fig. A-5, but with the magnitude
of the peaks of each polarity decreased about 50%. In the unplated half of the
sample the critical current went through a maximum as a function of magnetic
field just below H_{C2} when the magnetic field vector simultaneously made an
angle of at least 30° with each of the three surfaces. No critical current
maxima were observed as a function of magnetic field with the copperplated
section.

2. Surface Transport Currents in the Mixed State

In this section we wish to make a single point: the data reveal that
surface transport currents flow in the mixed state. The sharp angular
dependence of the critical transport current below H_{C2} measured on the
unannealed ribbon can tentatively be associated with internal planar defects
that originate in the rolling operation. This point has been demonstrated in
rolled Nb-Zr and Mo-Re alloys. [11] One would expect that this anisotropy,
if associated solely with internal defects, would decrease upon annealing in
a single-phase solid solution. We find instead that the anisotropy increases
with annealing. In Fig. A-6 we display for ribbons in different stages of
annealing the critical current as a function of angle at a field of 900 Oe,
which is well into the mixed state. With unannealed ribbon the critical current

178
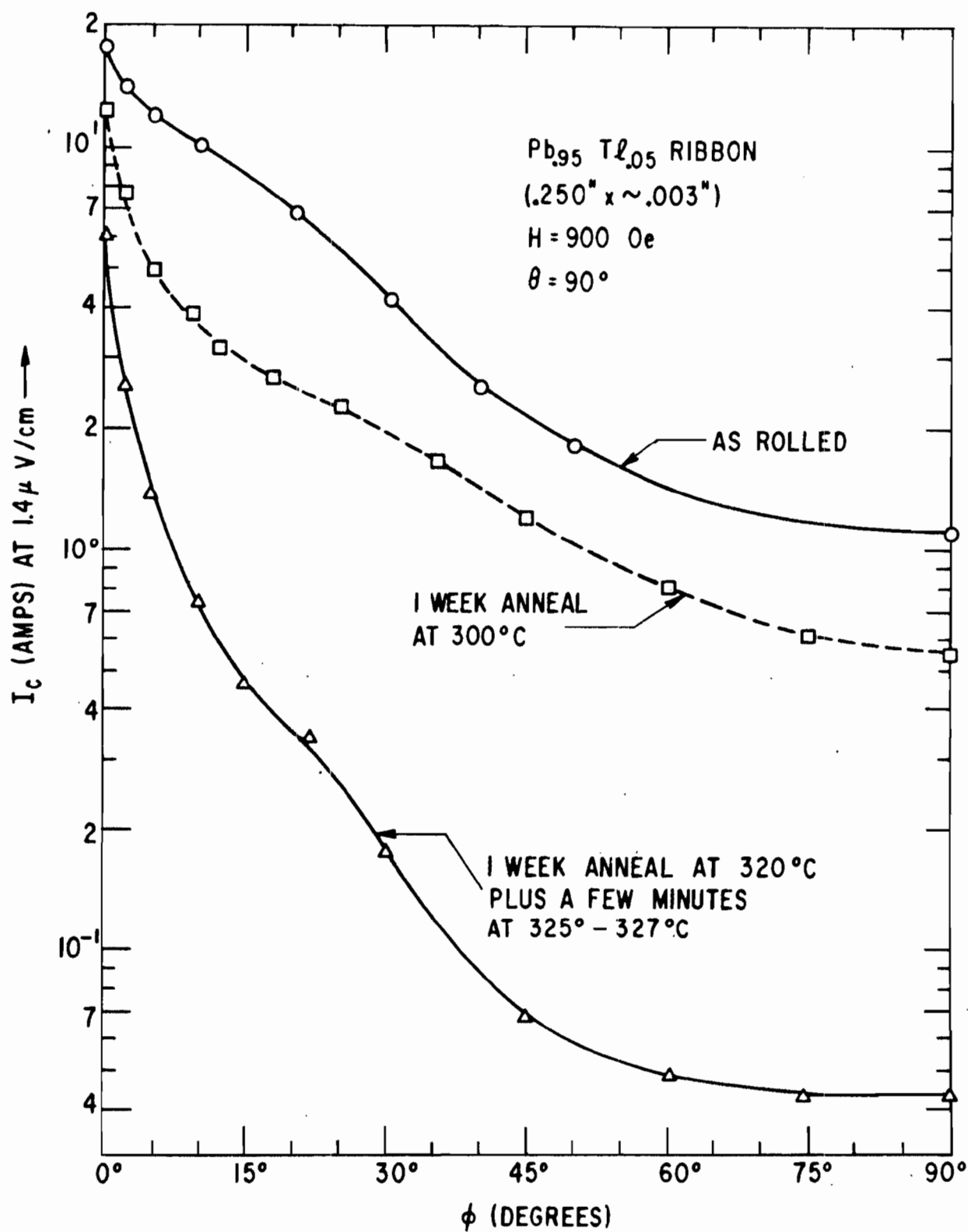
Figure A-6 The angular dependence of critical current for three different ribbons at a magnetic field of 900 Oe and H⊥I. The results indicate that the angular dependence of the critical current increases with annealing.

179

drops slightly over an order of magnitude between $\phi = 0°$ and $\phi = 90°$ (from 17.7 to 1.12 amperes). The well-annealed ribbon, however, shows a drop of over two orders of magnitude, from 6.1 amperes at $\phi = 0°$ to 0.043 ampere at $\phi = 90°$. This suggests that as the anisotropic bulk currents are removed by annealing, a second mechanism of much sharper angular dependence supports the transport supercurrents. We identify this second mechanism with the surface because of the following observations. When the annealed ribbon which displays the very sharp angular dependence is plated with only about 1000 Å of copper, the critical current is significantly reduced at all fields and angles above H_{c1}. The $\phi = 2°$ and $\phi = 30°$ curves before and after plating are taken out of Figs. A-3 and A-4 and displayed separately in Fig. A-7. This observation supports a surface mechanism since the strength of any bulk defect should be insensitive to a thin surface layer of copper. The point that surface currents are indeed sensitive to the copper film is demonstrated in Fig. A-7 by the observation that the critical current is reduced above H_{c2} with copperplating where only the Saint-James and de Gennes surface currents flow. [2, 6]

The argument for transport surface currents in the mixed state is strengthened by the results on the annealed cylinder of triangular cross section. Here the argument cannot be made that the peaks originate from internal rolling planes since only one pair of peaks ($\phi = -42°$) corresponds to a surface parallel to the rolling plane, and yet the three pairs of peaks are generally similar in height and breadth. It is unlikely that planar bulk defects with properties similar to those produced by rolling are introduced by the cutting and sanding operations. In addition, we remove a 0.002- to 0.003-inch surface layer during the polishing operation prior to the anneal.

One of the more convincing arguments for transport surface currents comes from the partial rectification (i.e., unequal critical currents of opposite polarity) of the applied current at and near each peak (Fig. A-5). If rectification were a phenomenon associated with the bulk, then it should appear with equal prominence in the ribbons near $\phi = 0°$, but does not. The triangle is distinguished from the ribbon in the essential feature that the magnetic field vector is parallel to only a single surface at a time rather than two surfaces that are mirror images of one another. We interpret the rectification of current applied to the triangles as one of the stronger arguments that the critical transport currents measured in the mixed state with the annealed ribbons and the cylinder of triangular cross section are predominantly surface currents.
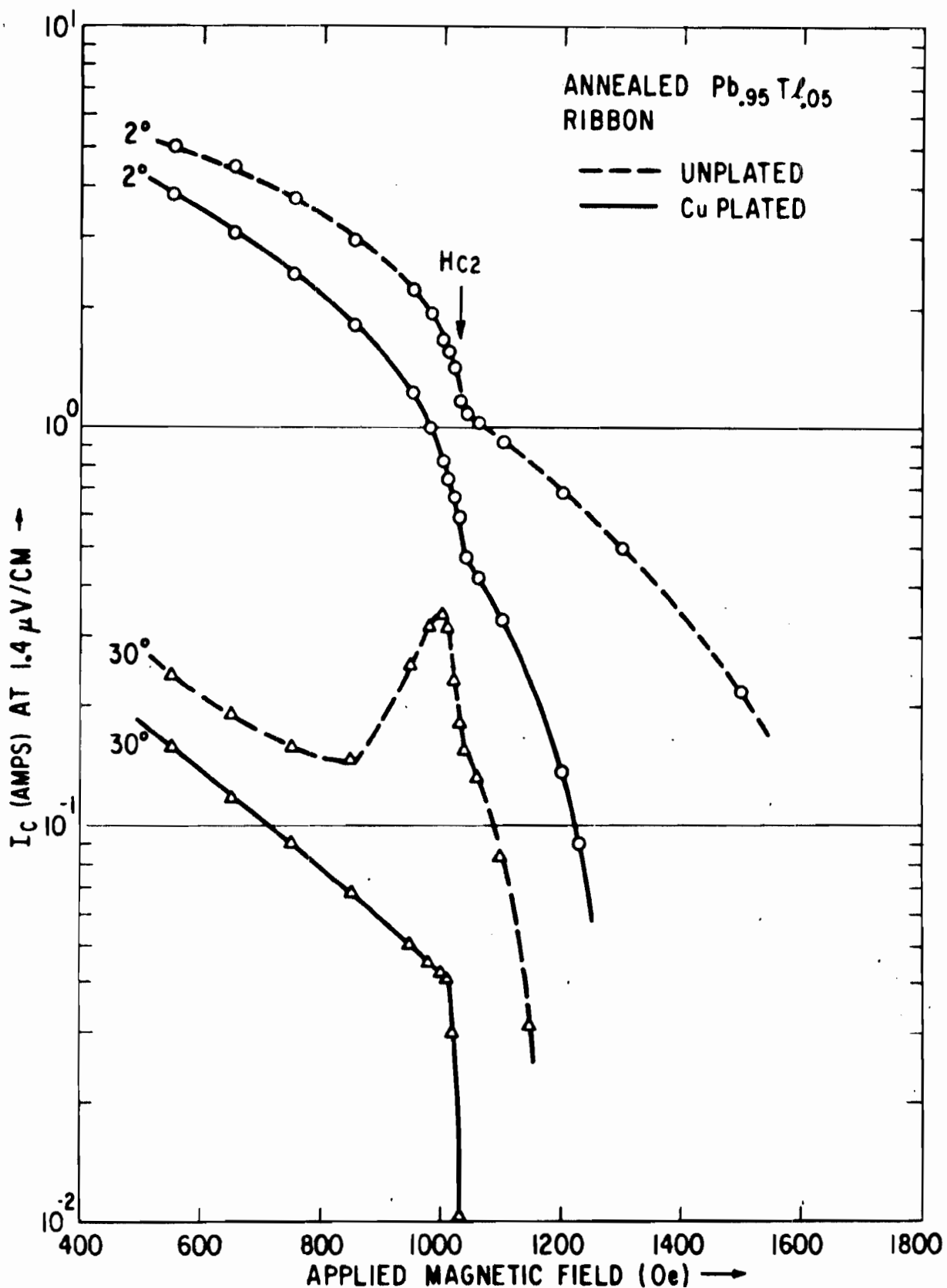
Figure A-7 The critical current as a function of magnetic field at φ = 2°
and φ = 30° of a well-annealed ribbon before and after copper electroplating.
The curves are taken directly from Figs. A-3 and A-4 and displayed
separately here for comparison.

181

3. The Argument for Two Surface Mechanisms in the Mixed State

In this subsection we wish to show that two separate and distinct surface mechanisms contribute to the mixed state surface currents measured on the two well-annealed ribbons (Figs. A-3 and A-4) and the annealed cylinder of triangular cross section. We arrive at this conclusion from the observation that the family of curves displayed in Figs. A-3 and A-4 can be constructed from the sum of two families of curves, each having a significantly different field dependence and each affected to a different degree by the copperplating. We display these two families of curves, denoted mechanism A and mechanism B in Figs. A-8 and A-9. Mechanism A has the assigned property that its contribution to the total mixed state surface current decreases approximately exponentially with increasing field strength and then cuts off sharply at H_{c2}. We tentatively assign to surface mechanism A an effective surface layer thickness on the order of the penetration depth λ. Mechanism B has the assigned property that it yields transport supercurrents that are a maximum at or just below H_{c2} and are roughly symmetric about their maximum. For the present discussion this family of curves is constructed by arbitrarily reflecting the critical current curves above H_{c2}, where no contribution from A exists, about a field just below H_{c2}. We identify mechanism B with the Saint-James and de Gennes surface film having an effective thickness on the order of the coherence length ξ. Following this interpretation, the effect of copper will be somewhat more severe on the currents related to a coherence depth than with a penetration depth as $\lambda \geqslant 2\xi$ in this material. [1]

The "anomalous peaks" that are found at angles intermediate between $\varphi = 0°$ and $\varphi = 90°$ in the annealed, unplated ribbon and in the unplated portion of the annealed triangle can be explained in terms of these two mechanisms. When the magnetic field vector is nearly parallel to a surface, contributions from mechanism A predominate. The currents associated with A show a sharper angular dependence at intermediate angles than those associated with the Saint-James and de Gennes surface sheath. Thus at intermediate angles, the Saint-James and de Gennes mechanism dominates and the currents go through a maximum as a function of magnetic field just below H_{c2}. In this view the current peaks near H_{c2} become sharper as $\varphi \to 90°$ because the critical current curves of the Saint-James and de Gennes surface film above H_{c2} (which are reflected below H_{c2} in mechanism B) drop more sharply with field as $\varphi \to 90°$. At $\varphi = 90°$ the peaks disappear because the Saint-James and de Gennes surface film does not exist; the critical current here is made up from mechanism A plus perhaps a small remnant contribution from the bulk.

Continuing this interpretation, we can understand the disappearance of the "anomalous peaks" after copperplating. The copper reduces the magnitude of the critical currents above H_{c2} where only the Saint-James and de Gennes mechanism exists by a significantly greater fraction than the critical currents well below H_{c2} where only mechanism A contributes. When the curves above H_{c2} (Fig. A-4) are reflected (Fig. A-9) and

182
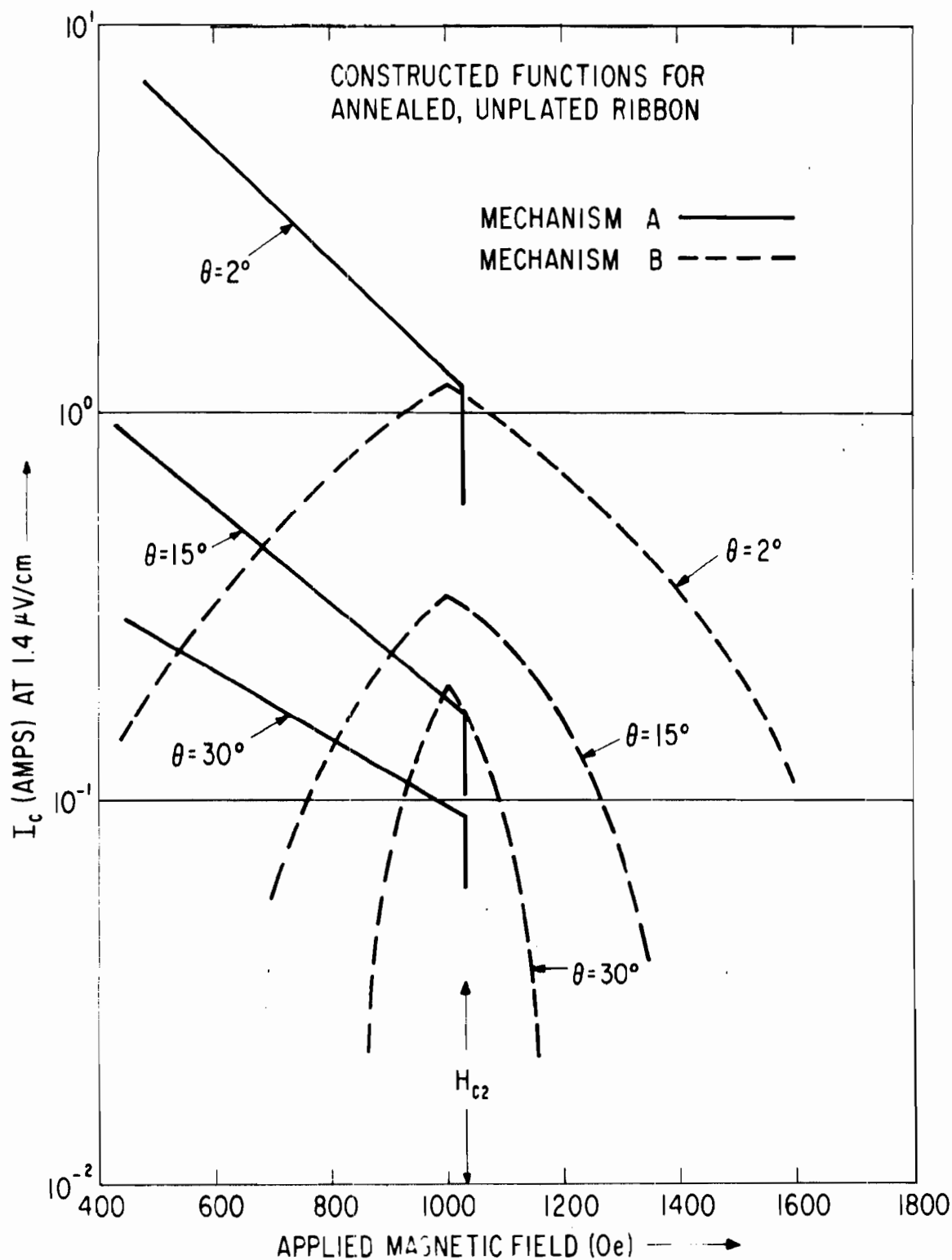
Figure A-8 Two families of constructed critical current curves for a well-annealed, unplated $Pb_{0.95}Tl_{0.05}$ ribbon. They have the property that when added together they result in a family of curves nearly identical to those of Fig. A-3.

183
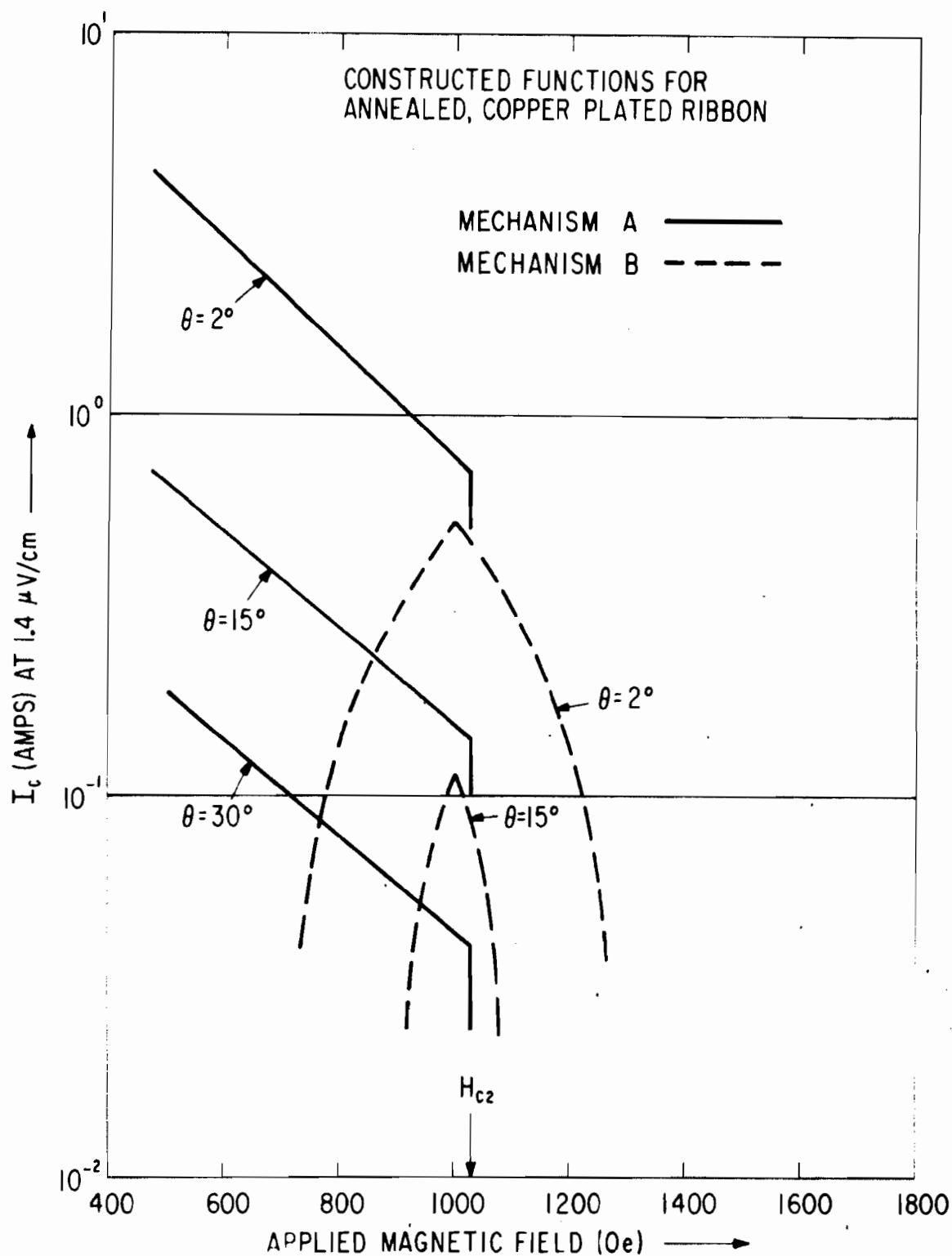
Figure A-9 Two families of constructed critical current curves for a well-annealed, copperplated $Pb_{0.95}Tl_{0.05}$ ribbon. The dashed curve at $\varphi = 30°$ falls below the abscissa and is not shown. The curves have the property that when added together they result in a family of curves nearly identical to those of Fig. A-4.

184

added to the family of exponential curves, which are determined by the critical current well below H_{c_2} in Fig. A-4, the peaks do not appear because the exponential curves dominate at all angles. The peaks do not appear for the unannealed ribbon because the bulk currents dominate at all angles (Fig. A-2).

With the cylinder of triangular cross section, as with the annealed ribbon, the peaks were observed just below H_{c2} (results not displayed) when the magnetic field vector made an angle of at least 30° with each of the three surfaces. The peaks were not present in the copperplated section.

The conclusion of the arguments presented in this subsection is that two mechanisms contribute to the surface supercurrents. Mechanism A is undefined in any detail, but may be associated with the bulk penetration depth λ since its contribution to the total surface current cuts off sharply at H_{c2} and since its contribution is less severely affected by copperplating than is the Saint-James and de Gennes surface film, which is associated with a smaller thickness. The "anomalous peaks" below H_{c2} are simply a measure of the strength of the Saint-James and de Gennes surface film below H_{c2}; the peaks are sharpest at angles where the surface currents above H_{c2} fall off most sharply; they disappear with the same copperplating that significantly reduces the strength of the Saint-James and de Gennes surface currents above H_{c2}.

The finding that above H_{c2} identical critical currents were measured for the annealed (Fig. A-3) and unannealed (Fig. A-2) ribbons for all angles except $\varphi = 0°$ suggests that these measured surface critical currents ($\varphi \neq 0°$) may be fundamental properties of the Saint-James and de Gennes surface film. The annealed sample was polished, then annealed, then tested; the unannealed sample was polished and immediately tested, presumably with a superior surface and thus a higher critical current at $\varphi = 0°$.

4. The Rectification of Surface Transport Currents (See Note Added in Proof)

In many of the ribbons tested we measured small differences in the critical currents of each polarity. [13] Typically this difference is 1% to 2% above H_{c2} and increases to 5% to 10% near H_{c1}; as $\varphi \to 90°$ the critical currents of each polarity become more nearly equal. In the annealed, copperplated ribbon (Fig. A-4) the critical currents of opposite polarity differ by as much as 50% at $\varphi = 0°$ near H_{c1}, but are essentially the same above H_{c2}. In Fig. A-4 the curves shown are those for "positive" current, except at 0° and 10°, where the "negative" critical currents are displayed as well. From 0° to 2° the positive critical currents are larger; at 2° the positive and negative critical currents are about equal; for $\varphi > 2°$ the negative critical currents are larger; as $\varphi \to 90°$ the critical current becomes independent of polarity.

In the cylinder of triangular cross section the difference between critical currents of opposite polarities become significantly more pronounced (Fig. A-5). At the peaks the critical currents of opposite polarities differ by about a factor of three. The signs of the larger and smaller current peaks interchange at each successive surface.

In order to understand better these unusual results, let us first note that the critical current is that current for which some small voltage drop is detected (in this report 1.4 uv/cm). Equivalently, [14] the critical current can be defined as that current which causes a specified amount of magnetic flux to cross the sample per unit time. When the applied magnetic field vector is parallel to a surface carrying a transport supercurrent and perpendicular to the current direction, magnetic flux will cross the surface under the action of the Lorentz force ($\vec{I} \times \vec{H}$) when the critical surface transport current (i. e., a critical surface field gradient) is exceeded. Critical currents of one polarity correspond to magnetic flux crossing the surface from the interior of the sample to the outside; critical currents of the opposite polarity correspond to magnetic flux crossing the surface from the outside in. Similarly, a reversal of magnetic field direction reverses the Lorentz force vector. In terms of this simple treatment it is evident that if magnetic flux can cross a type II surface more easily in one direction than the other, a single surface will support a larger superconducting transport current in one direction than the other. This model also indicates why the sign of the larger current peak reverses at successive surfaces (Fig. A-5) or when the magnetic field vector is rotated 180°; the direction of the Lorentz force reverses in this manner. We find that the larger critical current peaks (Fig. A-5) always correspond to a Lorentz force pushing the flux through the surface from without, revealing that it is more difficult for magnetic flux to cross a surface into a type II superconductor than out of a type II superconductor. The sharp angular dependence of the critical transport current of each polarity means simply that magnetic flux crosses a surface more easily when the flux crosses at an angle and the Lorentz force direction is not perpendicular to the surface. When the magnetic field vector makes a large angle with the surface, the flux crosses easily in either direction and the critical currents of each polarity are equal and very small, revealing that the surface is then ineffective as a barrier to the motion of magnetic flux.

In terms of the discussion above, one can understand why the critical transport current measured in type II ribbons is nearly independent of polarity, even at 0°. When the critical current is reached, magnetic flux crosses both surfaces of the ribbon. One surface is crossed from the outside in; the other, from the inside out. As the results from the triangle demonstrate, each surface of the ribbon will support a significantly different transport current when the critical electric field (1.4 uv/cm) is reached. A ribbon with two identical surfaces will not rectify, however, since the reversal of the Lorentz force simply causes the larger and smaller currents

186

to switch to the opposite surfaces while the total current is unchanged. We interpret the small differences between critical transport currents of opposite polarities occasionally observed in ribbons near $\varphi = 0°$ as caused by a slight difference in the properties of the two surfaces. The larger difference between currents of opposite polarities ($\sim$50%) observed in the annealed copperplated ribbon near H_{c1} and $\varphi = 0°$ is probably related to a better copperplating on one surface than the other.

Since there is at present no theory predicting that the surface of a type II superconductor in the mixed state should act as a barrier to the passage of magnetic flux or that this barrier should be crossed more easily from within than without, it is difficult to say whether the measurements displayed in Figs. A-5 and A-10 (the I-V characteristics of the triangle at H = 700 Oe and $\varphi = 50°$) are ultimate characteristics limited by the quality of the surfaces. Further careful experiments are needed to test this point.
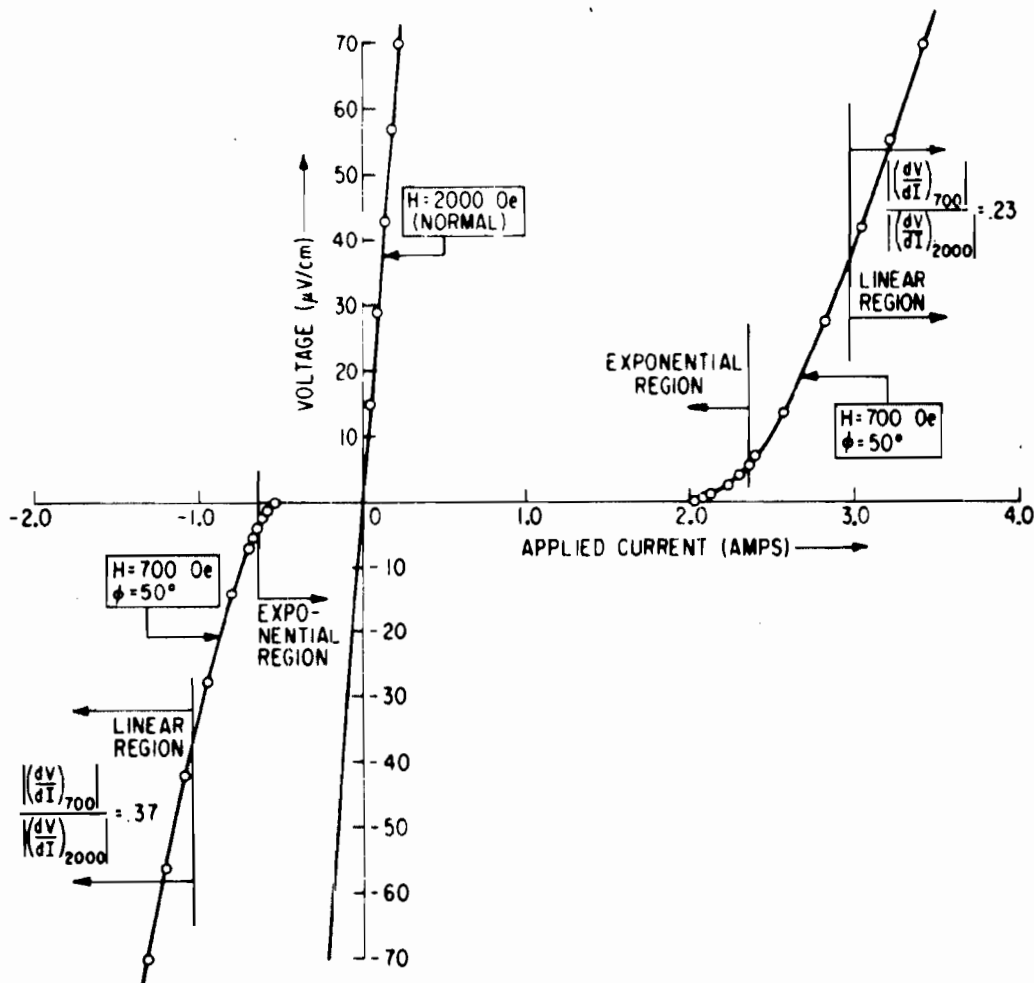
Figure A-10 The voltage vs current transition for the well-annealed cylinder of triangular cross section at H = 700 Oe and $\varphi = +50°$, demonstrating the partial rectification of a superconducting transport current. Initially, the voltage increases exponentially with increasing current, but becomes linear in current as the current is further increased.

187

It is possible that the apparent asymmetry of the surface barrier to the crossing of magnetic flux is not a fundamental property of the barrier but is a nucleation phenomenon related to the fact that any quantized flux line lying within a type II superconductor must break through the surface at some spot. Consider a flux line within the superconductor nearly parallel to a surface and being pushed against the surface barrier by the Lorentz force. The normal spot where the flux line breaks through the surface may weaken the surface barrier locally so that the spot moves down the surface under the influence of the Lorentz force. In this manner the flux line can cross the surface barrier. Magnetic flux being pressed against the surface barrier from without has no such automatic nucleating site available to weaken the barrier locally and permit it to cross. This view of rectification is consistent with the experimental observation that magnetic flux crosses out of a surface more easily than in.

E. SURFACE SUPERCURRENTS: θ VARIED, φ = 0°

We have measured the critical current of the annealed, copperplated ribbon as a function of the angle θ between the magnetic field vector and the transport current, keeping the magnetic field vector in the plane of the ribbon (φ = 0°). Cody, Cullen, and McEvoy[15] have found that Nb_3Sn films obey the Anderson-Kim[14] relationship:

$$J(H\sin\theta + B_0) = \alpha_C \tag{A1}$$

where α_C and B_0 are found to be constants. When we plot I_C^{-1} vs $\sin\theta$ (Fig. A-11) we also find a linear relationship and a constant B_0/α_C ratio. The linear relationship between I_C^{-1} and $\sin\theta$ implies that the Lorentz force controls the magnitude of the surface current when the magnetic field vector is kept in the plane of the surface. The convergence of the straight lines to a single intercept (B_0/α_C) at the ordinate reveals that the strength of the surface superconductivity in the absence of the Lorentz force is a constant independent of the magnetic field over the field range shown and, for this ribbon, equal to about 40 amperes (1/0.026). It is unlikely that this number has fundamental significance. The B_0/α_C ratio is probably a function of surface condition and impurity concentration near the surface. It is also likely that ground planes would further enhance this number by permitting the transport currents to flow more uniformly over the width of the surface. The calculated α_C is not the same at each magnetic field. A variation of α_C with field is not surprising for this low κ material (κ ~ 1.36).[14]

188
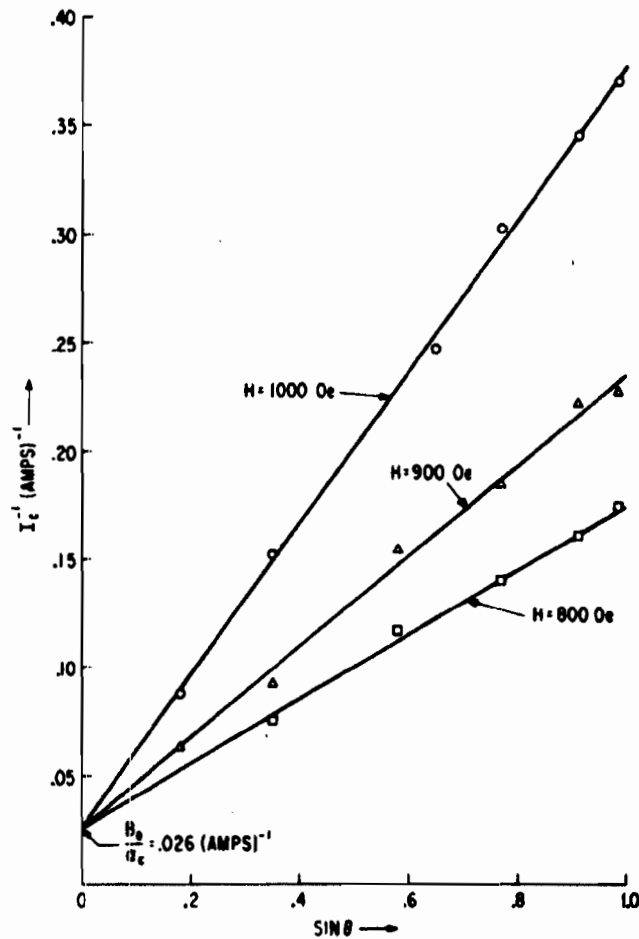
Figure A-11. The inverse of the critical current as a function of the sine of the angle θ between the field and current vectors in the annealed, copper-plated ribbon. The magnetic field vector is kept in the plane of the surface ($\varphi = 0°$). The linear relationship implies that the critical surface current is controlled by the Lorentz force.

F. MIXED STATE RESISTIVITY

The current-voltage transitions of the ribbons in the three different conditions were also studied. Initially the voltage drop increases exponentially with increasing current ($V/L \sim 5 \, \mu v/cm$). Although this exponential region of the transition was not studied in great detail, we developed sufficient data to show that the Anderson-Kim[14] relationship

$$\ln V = K_1 + K_2 J \, (H + B_0) \qquad (A2)$$

does not hold.

As the voltage drop is increased beyond about 40 $\mu v/cm$, the incremental voltage becomes linear with incremental current.[2, 16] Figure A-10 shows the exponential and linear regions observed in the triangle. The linear region

189

covers an order of magnitude in voltage, beyond which the voltage increases faster than linearly with current, suggesting sample heating.

In the linear region we define a differential resistivity dV/dI; in the mixed state dV/dI is smaller than in the normal state. In Fig. A-12 we display for the annealed, unplated ribbon the measured differential resistivity divided by the normal state resistivity (measured at 4.2°K and H = 2000 Oe) vs applied magnetic field for φ equal to 5°, 15°, and 90°. These curves display some interesting features. The resistivity at φ = 90° increases smoothly from zero at a very low magnetic field strength to the normal state resistivity at H_{c2}. We associate this resistivity with the bulk rather than the surface of the ribbon since at 90° the surfaces support very little supercurrent and are ineffective in impeding the motion of the magnetic flux. It is also interesting that the resistivity curve shows no break or change of slope at H_{c1} (~350 Oe).[12] This suggests that the sample enters the mixed rather than the intermediate state when flux first penetrates at a low field. (Because of the large demagnetizing factor of the ribbon at φ = 90°, magnetic flux will break into the surface at a few oersteds rather than at H_{c1}.) As the angle φ is decreased from 90°, the differential resistivity above H_{c2} becomes less than the normal state resistivity and the differential resistivity below H_{c2} becomes less than that measured at φ = 90°. This suggests that surface superconductivity, being strengthened by the decreased angle, is able to participate with the bulk in retarding the motion of magnetic flux through the sample. It may be meaningful to calculate a differential resistivity associated with the surface as a function of angle and field by assuming that the lowering of the resistivity with decreasing angle φ arises from a low resistivity surface layer or flux barrier in addition to the bulk.

The jog in the resistivity curve at H_{c2} for $\varphi \neq 90°$ is not understood. The resistivity curve at φ = 0° could not be determined accurately for the ribbons, because the sample began to heat up soon after the linear region was reached and because the transition became noisy. The scant data we have at 0° indicate that the resistivity is reduced considerably below the curve at φ = 5°.

After the annealed ribbon was copperplated, the resistivity was measured again. The differential resistivity at 90° was unchanged, but the resistivity at the other two angles investigated (φ = 15° and φ = 5°) showed that the differential resistivity had increased and lay closer to the φ = 90° curve. This is consistent with the interpretation of the data taken prior to plating; the copper film weakens the surface contribution to the resistivity, but has no effect on the bulk properties.

The differential resistivity curve was measured on the unannealed ribbon at φ = 90°. This curve was essentially the same as that measured on the annealed sample, though the current at which this linear current-voltage

190
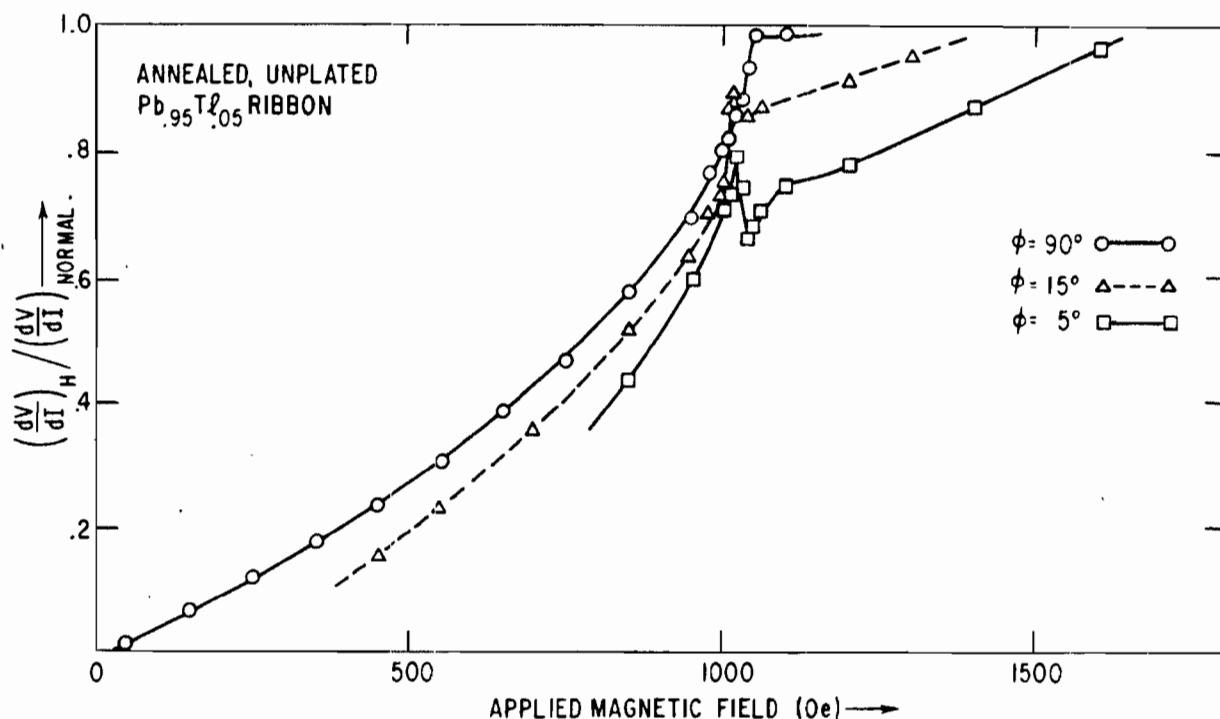
Figure A-12 The normalized differential resistivity of the annealed, unplated
$Pb_{0.95}Tl_{0.05}$ ribbon as a function of magnetic field and azimuthal angle φ
when $H \perp I$. The decrease of resistivity with decreasing angle indicates that
the surfaces contribute to the resistivity when φ is small.

region is found is ~10 times larger. This observation supports the conclusion
that beyond a certain critical current the differential resistivity associated
with the bulk in the mixed state is insensitive to the defect structure. [2, 16]

The angular dependence of the differential resistivity and its interpretation
in terms of a combined surface and bulk resistivity suggests that resistivity
data taken on round wires may include both a bulk and surface contribution.
To minimize the contribution that the surface might make to the determination
of the bulk resistivity in the mixed state, it may prove desirable to choose
a geometry such as a ribbon or film in which the portion of the surface not
orthogonal to the flux lines can be made arbitrarily small.

G. HALL VOLTAGES

An attempt was made to measure the Hall voltage in the mixed state
in the annealed, copperplated ribbon. Voltage probes were placed on
opposite edges of the ribbon. The magnetic field vector was directed
perpendicular to the major surfaces of the ribbon (φ = 90°). This mea-
surement was limited by a spurious effect presumably due to a residual
sample imperfection. Upon our reversing the direction of current flow, the
small transverse electric field did not simply reverse polarity; there was
a change in magnitude as well. This discrepancy (reproducible and magnetic

191

field dependent) was on the same order as the change in magnitude of the transverse electric field upon reversing the applied magnetic field. We thus report that in our sample in the mixed state in the linear portion of the I-V curve the transverse or Hall electric field is less than 2% of the longitudinal electric field. [16]

H. SUMMARY

The basic conclusion of this work is that the surface of a type II superconductor is capable of supporting transport supercurrents in the mixed state, as well as above H_{c2}. The magnitude of these currents is extremely sensitive to the angle between the magnetic field vector and both the surface plane and the current direction. In addition, when the magnetic field vector is perpendicular to the transport current and nearly parallel to a single isolated surface, rather than a pair of parallel surfaces, the magnitude of the critical transport current of each polarity is significantly different.

The family of curves that describes the total superconducting transport current as a function of angle in unplated, and plated annealed ribbons can be related to the sum to two significantly different empirical functions. This leads to the hypothesis that two separate mechanisms contribute to the transport surface current. One of these mechanisms is the Saint-James and de Gennes surface film. It has the postulated property that its strength in supporting transport currents is a maximum at or just below H_{c2} and that its strength, which is strongly angular dependent, falls off roughly symmetrically on each side of H_{c2} (or a field slightly below H_{c2}). The second surface mechanism is undefined, but characterized by the property that its current-carrying capacity decreases approximately exponentially with increasing field beyond H_{c1} and cuts off sharply at H_{c2}. The Bean-Livingston surface barrier may contribute to such a mechanism.

The "anomalous peaks" in the curves of critical current vs magnetic field are observed experimentally in annealed $Pb_{0.95}Tl_{0.05}$ when the magnetic field vector makes an angle intermediate between $\varphi = 0°$ and $\varphi = 90°$. They disappear when copper is plated on the sample, supporting the interpretation that they are of a surface origin in the samples investigated. They apparently result from the field and angular dependence of the Saint-James and de Gennes surface film below H_{c2}.

The absolute magnitude and angular dependence of the critical currents reported for the triangle and the ribbons are probably not a true measure of surface properties. They are certainly sensitive to some degree to surface contamination and surface smoothness. These transport current curves also probably include a small bulk contribution. The presence of a ground plane should serve to increase the magnitude of the surface transport currents when the magnetic field vector lies parallel to the surface plane. The transport current curves measured on the ribbons suffer from an effect revealed by the

192

results of the triangle--when the magnetic field is nearly parallel to the ribbon, the two surfaces contribute unequally to the total transport current. Moreover, the larger of the two currents has a much sharper angular dependence. These currents can be separated in the case of the cylinder of triangular cross section. Even here there was no ground plane and the faces of the cylinder could not be made as smooth and planar as those of the ribbon.

A differential resistivity can be measured in the mixed state when the transport current significantly exceeds the critical transport current. This mixed state resistivity drops sharply from the normal state resistivity below H_{c2} and approaches zero resistivity at very low magnetic fields. When the magnetic field vector is perpendicular to the plane of the ribbon and the contribution of the surfaces to the critical current is virtually eliminated, the measured mixed state resistivity is attributed to the bulk. This resistivity is the same in the annealed and unannealed ribbons and consequently independent of the defect structure. At intermediate angles the surfaces contribute to the superconductivity and the measured differential resistivity is decreased.

In the absence of theories predicting the phenomena we have observed, we cannot state the generality of the various effects. It should prove interesting and fruitful to explore these phenomena as a function of surface preparation and contamination, of geometry, and of the Ginzburg-Landau parameter κ.

NOTE ADDED IN PROOF

Further studies of rectification (to be published) indicate that the mechanism described below is more likely than that described in Appendix D-(D). Figures A-2 through A-6 show that the surface critical current for a macroscopic sample exhibits a sharp angular peak; any small magnetic field component perpendicular to the surface decreases the critical current. If a sharp angular peak occurs locally for each microscopic region, we can obtain the critical current for the sample by summing the critical currents for the microscopic regions where the local critical currents are determined by the local perpendicular fields $H_\perp(\vec{r})$:

$$H_\perp (\vec{r}) = H_{\perp a}(\vec{r}) + H_{\perp d}(\vec{r}) + H_{\perp j}(\vec{r}) \; . \tag{A3}$$

Here $H_{\perp a}$ is the local perpendicular field applied externally, $H_{\perp d}$ is that resulting from the superconducting diamagnetic currents, and $H_{\perp j}$ is that due to the applied transport current in the sample. If an applied current of one sign gives an $H_{\perp j}(r)$ which tends to cancel the other two terms, a large critical current will be measured, for $H_\perp(r)$ will be small. An applied current of the opposite sign then yields an $H_{\perp j}(r)$ which adds to the other two terms, increasing $H_\perp(r)$ and decreasing the critical current. Rectification can thus occur in a type II superconductor that has a sharp angular peak in the critical current (it is not necessary that the current be a surface current) and some appropriate local perpendicular field distribution. All rectification experiments performed to date are consistent with this interpretation.

A simple example is a strip having a cross section, viewed along the long axis, of a circular arc of a large radius of curvature. The applied magnetic field, when parallel to the chord of the arc, yields a perpendicular field component varying linearly with distance across the strip, going through zero and changing sign at the midpoint. Applied currents of one polarity decrease the total perpendicular field, yielding a large critical transport current. With the opposite polarity, the perpendicular components add and a small critical transport current results. Rectification ratios as large as 5:1 have been obtained in this way. The triangular sample described in this report apparently rectified because the polishing yielded slightly curved surfaces. It is also possible to rectify with a flat sample and a curved applied field, achieved from separate current-carrying field control wires. Rectification ratios as large as 3:1 have been observed in this manner. In 1962, H. H. Edwards and V. L. Newhouse observed rectification in thin tin films using this technique [J. Appl. Phys., 33, 868 (1962)].

REFERENCES FOR APPENDIX A

1. A. A. Abrikosov, J. Phys. Chem. Solids, 2, 199 (1957).

2. C. F. Hempstead and Y. B. Kim, Phys. Rev. Letters, 12, 145 (1964).

3. H. R. Hart, Jr. and P. S. Swartz, Phys. Letters, 10, 40 (1964).

4. G. Bon Mardion, B. B. Goodman, and A. Lacaze, Phys. Letters, 8, 15 (1964).

5. W. J. Tomasch and A. S. Joseph, Phys. Rev. Letters, 12, 148 (1964); M. Cardona and B. Rosenblum, Phys. Letters, 8, 308 (1964); S. Gygax, J. L. Olsen, and R. H. Kropschot, ibid., p. 228; Myron Strongin, Arthur Paskin, Donald G. Schweitzer, O. F. Kammerer, and P. P. Craig, Phys. Rev. Letters, 12, 442 (1964); J. P. Burger, G. Deutscher, E. Guyon, and A. Martinet, Phys. Rev., 137, A853 (1965).

6. D. Saint-James and P. G. de Gennes, Phys. Letters, 7, 306 (1964).

7. C. P. Bean and J. D. Livingston, Phys. Rev. Letters, 12, 14 (1964).

8. R. W. DeBlois and W. DeSorbo, ibid., p. 499.

9. A. S. Joseph and W. J. Tomasch, ibid., p. 219.

10. W. DeSorbo, Rev. Mod. Phys., 36, 90 (1964); S. H. Autler, E. S. Rosenblum, and K. H. Gooen, Phys. Rev. Letters, 9, 489 (1962); J. F. Schenk, J. S. Willis, and R. W. Shaw, Phys. Letters, 11, 285 (1964).

11. T. G. Berlincourt, R. R. Hake, and D. H. Leslie, Phys. Rev. Letters, 6, 671 (1961); J. J. Hauser and R. G. Trenting, J. Phys. Chem. Solids, 24, 371 (1962); R. R. Hake and D. H. Leslie, J. Appl. Phys., 34, 270 (1963); R. R. Hake, D. H. Leslie, and C. G. Rhodes, Proc. 8th Intern. Conf. Low Temp. Physics, Butterworth's Scientific Publications, Ltd., London (1963), p. 342.

12. J. D. Livingston, Phys. Rev., 129, 1943 (1963).

13. M. A. R. LeBlanc, Rev. Mod. Phys., 36, Discussion, p. 97 (1964).

14. P. W. Anderson and Y. B. Kim, Rev. Mod. Phys., 36, 39 (1964); Y. B. Kim, C. F. Hempstead, and A. R. Strnad, Rev. Mod. Phys., 36, 43 (1964).

15. G. D. Cody, G. W. Cullen, and J. P. McEvoy, Jr., ibid., p. 95.

16. J. Volger, F. A. Staas, and A. G. van Vijfeijken, Phys. Letters, 9, 303 (1964); P. H. Borcherds, C. E. Gough, W. F. Vinan, and A. G. Warren, Phil. Mag., 10, 349 (1964); W. F. Druyvesteyn and J. Volger, Philips Res. Repts., 19, 359 (1964).

PARTIAL RECTIFICATION IN TYPE II SUPERCONDUCTORS
(P. S. Swartz and H. R. Hart, Jr.)

A. INTRODUCTION

It is well accepted that the large critical current densities which certain type II superconductors can support in the mixed state ($H_{c1} < H < H_{c2}$) are predominantly bulk currents. [1] It has recently been shown, however, that the surfaces of a type II superconductor can support a supercurrent in addition to that associated with the intrinsic or reversible magnetization of the mixed state itself. The work of the Brookhaven group[2] has demonstrated that diamagnetic a-c surface currents can be induced by a small alternating magnetic field collinear with a steady field, both in the mixed state and also in the region of the Saint-James and de Gennes[3] surface film ($H_{c2} < H < H_{c3}$). Swartz and Hart[4] have shown that the surface of a type II superconductor is capable of supporting a superconducting transport current between H_{c1} and H_{c3}. The magnitude of this surface current is found to be very sensitive to the angle that the magnetic field vector makes with the surface being explored; the current-carrying capacity is large when the magnetic field is parallel to this surface, and drops sharply as the magnetic field vector is turned into the plane of the surface. As we shall see, the diamagnetism of the surface to small alternating magnetic fields and the ability of the surface to support a superconducting transport current both demonstrate that the surface of a type II superconductor is effective as a barrier to the crossing of magnetic flux. (See Note Added in Proof, p. 220.)

In this Appendix, we illustrate several methods by which the surface properties of a type II superconductor can be utilized to make the critical transport currents of opposite polarity unequal. We define this property as "partial rectification" since such a superconductor displays I-V characteristics as those shown in Fig. B-1. We have found that there are two separate and distinct surface properties that make partial rectification possible. One type of rectifier, which we denote as the "class I rectifier," rests on the newly found phenomenon that the effective height of the surface barrier to the crossing of magnetic flux depends on the direction from which the magnetic flux encounters the surface barrier. Magnetic flux that encounters the surface barrier from the inside of the specimen crosses the surface barrier more easily than magnetic flux encountering the surface barrier from the outside. The largest rectification ratios (i. e., critical transport currents of one polarity divided by the critical currents of the opposite polarity) that we have observed in class I rectifiers are ∼1. 4:1.

A second type of rectifier, which we denote as the "class II rectifier," relates only to the sharp dependence of the transport surface currents with the angle that the local magnetic field vector makes with each element of the surface plane. [5] Edwards and Newhouse[6] have earlier produced

VOLTAGE (μV/cm) →

H=2000 Oe (NORMAL)

$$\frac{\left|\left(\frac{dV}{dI}\right)_{700}\right|}{\left|\left(\frac{dV}{dI}\right)_{2000}\right|} = .23$$

LINEAR REGION

EXPONENTIAL REGION

H=700 Oe ϕ=50°

70
60
50
40
30
20
10

-2.0   -1.0   0   1.0   2.0   3.0   4.0

APPLIED CURRENT (AMPS) →

H=700 Oe ϕ=50°

EXPO-NENTIAL REGION

-10
-20
-30
-40
-50
-60
-70

LINEAR REGION

$$\frac{\left|\left(\frac{dV}{dI}\right)_{700}\right|}{\left|\left(\frac{dV}{dI}\right)_{2000}\right|} = .37$$
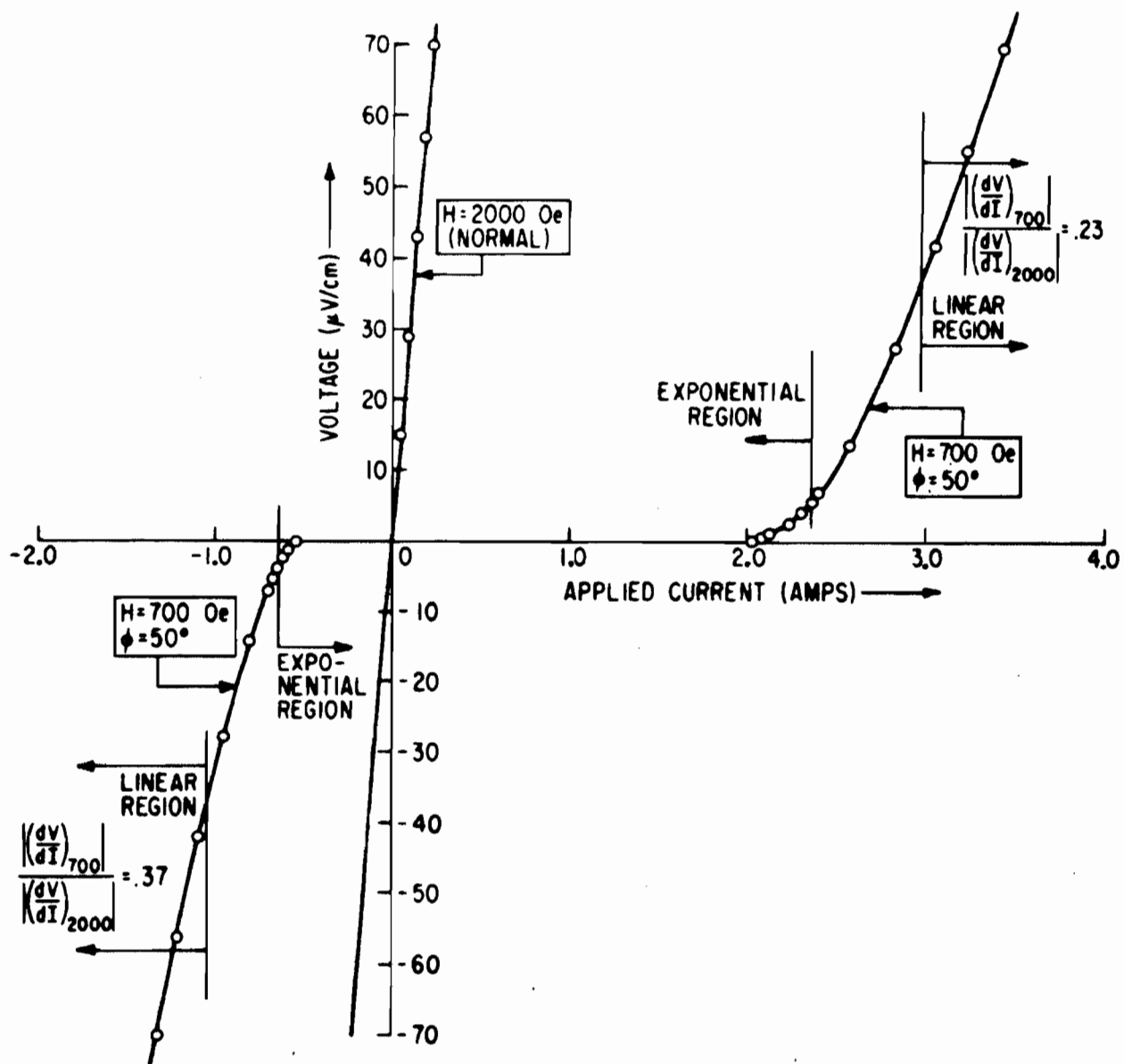
Figure B-1 The voltage vs current transition for a well-annealed triangular prism of $Pb_{0.95}Tl_{0.05}$. A magnetic field of 700 Oe is directed parallel to one of the surfaces and perpendicular to the transport current. The curve demonstrates that the critical currents of opposite polarity are unequal (reproduced from Ref. 4).

partial rectification in cryotron devices utilizing this angular dependence in evaporated type I films. With class II rectifiers we have achieved rectification ratios as large as 5:1 in bulk type II samples in the mixed state.

We divide this Appendix into three sections. The first two sections are devoted to the class I and II rectifiers, respectively. Each of these sections

is divided into three parts: 1. Principles of Operation; 2. Experiments; and 3. Discussion. The final section is devoted to general remarks and a summary.

B. CLASS I RECTIFIERS

1. Principles of Operation

It is convenient to describe class I rectifiers in terms of the properties of a surface barrier to the crossing of magnetic flux in the mixed state. We shall show first that the ability of a superconductor to support a superconducting surface transport current in the mixed state can be interpreted as evidence for a barrier to the crossing of magnetic flux. We shall then show how partial rectification of a transport supercurrent can come about if the surface barrier has certain properties.

Consider a type II superconducting ribbon of unit width that is well annealed and homogeneous so that no pinning sites exist in the bulk, and no bulk supercurrents flow. We apply a magnetic field of magnitude between H_{c1} and H_{c2} parallel to the surface planes and perpendicular to the long axis of the ribbon. We find experimentally that such a ribbon will support a surface transport current, I_t. We define the critical surface transport current, I_c, as that current for which some small voltage drop is detected. Equivalently, I_c can be defined as that current which causes a specified amount of magnetic flux to cross the sample per unit time. [7] When the magnetic field vector is parallel to a surface carrying a transport super-current and perpendicular to the current direction, magnetic flux will cross the surface under the action of the Lorentz force ($I \times H$) when I_c is exceeded. Since a surface transport current produces a field change at the surface, we may equivalently define a critical surface field drop, or barrier, that must be exceeded before magnetic flux can cross the surface. If we assume for the example given here that the transport current divides equally between the two surfaces, we may define the critical barrier height as

$$\Delta H_{crit} = 4\pi I_c/20 \ . \tag{B1}$$

When critical conditions are reached, equal magnetic flux crosses both surfaces of the ribbon. For critical current of one polarity, one of the surface barriers is crossed from the outside-in and the second surface from the interior to the outside; for critical currents of the opposite polarity, the first surface barrier is crossed from the interior to the outside and the second surface from the outside-in. Similarly, a reversal of magnetic field direction reverses the Lorentz force vector. In terms of this simple treatment it is evident that, if magnetic flux can cross the surface barrier more easily in one direction than the other, a single surface will support a larger superconducting transport current in one direction than the other, and partial rectification will occur. A ribbon, having two oppositely directed

surfaces, will not rectify. In that case the total transport current measures the sum of unequal transport current supported by each surface. When either the polarity of the transport current or the direction of the applied magnetic field is reversed, the accompanying reversal of the Lorentz force vector simply switches the larger and smaller transport currents to the opposite surface, and no rectification of the total transport current is detected. It is evident, then, that if the barrier to the crossing of magnetic flux is direction dependent, rectification by this mechanism cannot be observed in type II superconductors in which the effects cancel through symmetry arguments.

2. Experiments

In our earlier work, [4] we attempted to test this hypothesis of rectification by measuring the critical transport current of a well-annealed $Pb_{0.95}Tl_{0.05}$ triangular prism in which the only transport supercurrents that could flow were found to be surface currents. Since the critical transport current is observed to decrease rapidly with the angle that the applied magnetic field vector makes with the surface, we were able to explore the properties of a single surface when the applied magnetic field was aligned parallel to one of the three surfaces of the prism. We observed rectification ratios as large as 3:1 (see Fig. B-2) and, at the time, concluded that this experimental evidence supported the hypothesis given above. The surfaces
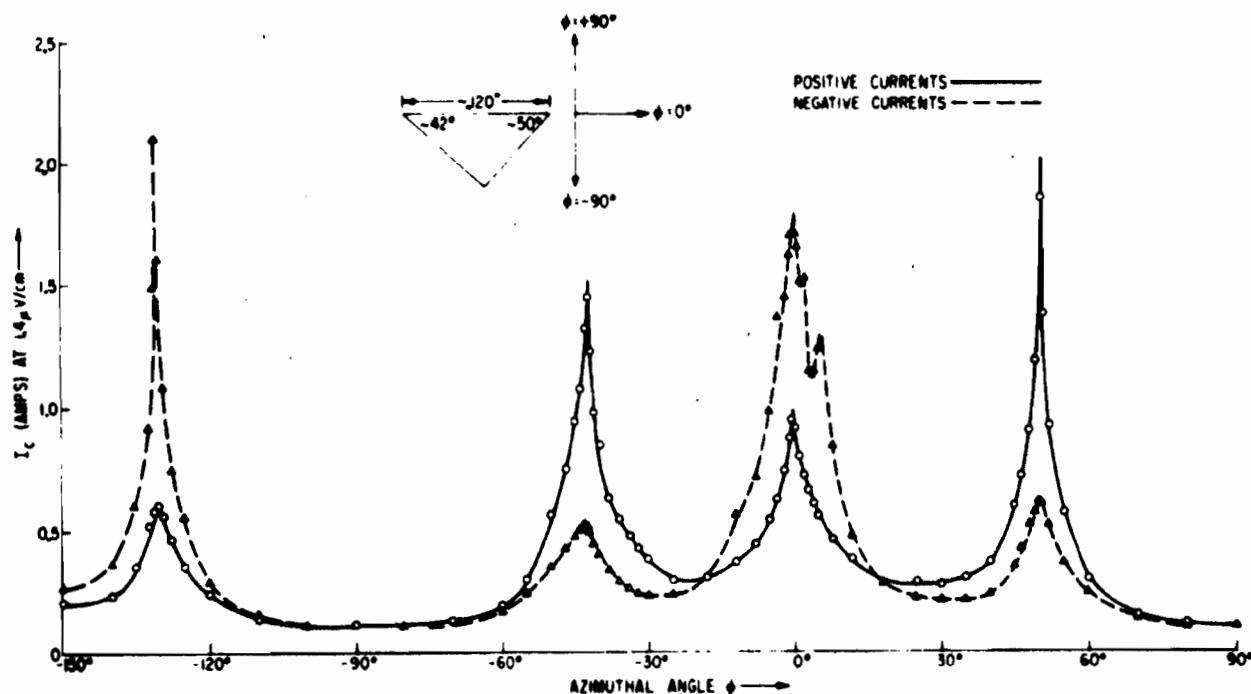
Figure B-2 The critical current of a well-annealed triangular prism of $Pb_{0.95}Tl_{0.05}$ as a function of azimuthal angle φ (H⊥I) at a magnetic field of H = 700 Oe. The results demonstrate that the critical currents of opposite polarities go through maxima of significantly different magnitudes when the magnetic field vector is aligned parallel to a surface (reproduced from Ref.4).

of this prism were very slightly curved through the polishing operation and, as we later came to appreciate (see Note in Proof in Ref. 4), such a sample rectifies for wholly different reasons. A triangular prism with slightly curved surfaces is an excellent example of the class II rectifier to be discussed in Section C.

In an attempt to provide a valid test to the hypothesis that magnetic flux can cross the surface barrier more easily in one direction than the other, a sequence of experiments has been performed with ribbons having compositional gradients across their thickness. We describe these experiments below and outline the significant features of the results. The discussion follows the description of all of the experiments. In each of the five experiments, we report the results only for magnetic field orthogonal to the transport current and parallel to the surface plane(s) carrying the transport current.

(a) Experiment I

An alloy of $Pb_{0.90}Tl_{0.10}$ is cold-rolled to 0.009 inch and polished. A ribbon 2 inches by 0.250 inch is cut from this sheet, and current and voltage leads are attached. The critical current (defined at a voltage level of 0.5 $\mu v/cm$) is measured at 4.2°K as a function of a perpendicular magnetic field applied parallel to the major planes of the strip. The results are shown in Fig. B-3. We summarize the significant features as follows:
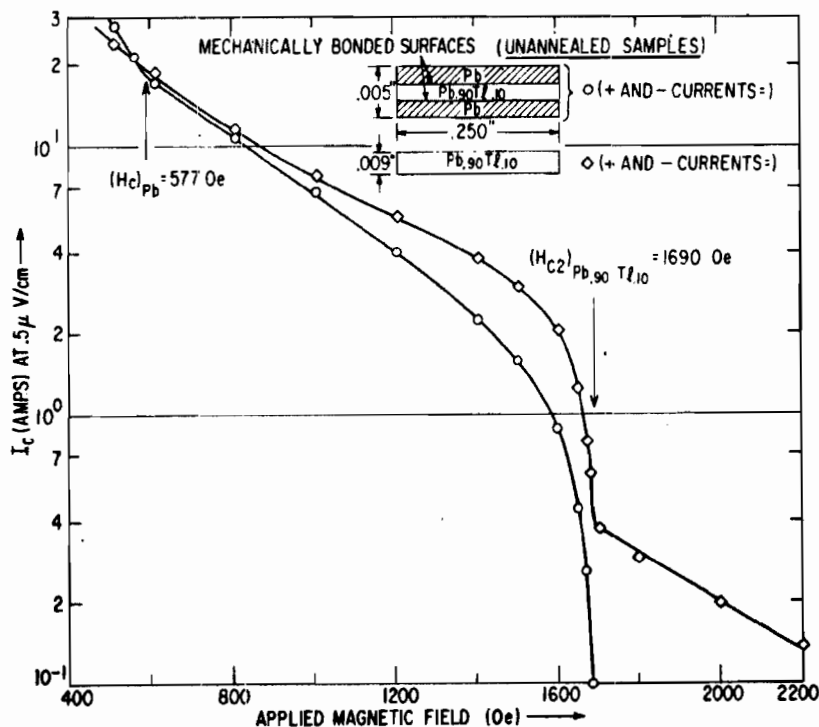
Figure B-3 The critical currents of an unannealed $Pb_{0.90}Tl_{0.10}$ ribbon and an unannealed Pb-$Pb_{0.90}Tl_{0.10}$-Pb "sandwich" with the magnetic field parallel to the surface plane. The results show that no rectification occurs.

(i) The critical transport currents of opposite polarity are equal.

(ii) H_{c_2} is measurable as the sharp change in critical current at 1690 Oe.

(b) Experiment II

A metal sandwich of Pb-Pb$_{0.90}$Tl$_{0.10}$-Pb is formed by cold-rolling together equal thicknesses of the three metal sheets. At the final total sandwich thickness of 0.005 inch, the three metal sheets are mechanically inseparable. A ribbon is cut, polished, mounted, and tested in the same manner as in Experiment I. The results are also shown in Fig. B-3. The significant features are:

(i) The critical currents of opposite polarity are equal.

(ii) The critical current drops essentially to zero at H = 1690 Oe.

(iii) The slope of the critical current with field changes in the vicinity of the pure lead transition (577 Oe).

(c) Experiment III

A bimetallic strip of Pb-Pb$_{0.90}$Tl$_{0.10}$ is formed by cold-rolling together equal thicknesses of the two metal sheets. At its final total thickness of 0.005 inch, the two metal sheets are mechanically inseparable. Subsequent procedure follows that described in the preceding experiments. The significant results are (see Figs. B-4 and B-5):

(i) The critical currents of opposite polarity are unequal from the lowest fields tested (500 Oe) to magnetic fields close to H_{c_3} ($\sim$2900 Oe).

(ii) From about 600 Oe to fields close to H_{c_3}, the larger critical currents correspond to magnetic flux crossing the outer Pb$_{0.90}$Tl$_{0.10}$ surface from the outside-in.

(iii) Below about 600 Oe the larger critical currents correspond to magnetic flux crossing the outer pure Pb surface from outside-in.

(iv) The largest rectification ratio occurs near H = 1200 Oe and is about 1.3:1.

(v) The pure lead transition at 577 Oe and the H_{c_2} transition of the alloy at 1690 Oe are clearly defined in the figure by the sharp change in slope.

(d) Experiment IV

A bimetallic strip prepared in a manner identical to that used in Experiment III is annealed for 60 hours at 200°C and 1 hour at 320°C in a vacuum of 10^{-6} to 10^{-7} mm Hg. The sample is then mounted and tested in the way described earlier. The significant results are summarized as follows (see Figs. B-6 through B-8).
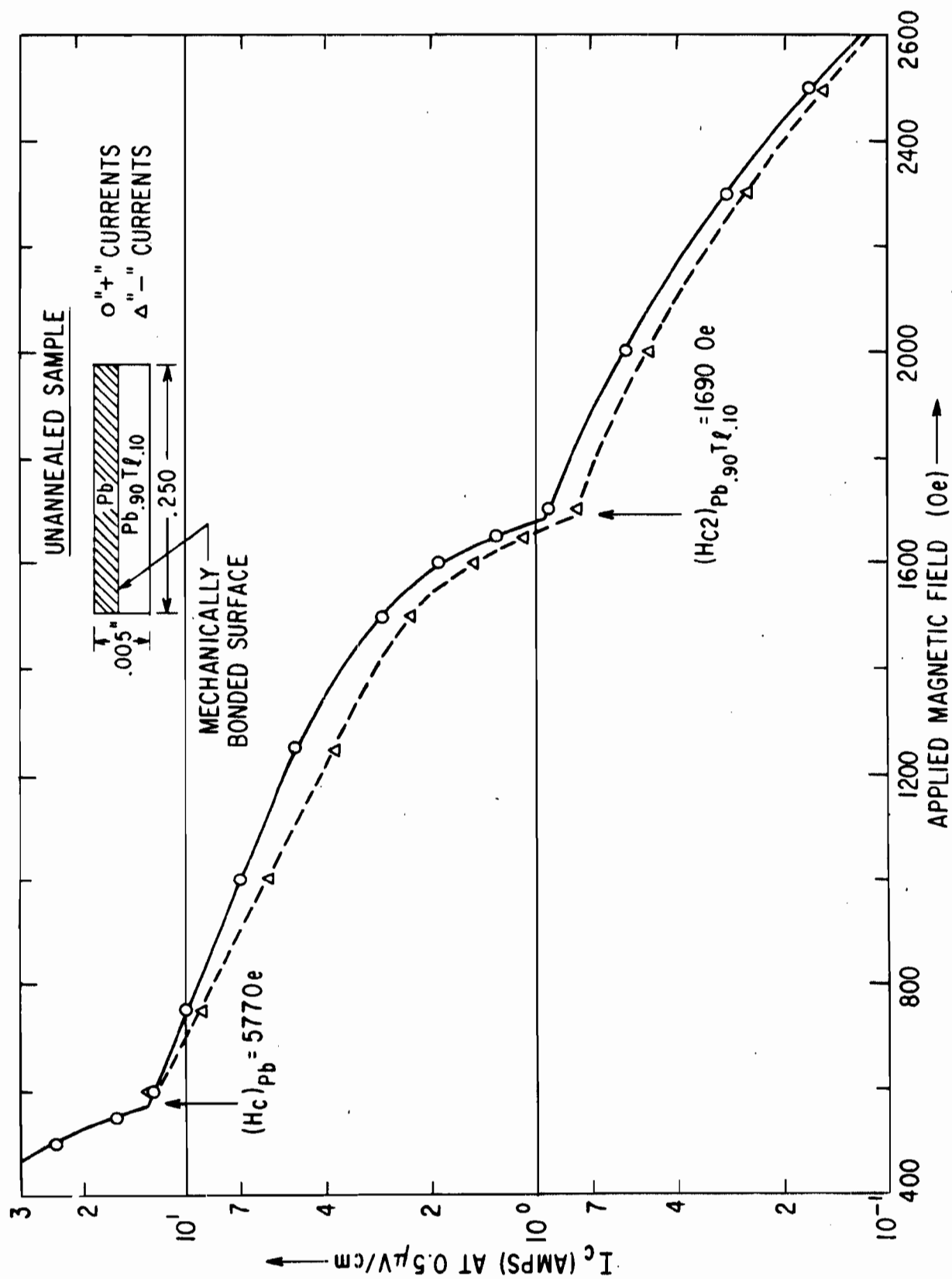
Figure B-4 The critical currents of an unannealed $Pb-Pb_{0.90}Tl_{0.10}$ bimetallic strip as a function of magnetic field applied parallel to the surface plane. Partial rectification of the transport current is observed.
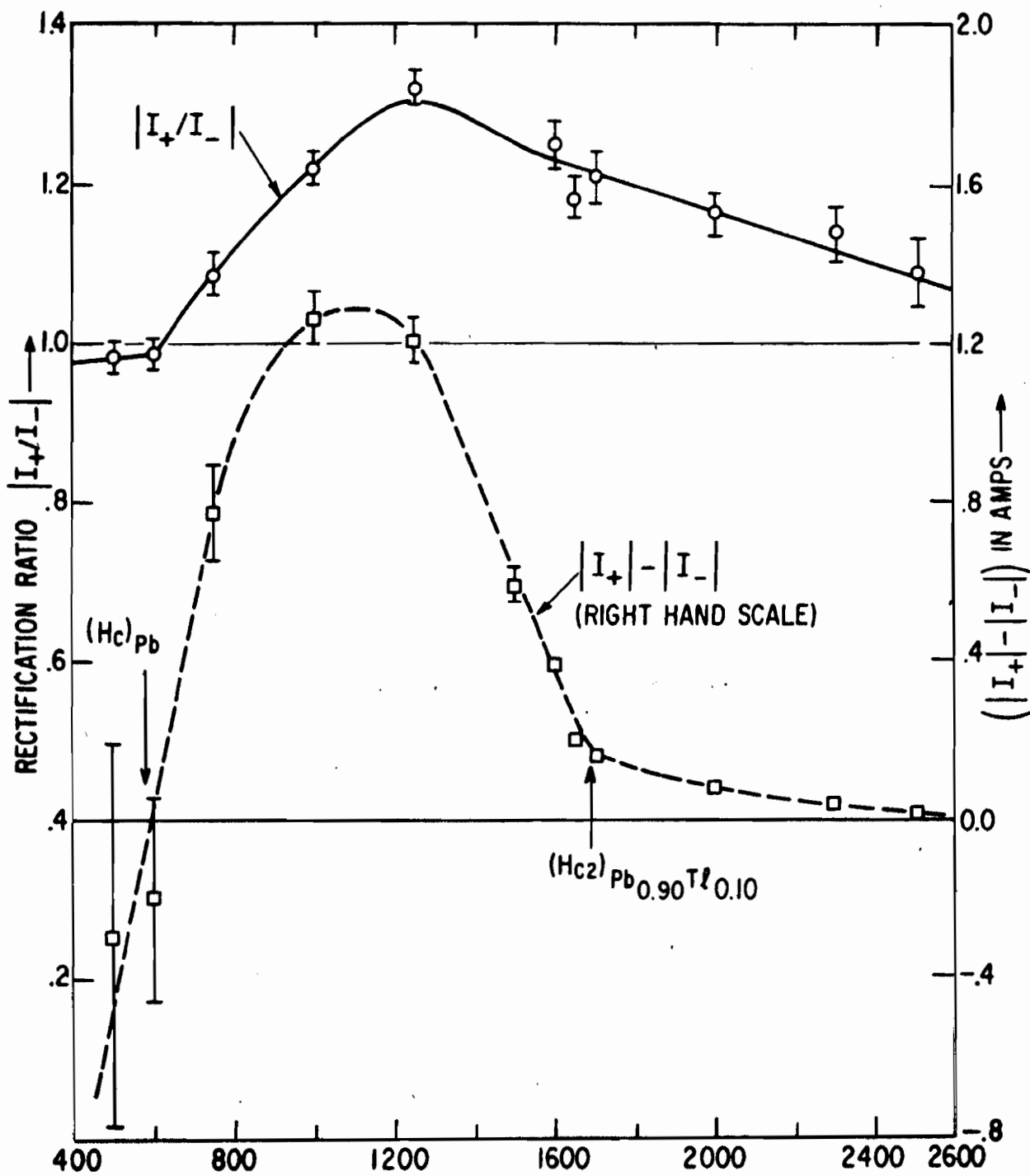
Figure B-5 The rectification ratio ($|I_+/I_-|$) and the difference in critical currents of opposite polarity ($|I_+| - |\bar{I}_-|$) for the curves of Fig. B-4.
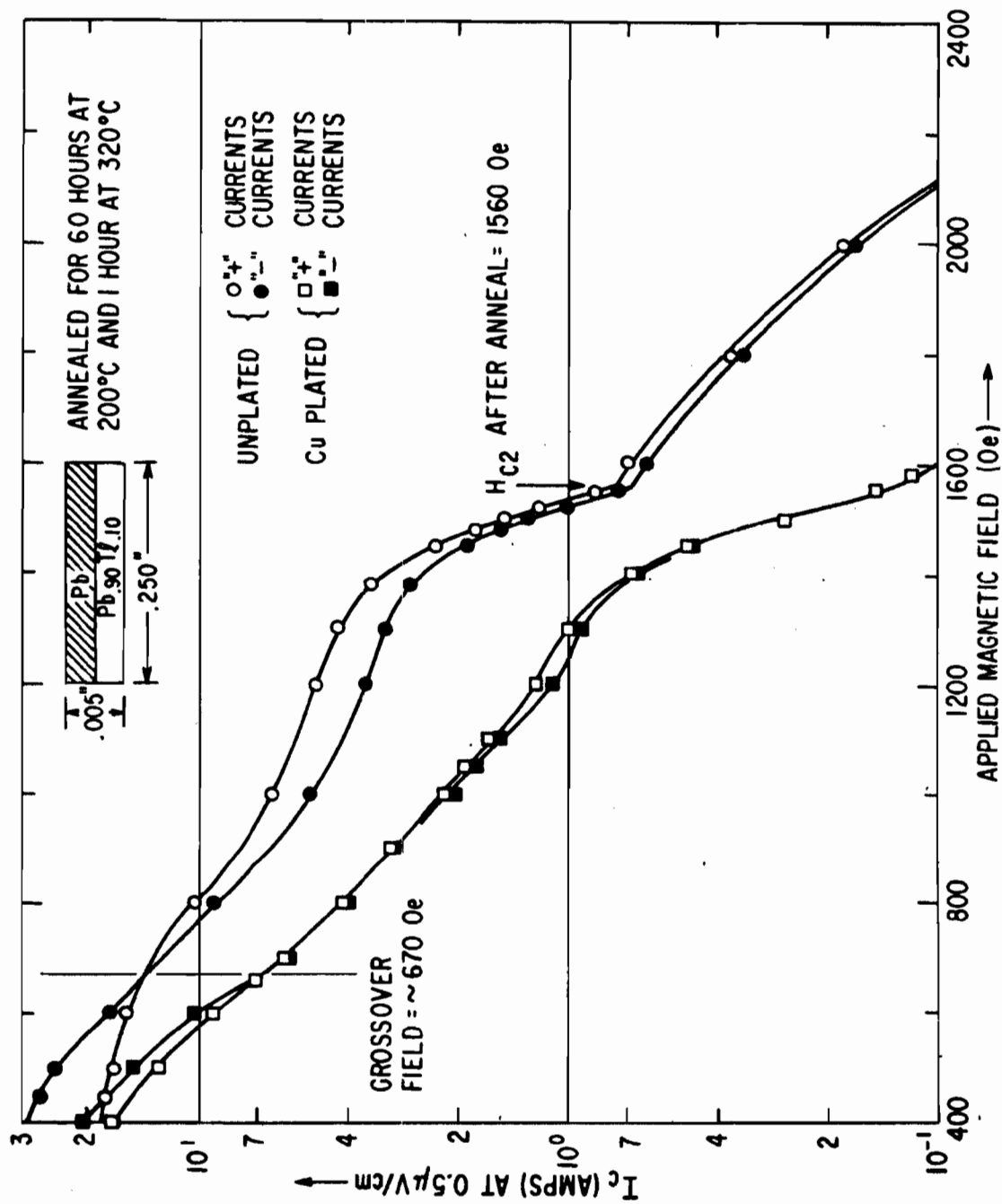
Figure B-6 The critical currents of an annealed Pb-Pb$_{0.90}$Tl$_{0.10}$ bimetallic strip before and after copperplating as a function of magnetic field applied parallel to the surface plane. Partial rectification is observed.
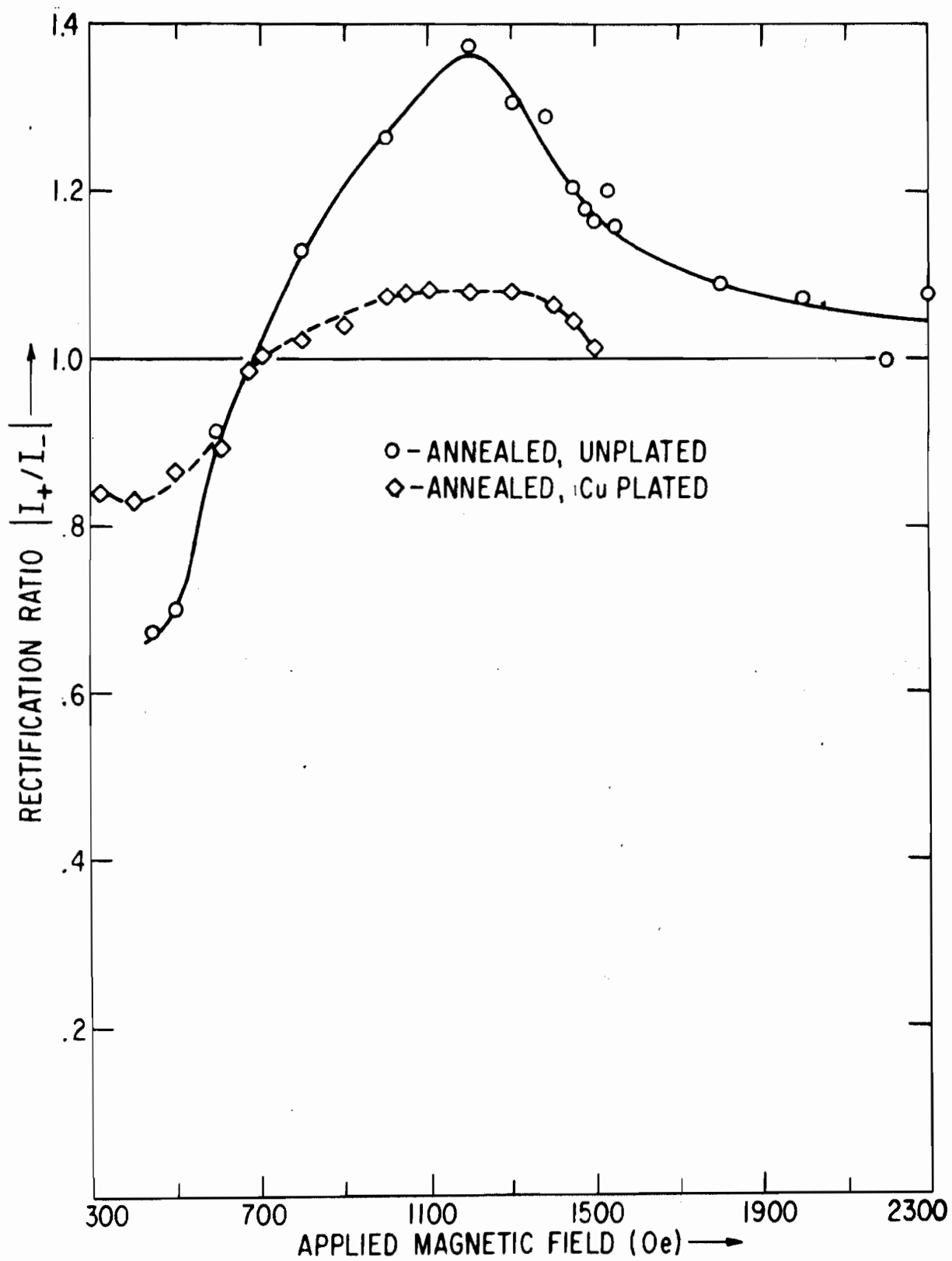
Figure B-7 The rectification ratio ($|I_+/I_-|$) vs applied magnetic field for the curves of Fig. B-6.

206
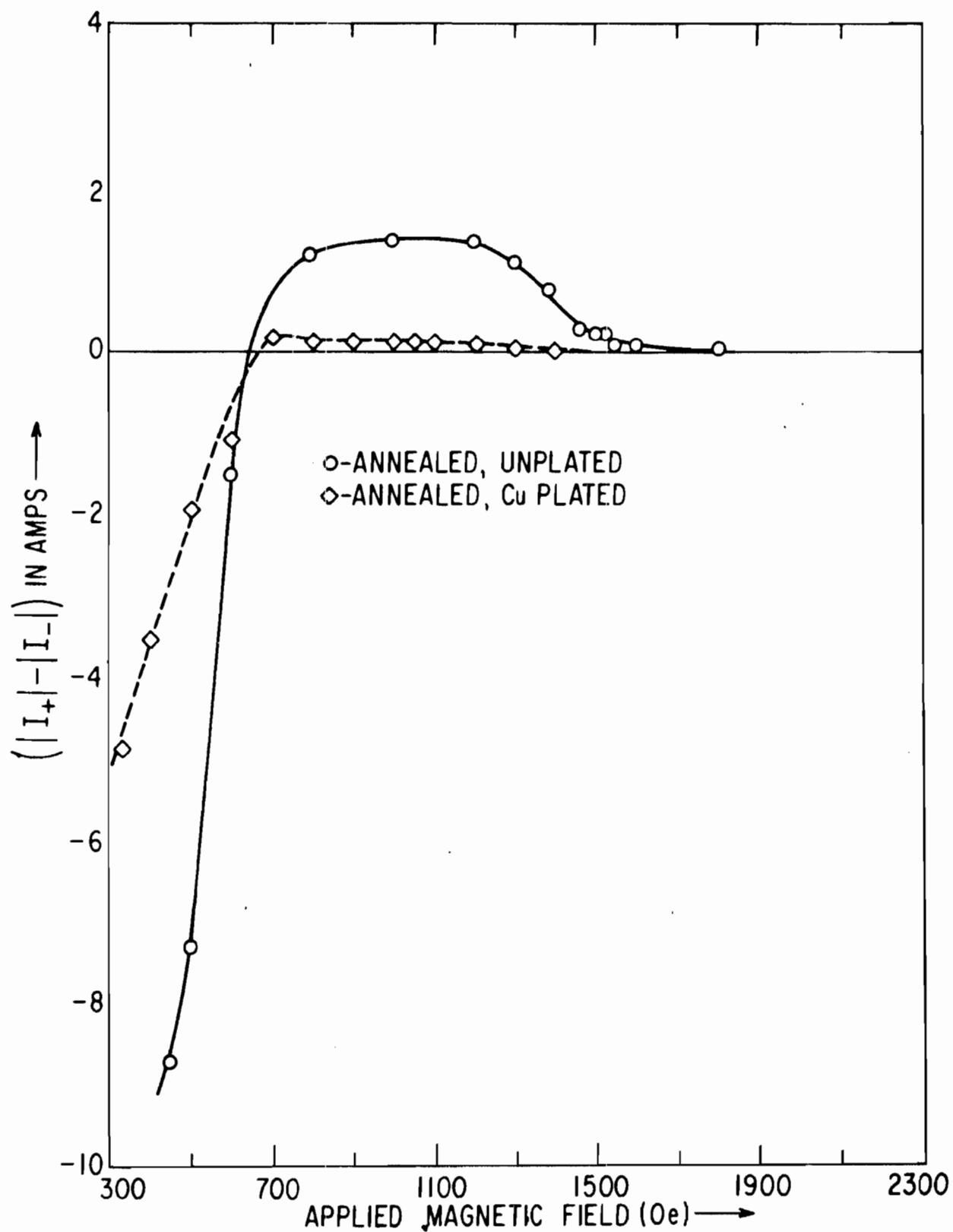
Figure B-8 The difference between critical currents of opposite polarity
($|I_+|$ - $|I_-|$) vs applied magnetic field for the curves of Fig. B-6.

(i) The critical currents of opposite polarity are <u>unequal</u> from the lowest field tested (400 Oe) to a field approaching 2400 Oe.

(ii) From 400 Oe to about 670 Oe the larger critical current corresponds to magnetic flux crossing the outer Pb surface from the outside-in.

(iii) The sense of the rectification switches at 670 Oe; between this crossover field and a field approaching 2400 Oe the larger critical currents correspond to magnetic flux crossing the outer $Pb_{0.90}Tl_{0.10}$ surface from the outside-in. Beyond the field of 2400 Oe the critical currents of both polarities were reduced to a few milliamperes, and it became impossible to detect any significant difference in their magnitudes.

(iv) An H_{c2}-type transition appears to take place at 1560 Oe.

(v) The rectification ratio assumes a maximum value of about 1.3:1 in the vicinity of 1200 Oe.

(vi) The rectification ratio shows no abrupt change at 1560 Oe (Fig. B-7).

(vii) The magnitude of the difference between the critical currents of opposite polarity (Fig. B-8) is changing sharply with field in the low field range and is essentially constant over the range between about 800 and 1200 Oe.

(e) <u>Experiment V</u>

The <u>same</u> strip used in Experiment IV is electroplated with a few microns of copper and retested. The significant results (see Figs. B-6 through B-8) are:

(i) The magnitude of the critical currents of both polarities is significantly reduced at all fields.

(ii) Both the relative (Fig. B-7) and absolute (Fig. B-8) difference between the critical currents of opposite polarity is significantly reduced.

(iii) The crossover field remains at about 670 Oe.

(iv) The critical currents of both polarities become too small (less than a few milliamperes) to detect beyond about 1700 Oe.

3. Discussion

Experiments I and II (Fig. B-3) are reference experiments for the three that follow. Experiment I demonstrates that a flat, polished, unannealed ribbon of type II superconductor will not rectify a transport current. Experiment I also shows (as reported earlier) that the H_{c2} transition is clearly recognizable on such an I_c vs H plot. Experiment II demonstrates that when a $Pb_{0.90}Tl_{0.10}$ ribbon is bonded to pure Pb at both surfaces, the effect is similar to that of copperplating (Refs. 4 and 8), i.e., the surface currents are decreased. The most significant result of Experiment II is that no rectification is measured.

Experiment III (Figs. B-4 and B-5) differs from Experiment II in that only one of the $Pb_{0.90}Tl_{0.10}$ surfaces is bonded to pure Pb. Consequently, the current-carrying capacity of one surface only is diminished. If the barrier

of each surface is insensitive to the direction in which magnetic flux crosses, then each surface will support a critical current that is independent of the direction of the transport current; and consequently the sum of these two currents, which is the total transport current, would not be rectified. On the other hand, if each surface barrier can be crossed more easily in one direction than in the other, and the barrier at one of the two surfaces is weaker (due to the proximity of pure Pb), then partial rectification should be observed. As Figs. B-4 and B-5 demonstrate, rectification is indeed observed and changes sense at about 600 Oe. As mentioned earlier, above about 600 Oe the larger of the two critical currents corresponds to magnetic flux crossing perpendicular to the free $Pb_{0.90}Tl_{0.10}$ surface from the outside-in. Correspondingly, below about 600 Oe, magnetic flux crosses the sample more easily in the opposite direction, as the sense of the rectification switches. These observations are consistent with the following two statements:

(a) Between H_{c1} and a field close to or equal to H_{c3}, magnetic flux can cross the surface barrier of a type II superconductor more easily from the inside of the specimen.

(b) Below H_c, magnetic flux can cross the surface barrier of a type I superconductor more easily from the inside of the specimen.

In Experiment III the magnitude of the rectification is probably diminished by the presence of the internal surface. Although the current-carrying capacity of the inner surface is less than that of the free surfaces (as Experiment II demonstrates), the sense of any rectification there probably opposes the rectification of the free outer surfaces. Further, since the ribbon used in Experiment III was not annealed, some portion of the total transport current must have been flowing in the bulk where rectification does not occur.

Experiment IV (Figs. B-6 through B-8) is designed to remove these complications. A bimetallic ribbon is well annealed (60 hours at 200°C and 1 hour at 300°C) to remove much of the bulk current-carrying capacity and to permit the internal boundary to become smeared through the diffusion that takes place at these elevated temperatures. As our earlier work shows, [4] the transport current-carrying capacity remaining is essentially that associated with the free surfaces. Calculations show that after this annealing treatment employed, a significant fraction of the thallium should diffuse from the thallium-rich side into the pure lead. The experimental results suggest that the H_{c2} transition at the thallium-rich surface is reduced to 1560 Oe, corresponding to a thallium concentration of 9.0% (upper arrow in Fig. B-9). The switch in the sense of the rectification at ~670 Oe suggests that at this field the second of the two surfaces is suddenly able to support an increased supercurrent. If we associate an H_{c2} of 670 Oe with the second surface, a thallium concentration of 1.6% is indicated (Fig. B-9). The excess of thallium (9.0% + 1.6% = 10.6%) over the 10% starting concentration that the sum of these surface concentrations indicate can be explained by a possible small difference in the initial thickness of the two metal layers. The sense of the rectification above 670 Oe is consistent with the

209
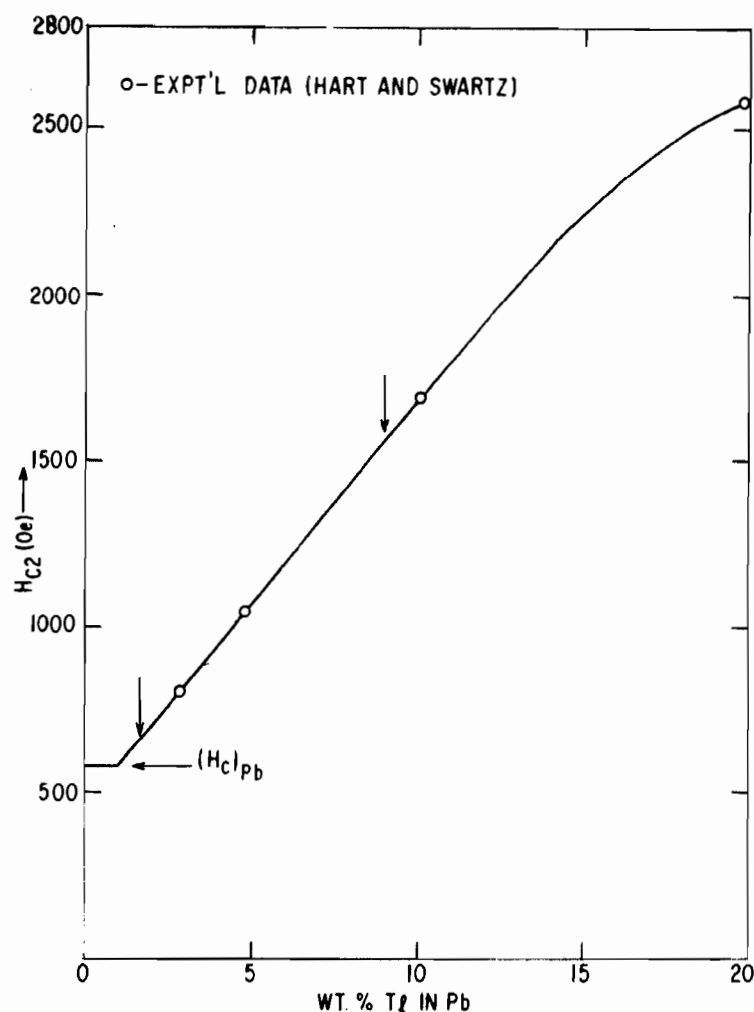
Figure B-9 The relationship between H_{c2} and the weight per cent of Tl in Pb as determined from the data of Hart and Swartz.[9] The arrows indicate the two values of H_{c2} suggested by the results of Experiments IV and V.

observations of Experiment III; namely, that magnetic flux crosses the surface barrier of a type II superconductor more easily from the inside. The greatly magnified rectification effect below 670 Oe, and, in the opposite sense, suggests that the absolute magnitude of the asymmetry in the barrier increases as one approaches type I behavior.

Experiment V provides conclusive evidence that the transport currents flowing in Experiment IV, and the associated rectification, are a surface phenomenon. When the ribbon of Experiment IV is copper electroplated and retested, the absolute magnitude of the critical transport currents of both polarities is significantly reduced. Further, both the absolute magnitude of the asymmetry in barrier height (Fig. B-8) and the relative magnitude of the asymmetry in the barrier (as measured by the rectification ratio and plotted in Fig. B-7) are substantially reduced. The "crossover field" of 670 Oe is

210

essentially unchanged (Figs. B-6 through B-8), suggesting that the copper is about equally effective on each surface.

Experiments I through V leave unanswered the question of the fundamental origin of the asymmetry of the surface barrier. Experiments I through V reveal only that the surface barrier can be crossed more easily from the inside in the particular geometries and systems explored. A recent calculation by Park predicts that the diamagnetic surface transport currents should be smaller than the paramagnetic currents. The experimentally measured ratio of the critical currents of opposite polarity are in essential agreement with Park's prediction, but the sign is wrong, i.e., we measure larger diamagnetic currents.

C. CLASS II RECTIFIERS

1. Principles of Operation

In this section, we shall show how the sharp dependence of the critical surface transport current on the angle that a perpendicular magnetic field makes with the surface leads naturally to partial rectification for certain geometries. Previous work[4] has shown that the magnitude of the critical surface transport current of a well-annealed $Pb_{0.95}Tl_{0.05}$ ribbon drops sharply as an applied magnetic field, of magnitude between H_{c1} and H_{c3}, is rotated into the plane of the surfaces. The critical transport current typically drops a factor of two when the magnetic field vector is rotated as little as $\sim 2°$ from its parallel alignment.

To begin, we assume that every element of the surface of a type II superconductor has the property suggested by the macroscopic sample, that the critical transport current-carrying capacity $I_{ce}(\varphi)$ of any small element of the surface drops sharply as the local magnetic field vector is rotated out of parallel alignment with the surface (Fig. B-10). Let us determine in a qualitative way the distribution of transport current across the width of a finite, plane macroscopic surface in the presence of an external magnetic field H applied parallel to the surface and perpendicular to the transport current [Fig. B-11(a)]. The element along the centerline of the strip always sees a local magnetic field parallel to its surface; consequently, the maximum transport current, $I_{ce}(0°)$, will flow there. This current produces a magnetic field that is perpendicular to all other surface elements. Thus the two surface elements adjacent to the centerline element will see a total magnetic field that has both a parallel (the applied field) and a perpendicular component, and consequently the resultant magnetic field vector will not be parallel to the surface of these two elements. Because of the assumed dependence of I_{ce} with angle, the current-carrying capacity of the two adjacent elements will be less than the current $I_{ce}(0°)$ that flows in the centerline element. When these arguments are carried out for all elements across the surface plane, it can be seen that the maximum transport current flows in the centerline element and that the current in all other elements decreases continuously with distance from the centerline element [schematically
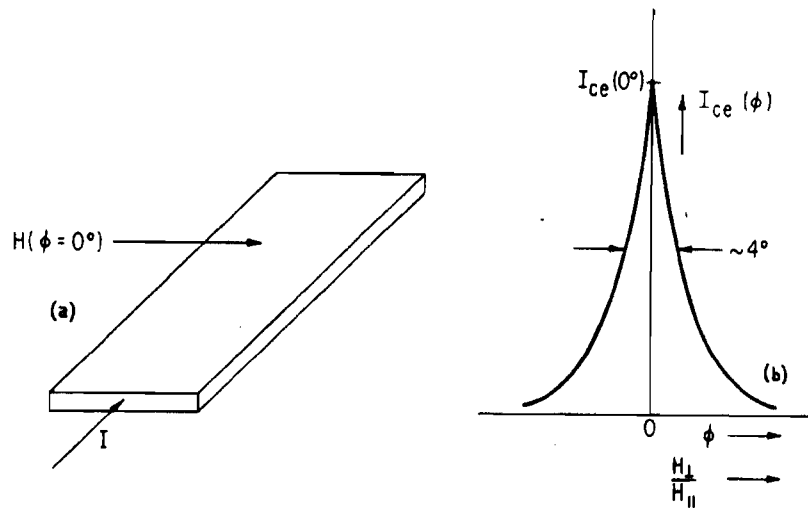
Figure B-10 (a) A schematic of the configuration of the ribbon and the applied magnetic field. (b) A plot of the critical surface transport current vs the angle that the applied magnetic field makes with the surface plane. Typically, the critical surface current drops by a factor of 2 when the magnetic field makes an angle of about 2° with the surface plane.
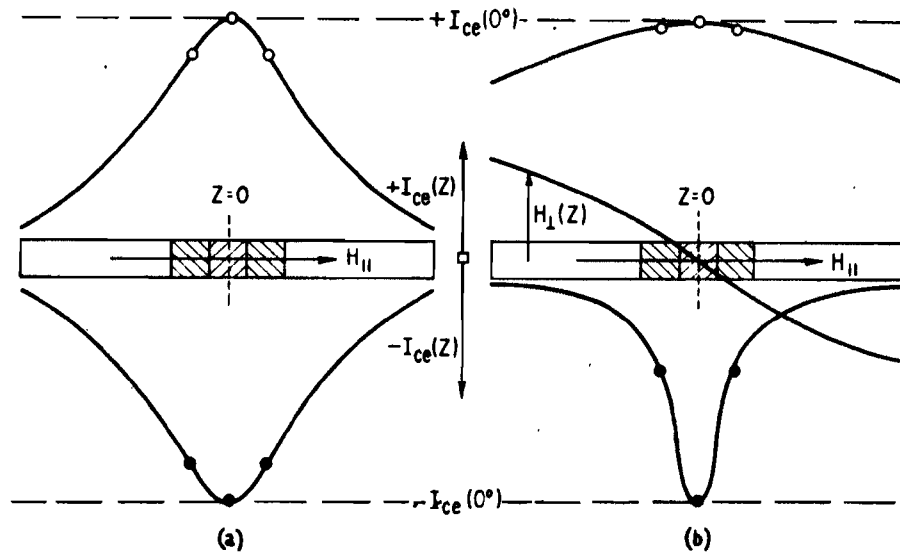
Figure B-11 (a) A schematic of the distribution of critical surface transport currents over the width of planar surface of finite width for the case that the applied magnetic field is everywhere parallel to the surface. No rectification occurs. (b) A schematic of the distribution of critical surface transport current over the width of a planar surface of finite width for the case that the applied magnetic field has a perpendicular component as shown. The total critical currents of opposite polarity are unequal and partial rectification occurs.

shown in Fig. B-11(a)]. The total transport current that a macroscopic surface composed of such elements will carry is the integral of the curve shown in Fig. B-11(a) and will not scale linearly with the width of the surface. Such a surface is not expected to rectify a transport current by this mechanism, as the arguments given above are independent of the polarity of the transport current.

Consider the same problem again with a slightly altered starting condition. In addition to the magnetic field applied parallel to the surface everywhere, we also apply a small perpendicular magnetic field $H_\perp(z)$ which will be zero along the centerline ($z = 0$) of the finite plane, will increase continuously with increasing distance from the centerline, and will have the symmetry that $H_\perp(+z) = -H_\perp(-z)$ [see Fig. B-11(b)]. The surface element along the centerline always sees only a magnetic field parallel to its surface, independent of the polarity of the transport current; consequently, the maximum transport current $I_{ce}(0°)$ will flow there. The current that can flow in all other surface elements, however, is polarity dependent in this situation. Currents in the centerline element of one polarity will produce a perpendicular magnetic field in each of the two adjacent elements that reduces the magnitude of the applied perpendicular magnetic field in both of these elements. Currents of the opposite polarity will produce a perpendicular field that increases the magnitude of the applied perpendicular magnetic field in each of the two adjacent elements. When these arguments are carried out for all surface elements, it is seen that the total current of one polarity will be larger than the total current of opposite polarity. The distribution of critical transport current of each polarity over the width of the surface will be qualitatively similar to that shown in Fig. B-11(b), and partial rectification will be observed.

2. Experiments

The foregoing arguments suggest a number of techniques by which partial rectification should be observable in type II superconductors. We require only that the current-carrying capacity decrease sharply with the perpendicular field component and that we have means available for externally applying a small perpendicular field that varies across the width of the plane in the manner indicated above. Two simple systems for satisfying these requirements are illustrated in Fig. B-12. In both cases we start with a type II ribbon in which the bulk currents, which tend to be insensitive to the angle that the applied field makes with the surface, are essentially decreased to zero by annealing. The remaining current-carrying capacity is that associated with the surfaces and is highly sensitive to the perpendicular field. In the first example the ribbon is planar, and a steady applied magnetic field is directed parallel to the surface and perpendicular to the long axis and the transport current direction. In addition, a small perpendicular magnetic field is produced by two wires laid parallel to the ribbon at its edges through which applied control current I_{con} is equally divided. [6] The magnitude of the perpendicular field is controlled by the magnitude of the control current. We carried out this experiment using a well-annealed $Pb_{0.95}Tl_{0.05}$ ribbon ($H_{c1} \approx 350$ Oe; $H_{c2} = 1030$ Oe) 0.250 inch

213
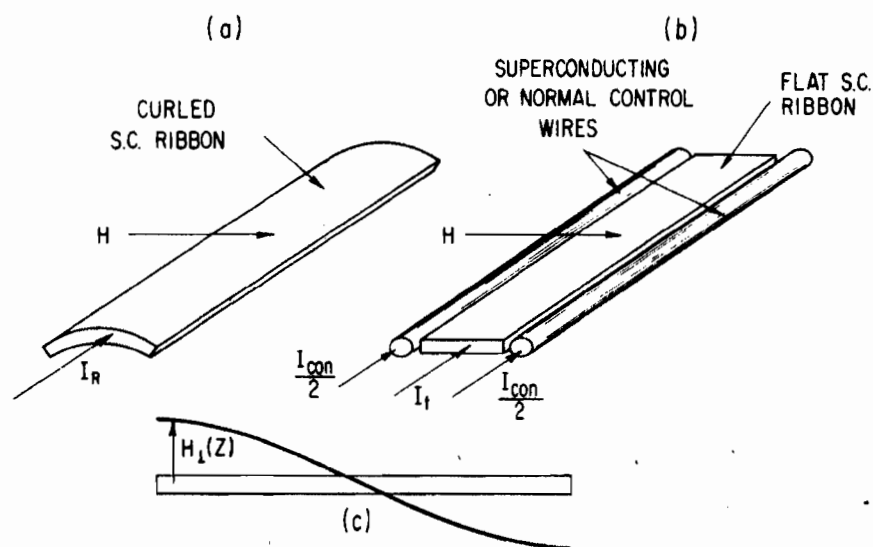
Figure B-12 Two arrangements of type II superconducting ribbons by which a perpendicular magnetic field distribution such as that shown in the lower portion of the diagram will be achieved.

wide for the superconductor and copper for the control wires. As I_{con} is increased, the critical transport current through the ribbon of the same polarity as the control current is increased, while the critical current of the opposite polarity is decreased. The results are shown in Fig. B-13 for a steady field of 400 Oe.

A second example is also illustrated in Fig. B-14. In this case, the ribbon is curled about its long axis. A magnetic field is rotated about the long axis. When $\varphi = 0°$ (applied magnetic field parallel to the chord of the arc), the applied magnetic field can be divided into parallel and perpendicular components that satisfy the criteria set down for partial rectification. The experiment was carried out using a well-annealed $Pb_{0.95}Tl_{0.05}$ ribbon 0.240 inch wide and wrapped on an insulating cylinder of 0.39-inch radius. Between the angles $\varphi = + 18°$ and $\varphi = -18°$, the applied magnetic field is tangent to some portion of the major surfaces of the ribbon. Some of the experimental results are shown in Fig. B-14 for applied fields of 400 and 900 Oe. In both fields, rectification begins at $\varphi = \pm 18°$, when the applied magnetic field first becomes parallel to some portion of the major surfaces of the ribbon. The rectification ratio increases until $\varphi = \pm 12°$ is reached in a field of 400 Oe and to $\varphi = \pm 16°$ in a field of 900 Oe. Between these limits the rectification ratio is essentially constant. The angular breadth of this plateau region is significant since it enables one to calculate the angular and fractional width of the surface that carries supercurrent. At 400 Oe the angular width of the current-carrying zone is $\sim 12°$, while at 900 Oe the angular width is reduced to $\sim 4°$.

214
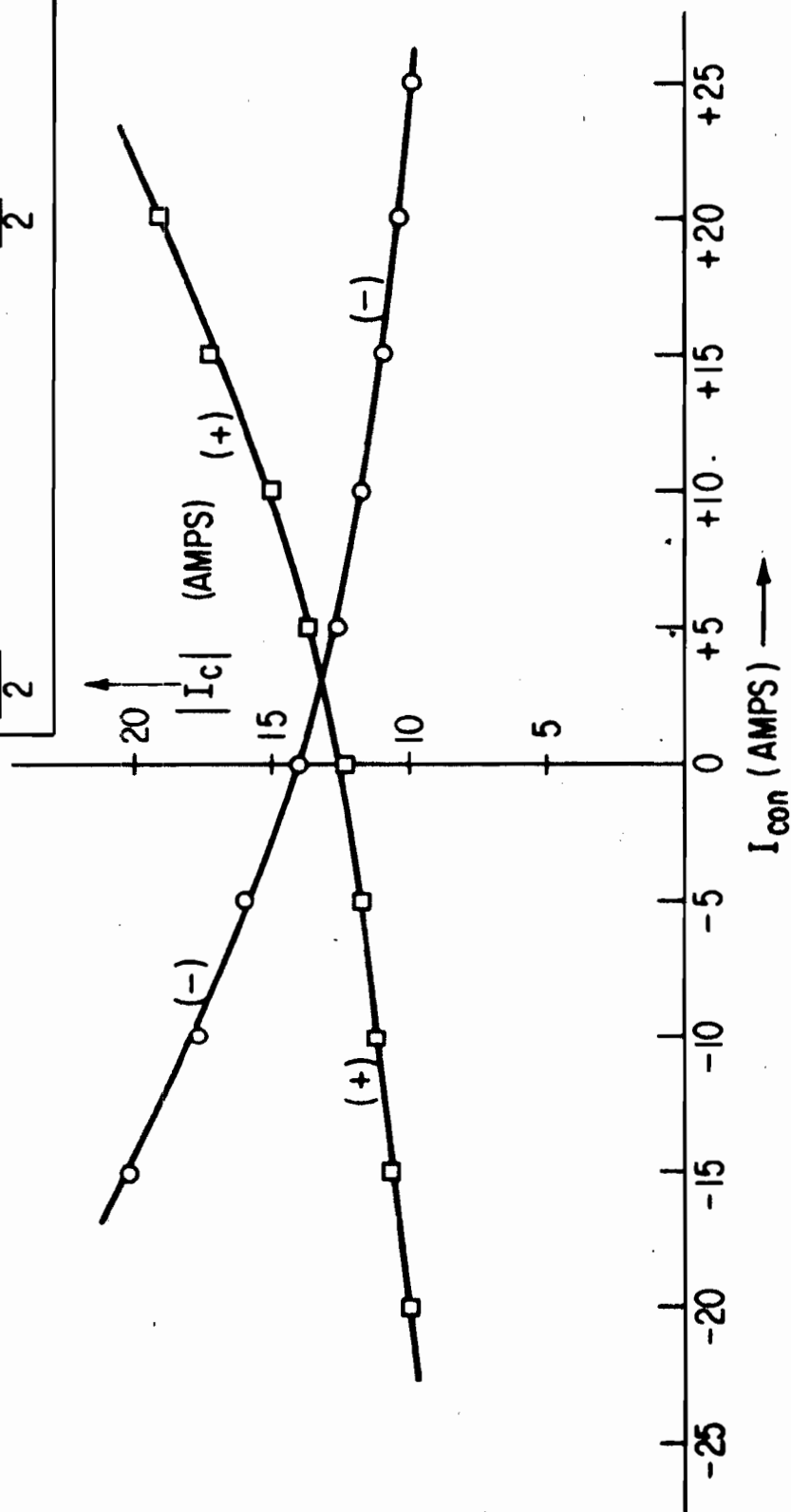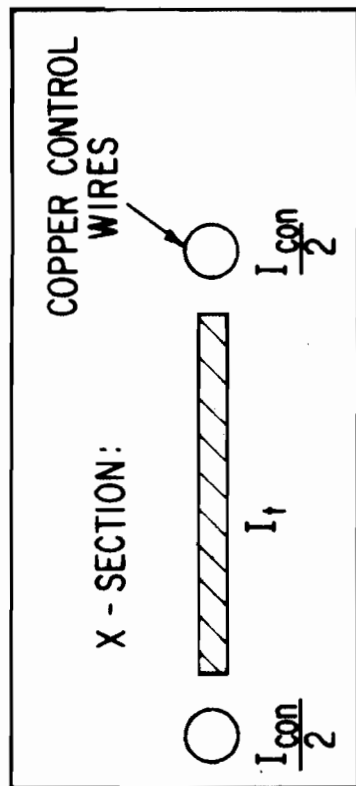
Figure B-13 The critical transport currents of opposite polarity in an annealed $Pb_{0.95}Tl_{0.05}$ ribbon vs the current in the control wires. The results demonstrate that partial rectification occurs in the presence of a perpendicular field distributed across the width of the strip in the manner shown in Fig. B-12.
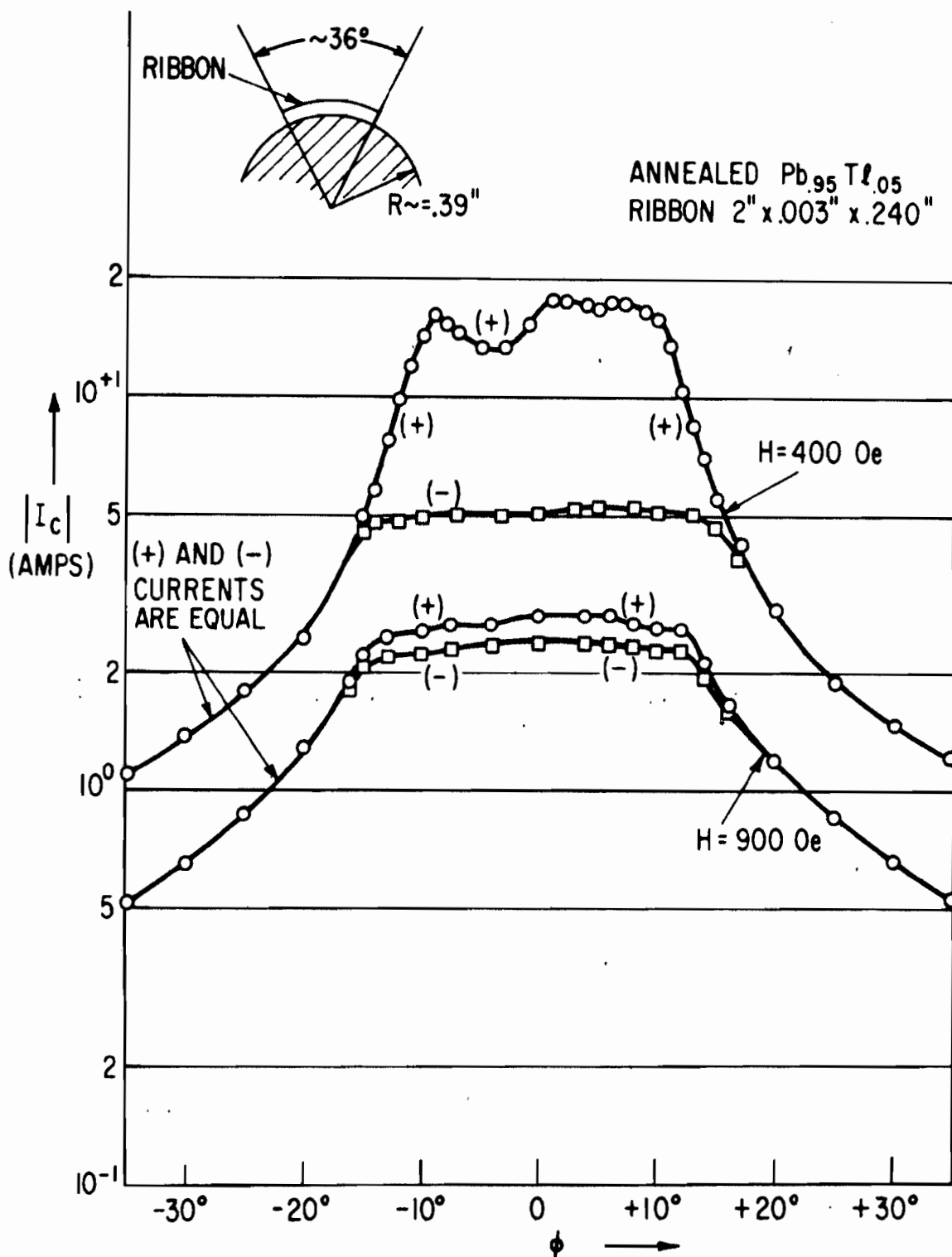
Figure B-14 The critical transport currents of opposite polarity in an annealed and curled $Pb_{0.95}Tl_{0.05}$ ribbon vs the angle that steady fields of 400 and 900 Oe make with the chord of the arc.   The results demonstrate that partial rectification occurs when the magnetic field becomes tangent to some portion of the major surfaces.

216

3. Discussion

The two experiments described above demonstrate that the mechanism for partial rectification proposed at the beginning of this section is valid. It is possible to go further than we have gone here and develop a mathematical framework for predicting the magnitude of the rectification ratio in class II rectifiers as a function of the parallel and perpendicular fields, the width of the surface carrying the current, and the critical surface current and its angular dependence.

One can imagine that such an analysis will suggest how the maximum rectification ratio can be achieved and, coupled with experiments, will reveal the magnitude and angular dependence of critical surface current density of a microscopic surface element. Such an analysis must presume, however, that experiments are reproducible. In spite of considerable effort on our part to develop recipes for preparing surfaces so that results can be accurately reproduced, we have found that both the magnitude of the critical surface supercurrents and their dependence on the angle of the applied magnetic field vector are sensitive beyond our control to surface preparation. Our best surfaces (achieved according to the recipes described in Ref. 4) give superconducting properties that are reproducible only to about a factor of two. In general, the smoother the surface on the microscopic scale, the sharper is the observed angular dependence of the critical surface transport current. Consequently, we are quite certain that the various numbers mentioned for critical surface currents and rectification ratios, both in this report and in our previous report, cannot be taken as a quantitative measure of fundamental surface properties; as more perfect surfaces are tested, the angular dependence will increase along with achievable rectification ratios. Since we have been able to achieve rectifications ratios in class II rectifiers of 5:1 without optimizing the various parameter and on a system with a less-than-perfect surface, it seems reasonable to guess that rectification ratios between 10:1 and 100:1 are possible.

An experiment reported in our earlier work[4] of rectification in a well-annealed triangular prism of $Pb_{0.95}Tl_{0.05}$ is reproduced in Fig. B-2. Here rectification ratios of ~3:1 are observed. We associate this rectification with a slight curvature of the three surfaces introduced during the polishing operation. Rectification comes about in the same way as it does in the curled ribbon discussed above.

We have repeated these experiments with the prism, taking great care to achieve planar surfaces. Under this condition, we are able to examine the properties of a single planar surface since transport currents in two surfaces are reduced essentially to zero when the magnetic field vector is parallel to the third surface. The prism then behaves as a class I rectifier, and rectification ratios in the range of 1.2:1 to 1.5:1 (results not displayed) are typically observed.

D. GENERAL REMARKS AND SUMMARY

In Section II we have shown that the ability of a type II superconductor to support a superconducting transport current in the mixed state is consistent with a barrier at the surface to the crossing of magnetic flux. Although we indicate that the height of the barrier may be measured experimentally by the critical transport current that the surface will support [Eq. (B1)], the actual barrier height is larger than what this expression suggests. This statement is supported by the arguments presented in Section C-1 that show that the transport current is not uniformly distributed over the surface when the critical current is achieved.

We have presented no argument to show that a surface barrier should exist. We have only presented experimental results showing that a surface barrier does exist and that two different properties associated with the barrier lead to two different classes of rectifiers. Class I rectification can be observed in certain geometries both in type I superconductors below H_c and in type II superconductors to a field close to or equal to H_{c3}. Partial rectification has recently been predicted by Park.[10] This predicted asymmetry is caused by the nonlinearity of the Ginzburg-Landau equations. The absolute magnitudes of the predicted and measured rectification ratios are in essential agreement. Unfortunately, the agreement between theory and experiment seems to end here. Our experimental measurements (1) show that the diamagnetic rather than the paramagnetic surface currents are larger;[10] (2) show that the critical surface currents as a function of magnetic field change significantly in slope at H_{c2}, contrary to prediction;[10-12] and (3) the measured critical surface currents between H_{c2} and H_{c3} are nearly an order of magnitude smaller than predicted.[10, 11]

In Section C we have shown that a second class of rectifiers can be produced from a superconductor in which the current-carrying capacity depends strongly on the angle that the magnetic field vector makes with some plane fixed within the superconductor. Because the barrier at the surface to the crossing of magnetic flux drops sharply with angle, the transport surface currents can be rectified.

It is important to note that a surface barrier that supports a superconducting transport current in the mixed state is inconsistent with a reversible magnetization curve. A reversible mixed-state magnetization implies that no bulk supercurrents and no bulk field gradients exist; for every surface field H, there is a unique internal field B that is in equilibrium with H, independent of the magnetic history of the sample. A transport surface supercurrent that flows on two symmetrically disposed surfaces (consider a ribbon geometry as an example) increases the magnetic field at one surface and decreases the magnetic field at the second surface; the internal magnetic field cannot be in equilibrium with each of these two different surface fields at the same time if the magnetization is reversible. This analysis suggests either (a) that the surface

218

transport current is not truly superconducting, and that magnetic flux creep across the surface barrier accounts for the reversibility observed in the d-c magnetization curves[13] of the mixed state; or (b) that the reversibility observed is a result of not having the magnetic field perfectly parallel to the surface everywhere. The results of our previous work indicate that the surface barrier drops sharply if the magnetic field is not perfectly aligned with the surface. Even if the applied magnetic field were everywhere parallel to the surface of the sample, however, the demagnetizing factor of the sample would still cause magnetic flux to break through the surface. Thus, if a true superconducting transport current does flow on the surface, the associated irreversible d-c magnetization curve should be observable only if great care is taken to assure that the total magnetic field is essentially parallel to the surface everywhere.

The experiments of Tomasch[14] and the theories of Marcus[15] and Fink[12] indicate that for magnetic fields of magnitude between H_{c1} and H_{c2} and parallel to the surface, there exists a superconducting surface sheath surrounding the Abrikosov[16] bulk mixed state. In this surface sheath the order parameter, or the density of superconducting electrons, remains very near its zero field value up to fields just below H_{c2}. It is presumably these superconducting electrons which, for a well-prepared surface, can carry transport supercurrents and which should give rise to an associated magnetic hysteresis.

NOTE ADDED IN PROOF

·A few further words of caution should be given to the experimentalist. In
the text, we point out that when the properties of a single surface are explored
the diamagnetic surface currents are found to be the larger. This type of
rectification, which we designate as class I, is apparently extremely sensitive
to surface condition. In more recent experiments we have often observed some
rectification in flat annealed strips and evaporated films. This rectification is
unexpected if the two surfaces are identical; we can account for this rectification
only by assuming that the two surfaces are different (perhaps one is rougher)
on a microscopic scale.

REFERENCES FOR APPENDIX B

1. J. D. Livingston and H. W. Schadler, Progr. Mat. Sci., $\underline{12}$, 183 (1964).

2. D. J. Sandiford and D. G. Schweitzer, Bull. Am. Phys. Soc., $\underline{10}$, 59 (1965); D. G. Schweitzer et al., ibid.

3. D. Saint-James and P. B. de Gennes, Phys. Letters, $\underline{7}$, 306 (1964).

4. P. S. Swartz and H. R. Hart, Jr., Phys. Rev., $\underline{137}$, A818 (1965).

5. P. S. Swartz and H. R. Hart, Jr., Bull. Am. Phys. Soc., $\underline{10}$, 59 (1965).

6. H. H. Edwards and V. L. Newhouse, J Appl. Phys., $\underline{33}$, 868 (1962).

7. P. W. Anderson and Y. B. Kim, Rev. Mod. Phys., $\underline{36}$, 39 (1964).

8. Y. B. Kim, C. F. Hempstead, and A. R. Strnad, ibid., p 43; C. F. Hempstead and Y. B. Kim, Phys. Rev. Letters, $\underline{12}$, 145 (1964).

9. H. R. Hart, Jr., and P. S. Swartz, Phys. Letters, $\underline{10}$, 40 (1964).

10. J. G. Park, Phys. Rev. Letters, $\underline{15}$, 352 (1965).

11. A. A. Abrikosov, Zh. Eksper. i. Teor Fiz., $\underline{47}$, 720 (1964); transl. Soviet Phys.--JETP, $\underline{20}$, 480 (1965).

12. H. J. Fink, Phys. Rev. Letters, $\underline{14}$, 309 (1965); ibid., $\underline{14}$, 853 (1965).

13. W. DeSorbo, Rev. Mod. Phys., $\underline{36}$, 90 (1964); T. F. Stromberg and C. A. Swenson, Bull. Am. Phys. Soc., $\underline{10}$, 358 (1965).

14. W. J. Tomasch, Phys. Letters, $\underline{9}$, 104 (1964).

15. P. Marcus, Conference on the Physics of Type II Superconductivity, Vol. III, Cleveland, Ohio (August 1964).

16. A. A. Abrikosov, J. Phys. Chem. Solids, $\underline{2}$, 199 (1957).

A COMPARISON OF THE HEAT GENERATION IN SUPERCONDUCTING
AND NONSUPERCONDUCTING HIGH FIELD A-C SOLENOIDS (P. S. Swartz)

In this Appendix, we address ourselves to the question of heat generation in the windings of multiturn a-c solenoids made both from pure aluminum and operated at 20.4°K and from high field superconductors and operated at some temperature below $\sim 18°$K (the highest T_C now known). It has already been shown[1] that the total power dissipation (including refrigeration requirements) is much less for pure aluminum or copper at the optimized temperature of $\sim 20°$K than at room temperature. These observations open the possibility of using pure nonsuperconducting metal at cryogenic temperatures for various a-c applications such as motors, generators, transformers, and the like. In the analysis below, we show that less power is required to operate an a-c cryogenic solenoid made from aluminum than from a high field superconductor.

In Section II of this report, Hart and Swartz have shown that the heat generated per unit winding length in a multiturn a-c solenoid made of hard superconductor is given as:

$$\left(\frac{P}{L}\right)_{s.c.} = \frac{5 \times 10^{-8} R H_0^2 f d\,(1 + \alpha^2/3)}{2\alpha} \quad \text{watts/cm,} \qquad (C1)$$

where

R   is the mean winding radius (in cm)

H_0 is the maximum solenoidal field (in Oe)

f   is the frequency (cps)

d   is the individual strand diameter (in cm)

α is a parameter that defines the applied transport current divided by the critical transport current $[I_c(H) = J_c(H)\pi d^2/4]$ averaged over the windings. The maximum value of α is unity. In solenoids in which the maximum design field is small $(<\sim 10^4$ Oe$)$, α will typically lie between 0.5 and 1.0. For high field solenoids, however, α will typically be 0.1 to 0.5.

In the text to follow we shall calculate the power losses in a cryogenic aluminum solenoid operating at 20°K (in liquid hydrogen) and compare the result with Eq. (C1).

We begin with the definition that

$$\rho_{20°} = \rho_{300°}/m \cong \frac{2.7 \times 10^{-6}}{m} \quad \text{ohm-cm} \qquad (C2)$$

where m is the resistivity ratio. We shall treat m as a variable that can assume any value over the practical range between unity and 10^3. The

calculation of heat generation in the windings depends on the diameter d of the individual current-carrying strand and on the dimension d relative to the skin depth λ and the electronic mean free path ℓ. We first write an expression for λ and ℓ in terms of m:

$$\lambda = \left(\frac{\rho_{20^\circ}}{\pi f \mu}\right)^{1/2} = \left(\frac{\rho_{300^\circ}}{\pi f \mu m}\right)^{1/2} \tag{C3}$$

taking

$$\rho_{300^\circ} = 2.7 \times 10^{-6}, \quad f = 60, \quad \mu = 1.25 \times 10^{-8}$$

we have

$$\lambda \approx m^{-1/2} \quad . \tag{C4}$$

Assuming that $1 < m < 10^3$, the limits on λ are given as

$$3 \times 10^{-2} \, cm < \lambda < 1 \, cm \quad . \tag{C5}$$

The calculation of the mean free path ℓ is also straightforward[2]

$$\ell \simeq \frac{10^{-11} m}{\rho_{300^\circ}} \approx 4 \times 10^{-6} m \quad . \tag{C6}$$

Assuming the same limits as before for m, then the limits on the mean free path are given as:

$$4 \times 10^{-6} \, cm < \ell < 4 \times 10^{-3} \, cm \quad . \tag{C7}$$

Equations (C5) and (C7) show that over the entire range of allowed values of $m, \ell < \lambda$. We now must consider the loss calculation for two cases, (1) where $\ell < d < \lambda$ (i.e., the "normal" situation), and (2) where $d < \ell < \lambda$ and the effective resistivity is determined by ℓ/d.

CASE I $(\ell < d < \lambda)$

The power or heat generation P/V (watts/cm^3) of a single wire exposed simultaneously to an alternating current density $j = j_0 \sin \omega t$ and alternating magnetic field $B = B_0 \sin \omega t$ is given as:

$$\frac{P}{V} = \frac{10^{-16}(B_0 \omega d)^2}{24\rho} + \frac{j_0^2 \rho}{2} \quad . \tag{C8}$$

The first term in Eq. (C8) represents the eddy current losses, and the second, the resistive heating. The total heat generation (watts/cm) per unit axial length in a multiturn solenoid whose mean radius $R \gg \Delta$, the winding thickness, and whose central field is $H = H_0 \sin \omega t$ can be derived from (C8) as

$$\frac{P}{L} = \left[\frac{10^{-6}(H_0\omega d)^2}{72\rho} + \frac{j_0^2\,\rho}{2} \right] A_m \tag{C9}$$

where $A_m(cm^2)$ is the conducting portion of the cross-section area of the windings. The resistivity that minimizes the total losses is found by setting $\frac{\partial}{\partial\rho}\,\frac{P}{L} = 0$ from which

$$\rho_{opt} = \frac{10^{-8} H_0\omega d}{6 j_0} \approx \frac{10^{-8} H_0 f d}{j_0} \tag{C10}$$

and from (C9) and (C10), the minimum power losses are given as

$$\frac{P}{L} = 10^{-8} H_0 f d j_0 A_m \quad . \tag{C11}$$

Equation (C11) will apply only for those wire diameters where the optimization of ρ [Eq. (C10)] places the resistivity ratio, m, within the allowed range $(1 < m < 10^3)$. We can derive a relationship between d and m in the following way.

From (C10),

$$m = \frac{10^8 j_0\,\rho_{300^\circ}}{H_0 f d} \quad . \tag{C12}$$

For $\rho_{300^\circ} = 2.7 \times 10^{-6}$ ohm-cm and, in the typical case where f = 60, Eq. (C12) simplifies to

$$m \approx \frac{4.5\,j_0}{H_0 d} \quad . \tag{C13}$$

A rough value of j_0/H_0 can be determined by the observation that, for typical cryogenic solenoids,

$$2 \times 10^3 \, Oe < H_0 < 2 \times 10^4 \, Oe$$

and

$$10^3 \, amp/cm^2 < j_0 < 10^4 \, amp/cm^2 \quad . \tag{C14}$$

Generally, the higher and lower values of H_0 and j_0 go together and we may take as an approximate median value $j_0/H_0 \sim 1/2$. Thus, in order for optimization of losses to be possible,

$$m \times d \approx 2.25 \, cm \quad . \tag{C15}$$

225

In order for the underlying Eq. (C9) to be valid, the condition that

$$\ell(=4 \times 10^{-6}m) < d < \lambda(=m^{-1/2}) \tag{C16}$$

must also be satisfied. Equations (C15) and (C16) together with the assumption that $1 < m < 10^3$ yield the limits on the wire diameter, d, for which Eq. (C11) is valid:

$$3 \times 10^{-3} \text{ cm} < d < .45 \text{ cm} \quad . \tag{C17}$$

We can put Eq. (C11) in a form comparable to Eq. (C1) as follows. For a solenoid whose mean winding radius, $R >> \Delta$, the winding thickness, then A_m is given as

$$A_m = 2\pi R \xi \Delta \tag{C18}$$

where ξ is the packing factor. For a solenoid whose length $L >> R$,

$$H_0 = \frac{4\pi}{10} \xi j_0 \Delta \tag{C19}$$

and from Eqs. (C18) and (C19)

$$A_m = \frac{5RH_0}{j_0} \quad . \tag{C20}$$

from Eqs. (C20) and (C11), we get for the heat generation in a cryogenic nonsuperconducting solenoid per unit axial length

$$\left(\frac{P}{L}\right)_{cryo} = 5 \times 10^{-8} RH_0^2 fd \text{ watts/cm} \tag{C21}$$

for 0.001 inch < d < 0.200 inch.

The heat production ratio between a superconducting solenoid operating below 18°K and a nonsuperconducting aluminum solenoid at 20.4°K is given from Eqs. (C1) and (C21) as

$$\frac{\left(\frac{P}{L}\right)_{s.c.}}{\left(\frac{P}{L}\right)_{cryo}} = \frac{(1 + \alpha^2/3)}{2\alpha} \approx \frac{1}{2\alpha} \quad . \tag{C22}$$

The minimum value that Eq. (C22) can adopt is 1/2 (for $\alpha = 1$). The implications of Eq. (C22) are discussed following the derivation of losses for the second case.

CASE II $(d < \ell < \lambda)$

Here the eddy current losses become much less than the resistive losses [see Eq. (C9)] if transposition is good. The losses in the solenoidal windings may then be approximated by

$$\frac{P}{L} \cong \frac{j_0^2 \rho_{eff} A_m}{2} = \frac{5RH_0 \rho_{eff} j_0}{2} \tag{C23}$$

where, [3] from Nordheim's formula,

$$\rho_{eff} \cong \rho_{20^\circ} \left(1 + \frac{\ell}{d}\right) . \tag{C24}$$

If we make the substitution that $10^{11} \rho_{20^\circ} \ell = 1$, then from Eq. (C24)

$$\rho_{eff} = \rho_{20^\circ} \left(1 + \frac{10^{-11}}{d\rho_{20^\circ}}\right) = 2.7 \times 10^{-6} \left(\frac{1}{m} + \frac{4 \times 10^{-6}}{m}\right) . \tag{C25}$$

For $d < \sim 4 \times 10^{-3}$ cm and $m_{max} = 10^3$, (C25) reduces to

$$\rho_{eff} \cong \frac{10^{-11}}{d} . \tag{C26}$$

From Eqs. (C23) and (C26)

$$\left(\frac{P}{L}\right)_{cryo} \approx 2.5 \times 10^{-11} \frac{RH_0 j_0}{d} \quad \text{watts/cm} \tag{C27}$$

for $d < \sim 0.001$ inch. From Eqs. (C1) and (C27) we get for the heat generation ratio

$$\frac{\left(\frac{P}{L}\right)_{s.c.}}{\left(\frac{P}{L}\right)_{cryo}} = \frac{10^3 H_0 fd^2}{\alpha j_0} . \tag{C28}$$

For the case where $f = 60$ and in general (as mentioned earlier) $H_0/j_0 \sim 2$, Eq. (C29) becomes

$$\frac{\left(\frac{P}{L}\right)_{s.c.}}{\left(\frac{P}{L}\right)_{cryo}} = \frac{1.2 \times 10^5 d^2}{\alpha} \tag{C29}$$

227

for $d < \sim 0.001$ inch.

DISCUSSION

It is interesting to summarize graphically the heat generation per unit axial length for each cryogenic and superconducting a-c solenoid. In Fig. C-1 we plot a normalized heat generation in units of $(5 \times 10^{-8} RH_0^2 fd)^{-1} \times P/L$ for the cryogenic a-c solenoid (aluminum at $20.4°K$) for each of the two cases treated and for the hard superconducting a-c solenoid. In order that we may plot Eq. (C27) in these normalized units, we make assumptions that $H_0/j_0 \sim 2$ and that $f = 60$, yielding

$$\left(\frac{P}{L}\right)_{cryo} \approx \frac{2 \times 10^{-13} RH_0^2 f}{d} \qquad (C30)$$

for $d < \sim 0.001$ inch.

The two solutions for the cryogenic solenoid are joined smoothly in the region of $d \sim 2 \times 10^{-3}$ cm, where neither solution is exactly correct. The heat generated for the hard superconducting solenoid is plotted for the most optimistic case (i.e., $\alpha = 1$).

Because the superconductor presumably will be operated at a temperature below $20.4°K$, more input power to the refrigeration system will therefore be required to remove a given heat loss from the superconducting solenoid. We estimate this refrigeration factor to be ~ 3 at $15°K$ and ~ 30 at $4.2°K$. Thus, for a superconductor operating at some temperature $T < 20.4°K$ to have a favorable loss compared to aluminum at $20.4°K$, it is necessary that the losses in the superconducting solenoid be smaller by a factor γ than the losses in the aluminum. The dashed curves in Fig. 1 represent the hard superconductor curve multipled by γ. In order for superconductors to be more favorable from a loss standpoint, a wire diameter must be chosen for which the losses in the superconductor fall below the minimum of the "cryogenic a-c solenoid" curve. Thus, if the superconductor is to be operated at $15°K$, the individual wire strand diameter must be less than $\sim 2 \times 10^{-3}$ cm (point (A)) to have lower losses than Al at $20.4°K$. At $4.2°K$, the superconducting strand must be less than $\sim 2 \times 10^{-4}$ cm (point (B)).

228
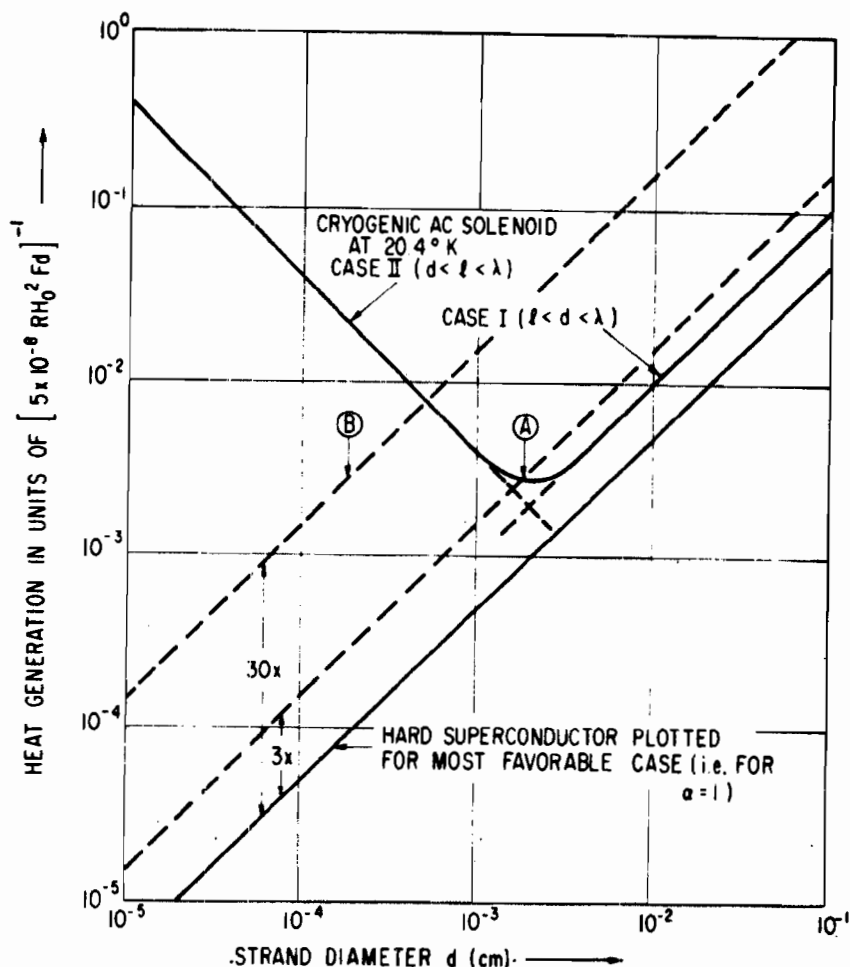
Figure C-1   The solid lines refer to the losses in a cryogenic a-c aluminum
solenoid operated near 20°K and a hard superconducting a-c solenoid
operated at any temperature below its critical temperature.   A further
discussion of the figure is found in the text.

SUMMARY

The calculations show that the power requirements of multiturn a-c
solenoids made from aluminum and operated at 20.4°K will have a lower total
power requirement than comparable a-c solenoids made of hard supercon-
ductor unless the individual superconducting strand is made less than some
very fine dimension that is of the order of 1μ to 10μ.   Since the technology
required to develop a reliable multiturn a-c solenoid from a hard supercon-
ductor is more difficult and expensive in many respects, it seems sensible
to favor aluminum for any a-c application requiring the production of high
a-c fields.

For application where only low a-c fields (a few kOe or less) are required,
the comparisons provided in this Appendix do not pertain.   Such a comparison

229

(not yet performed) will show that, from a loss standpoint, the hard super-conductor is the better performer.

ACKNOWLEDGMENTS

It is a pleasure to acknowledge helpful conversations with T. A. Buchhold, H. R. Hart, Jr. , and T. W. Moore.

REFERENCES

1. P. Burnier, Cryogenic Conf. , Houston, August 23-25, 1965. For an excellent series of papers on the electrical use of pure metals at low temperatures, see Rev. Gen. Elec. , 74, 609-647 (1965).

2. F. Montariol and R. Reich, Compt. Rend. , 254, 3357 (1962).

3. J. T. Olsen, Electron Transport in Metals, Interscience Publishers (1962), Chap. 4.

DOCUMENT CONTROL DATA - R&D

(Security classification of title, body of abstract and indexing annotation must be entered when the overall report is classified)

1. ORIGINATING ACTIVITY (Corporate author)	2a. REPORT SECURITY CLASSIFICATION
General Electric Research and Development Center General Electric Company Schenectady, New York	Unclassified
	2b. GROUP N/A

3. REPORT TITLE

A Research Investigation of the Factors that Affect the Superconducting Properties of Materials

4. DESCRIPTIVE NOTES *(Type of report and inclusive dates)*

Summary Technical Report   June 15, 1963 to October 15, 1965

5. AUTHOR(S) *(Last name, first name, initial)*

Bean, Charles P. et al.

6. REPORT DATE	7a. TOTAL NO. OF PAGES	7b. NO. OF REFS
March 1966	230	101

8a. CONTRACT OR GRANT NO.	9a. ORIGINATOR'S REPORT NUMBER(S)
AF 33(657)-11722	
b. PROJECT NO. 7371	66-GC-0325
c.	9b. OTHER REPORT NO(S) (Any other numbers that may be assigned this report)
d. BPSN 63-6899-7371-737102	AFML-TR-65-431

10. AVAILABILITY/LIMITATION NOTICES

This document is subject to special export controls and each transmittal to foreign governments or foreign nationals may be made only with prior approval of AFML (MAYP), WPAFB, Ohio 45433.

11. SUPPLEMENTARY NOTES	12. SPONSORING MILITARY ACTIVITY
	Air Force Materials Laboratory Research and Technology Division Wright-Patterson AFB, Ohio

13. ABSTRACT The extension of the critical state model (Bean model) of the homogeneous type II superconductor to include alternating field excitation, alternating current excitation, and rotating field excitation is reported. The alternating current and alternating field losses in intermetallic high critical current density superconductors have been measured in several experimental situations and found to be substantially as predicted. The surface flux penetration and alternating field losses in niobium have been measured below H_c^{xx} as functions of temperature, field, and surface preparation. The concepts of the critical state model have been used to determine the conditions necessary for a magnetic instability or flux jump to develop in a type II superconductor. The theory suggests several ways of forestalling or eliminating flux jumps. These critical state model and instability concepts have been extended to include the prediction of the critical transport current, often found to be much less than the product of critical current density and area. The angular dependence of the critical field of the superconducting surface sheath above H_{c2}^{xxx} has been measured as a function of the Ginzburg-Landau parameter $\varkappa$. The prediction of a surface barrier to the entry of flux into a type II superconductor in the case of a perfect surface is reported, and the experimental confirmation of this prediction is discussed. A new method has been developed for determining the critical current density of small amounts of superconducting material. A marked increase has been found in the critical current density of------

DD FORM 1473 (1 JAN 64)   xx

14. KEY WORDS	LINK A		LINK B		LINK C	
	ROLE	WT	ROLE	WT	ROLE	WT

INSTRUCTIONS

1. ORIGINATING ACTIVITY: Enter the name and address of the contractor, subcontractor, grantee, Department of Defense activity or other organization (*corporate author*) issuing the report.

2a. REPORT SECURITY CLASSIFICATION: Enter the overall security classification of the report. Indicate whether "Restricted Data" is included. Marking is to be in accordance with appropriate security regulations.

2b. GROUP: Automatic downgrading is specified in DoD Directive 5200.10 and Armed Forces Industrial Manual. Enter the group number. Also, when applicable, show that optional markings have been used for Group 3 and Group 4 as authorized.

3. REPORT TITLE: Enter the complete report title in all capital letters. Titles in all cases should be unclassified. If a meaningful title cannot be selected without classification, show title classification in all capitals in parenthesis immediately following the title.

4. DESCRIPTIVE NOTES: If appropriate, enter the type of report, e.g., interim, progress, summary, annual, or final. Give the inclusive dates when a specific reporting period is covered.

5. AUTHOR(S): Enter the name(s) of author(s) as shown on or in the report. Enter last name, first name, middle initial. If military, show rank and branch of service. The name of the principal author is an absolute minimum requirement.

6. REPORT DATE: Enter the date of the report as day, month, year; or month, year. If more than one date appears on the report, use date of publication.

7a. TOTAL NUMBER OF PAGES: The total page count should follow normal pagination procedures, i.e., enter the number of pages containing information.

7b. NUMBER OF REFERENCES: Enter the total number of references cited in the report.

8a. CONTRACT OR GRANT NUMBER: If appropriate, enter the applicable number of the contract or grant under which the report was written.

8b, 8c, & 8d. PROJECT NUMBER: Enter the appropriate military department identification, such as project number, subproject number, system numbers, task number, etc.

9a. ORIGINATOR'S REPORT NUMBER(S): Enter the official report number by which the document will be identified and controlled by the originating activity. This number must be unique to this report.

9b. OTHER REPORT NUMBER(S): If the report has been assigned any other report numbers (*either by the originator or by the sponsor*), also enter this number(s).

10. AVAILABILITY/LIMITATION NOTICES: Enter any limitations on further dissemination of the report, other than those imposed by security classification, using standard statements such as:

(1) "Qualified requesters may obtain copies of this report from DDC."

(2) "Foreign announcement and dissemination of this report by DDC is not authorized."

(3) "U. S. Government agencies may obtain copies of this report directly from DDC. Other qualified DDC users shall request through

_____ ."

(4) "U. S. military agencies may obtain copies of this report directly from DDC. Other qualified users shall request through

_____ ."

(5) "All distribution of this report is controlled. Qualified DDC users shall request through

_____ ."

If the report has been furnished to the Office of Technical Services, Department of Commerce, for sale to the public, indicate this fact and enter the price, if known.

11. SUPPLEMENTARY NOTES: Use for additional explanatory notes.

12. SPONSORING MILITARY ACTIVITY: Enter the name of the departmental project office or laboratory sponsoring (*paying for*) the research and development. Include address.

13. ABSTRACT: Enter an abstract giving a brief and factual summary of the document indicative of the report, even though it may also appear elsewhere in the body of the technical report. If additional space is required, a continuation sheet shall be attached.

It is highly desirable that the abstract of classified reports be unclassified. Each paragraph of the abstract shall end with an indication of the military security classification of the information in the paragraph, represented as (TS), (S), (C), or (U).

There is no limitation on the length of the abstract. However, the suggested length is from 150 to 225 words.

14. KEY WORDS: Key words are technically meaningful terms or short phrases that characterize a report and may be used as index entries for cataloging the report. Key words must be selected so that no security classification is required. Identifiers, such as equipment model designation, trade name, military project code name, geographic location, may be used as key words but will be followed by an indication of technical context. The assignment of links, rules, and weights is optional.

GPO 886-551

Abstract (continued)

intermetallic type II superconductors following fast neutron irradiation, or irradiation-induced fission of impurity nuclei. (Critical current densities as high as 2×10^6 amp/cm^2 at 30 kOe have been obtained.) Preliminary studies attempting to determine the relationship between metallurgical structure on a local scale and the critical current density are reported. In the Appendices, the following extensions of the above contract-supported studies are reported: the discovery of surface superconductivity in the mixed state, rectification in type II superconductors, and a technical comparison of cryogenic normal metals and inhomogeneous type II superconductors.